THE UNIVERSITY OF SHEFFIELD

In Situ Surface Studies of III-V Semiconductor Compounds

by

FAEBIAN BASTIMAN

A thesis submitted for the degree of Doctor of Philosophy

Department of Electronic and Electrical Engineering

June 2010

Abstract

Since its advent in the early 1980s, Scanning Tunnelling Microscopy (STM) has been used to advance the knowledge of semiconductor grow processes. Hybridisation of STM with other analytical methods and the Molecular Beam Epitaxy (MBE) growth technique allowed a flexible and diverse approach to growth front exploration. The first hybrid, limited the applicability of STM to *in vacuo* operation whereby the sample is rapidly cooled or "quenched" in an attempt to preserve the growing surface, before imaging can commence. This technique suffers dually from the unknown effects of the quenching procedure and the limiting ability to only capture frozen-in-time images of the surface.

The ultimate evolution of STM would be to allow concurrent or *in situ* MBE and STM operation. The ability to perform concurrent MBE and STM requires three basic criteria: accurate and stable control of the sample temperature, reliable and maintainable STM tunnelling tip procedures and controlled, sustained emission from the MBE effusion cells within the STM chamber.

Samples are slivers 8 x 1 mm^2 to 12 x 4 mm^2 of wafer mounted for either direct current heating or radiative pyrolytic boron nitride heating within the STM chamber. No direct temperature monitoring method is available and thus a myriad of techniques were employed to map the current-temperature response for samples including Reflection High Energy Electron Diffraction (RHEED), thermocouples and thermography, yielding a reliable heating profile.

Tunnelling tip fabrication involves manufacturing an atomically sharp tip via a two-step electrochemical etching and annealing procedure. An extensive and exhaustive investigation sought to produce a quantitative method for tip identification and etching parameterisation based on the available variables of differential sensitivity, etching voltage, immersion depth and etchant concentration. An optimised tip type transfer diagram of tip fabrication resulted, after which, an anneal algorithm was formulated resulting in clean, sharp tips without the side effect of apex distortion and melting.

Quality of the initial growth layer depends strongly on the clean-up conditions. As a prequel to growth, sample preparation methods are investigated via STM analysis to

determine the best preparation conditions in order to achieve high quality MBE growth in the STM chamber.

The final stage involves MBE source operation during STM. Initial investigation focused on flux alteration of surface reconstructions and allowed the effects of As_4 on the STM stage to be investigated. This is the first documented case where an e-beam As_4 source has been successfully operated within an STM system, during imaging.

The inclusion of group III elements in the evaporation flux proves unequivocally that III-V Molecular Beam Scanning Tunnelling Microscopy (MBSTM) is a realisable investigatory technique. Simultaneous deposition of In and As whilst imaging allowed dynamic observation of the InAs/GaAs wetting layer evolution on GaAs(001)-(2 × 4). The experiment followed initial heteroepitaxial growth through wetting layer evolution to the onset of 3D growth.

Acknowledgement

I would like to express my gratitude to my supervisor Prof. A. G. Cullis, first and foremost for offering me the opportunity to embark upon this pioneering project and secondly for remaining persistently optimistic and encouraging during the constant trials and tribulations, pitfalls and multiple (part-wise) destructions of this prototype kit. Furthermore I would like to thank Prof. M. Hopkinson for patiently enduring a barrage of MBE questions and offering the assistance of his staff and students in the NC.

I would like to extend deep thanks to R. Frith for constantly offering time and effort during the afore mentioned pitfalls and A. Walker and I. Lyne (and his workshop team) for patience and advice and generally contributing the little things to make the big things happen. Further to Y. Peng for taking time to indulge my request for FIB work and C. Celebi (University of Eindhoven) for enduring my many questions regarding tip fabrication.

Thanks to my good friend F. Stolze who thrust a thermography camera towards me and to K. Briston for the late nights on the TEM until we got it right. I would also like to G. Hill for his amicable acceptance of my SEM requests and J. Lin for believing in my machine and spending his last few days in the department burning that midnight oil.

Thanks too to the network of people who are indispensable within the department, H. Levesley (God bless her) and the other staff in the Semiconductors Group who I sought with the random questions only I could envisage.

Thanks to you all.

Faebian Bastiman

University of Sheffield

List of Publications

Conference Papers:

[1] **F. Bastiman,** A.G. Cullis, M. Hopkinson, M. Green, "Growth and *in vivo* STM of III-V Semiconductor Surfaces", Microscopy of Semiconducting Materials 2007, Proceedings of the 15th Conference (2008) 471

[2] **F. Bastiman**, A.G. Cullis, M. Hopkinson, "InAs/GaAs(001) Molecular Beam Epitaxial Growth in a Scanning Tunnelling Microscope" *J. Phys.: Conf. Ser.* **209** (2010) 012048

[3] **F. Bastiman**, R. Hogg, M. Skolnick, A.G. Cullis, M. Hopkinson, "Temperature dependence of Ga-assisted oxide desorption on GaAs(001)" *J. Phys.: Conf. Ser.* **209** (2010) 012066

Journal Papers:

[1] **F. Bastiman**, A.G. Cullis, M. Hopkinson, "GaAs(001) (2 × 4) to c(4 × 4) transformation observed in situ by STM during As flux irradiation", *Surf. Sci.* **603** (2009) 2398

[2] **F. Bastiman**, A.G. Cullis, M. Hopkinson, "As-rich reconstruction stability observed by high temperature scanning tunnelling microscopy", *J. Cryst. Grow.* **311** (2009) 4478

[3] **F. Bastiman,** A.G. Cullis, M. Hopkinson, "InAs/GaAs(001) wetting layer formation observed in situ by concurrent MBE and STM", *Surf. Sci.* **603** (2009) 3439

[4] **F. Bastiman**, R. Hogg, A.G. Cullis, M. Skolnick, M. Hopkinson, "Ga assisted oxide desorption on GaAs (001) studied by scanning tunnelling microscopy", *J. Cryst. Grow.* **312** (2010) 1687–1692

[5] **F. Bastiman**, A.G. Cullis, "GaAs(001) planarization after conventional oxide removal utilising self-governed InAs QD site selection", *Appl. Surf. Sci.* **256** (2010) 4269–4271

[6] **F. Bastiman**, K. Briston, A.G. Cullis, M. Hopkinson, "Two step optimized process for scanning tunnelling microscopy tip fabrication", *J. Vac. Sci. & Tech. B* **28** (2010) 371

[7] **F. Bastiman**, A.R. Mohmad, A.G. Cullis, J. P. R. David "Preservation of GaAs (001) epi-ready surface features" **submitted**

Contents

Chapter 1: Introduction

1.1 Background

A vast wealth of understanding in the III-V semiconductor growth field has been obtained in recent years due to the hybridisation of growth procedures and analytical techniques (LaBella et al. 2005). More specifically insight into technologically attractive InAs/GaAs growth phenomenon has received extensive research through the advent of *in vacuo* Molecular Beam Epitaxy (MBE) in combination with the powerful Scanning Tunnelling Microscopy (STM) imaging technique.

In GaAs homoepitaxy the emphasis has been placed on understanding the kinetics of the underlying growth mechanisms, focusing in detail on the various surface reconstructions and the transitions that occur during growth (LaBella et al. 2005). However with the unique properties attainable through heteroepitaxy, a more extensive study has applied the basic theorems of homoepitaxy to this more intricate and complicated growth area. Semiconductor lasers, waveguides, photodiodes and transistors are a number of devices that can be realised due to the precision of heteroepitaxial structures. The interfacial quality between successive epilayers is essential to high quality device performance, hence the investigation into alloying and interface degradation provided vital insight into the growth process.

The realisation of the quantum dot (QD) as an atom-like discrete energy structures initiated an in-depth study into the Stranski-Krastanov (S-K) growth phenomenon that produces a dense array of QD structures. *In vacuo* MBE-STM has been used extensively to this end, enabling a number of theorems to be hypothesised regarding the intricacies of the growth process. However the dissociative nature of *in vacuo* MBE-STM delineated the requirement for a quenching process whereby an as-grown sample requires rapid thermal cooling and transportation into the STM chamber before imaging can commence. The indeterminate effects of the quenching process, place any results obtained regarding the intricacies under serious debate.

A combined Scanning Tunnelling Molecular Beam Epitaxy (STMBE) system capable of imaging during a growth cycle would determine the effects of the quenching process and circumvent any induced effects. A successful STMBE system for group IV research is in existence (Voigtlander et al. 1993) however the complications of III-V compounds have led to limited success in this area (Tsukamoto et al. 2006). The hybridisation of MBE and STM heralds a new frontier for III-V research.

1.2 Aims Of Work

Concurrent MBE and STM requires the control of three parameters: sample temperature, molecular beam operation and tip manufacture/maintenance. These simple requisites become non-trivial when combined within a concurrent MBE and STM system.

Chapters 2 and 3 are background reviews of III-V semiconductor growth and experimental methods respectively. The recent advances in III-V surface studies have been focused around combination of MBE and analytical methods, STM and MBE being particularly suited because of the ability to grow and scan within the same vacuum system (*in vacuo*). It is the hybridisation of these techniques that generates complications for the already established methodologies of operation.

Chapter 4 explores the problems surrounding accurate temperature control. Firstly, this required accurate estimates extrapolated from heating curves. Secondly, to explore both absolute temperature and variation, a number of methods were employed including Reflection High Energy Electron Diffraction (RHEED), thermocouples and thermography. The ability to accurately apply a number of discrete temperatures in the 400 – 580 °C range is essential for the III-V MBE growth of interest.

In Chapter 5 an exhaustive investigation into tip manufacture via differential etching was undertaken to formulate a quantitative approach to the manufacture process continuing into cleaning and maintenance of tips. The tunnelling tip is crucial to STM operation, however detailed methods for the production of suitable tips are scarce and usually qualitative in content. With the added contamination of group III and V sources in the STM sub-system, tip production and maintenance are even more crucial.

With both sample temperature control and tunnelling tips manufacture procedures under control, the ability for concurrent MBE and STM requires the integration of evaporation sources within the STM system. Careful control and operation of these sources enables *in situ* operation to be realised offering real time investigation into all aspects of MBE surface growth characteristics.

With single source operation surface reconstruction changes under varied fluxes are accessible in the first instance before more detailed growth can be investigated with dual sources. Of particular interest are the particularities of the growth procedure during Stranski-Krastanov (S-K) transitions in heteroepitaxial InAs/GaAs growth.

As a prequel to growth, chapter 6 first compares conventional of oxide sublimation to the newly emerging Ga desorption clean-up technique for GaAs oxide removal. In continuation, sample preparation techniques are compared in order to establish the system's capability to grow high quality III-V surfaces.

Finally chapter 7 investigates current capabilities of e-beam source Molecular Beam Scanning Tunnelling Microscopy (MBSTM) operation presenting the potential of the methodology and describing the present limitations and advances offered by this technique. The chapter discusses high temperature STM operation and systematically progresses to operation with As flux and finally utilising both In and As. Operation under an As flux allows dynamic observation of reconstruction changes. The inclusion of In allows MBE to be performed directly under the STM tip allowing the InAs wetting layer evolution to be observed in real-time.

1.3 References

V.P. LaBella, M.R. Krause, Z. Ding and P.M. Thibado (2005) Surf. Sci. Rep. **60**(1-4): 1.
S. Tsukamoto, G.R. Bell and Y. Arakawa (2006) Micro-elec. J. **37**(12): 1498.
B. Voigtlander and A. Zinner (1993) Appl. Phys. Lett. **63**(22): 3055.

Chapter 2: III-V Crystallography and Surface Structures

This chapter forms a literary review of III-V semiconductor crystallography and surfaces, focusing primarily on homoepitaxial GaAs(001) and heteroepitaxial InAs/GaAs(001), extending into a more general group III-As discussion where appropriate. Sections **2.1, 2.3, 2.4, 2.4.1** and **2.4.4** explore specifically the recent insight provided by *in vacuo* STM and discuss areas where the *in situ* method proposed herein can expand upon recent works and enable the often numerous and conflicting respective theoretical models to be definitively differentiated.

2.1 GaAs Crystal Structure

GaAs, and more generally all group III-As semiconductor crystals, form a zinc-blende lattice. The zinc-blende structure is based on a cubic space group $F\bar{4}3m$ (Adachi 1992) in which lattice atoms are tetrahedrally bound (**Figure 2.1**) similar to the configuration of group IV diamond-type semiconductors.

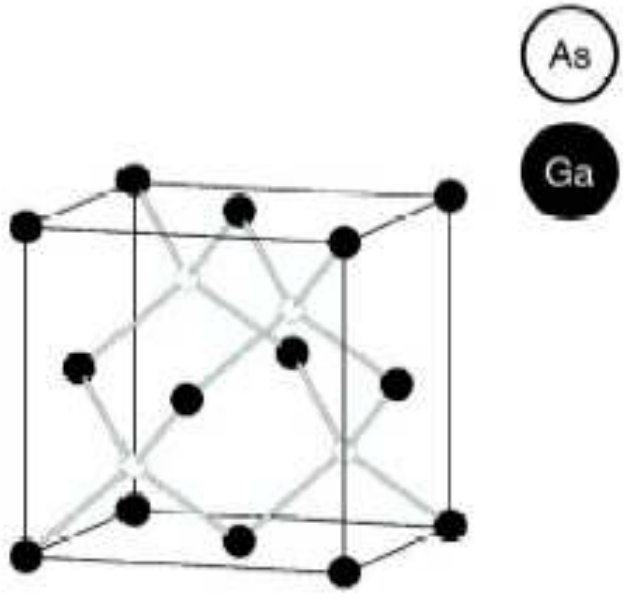

Figure 2.1: GaAs zinc-blende unit cell

Binding of the group III atoms' s^2p^1 configuration and the group V's s^2p^3 configuration result in an average of four valence electrons per atom. In the tetrahedral structure, each atom makes four nearest-neighbour bonds containing two spin paired electrons. Whilst both ionic and covalent bonding play a role, III-V compounds are largely assumed to behave as covalently bound materials with some ionic effects.

The lattice constant (a_0) is 5.6533 Å and 6.0584 Å for GaAs and InAs, respectively. The lattice constant can further be altered by the inclusion of impurity atoms in the crystal. Famously, results obtained by (Mullin et al. 1976) revealed dilation of the GaAs lattice induced by the incorporation of tellurium.

Nearest neighbour spacing between III(V) is 2.45 Å for GaAs and 2.62 Å for InAs, depicting the length of the bonds in the tetrahedron structure. The inter atomic distance of Ga-As and In-As varies by as little as 0.04 Å over the full possible range of InGaAs compositions (Boyce et al. 1982).

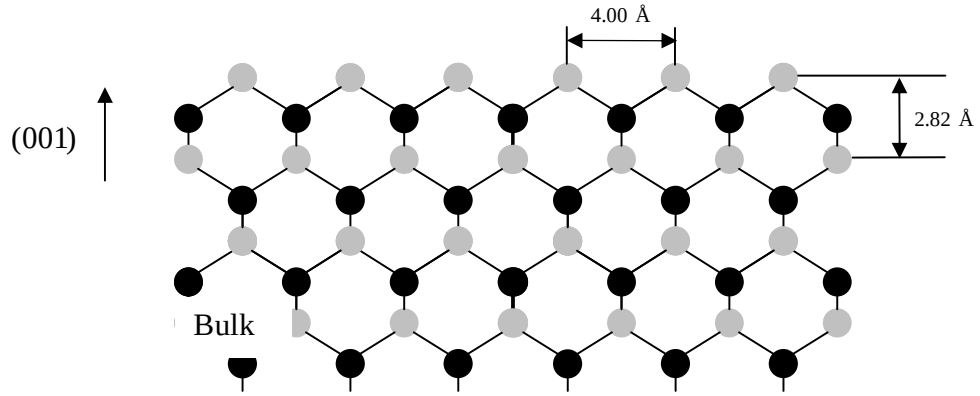

Figure 2.2: Cross-section of GaAs lattice structure perpendicular to (001) plane black (grey) circles represent As (Ga) atoms

The 7 % difference in lattice constant between GaAs and InAs, leads to highly strained heteroepitaxial layers (discussed in **2.4.1 Misfit Strain and Defects)** and the onset of S-K growth (discussed in **2.4.3 Stranski-Krastanov Transition**). Ga and As form bonds with a 1.41 Å length in the <001> direction. A monolayer consists of a Ga and As

bi-layer and thus has a height of 2.82 Å (LaBella et al. 2005). **Figure 2.2** depicts a 'perfect' lattice cross-section. The bulk is depicted by an ordered array of hexagonal cells, and the surface a seamless termination of this ordered pattern. In reality the bulk is infested with various defects causing divergence from this ideal (discussed in **2.4.1 Misfit Strain and Defects**) and the surface atoms reconfigure into various reconstructions to minimise their free energy (discussed in **2.2 GaAs Surface Reconstructions**).

2.2 GaAs Surface Reconstructions

Semiconductor surfaces exhibit reconstruction if their unit cell is greater than that of the underlying bulk solid, hence displaying a lower parallel symmetry (Duke 1996). The standard notation to describe these symmetrical structures (Unertl 1996) is given by GaAs(*hkl*)-($n \times m$), where hkl defines the lattice plane to which the reconstruction is parallel, with dimensions *n* times greater than the bulk in the *x* direction and *m* times greater in the *y* direction. Though a (1 × 1) reconstruction has the same spacing as the underlying bulk, the atoms therein move distances in the order of $^{1}/_{10}$s of angstroms compared to their position when bonded within the lattice. A (1 × 1) reconstruction is therefore more accurately termed 'relaxed' rather than 'reconstructed'. The distinction is noted for completeness, though the generic term 'reconstruct' will hereafter be used throughout.

Surfaces reconstruct in adherence to two principles: chemical bonding and charge neutrality (Duke 1996). A surface represents an abrupt termination of the lattice, hence a number of the bonds (discussed in section **2.1 GaAs Crystal Structure**) will be summarily broken, affecting an associated surface charge density containing a single unpaired electron. These so called 'dangling' bonds are shown schematically for GaAs in **Figure 2.3** for the 3 most commonly used crystal surface orientations.

The dangling bonds represent an inherent instability, hence atoms in the surface region relax and form new bonds in order to reduce the surface free energy. A structure which exhibits a local minima in the surface energy when the chemical atomicity (valency) of most atoms in that surface can be concluded to be satisfied. Most surfaces exhibit a number of local minima and thus a more rigorous method is needed to

determine which reconstruction occurs for a given situation, though each construct must adhere to the atomic chemical valency as stated.

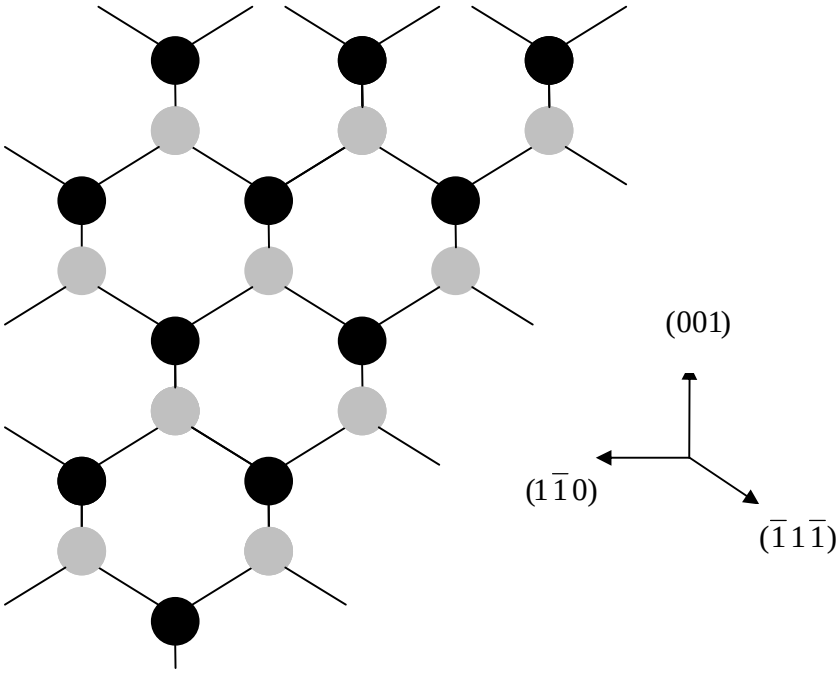

Figure 2.3: Cross-section of GaAs lattice normal to (001) plane. Black (Grey) circles indicate As (Ga) atoms, straight lines represent bonds.

Atomic position is but a single factor, generally reconstruction generates surfaces with different chemical composition from the bulk. Such compositions are governed by a requirement for neutral surface charge, limiting the number of allowed stoichiometries for a surface compound. The term autocompensated corresponds to an uncharged surface compound forming on an uncharged bulk lattice. Viewing the surface region as a new chemical compound whose only constraint is that its structure and composition must fit epitaxially onto the underlying bulk (Duke 1993) is a useful model to uncover the driving forces for reconstructions.

For autocompensated III-V tetrahedrally coordinated compounds three principles underpin the surface behaviour (Duke 1996; LaBella et al. 2005):

1. Lowest free energy vs. kinetic accessibility
2. Autocompensation leads to surface neutrality
3. Atomic geometry is determined by reduction of dangling bonds through rehybridization

The first principle allows for the condition that the surface observed depends on the process used to prepare the surface. Lowest free energy accesses a number of meta-stable local minima windows rather than a global minimum singularity. For compound semiconductors prepared by Molecular Beam Epitaxy (MBE) the processing steps can be varied by altering both beam pressure and substrate temperature, creating a 2D map of surface structures during growth on a Temperature vs. Ga/As flux ratio plot (**Figure 2.4)**.

Principle 2 calls upon all surfaces' unit cells to adhere to the Electron Counting Model (ECM). Comparing the dangling bond energies to the conduction-band minima and valance-band maxima reveals that Ga dangling bonds lie in the conduction band and should therefore be empty, similarly As dangling bonds lie in the valence band and should therefore be filled (Harrison 1980). The electron counting model requires that a surface structure is found where the number of available electrons in the surface layer exactly fills all the dangling-bond states in the valence band, leaving those in the conduction band empty (Pashley 1989). As stated, the restriction imposes allowed stoichiometries on a large but finite number of reconstructions and hence assumptions (theoretically or practically driven) are required on the nature of reconstructions. Furthermore, the ECM does not take into account the occurrence of transient, intermediate structures that do not obey the model though they could potentially affect the growth process (Joyce et al. 2004).

The third principle details the atomic geometries within the bounds of principle 2. The principle introduces the notion that a 2D surface compound epitaxially constrained to the underlying bulk will undergo surface chemical bonding as a result of delocalised electronic states. A common motif of this condition on (001) surfaces is the surface dimer which is back-bonded to two substrate species (**Figure 2.5**). Dimerization results in the formation of additional covalent bonds relative to the unreconstructed surface.

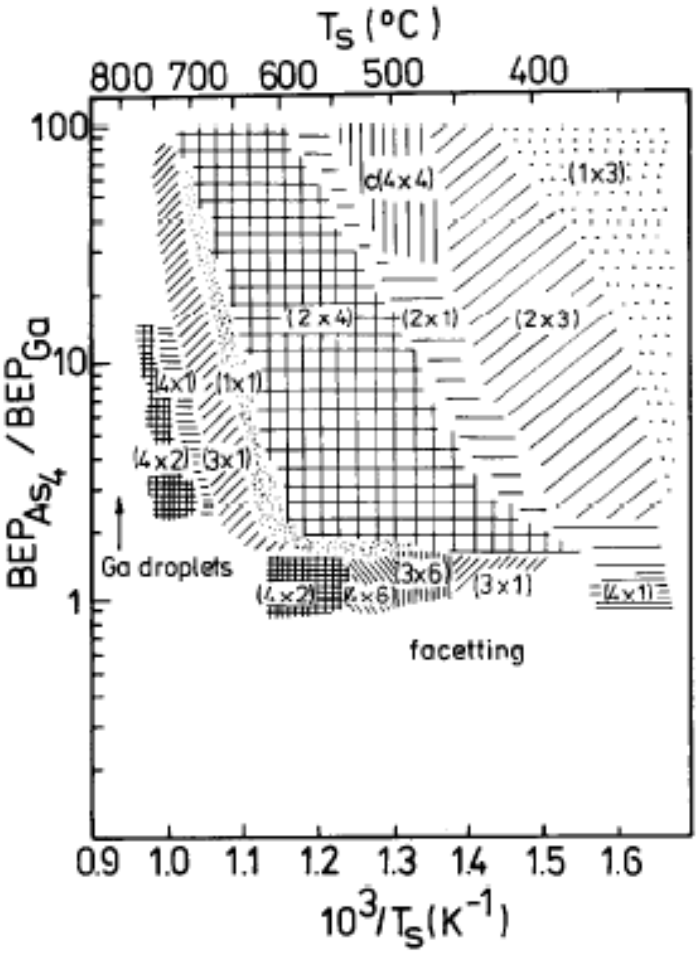

Figure 2.4: Surface phase diagram of GaAs(001) for MBE growth, taken from (Daweritz et al. 1990)

Initial work on GaAs(001) surface structures expanded upon earlier work on Si calculations (Appelbaum et al. 1976). Applying the ECM to the bonds of GaAs it is evident that group III (Ga) atoms donate 3 electrons to each of the 4 bonds, or 0.75 electrons per bond. Whereas group V (As) atoms donate 5 electrons to each of the 4 bonds, or 1.25 electrons per bond. Hence each As-Ga bond has 0.75 + 1.25 = 2 electrons per bond. Assuming an ideal lattice with broken bonds on the uppermost surface (**Figure 2.3**), a Ga terminated broken bond layer would contribute 0.75 electrons to each of its 2 back bonds, and hence has 3 – (2 × 0.75) = 1.5 electrons remaining to contribute to its broken bonds. Similarly As would contribute 1.25 electrons to a pair of back bonds, and

hence has 5 – (2 × 1.25) = 2.5 electrons to contribute to its broken bonds, constituting one filled band and one ¼ filled band per bond.

In order to accommodate these quarter fractions in filled bands, a unit cell must have an area equal to a multiple of 4. Hence, as mentioned earlier, the ECM has provided an area framework to which a detailed microscopic model is required to reveal an orientation (Appelbaum et al. 1976).

GaAs has been purported to have 11 reconstructions (Daweritz 1993), though notably most of these are transient in nature. For surfaces grown with increasing temperature (or decreasing As/Ga ratio) a series of 'stable' structures is formed. The distinction between 'transient' and 'stable' follows that 'stable' structures can be quenched to room temperature without altering the surface stoichiometry.

A number of phase progressions have been proposed:

c(4 × 4), c(2 × 8), (1 × 6), (4 × 6), c(8 × 2) (Cho 1971; Duke 1996)
c(4 × 4), c(2 × 8), (2 × 6), (4 × 6), c(8 × 2) (Biegelsen et al. 1990)
(1 × 3), (2 × 3), c(4 × 4), (2 × 1), (2 × 4), (1 × 1), (3 × 1), (4 × 1), (4 × 2) (Daweritz et al. 1990)
(2 × 4), (3 × 1), (4 × 2) (Yamaguchi et al. 1995)
(2 × 4), (3 × 1)/(3 × 6), (4 × 2) (Reginski et al. 1995)
c(4 × 4), c(2 × 8)/(2 × 4), (2 × 6), (4 × 6), c(8 × 2)/(4 × 2) (Kubby et al. 1996)
c(4 × 4), γ(2 × 4), β(2 × 4), α(2 × 4), (2 × 1) (LaBella et al. 2001a)
c(4 × 4), β2(2 × 4), (2 × 1) rough (LaBella et al. 2005)

The list does not represent a reduction in the number of surface structures, but more a honing toward the (2 × 4) domain. The mentioned (3 × 1) reconstruction, though stoichiometric, violates the ECM. The plethora of transitional reconstructions proclaimed between the generally accepted c(4 × 4), (2 × 4) and (4 × 2) reconstructions necessitate further investigation.

The c(4 × 4) surface has important niche high resistance (Whitaker 1993; Melloch et al. 1995) and ferromagnetic (Ohno et al. 1996; Dietl et al. 2001) applications. The most technologically important surface within the entire zinc-blende III-V semiconductor family is the As-rich GaAs(001)-(2 × 4)/c(2 × 8) surface (LaBella et al. 1999). As such it

has received an exhaustive study employing an expansive range of analytical tools and methods.

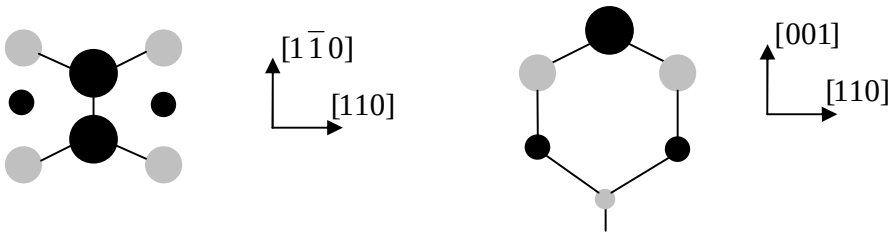

Figure 2.5: Plan and side view of As-As dimer on GaAs(001) surface
Black (grey) circles represent As (Ga) atoms

It should however be noted that the typical growth temperature for InAs quantum dots (QDs) occupies the c(4 × 4) to (2 × 4) transition temperature and that furthermore a c(4 × 4) reconstruction is sometimes reported immediately prior to the commencement of growth followed by an InGaAs alloy (n × 3) (Belk et al. 1997; Bell et al. 1999a) (discussed in **2.4.1 Misfit Strain**).

The (2 × 4) reconstruction was first observed by Low Energy Electron Diffraction (LEED) (Jona 1965), created by a combination of Ar ion bombardment and annealing at 500 °C. These initial observations were soon followed by homoepitaxial GaAs growth between 400 °C and 600 °C utilising a “three-temperature” method (Arthur 1968; Davey et al. 1968). A combination of MBE (discussed in **3.1 Molecular Beam Epitaxy**) and RHEED (discussed in **3.2 Reflection High Energy Electron Diffraction**) yielded the first observation of c(2 × 8) and c(8 × 2) surface reconstructions (Cho 1971; Chang et al. 1973). The combination of RHEED and MBE initiated a sudden wealth of understanding, most importantly that the observed reconstruction is a function of both substrate temperature and As:Ga ratio and, furthermore, that c(2 × 8) is As-terminated whereas c(8 × 2) is Ga-terminated.

Early work on surface stoichiometry (Arthur 1974) employed Auger Electron Spectroscopy (AES), Low Energy Electron Diffraction (LEED) and High Energy Electron Diffraction (HEED) revealing that 0.5 monolayer (ML) of As was lost in the transition from c(2 × 8) to c(8 × 2). Hence a reduction from ~0.5 - 0.6 to <0.1 ML.

Dimers were next incorporated to explain the 2× periodicity in the direction parallel to the dangling bonds (Cho 1976), yielding the result that As-dimers are parallel to the $[1\bar{1}0]$ direction. At this time the 4× periodicity was speculated to be either a result of vacancies or Fermi surface instabilities. Fermi surface instabilities were later proven to be an unlikely candidate (Appelbaum et al. 1976).

For several years additional methods confirmed but did not expound these basic models, until RHEED analysis (Joyce 1985) confirmed for the first time that c(2 × 8) and (2 × 4) reconstructions were distinct. Interpretation of the results lead to the conclusion that c(2 × 8) was constructed from out of phase (2 × 4) unit cells.

Missing As dimer models arose as a result of tight binding calculations (Chadi 1987; Frankel et al. 1987) supporting Cho's hypothesis that the 4× reconstruction arose from surface vacancies. The two non-metallic missing dimer models proposed were currently termed β(2 × 4) and β2(2 × 4). The β model results from a simple logical progression of the ECM: Each (2 × 4) cell can be considered to be an ideal Ga-terminated lattice with a number of As-dimers attached. Hence each As atom has 5 electrons available for bonding, so that an As-dimer has 10 electrons (Duke 1996). Two of these immediately occupy the As-As dimer bond and a further 4 are required to yield a full surface band state and $4 \times {}^{5}/_{4} = 5$ electrons are need to bond to the underlying substrate (back-bonding to the 4 available Ga sites). Hence each dimer requires one additional electron. Four Ga dangling bonds yield $4 \times ¾ = 3$ electrons, satisfying charge neutrality for 3 dimers in the unit cell. The β missing dimer model is shown in **Figure 2.6a**. On extension of the β model, the third dimer can be inserted into the third row and still satisfy the ECM model yielding the β2 model in **Figure 2.6b**. Both models have an As coverage of 0.75 ML.

Simultaneous HREELS and LEED studies (Frankel et al. 1987) confirmed an exposed As:Ga of 1.5, or that 6 As atoms were exposed for every 4 Ga atoms. Three models were independently produced. The first identical to the β model (**Figure 2.6a**), the second was the α model (**Figure 2.7a**) similar to the β2 model but with extra Ga in the trench and the third was the γ model (**Figure 2.7b**), an extension of the β model with an additional As-dimer rotated by 90° and positioned atop a pair of dimers.

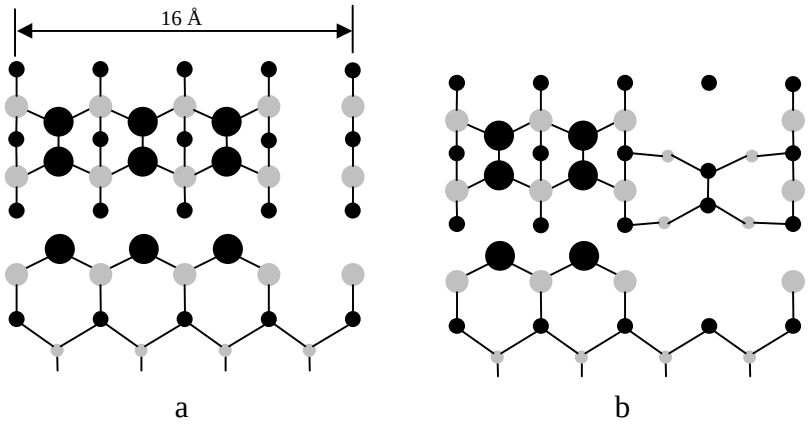

Figure 2.6: GaAs(001)-(2 × 4) missing dimer models a) β and b) β2

Investigations began thereafter to reveal which of the proposed models best captured the characteristics of the GaAs(001)-(2 × 4) surface. Two sequential papers (Larsen et al. 1988; Qian et al. 1988) concluded that:

1. The surface is non-metallic
2. 1 ML As surfaces are metallic
3. 0.5 – 0.75 ML of As coverage are non-metallic with lowest energy
4. The β model (0.75 ML) gives best match to photoemission data
5. Dimerization lowers the surface energy by 1.7 eV per dimer
6. Asymmetric dimers have higher energy than symmetric ones

In vacuo Scanning Tunnelling Microscopy (STM) images (Biegelsen et al. 1990) confirmed missing rows consistent with the β model, though results indicated out-of-phase (2 × 4) domains constituting larger c(2 × 8) reconstruction domains. Annealing at higher temperatures was purported to produce two As-dimers and two missing dimers consistent with both the β2 or α model.

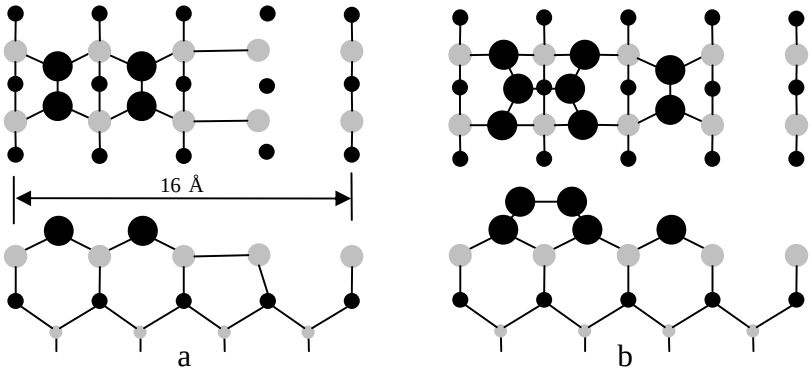

Figure 2.7: GaAs(001)-(2 × 4) additional dimer models a) α and b) γ

RHEED investigations along the [$\bar{1}$10] (4×) direction (Farrell et al. 1990) identified 3 distinct phases (namely α, β and γ). Both α and γ yielded similar diffraction patterns and formed a sandwich around the β phase. It was not noted at the time that the α and γ phases might represent transitional phases from β(2 × 4) to (4 × 2) and c(4 × 4) to β(2 × 4) respectively. Neither α or γ models had been confirmed by STM at this time.

STM images (Tanaka et al. 1991; Ohkouchi et al. 1994) agreed with total energy calculations (Ohno 1993), Density Functional Theory (DFT) (Northrup et al. 1993) and RHEED rocking curve analysis (McCoy et al. 1993) that the β (three dimer) model was most favourable. Whilst contradictory STM images (Pashley et al. 1992a; Pashley et al. 1992b) agreed with Scanning Tunnelling Spectroscopy (STS) (Bressler-Hill et al. 1992), DFT (Northrup et al. 1994; Moll et al. 1996; Ohno 1996) and total energy calculations (Schmidt et al. 2000) confirming that β2 was most favourable, and furthermore that the α model had a very small window and that the γ model was inaccessible, shown diagrammatically in **Figure 2.8**. Different preparation conditions were argued to defend the conflicting reports, though it is entirely plausible that the filled dangling bond orbitals of the As dimers in the top layer extended into the trench in STM images heralded as 3-dimer (β model), obscuring the actual 2-dimer (β2 model) reconstruction (Kratzer et al. 1999).

Further STM studies (Hashizume et al. 1994; Hashizume et al. 1995; Ichimiya et al. 1995; Xue et al. 1997b; Xue et al. 1999) set out to determine the nature of the α, β and γ phases. All images revealed two-dimers and two-missing-dimers per unit cell, with the

α and γ phases displaying long range disorder in the form of kinks and unit cell vacancies. Simultaneous dynamical RHEED revealed:

1. The three-dimer β model and the γ model could not account for the RHEED patterns
2. The calculated β2 RHEED pattern best agreed with the β-phase
3. The calculated α RHEED pattern best agreed with the α-phase
4. The calculated γ RHEED pattern had no fitting structural model

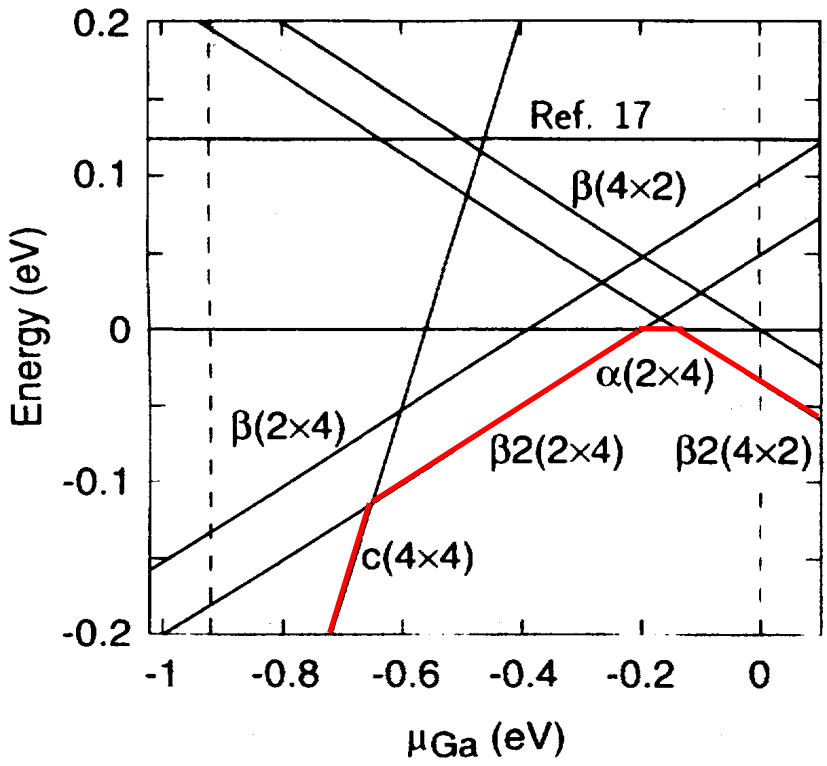

Figure 2.8: Formation energy for unit cell as a function of Ga chemical potential (μGa), adapted from (Northrup et al. 1994). Red line indicates equilibrium phases.

These results were expanded upon by further *in vacuo* STM (Broekman et al. 1995) confirming that the γ phase could not be explained by any previous model. Observations of disorder, kinks and trenches spanning several lattice constants in the γ phase led to the

conclusion that the γ phase was a combination of β-phase and c(4 × 4) structures. (Avery et al. 1995; Avery et al. 1996).

Finally STM images with sample biases of -3.0 V and -2.1 V revealed an electronic tip-sample effect (LaBella et al. 1999; LaBella et al. 2001b) exploited to reveal an out of phase As-dimer in the trench, in keeping with the β2 model.

Current theories hold that c(4 × 4) reconstruction evolves to β2(2 × 4) via a transient γ phase. β2 subsequently is thought to span the entire β phase until roughening evolves through an α phase to a (2 × 1) structure (LaBella et al. 2005). *In situ* STM can utilise the As:Ga flux ratio dependence of these reconstructions to explore and explain:

1. The relative widths of the α, β2 and γ phases as a function of flux
2. The special preparation conditions (if any) that lead to the observation of either c(2 × 8) or β(2 × 4) over the preferred β2(2 × 4) reconstruction.

2.3 Homoepitaxy

Epitaxy is the growth of crystal/mineral layers on the face of a substrate, such that the crystalline substrates of both materials have the same structural orientation. Homoepitaxy involves the growth of epitaxial layers of the same chemical species as the underlying substrate. GaAs(001)-(2 × 4) has been one of the most intensively studied surfaces of the last 30 years (Joyce et al. 2004). Despite this avid attention, fundamental questions remain concerning growth kinetics and mechanisms. All growth considered herein is based on Molecular Beam Epitaxy (MBE) discussed in section **3.1 Molecular Beam Epitaxy.**

2.3.1 Arsenic Incorporation Principles

Homoepitaxy of GaAs can utilise either As_2 or As_4 as the group V species. The Ga atoms and $As_{2,4}$ molecules undergo adsorption, desorption and migration before being incorporated into the growing lattice. Originally As_2 was produced by evaporating GaAs

within a standard effusion cell (Joyce 1985) though this technique led to ~15% Ga in the As_2 flux. It is more recently standard practice to utilise an As cracker loaded with metallic As crystals (see **section 3.1.1** for further details).

For growth with As_2, the incorporation coefficient of As_2 (S_{As_2}) is zero in the absence of a surface Ga population (Arthur 1968). The relative As:Ga flux ratio ($J_{As_2} : J_{Ga}$) has a notable effect on S_{As_2}. For $J_{Ga} < J_{As_2}$, S_{As_2} is proportional to J_{Ga} (Foxon et al. 1977). Under this regime each Ga atom interacts with an As atom, and excess As_2 is lost via desorption. S_{As_2} has a maximum value of unity when Ga is supplied in excess (when $J_{Ga} > 2 J_{As_2}$).

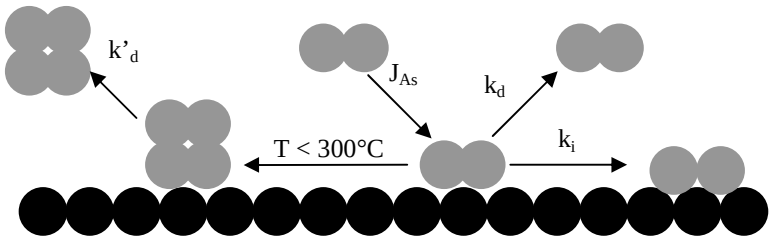

Figure 2.9: Schematic of As_2 incorporation on GaAs(001) adapted from (Tok et al. 1997)

A model for the incorporation process of As_2 involves a precursor state or reservoir termed As_2*, without which unrealistically high flux ratios J_{As}:J_{Ga} of 50 - 100 are necessary to model growth (Kratzer et al. 2003). Typical values used in MBE range from 2-10. The As_2 incorporation kinetics can be given as:

$$As_{2(v)} \underset{k_d}{\overset{J_{As}}{\rightleftharpoons}} As_2^* \xrightarrow{k_i} As_{2(l)}$$

Where $As_{2(v)}$ represents As_2 in the vapour phase, $As_{2(l)}$ represents As_2 incorporated into the lattice and k_d, k_i are the rate constants for desorption and incorporation respectively.

This is shown schematically in **Figure 2.9**. For growth under 300 °C and with J_{Ga} = 0, a fraction of the As_2 associates on the surface to form As_4, with a rate constant given by k'_d. Notably no As_4 was detected above this temperature.

Both the incident and desorbing flux contain no As single atoms (Arthur 1967), which implies that the As_2 incorporation is a first-order pair-wise reaction (Foxon et al. 1977). The role of a mobile Ga-As_2 molecule in growing layer (Fukunishi et al. 1993) is supported by an argument of very low formation energy, however since the desorbing flux contains no trace of these molecules it can only be argued that they dissociate before desorbing and that the molecular beams only react on the substrate surface and not whilst in transit.

For growth with As_4, early work revealed As_4 is mobile down to -200 °C while desorbing rapidly at 250 °C (Arthur 1966). By direct comparison to As_2, the As_4 reaction kinetics are notably more complex. As with As_2, in the absence of a Ga surface population the sticking coefficient of As_4 (S_{As_4}) is zero (Foxon et al. 1975). Similarly when $J_{Ga} < J_{As_4}$, S_{As_4} is proportional to J_{Ga}, where each Ga atom interacts with an As atom once more. However for $J_{Ga} > 4 J_{As_4}$, S_{As_4} saturates to the value of ½.

At low temperatures up to 150 °C no dissociation takes place and hence any growth occurs from a non-dissociative precursor state. At high temperatures dissociation takes place.

At high temperatures under As-rich conditions the reaction is based on a first order supply limited desorption, shown by As_2 desorbing form the surface at ~300 °C.

At high temperatures under Ga-rich conditions, the model for As_4 incorporation again involves a precursor state As_4*, where $J_{Ga} > 4 J_{As_4}$ the desorption of As_4 is second order and the incorporation kinetics can be given as:

$$2As_4^* \xrightarrow{k_r} 2As_2^* + As_{4(v)}$$

Where $As_{4(v)}$ represents As_4 in the vapour phase and k_r is the rate constant of As_2 production. Furthermore for a As_4* population, θ_p:

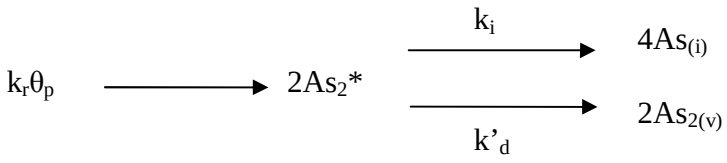

Where k'_d and k_i are the rate constants for desorption and incorporation associated with the As_2* intermediate . These two equations are shown schematically in **Figure 2.10**.

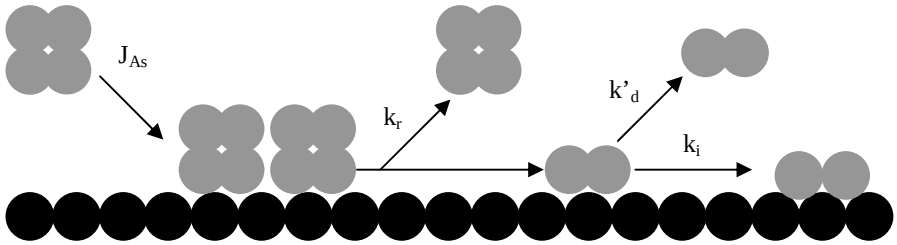

Figure 2.10: Schematic of As_4 incorporation on GaAs(001) adapted from (Tok et al. 1997)

The morphology of the growing surface is dominated by the Ga kinetics, with As supplied in excess to ensure stoichiometry (Joyce et al. 2004). RHEED intensity observations reveal surfaces prepared by As_2 are more ordered and more closely follow ideal 2D growth when compared to As_4, thought to result from the dimer yielding a simple first order dissociative chemisorption reaction (Neave et al. 1983b).

Moreover, several effects are directly attributable to As kinetics, namely, influence of J_{As} on the step flow transition on vicinal surfaces and the sensitivity of Ga adatom mobility to variations in J_{As_4} (discussed in **2.3.3 Stoichiometry and Roughness**).

2.3.2 Gallium Incorporation Principles

Below 470 °C the sticking coefficient of Ga (S_{Ga}) is unity. At temperatures in the range 600 - 680 °C surface lifetimes of Ga are between 1 and 10 seconds (Foxon et al. 1975), with a desorption energy of approximately 2.5 eV. Notably at temperatures above 500 °C and in the absence of a group III flux the As_2 sticking coefficient becomes non-zero which implies that there is Ga exposed and possibly mobile on the surface.

In the interest of growing stoichiometric films, As is generally over supplied with a ratio $J_{As_2} : J_{Ga}$ of 3 - 8 (Bell et al. 1999b). For unity S_{Ga}, J_{Ga} can therefore be used to directly control the growth rate under stoichiometric conditions (Joyce et al. 1999b), hence growth rate $\propto J_{Ga}$.

2.3.3 Stoichiometry and Roughness

RHEED oscillations obtained *in situ* during film deposition have been interpreted as a variation of surface reflectivity (Neave et al. 1983a). In this model the growth of a monolayer proceeds by the formation of a number of 2D islands which eventually coalesce entirely yielding a complete layer. A minimum in intensity corresponds to half a monolayer of coverage, similarly a full monolayer relates to a maximum. Hence the rate of oscillation corresponds exactly with the ML growth rate.

Investigation of the intensity variations along several azimuths led to the conclusion that maximal scattering along the [110] indicates multiple steps along this azimuth and hence an alignment of the islands to the $[\bar{1}10]$ direction (**Figure 2.11**). However a decay in the amplitude of oscillations during a growth cycle indicates that the growth of a new monolayer initiates before the completion of a previous one. Such is the situation generally observed in practice.

The intensity in both the static state, I_s, and that of the dynamic, growing surface, I_d, can be compared as a measure of surface roughness (Moreira et al. 1991). Here a minimally rough surface is one whose I_d is a relative maximum (when compared to other surfaces) and remains approximately constant during growth. Comparing roughness of growth conditions revealed that:

1. A higher sample temperature, T_s, yields a smoother surface
2. An optimum (peak) As_4 beam pressure (P_{As_4}) exists for each temperature
3. Lowering the growth rate V_{GaAs} while maintaining identical T_s and keeping the same J_{As_4} ratio results in a smoother surface. However, reducing the growth rate without reducing J_{As_4} ratio in line with the Ga flux results in a rougher surface.

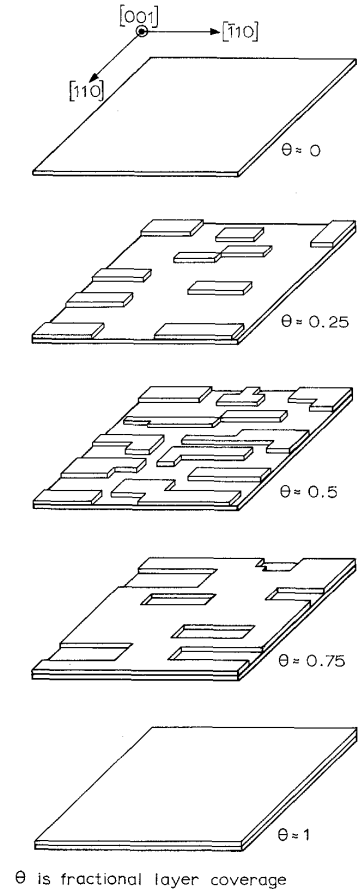

Figure 2.11: 2D layer-by-layer growth
taken from (Neave et al. 1983a)

In line with point 1, it is noted from photoluminescence (PL) spectra that the optical quality of layers grown at 620 °C is superior to those grown at 580 °C (Moreira et al.

1991). It seems possible, though has not been proven, that growing under Ga-rich conditions and a (4 × 2) reconstruction at the higher temperature alters the window size for stoichiometry.

With reference to point 2, varying the As flux has two pronounced effects. At high J_{As_4}, roughness increases (Lewis et al. 1985) supporting the argument. Whereas at low J_{As_4}, nonstoichiometric growth occurs leading to excess Ga incorporation (Foxon et al. 1975). For growth at 580 °C the smoothest growth requires an As:Ga flux ration of 1:1 providing nonstoichiometric growth, whereas a higher ratio results in stoichiometry at the cost of a rougher surface (Heyn et al. 1995).

As an extension of this principle, it has been shown that a reduced As:Ga ratio results in an increase in the mean island size (Joyce et al. 1999b), arguing that at lower ratios the $As_{2,4}$* reservoir is less full and the sticking coefficient of $As_{2,4}$* is reduced, resulting in island growth at a cost of nucleation. The dynamic intensity, I_d, can thus be attributed to a saturation in the nucleation rate for any given system

The decrease in RHEED oscillations as the Ga shutter is opened to begin growth is followed by an increase when the shutter is subsequently closed (Heyn et al. 1997b). An increase in intensity is attributed to a restorative smoothing of the grown surface. When the rate of recovery is determined solely by the residual Ga adatoms reacting on the surface (Shitara et al. 1992), recovery is found to proceed too quickly. Hence another mechanism must hold influence. The inclusion of step edge barriers allowed accurate simulation (Smilauer et al. 1993), however the growing surface resulted in large mound structures (discussed in **2.3.6 Large Scale Mound Formation**). Another possible mechanism is the inclusion of mobile GaAs molecules (Heyn et al. 1997a) or $GaAs_2$ intermediates (Tok et al. 1997) on the surface (discussed in **2.3.4 Growth Modes Transitions**).

In situ STM can, in principle, be used to monitor the surface morphology during a growth interruption, identifying whether GaAs molecules are in fact mobile and on what scale. Unfortunately the mound structures cannot be easily imaged since their dimensions are larger than a typical STM image.

2.3.4 Growth Modes Transitions

Step flow and layer-by-layer (also known as "islanding") represent two broad, but not necessarily exclusive, growth modes for homoepitaxy. For sufficiently high temperature growth the diffusion length of an adatom, λ, exceeds the average terrace/step length, l, and most adatoms reach step edges where they are incorporated. Step edges then propagate across the surface in a uniform manner resulting in a constant step density and small variations in RHEED oscillation intensity (**Figure 2.12a**). At sufficiently low temperatures $\lambda << l$, under this regime adatoms rarely reach step edges and instead nucleate immobile islands where they collide on the terraces (**Figure 2.12b**, discussed in **2.3.5 Island Nucleation on GaAs(001)-(2 × 4)**). The growing islands coalesce to complete a full monolayer (as discussed in **2.3.3 Stoichiometry and Roughness**).

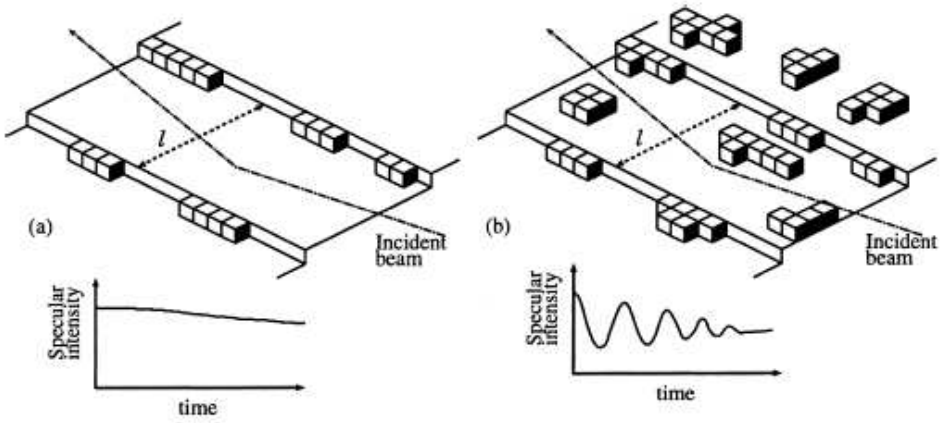

Figure 2.12: Growing surface morphology a) step flow and b) islanding taken from (Itoh 2001)

The vicinal angle determines l and hence tailoring of vicinal surfaces had been employed to suppress the nucleation rate of islands and to obtain smooth layers (Itoh et al. 2001a). Miscut via [110], $[\bar{1}10]$ and [010] directions produces A, B or C (a combination of A and B) steps, respectively.

Simulations of step-flow growth modes of GaAs(001)-(2 × 4) indicate that an initially straight A step displays progressive roughening of step edges, a fact attributed to the assumed anisotropic diffusion of Ga adatoms favoured parallel to the step edge.

Islands begin to nucleate within 0.2 ML of deposition (Itoh et al. 2001a), whereas growth on B steps progresses much more smoothly, owing to enhanced Ga diffusion perpendicular to step edges (Itoh et al. 2001b). However in these simulations Ga adatoms form clusters at the lower side of the steps and growth is reported as unstable. Both results indicate that the vicinal angle needs to be greater on A steps with respect to B steps to suppress island formation. The ideal vicinal orientation does not lie parallel or perpendicular to the (2 × 4) unit cell.

A temperature study on A, B and C steps revealed that the critical temperature for the transition between step-flow and islanding, T_c, can be expressed as: $T_c(A) > T_c(C) > T_c(B)$ (Shitara et al. 1992). Either increasing the l or increasing the Ga flux increases T_c. Hence, reducing T_c involves enhancing Ga adatom migration.

Supporting evidence for this theorem utilises an alternative growth technique where Ga and As fluxes are supplied alternately, allowing Ga to migrate at very low or zero As pressure (Yamaguchi et al. 1988). So called Migration Enhanced Epitaxy, MEE, reports a self flattening effect where rapid migration causes preferential absorption at steps or kinks. Notably, migration is also enhanced at lower temperatures, allowing layer growth at 300 °C with similar impurity doping as at 580 °C. All aspects of the smoothing mechanism can be investigated via *in situ* STM where both group III and group V sources support rapid switching. The ramifications of MEE on quantum dot generation can henceforth be investigated.

Evidentially the conglomeration of these two growth modes gives traditional step flow more complicate dynamics than a simple uniform progression of a regular step train (Johnson et al. 1994b). However, surfaces have been shown to evolve toward a constant step density (where a step is either a terrace step or an island edge. A randomly deposited adatom has a probability to either nucleate an island or combine at a step edge depending on its relative position to said step edge. Hence the step edge density increases for nucleation, remains unchanged for step edge incorporation or decreases for surface healing (hole occlusion) and island coalescence. The competition between these various processes results in a self regulating mechanism to achieve a constant step density. Hence the transition is not strictly step-flow to islanding but more a relative mix of the two mechanisms.

A prediction of the surface growth mode can be ascertained from the island separation during the initial stages of growth. The distance, *d*, of a randomly deposited adatom to the nearest step edge varies initially during nucleation, though settles to an average time invariant value $\bar{d}$. Comparing this to the initial stage island spacing, σ, a transition from nucleation to constant step density (generalised step-flow) occurs when $\bar{d} < \sigma/4$. Initial stages of nucleation are discussed further in **2.3.5 Island Nucleation on GaAs(001)-(2 × 4)**.

2.3.5 Island Nucleation on GaAs(001)-(2 × 4)

The nucleation and growth of 2D islands is fundamental to the fabrication of all quantum heterostructures (Avery et al. 1997). Thus far the surface kinetics of adatom mobility, island coalescence and step edge effects have been considered, but equally important are the effects of surface orientation and reconstruction.

In addition to the basic tenets of island nucleation and growth (Venables et al. 1984) the advent of *in vacuo* STM enabled quenched surfaces (often heralded as "as-grown") to be imaged in real space. Data retrieved clearly depicts the size, density and distribution of islands for a range of growth conditions. Critically the density, n_s, of islands containing *s* atoms can be calculated from:

$$n_s = \frac{\theta}{\langle s \rangle^2} f\left(\frac{s}{\langle s \rangle}\right) \qquad \textbf{Equation 2.1}$$

Where $\langle s \rangle$ is the average island size, θ is the coverage and f is a scaling function dependent upon adatom incorporation (Ratsch et al. 1995; Kandel 1997) and cluster mobility (Bartelt et al. 1996; Kuipers et al. 1996; Furman et al. 1997).

On GaAs(001)-(2 × 4) growth can be initiated by Ga adatoms combining in two key positions:

1. In trench site (trench filling)
2. On As dimer rows (mountain peaking)

Principally both these mechanisms can involve either As-dimer breaking or Ga vacancy filling. A comprehensive list of 16 total sites has been listed (Kratzer et al. 1999) as shown in **Figure 2.13**.

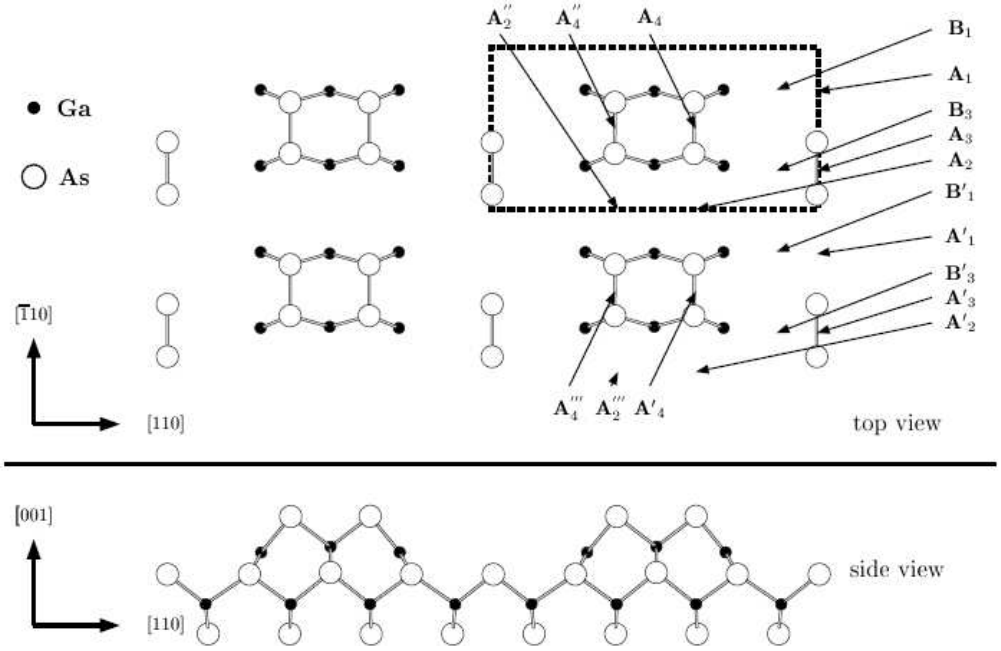

Figure 2.13: Ga adsorption sites in GaAs(001)-(2 × 4)
taken from (Kratzer et al. 1999)

Growth from first principles involves single Ga atoms or clusters of 2 - 4 forming structures by occupying adjacent sites. *Ab initio* calculations revealed that B_1, B_3 and A_4 trench sites posses the smallest repulsive interaction energies. Where simultaneous occupancy of both B_1 and B_3 or A_4 and A_4'' sites represents an attractive interaction, with the latter constituting the higher energy case. Interestingly attaching a third adatom to a B-pair further increases the attractive energy, whereas a similar third adatom appended to an A-pair decreases the stability of the cluster. Furthermore, Ga adatoms diffusing along a trench sites are aligned in a string B_3-B_1-B_3-B_1-$B_{3...}$ where B_1 represents a vacancy and B_3 represents a broken dimer. Hence a next-nearest neighbour to nearest-neighbour Ga

adatom hop involves the restoration of a As-dimer with respect to a B_3 site, enhancing the B-pair stability. This indicates that while trench filling can proceed via nearest-neighbour hops of single Ga adatoms, mountain peaking requires simultaneous interaction of a pair of Ga adatoms to be favourable. Thus from purely Ga kinetics surface growth would proceed first via trench filling and later by mountain peaking.

However the role of As kinetics cannot be ignored. A stable As ad-dimer is duly back-bonded onto 4 Ga atom sites, whilst an ad-dimer bound to an existing dimer pair (**Figure 2.14a**: trimer (Joyce et al. 2004)) or 3 Ga atom sites (**Figure 2.14b**: Ga-As-As-Ga_2 complex (Kratzer et al. 2002)) are weakly bound transients that are either desorbed or react with diffusing Ga atoms. The reaction of trimers favours mountain peaking by trapping Ga adatoms in A_4 positions and similarly the Ga-As-As-Ga_2 complex favours trench filling by trapping a Ga adatom in a B_1 site.

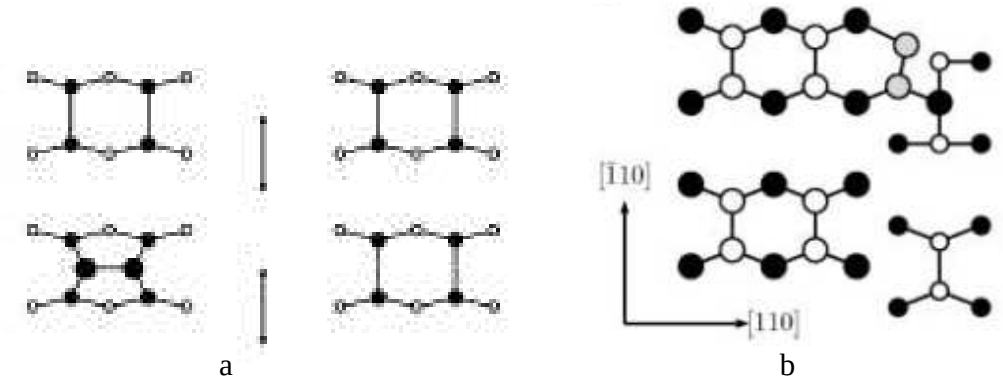

Figure 2.14: Transient ad-dimer structures a) trimer and b) Ga-As-As-Ga_2 complex

Initially it would seem that As has gracefully positive effects on the incorporation process, however a number of neighbouring dimer-dimer and dimer-Ga interactions also exist (Itoh et al. 1998). Importantly Coulomb repulsion presents a large energy barrier for a three-abreast dimer alignment in the [110] direction (i.e. trench filling). Not only will this result in a dramatically short life time for Ga-As-As-Ga_2 complexes, but the compound effect of a four-wide dimer row (hence a full trench) involves a dramatic

increase in the energy barrier with respect to 3 dimers (Vvedensky et al. 1999). This results in a possible generation mechanism for point defects in the growing layer.

The compound effect is an anisotropic island shape commonly observed in STM images (Avery et al. 1997; Itoh et al. 1998; Bell et al. 1999b; Vvedensky et al. 1999; Joyce et al. 2004). Such islands involve string like structures of As-dimers along the $[\bar{1}10]$ direction, whilst a width of 5 dimers in the [110] direction is followed by 'splitting' restoring the (2 × 4) surface reconstruction.

Attempts to model the growth process have involved kinetic Monte-Carlo (KMC) simulations based on either top-down calculations (effective reverse engineering from STM images (Itoh 2001) or a bottom-up methodology based on *ab initio* calculations. (Kratzer et al. 2002).

Broad assumptions regarding Ga diffusion and sticking anisotropies resulted in two different but equally applicable nucleation models. Evidently the nucleation and growth process is not fully understood.

The smaller structures formed in the initial stages of nucleation are weakly bound to the substrate. Evidence of island mobility in metal systems (Bartelt et al. 1996; Kuipers et al. 1996; Furman et al. 1997) indicates the possibility that such a phenomenon exists on semiconductors. In light of this, small islands of several dimers could be mobile on GaAs MBE surfaces, as such the effect of quenching on the STM images is questionable (Joyce et al. 2004). The ability to capture *in situ* images of the nucleation process would deftly resolve the speculative effects of such quenching.

Ultimately the islanding occurring during normal growth conditions is a multi-layer mechanism, spawning a quasi-3D structure as oppose to the idealistic 2D model. Moreover long range order defects owing to the coalescence of out-of-phase (2 × 4) reconstructions of neighbouring islands are inherent to this growth mode (Joyce et al. 2004) and possibly result in the overlapping c(2 × 8) and (2 × 4) reconstructions mentioned in **2.2 GaAs Surface Reconstructions**.

2.3.6 Large Scale Mound Formation

The formation of large, regular mounds during homoepitaxy has been shown by simulation and experiment (Johnson et al. 1994a). The origin of mounding was initially attributed to a growth instability in the presence of Ehrlich-Schwoebel (ES) diffusion barriers (Schwoebel et al. 1966). ES barriers effectively inhibit the downward motion of adatoms (preventing incorporation into the theorised favourable step edge positions) resulting in an increased population density on top of existing islands, hence supporting a mechanism for island on island formation and 3D growth. Repetition leads to multi monolayer (ML) mounds.

Typical mound dimensions on GaAs(001) are 15 ML in height and approximately 4 x 1 μm^2 at the base, with a maximum slope of ~ 1° (Orme et al. 1994). As a result of their large scale dimensions they can only be observed in their entirety using Atomic Force Microscopy (AFM) imaging on large surface areas (5 x 5 μm^2), whereas typical large STM images of the order of 1.5 x 1.5 μm^2 reveal only pieces of the structures.

Mounds were originally purported to be a direct influence of islanding on initially flat surfaces (Orme et al. 1994). Work on vicinal surfaces at high temperature (Orme et al. 1995b) suppressed mound formation by initiating growth in the step flow regime. Emphasising this, a further experiment was carried out on a thermal gradient. Here the hottest area of the same sample showed 1 - 3 ML differences, whereas in the cooler region there was evidence of mounding and much larger height variations. Clearly mounds can be suppressed by step flow growth. Furthermore, their inherent unstable nature indicates they can be annealed away, though their relatively large size means this is a lengthy process (Orme et al. 1995a).

More recent work attributed mound formation to surface 'healing' after the formation of randomly scattered micro pits resultant from oxygen desorption (Coluci et al. 1998; Ballestad et al. 2001). Hence the initial mounds observed at relatively low coverage began to coalesce until, at a coverage of 150 nm, the surface evolved into a typical 2D growth mode. This work concluded that mounds are a result of the initial surface condition and the presence of ES barriers was of negligible effect, noting that no mounds were formed on surfaces that were observed to be ideally flat before growth, regardless of vicinal or nominal orientation.

Attempts to reduce the formation of μpits and hence produce a less damaged surface are investigated in section **6.3 Clean-up Techniques (PBNRH)**.

2.4 Heteroepitaxy

Heteroepitaxy involves the growth of epitaxial layers with a different atomic spacing or even a different crystallographic structure than the underlying substrate. Investigation into heterostructures has produced an avid interest in small, strain-induced islands that can be employed as quantum confinement zones and used in the development of quantum devices. Minimising the occurrence of strain-induced defects at heterojunctions is essential to enhance device performance (Mayer et al. 1990a).

2.4.1 Misfit Strain and Defects

Heteroepitaxy was initially employed to realise quantum wells and superlattices for advanced device properties. Here, alternate layers of material are deposited repeatedly with the goal of achieving defect free epitaxial layers of several monolayer (ML) thickness. To alleviate the effects of strain, lattice matched AlGaAs/GaAs was used in this endeavour, though it suffers from AlO_2 generation and poor Al sticking coefficients at growth temperatures.

The $In_xGa_{1-x}As$/GaAs epitaxial system was alternatively employed for heteroepitaxy. The lattice constant for GaAs substrate (a_s) = 5.6533 Å and for the InAs epitaxial overlayer (a_o) = 6.0584 Å. However, $In_xGa_{1-x}As$ alloys obey Vegards' Law where a_o varies linearly with alloy composition. Hence it can be shown that:

$$a_o = 0.4051x + 5.6533 \qquad \textbf{Equation 2.2}$$

The misfit (f) generated by the two competing periodicities can be expressed as (Van der Merwe 1991):

$$f = \frac{a_o - a_s}{a_{avg}} \qquad \textbf{Equation 2.3}$$

Where a_{avg} takes the values of a_s for the first monolayer. Hence f varies from 0 to ~7.2 % for In content $0 \leq x \leq 1$.

Growth initiates pseudomorphically, with the $In_xGa_{1-x}As$ overlayer adopting the in plane lattice constant of the underlying GaAs substrate (**Figure 2.15**). Arguments for isotopic growth driven by strain have been presented (Bressler-Hill et al. 1995) though since isotropy is inherent in homoepitaxy, arguments followed that pseudomorphic growth is virtually identical to the homoepitaxial growth (Bell et al. 2000; Rodriguez et al. 2004) method mentioned in **2.3.4 Growth Modes Transitions,** with 2D island formation and coalescence for As-rich conditions. The epilayer hence initially 'wets' the surface, the particulars of which are discussed in **2.4.2 Wetting Layer Formation.**

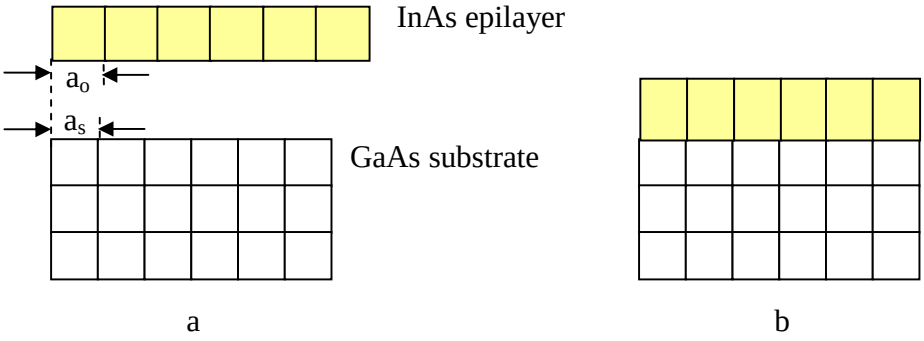

Figure 2.15: Schematic of $In_xGa_{1-x}As$ layer and GaAs substrate a) before and b) after 'merging'

Misfit thus far has been accommodated by homogeneous misfit strain (MS). Such elastic relaxation continues until a critical thickness is reached, thereafter plastic deformation occurs via misfit dislocations which punctuate the interface (Frank et al. 1949).

The stages of the InGaAs/GaAs epitaxial system have been mapped from the initial pseudomorphic regime through a roughening phase with slow relaxation into a sudden and fast relaxation phase with a noticeably smoother surface and finally into saturation (Rodriguez et al. 2004).

The slow relaxation phase possess two competing processes. The elastic deformation of the film partially relaxes the strain, however the process is opposed by the consequent increase in the surface free energy attributed to the increasing surface area (Cullis et al. 1992; Tersoff et al. 1994). Hence the process is self-limiting.

The fast relaxation phase has been attributed to misfit dislocation (MD) generation manifesting due to the ineffective relaxation of the roughening phase which does not cope with the strain build-up as more layers are deposited. The smoothening of the surface is indicative of up to 100 % strain accommodation by MDs. In the saturation regime, the limited density of MDs restricts the films capacity to relax via MDs and hence re-entrant surface roughening arises to accommodate excess strain. This is shown schematically in **Figure 2.16**.

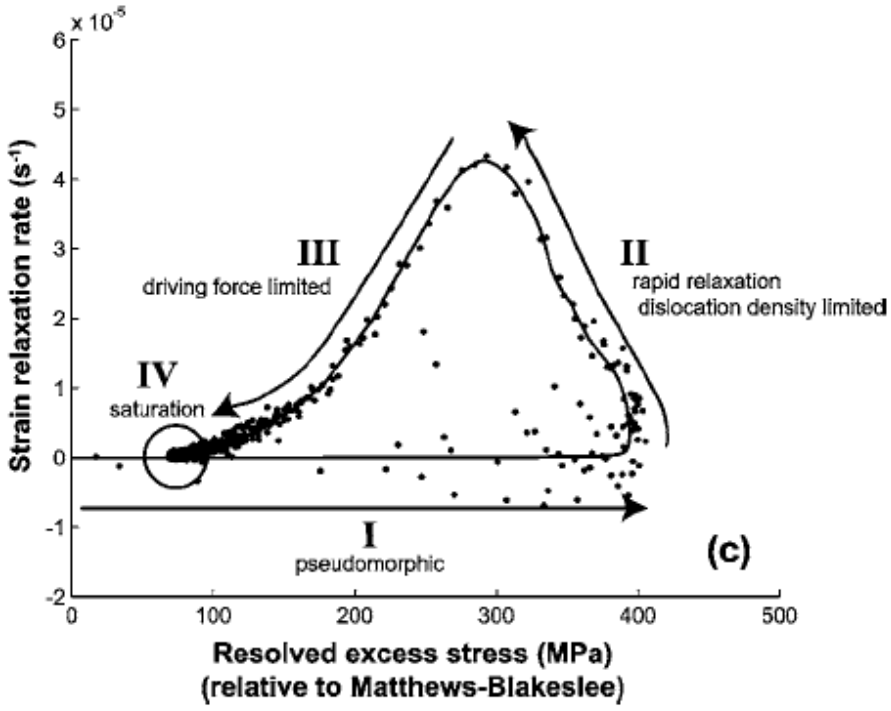

Figure 2.16: Relaxation Regimes taken from (Lynch et al. 2006)

The morphological response of the $In_xGa_{1-x}As/GaAs$ epilayer in the slow relaxation regime is notably effected by In content x (Cullis et al. 1996). For x values below 20 %

the response is pseudomorphic throughout. However the range 20 % > x > 25 % presents a notable change. Step front distortion during growth preclude nm-height ridges on the growth surface thought to be produced by MDs. For x ≈ 25 % 3D islands begin to form with undulating ripple particulates. The ripples and islands have been shown to exhibit near 100 % relaxation at near-surface peaks (Androussi et al. 1994) and significantly strained troughs where cusps have been shown to form (Jesson et al. 1993) and threading dislocations nucleate (Cullis et al. 1995; Androussi et al. 1996).

Values of x > ~25 % and the inherent 3D islands generated are focused upon in greater detail in sections **2.4.3 Stranski-Krastanov Transition** and **2.4.4 Quantum Dot Growth**.

A basic edge dislocations is defined by a perpendicular shift, effectively an extra half-plane being inserted into the epilayer (Mayer et al. 1990b). Edge dislocations, often termed perfect dislocations, are the most efficient dislocation with respect to strain relaxation. Mixed (60°) MDs are also common dislocations in $In_xGa_{1-x}As/GaAs$ systems and occurring concurrently with a cross-hatch pattern upon the upper epilayer surface (Giannakopoulos et al. 1998).

MD nucleation requires up to 200eV (Van der Merwe 1991), a barrier that can be significantly reduced by MD nucleation sources. Such sources include inhomogeneous centres (Zou et al. 1997) and existing threading dislocations (Van der Merwe 1991; Tamura et al. 1992). Threading dislocations (TD) formed can further generate edge dislocations via a glide mechanism **Figure 2.17**.

A perfect crystals suppresses MD nucleation, however the production of crystals with neither TD nor point defects is nigh on impossible. Furthermore, ripple troughs and 3D islands add further sources, where the density of the MD is delineated from the diameter of the 3D islands or, in the case of coalescence, the frequency of the undulations (Androussi et al. 1995).

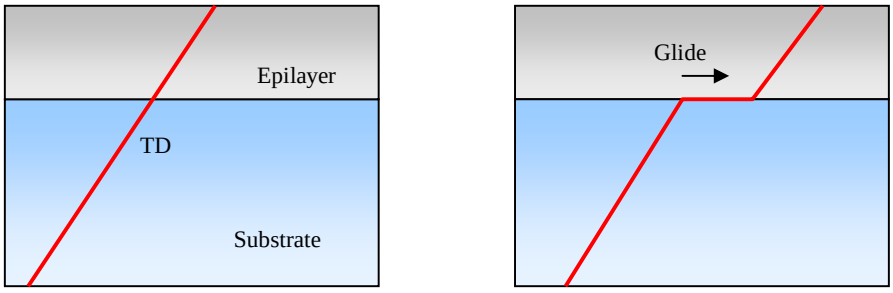

Figure 2.17: Misfit dislocation nucleation via glide of existing Threading Dislocation

All the dislocations mentioned thus far are parasitic to device performance, causing a drop in carrier lifetime (Patriarche et al. 2001). A number of methods have been employed to suppress MD generation in 2D layer growth: compliant substrates (Moran et al. 1999; Patriarche et al. 2001), surfactants (Jesson et al. 1993), In-rich virtual surfactants (Tournie et al. 1993; Xue et al. 1997a) and dislocation confinement (Uchida et al. 1993). In respect to 3D islanding the identification of coherent (dislocation free) islands proposed an exciting prospect (Eaglesham et al. 1990; Guha et al. 1990), especially when such islands can be employed as 0D quantum confinement centres for enhanced devices. However successive build up of strain produces incoherent islands, with incremental 'jumps' in growth attributed to each dislocation formation event (Legoues et al. 1994). The details of quantum dot growth are discussed in **2.4.4 Quantum Dot Growth**.

2.4.2 Wetting Layer Formation

InAs deposition onto the GaAs(001) surface possess unique morphological behaviour in comparison to other low index surfaces. In fact the specific transition behaviour discussed herein is further limited to the (2 × 4) and c(4 × 4) As-rich reconstructions upon said surface. In section **2.4.1 Misfit Strain and Defects** the morphological response to relatively small misfit was presented, however henceforth the highly strained InAs/GaAs epilayer system will be presented.

To establish and categorise the varying influences of the initial starting surface and inherent strain build up it is useful to consider the growth process in a number of discrete phases. Wetting layer (WL) formation represents an initial phase with a range extending from the first incorporated In atom on the GaAs surface to a critical thickness (t_c) defining an abrupt transition from 2D to 3D growth.

Under normal growth conditions, binary InAs deposited on binary GaAs always produces a ternary alloy (Joyce et al. 1999a). The composition and thickness of the alloy depend upon As:In flux ratio and substrate temperature. Alloying is significant above 470 °C and increases with both InAs coverage and increasing temperature (Belk et al. 1996).

At the low substrate temperature of 350 °C As-deficient growth has been shown to support In segregation toward the surface, yielding a highly In rich near surface layer. Such low temperature segregation cannot be accounted for by diffusion and hence near surface atom exchange is theorised as the rearrangement process (Dehaese et al. 1995). Whilst increasing the As supply suppresses segregation, alloyed island formation is enhanced (Ohtake et al. 2002). Notably a window exists around 420 °C where In segregation is minimised and laterally homogeneous interfaces are evident (Belk et al. 1996).

For binary InAs coverages < 0.8 ML the independent behaviour of the (2 × 4) and c(4 × 4) starting surface is observed. In the case of growth on (2 × 4) the InAs islands formed above the existing reconstruction, creating a uniform wetting layer after an entire ML has been deposited (Krzyzewski et al. 2002a). Growth of small (2 × 4) InAs islands obeys the scaling laws established in the GaAs homoepitaxial system: key to this argument is that anisotropic growth is the effect of coulomb repulsion and surface reconstruction binding and migration (Bell et al. 2000) and not In induced anisotropic strain (Bressler-Hill et al. 1995). For the c(4 × 4), InAs incorporates directly into the existing reconstruction, creating (n × 3) alloyed domains.

Continued deposition to > 0.8 ML InAs coverages evolves both the (2 × 4) and c(4 × 4) GaAs starting reconstruction toward a (n × 3) reconstruction; a consequence of the strain-driven alloying (Krzyzewski et al. 2001). It is however notoriously difficult to maintain a (2 × 4) reconstruction for the conditions used during InAs deposition (Joyce et

al. 2004). Other work showed that the (n × 3) reconstruction forms one atomic plane *below* the (2 × 4) reconstruction (comparable to homoepitaxy where c(4 × 4) forms beneath (2 × 4) during the transition), further supporting a link between to the c(4 × 4) reconstruction and alloying (Belk et al. 1997).

The reconstruction of the alloy is under disrepute. Whilst a (1 × 3) is frequently observed, alternate experimentally observed (1 × 2) (Belk et al. 1997) and theoretically favourable (2 × 3) (Kratzer et al. 2003) have been reported. The [110] reportedly displays both 3× and 6× RHEED diffraction patterns, where as the $[1\bar{1}0]$ direction has displayed 1×, 2×, 4× and 6× patterns (Patella et al. 2003). These patterns yield a number of (often concurrent) reconstruction domains. The exact inter-relationship between these reconstructions requires further study.

The growth conditions can lead to a complex relationship that extrapolates to two extremes (Belk et al. 1997):

1. Maximal alloying: the area of the alloy reconstruction far exceeds the amount of InAs deposited.
2. Maximal segregation: the amount of InAs deposited far exceeds the InAs composition in the buried bulk

For binary InAs deposited onto GaAs(001) the WL is reported to be between 1.4 and 1.8 ML (Joyce et al. 2004). The relatively large range was thought to be attributed to the quality of the initial surface. A smooth initial surface was purported to yield a thicker layer (Hollinger et al. 1992), a result supported by an early RHEED observation (Joyce et al. 1986). Later, the critical thickness (t_c) was shown to have a temperature dependence, where growth at high temperatures supports thicker layer formation (Hollinger et al. 1992). For the pure binary InAs/GaAs system, t_c varies from 1.4 ML at T_s = 350 °C to 1.8 ML at T_s = 500 °C. This is discussed more fully in **2.4.3 Stranski-Krastanov Transition**.

Growth under In-rich conditions produces a (4 × 2) reconstruction and enables 2D growth beyond t_c (Xue et al. 1997a; Cai et al. 1999). Whilst not strictly WL formation per say, further investigation into the phenomenon may produce an explanation for a number

of WL effects by simple comparison. Section **3.6 Concurrent MBE-STM** shows that the *in situ* growth technology is particularly suited to exploring Migration Enhanced Epitaxy (MEE) that has proved to utilise both anion-rich and cation-rich growth conditions in rapid succession (Horikoshi et al. 1989) to enhance 2D growth.

2.4.3 Stranski-Krastanov Transition

In Stranski-Krastanov (S-K) growth, initial wetting layer (WL) formation is followed by a transition from 2D to 3D, with 3D islands forming atop the established WL. The actual critical thickness (t_c) varies as a function of both In composition (x) and substrate temperature (T_s) (Joyce et al. 2004).

In the classic S-K system an epitaxial thin film wets a rigid substrate. The first attempt to model the dislocation-free stained epitaxial layer considered a dynamic description of the morphology of the growing film (Spencer et al. 1991). The model predicted a transition thickness:

$$t_c = \frac{\sigma'}{\varepsilon_0}\frac{(\lambda+2\mu)(1-E)}{2(\lambda+\mu)} \qquad \textbf{Equation 2.4}$$

where:

$$\varepsilon_0 = \frac{2f^2\mu(3\lambda+2\mu)^2}{(\lambda+\mu)(\lambda+2\mu)} \qquad \textbf{Equation 2.5}$$

$$E = \frac{\eta(3\lambda+2\mu)}{(\lambda+2\mu)} \qquad \textbf{Equation 2.6}$$

f is the misfit strain defined in **2.4.1 Misfit Strain and Defects,** σ' is the surface free energy and λ and μ are the Lamé elastic constants. The model failed to predict observed experimental results, arguing that substrate-epilayer interactions account for some degree of the discrepancy.

A thickness-composition diagram can be constructed for $In_xGa_{1-x}As/GaAs(001)$ epitaxy (**Figure 2.18**), similar to those realised for GaAs(111) (Nakajima 1999). The

nominal growth temperature is 480 °C. There is a notable absence in the S-K transition for x < ~ 0.25, as discussed in section **2.4.1 Misfit Strain and Defects.** The origin and ramification of which is discussed below.

A basic overview of the S-K transition (Snyder et al. 1991) relies on a strain induced cost of adatom incorporation at step edges. Whereby a strain-induced deformation of the WL makes it energetically unfavourable for 2D islands to merge. Hence an increasing number of atoms are available for the next layer generation. The culmination theorises a kinetically controlled coarsening process whereby 3D islands nucleate rapidly. Whilst this theory accommodates a driving force for the 2D to 3D transition, predicted values of the critical thickness, t_c, are incorrect, indicating the influence of another factor.

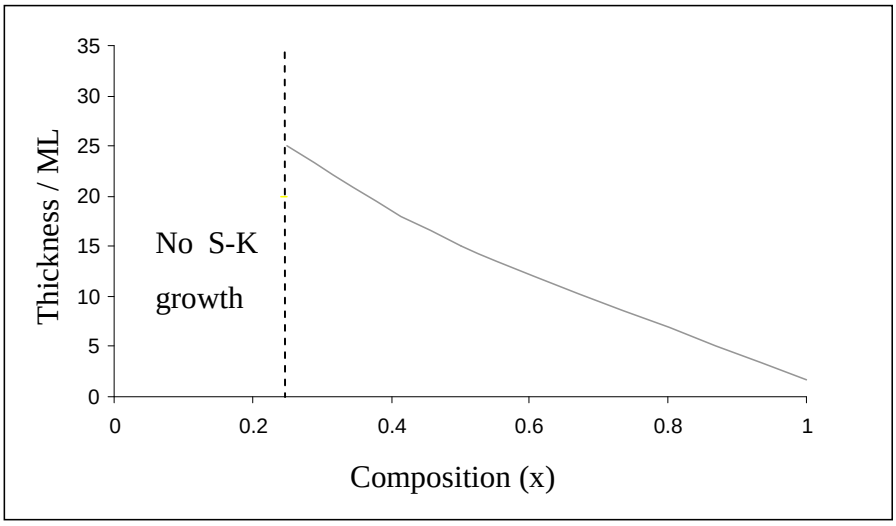

Figure 2.18: Composition-Thickness Diagram

The 3D islands resultant from the S-K transition form as a consequence of adatom migration. The areal density of adatoms, 2D and 3D islands involves 5 processes (Dobbs et al. 1998; Joyce et al. 1999a):

1. Adsorption of adatoms onto the surface
2. Surface diffusion of adatoms
3. Nucleation of 2D islands (strictly a WL occurrence)

4. Adatom attachment and detachment from 2D and 3D islands
5. Transformation of 2D islands to 3D islands

This qualitative overview can firstly be compounded by a number of features (Joyce et al. 2004):

1. Islands grow after formation of a WL and are coherent (defect-free)
2. 2D to 3D transition is very rapid (less than 1 ML deposition)
3. Temperature and flux dependencies of t_c are relatively weak
4. QDs are of alloy composition, even for binary deposition
5. QD distribution obeys 2D scaling laws (hence not strain driven)

Observed via RHEED, the S-K transition yields initially a "streaky" pattern (indicative of a flat layer with some roughness) through to a brief dimming (indicative of a highly disordered transient state and compounding high mobile adatom population) and finally a "spotty" pattern (indicative of 3D island formation) (Joyce et al. 2004).

In vacuo STM via quenching has extensively been utilised to investigate these stages further. However the effectiveness of the quenching process to "freeze" the as-grown surface is under heavy dispute. One key argument in the S-K transition is the validity of the existence of precursors. Here a precursor is a quasi-3D structure that provides a site for a mature QD to develop.

There is much evidence linking the *formation* of such structures to poor quenching procedures (Krzyzewski et al. 2002b; Krzyzewski et al. 2003; Joyce et al. 2004; Krzyzewski et al. 2004), where background In and As have condensed onto the growth surface prior to imaging. Most notable of all is the reputed re-entrant 3D island formation at 1.27 ML (Ramachandran et al. 1997b) strongly argued as quenching effects and not multiple S-K transitions (Joyce et al. 2004).

Furthermore, the observed density of quasi-QD is often far lower than the mature number density (N_s) (Patella et al. 2003). Hence the clandestine effects of quenching can be equally used to argue that quenching leads to the *elimination* of quasi-QD structures. The existence of 2D platelets as precursors (Priester et al. 1995) was later argued when

considering the number density of these structures remaining constant throughout the S-K transition (Ramachandran et al. 1997a) (**Figure 2.19**). A similar evolution of 3D features at the expense of 2D features has also been observed elsewhere (Ratsch et al. 1996).

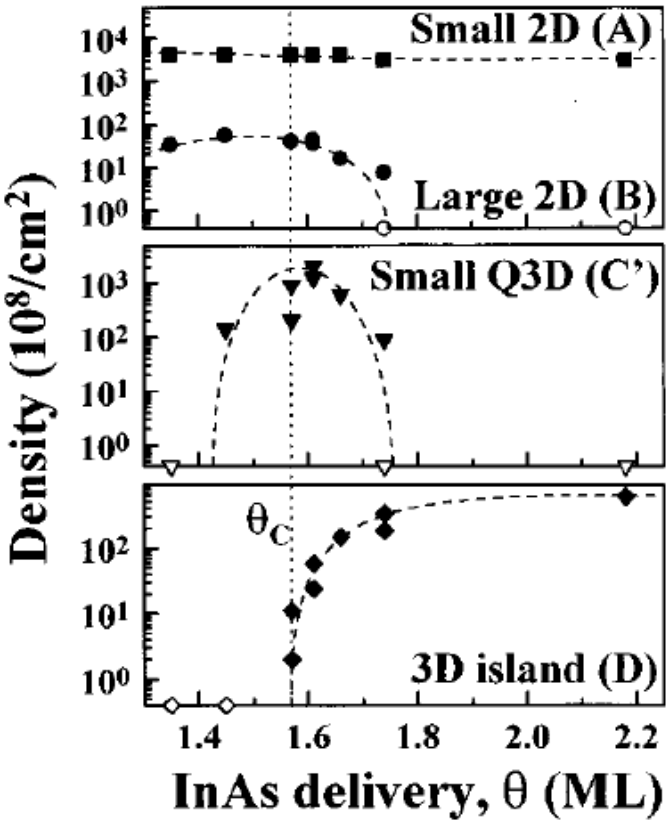

Figure 2.19: Density of 2D and 3D structures during S-K transition.
Taken from (Ramachandran et al. 1997a)

A number of theoretical models have been employed to predict the S-K growth process (Joyce et al. 2004). The essential multi-scale nature makes it difficult to explain all the observed experimental features.

First principle calculations are chiefly employed to measure the effects of strain on the diffusion of In and Ga on both the substrate and wetting layer and the likelihood of competing reconstruction formation (Lee et al. 2000; Schmidt et al. 2000).

Kinetic Monte Carlo (KMC) simulations focus more on QD growth and size distributions and hence belong in **2.4.4 Quantum Dot Growth.** However off-lattice

kinetic simulations suggest that the 2D-3D transition results from upward adatom hops, thus predicting to an extent the critical thickness for the WL (Much et al. 2001; Much et al. 2003)**.**

Thermodynamic arguments for the S-K transition employ 2D precursors and multiple critical sizes for the ML to bilayer transition, bilayer to trilayer and upwards (Ratsch et al. 1993) 3D islands are essentially sequential. This approach relies on pre-existing WL formation, hence ignoring the effects of reconstruction and the rate of the transition.

Non-linear equation theory employs linear stability (Spencer et al. 1993) to predict a critical thickness below which a film is stable and hence above which it is unstable. Whilst equations therein predict a number of growth morphologies, appropriate values for said equations are difficult to determine and the relationship to atomistic processes that underpin the theory are not clear.

A number of papers decry the S-K transition on InAs/GaAs (Moison et al. 1994; Joyce et al. 1999b; Garcia et al. 2000) spawning the phrase pseudo S-K. Supporting arguments include the acclaimed active involvement of the WL in QD formation and its dependency on growth rate (Joyce et al. 1999a) and a fundamental S-K transition only strictly observed at low deposition rates (Joyce et al. 2000). It has also been theorised that the growth mode is S-K at and just before t_c (Sasaki 1996), and that beyond this classical classifications are no longer relevant.

The true S-K transition is though to be strain driven and occurs to provide low-barrier dislocation sources (Eaglesham et al. 1990). However the experimentally observed coherent S-K is arguably not strain driven (Joyce et al. 1999b) and seems to adhere to segregation effects (Heyn 2001). Segregation effects are discussed more fully below.

Enhanced In content in the upper growth layer at and around the S-K transition has spawned two conflicting origination arguments, namely:

1. Stress Induced Melting of InAs
2. In segregation toward the surface

Stress induced melting of III-V compounds, follows from a similar argument regarding melting at high pressure for grey to white tin (Jayaraman et al. 1963). The proposed melting phenomenon argues to explain intermixing and realization of Gibbs free energy (Bottomley 1998) and the strain free InAs reportedly observed during pseudomorphic growth (Bottomley 1999). The existence of a RHEED pattern throughout this melting regime is capriciously explained via a mesomorphic structure whereby it exhibits both liquid and solid properties.

Segregation effects on WL formation are discussed in **2.4.2 Wetting Layer Formation**. With regard to the S-K transition, segregation is reported to reduce the island nucleation barrier (Tersoff 1998) advancing 2D to 3D growth.

In segregation combined with increased adatom density around t_c have been linked to an increased In population (Belk et al. 1997) that was initially heralded as a "floating" In layer (Garcia et al. 2000). The speculated "floating" layer would participate in the mass transport during the rapid S-K transition. The said floating In population has also been attributed to In cluster formation upon the growing surface (Fawcett et al. 1992), however the tendency for droplet formation during over supply of the group III species during MBE means the existence of such a layer is doubtful.

More recently, In segregation has been quantitatively investigated using TEM (Cullis et al. 2002). Not only was In segregation reported to be significant, but segregation in the wetting-layer was argued to control the critical point at which the transition to islanding occurs. Under the WCNH mechanism therein, an In concentration of 80 - 85 % is required in the surface layer. $In_xG_{1-x}As$ with $x = 0.25$ is approximately the smallest In fraction for which islands form. At this concentration, 3 nm of deposition is required until sufficient segregation has occurred.

The work is expanded to the complete range of deposition concentrations (Cullis et al. 2002; Cullis et al. 2005) where the critical In surface fraction of 80 - 85 % is used to predict the critical thickness for $0.25 < x < 1$. The results are in close keeping with experimental observations, supporting the argument that it is segregation strain not misfit strain that determines whether 3D islands form (Snyder et al. 1991; Cullis et al. 2002).

The ability to observe the S-K transition in real time will allow the discrete time events witnessed thus far to be observed as a continuum. Moreover, any real time study

will help reveal the extent and validity to which "quenching" can be relied upon to investigate S-K growth procedure. Strictly the binding and accommodation of the segregated In requires investigation.

2.4.4 Quantum Dot Growth

Coherent QD growth (Guha et al. 1990; Leonard et al. 1993) is restricted to deposition after the S-K transition thickness t_c and before the later dislocation critical thickness h_c (Sasaki 1996; Hasegawa et al. 1998). For binary InAs on GaAs at typical growth temperatures ~ 500 °C, t_c is established at 1.68 ML and h_c between 3 and 4 ML. The behaviour of QD after h_c can be considered as coalescence and dislocation regimes and are suitably considered in **2.4.1 Misfit Strain and Defects**.

To realise the technological application of QD a number of parameters need to be categorically understood:

1. Shape
2. Mean size and standard deviation
3. Distribution
4. Composition (hence effective size)

Most theoretical models assume the QD to be a square based pyramid with low index {101} facets, such a model is supported by equilibrium theory (Ratsch et al. 1993). However a number of experimental observances argue that this is not the case. Chevrons observed on the $[\bar{1}10]$ RHEED pattern but not on the [110] azimuth immediately imply an asymmetry (Joyce et al. 2004). Faceted streaks along the $[3\bar{1}0]$ and $[1\bar{3}0]$ directions were interpreted as a trapezoidal pyramid (Lee et al. 1998) shown in **Figure 2.20a**. Whereas investigation into the intensity of diffraction spots and chevrons (Joyce et al. 2004) were interpreted in terms of the lenticular dot shape shown in **Figure 2.20b**.

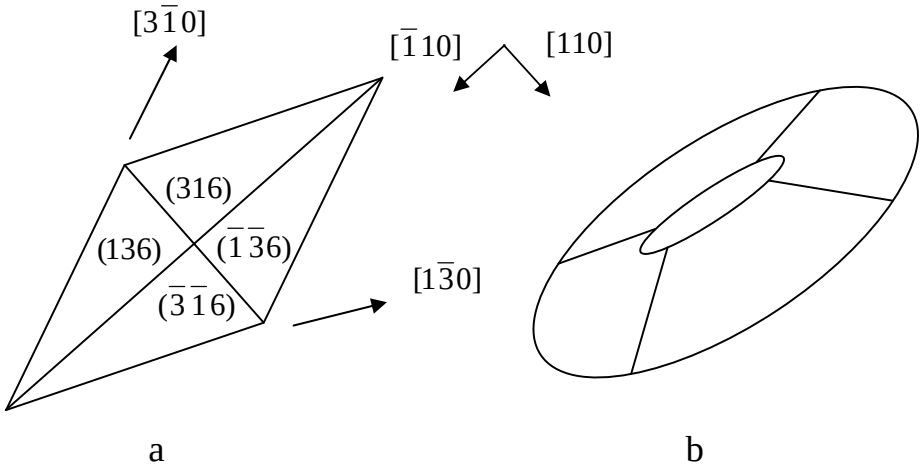

Figure 2.20: Proposed QD shapes a) trapezoidal and b) lenticular

The theoretically imperative square-pyramid QD with {101} side facets has been observed experimentally with high resolution (Ruvimov et al. 1995), though it should be noted at this time TEM suffered from strain-induced imaging problems that affect the reliability of results (Lee et al. 1998). Furthermore, STM is notoriously very useful for resolving height and distribution but tip-convolution problems hinder its application to dot shape (Shchukin et al. 1999; Joyce et al. 2004). However a combination of RHEED and these two disciplines reveal dots bound by higher index (113), (114) or (136) facets (Hasegawa et al. 1998; Lee et al. 1998; Joyce et al. 2004). Imaging of the side-wall facets speculatively reveals that the atomic structure is different to the flat facets (Hasegawa et al. 1998).

Fully formed InAs QDs have a height > ~3 nm (~10 ML) (Krzyzewski et al. 2002b). QDs of various heights have been reported, ranging from 2 - 4 nm (Bottomley 1999) though they can be grown coherently up to 8 nm (Guha et al. 1990). Base lengths of 20 nm (Bottomley 1999) to 25 nm (Guha et al. 1990) show that dots are broader than they are high.

The density n_s of islands containing *s*-atoms obeys the 2D scaling law given in **Equation 2.1** (Joyce et al. 2004). Growth observations indicate that 3D island size

distributions follow irreversible aggregation profiles (whereby adatoms that attach to islands do not subsequently detach), where island formation adheres strongly to In and Ga attachment and does not result from strain.

The relatively narrow size distribution is caused by a self-regulating growth process (Chen et al. 1996; Heyn 2001). The initial rapid growth rate at t_c slows down after coherent islands have reached a certain size, followed by a subsequent increase in growth rate at h_c corresponding to dislocation injection. This theorem assumes two points:

1. A strain induced energy barrier exists for attachment to an island
2. This energy barrier increases with island radius

It intuitively follows that larger islands grow more slowly than smaller ones, yielding the observed homogeneous size distribution. Furthermore, an increase in growth temperature allows more adatoms to overcome the attachment barrier, allowing a plausible explanation for the increase in island size with growth temperature (Sopanen et al. 1995). This theory is supported by thermodynamic arguments of upward atom migration from less-tightly-bound sites at islands peripheries to the upper dot surface (Joyce et al. 2004).

Equilibrium and kinetic arguments of QD growth dictate that whilst QD formation is not an equilibrium process (Heyn 2001) annealing reportedly forms an equilibrium state array of dots (Shchukin et al. 1999). Annealing and quenching studies *in vacuo* already reveal that annealing leads to lower density of larger dots (Krzyzewski et al. 2004). The *in situ* observations of the evolution of island size during annealing compared to any change during quenching will expound and clarify these theorems further.

Typical growth condition yielding dot densities of 10^{10} - 10^{11} cm^{-2} represent rather dilute arrays where the inter-dot distance is ~3 times the dot base area (Krzyzewski et al. 2004). Both rate equations (Dobbs et al. 1997) and equilibrium theory (Ratsch et al. 1993) have been employed successfully to predict dot densities, however they fail to convey convincing size and shape profiles.

The density is seen to be a function of both growth rate and substrate temperature. Where density is an increasing function of growth rate and a decreasing function of temperature (Dobbs et al. 1997; Joyce et al. 1998; Joyce et al. 2000; Krzyzewski et al. 2002b; Joyce et al. 2004). The growth rate response can be explained in terms of low In flux and hence higher As:In ratios significantly reducing In diffusion and hence promoting the formation of larger size dots at a smaller density. Similarly at high substrate temperatures the In diffusion rate increases promoting a higher probability of In-In interaction leading to nucleation.

Furthermore the total dot volume decreases with decreasing temperature and growth rate. Hence for dots grown at ~350 °C or ~0.01 ML s^{-1} the S-K growth mode is observed and dots are not involved in significant material transport from the WL and hence InAs dots are formed (Joyce et al. 2000). For growth rates of 0.13 ML s^{-1} the In composition drops to around 80 %. Similarly for temperatures exceeding ~420 °C alloying in the dots is evident (Dobbs et al. 1997; Joyce et al. 1998; Joyce et al. 2004).

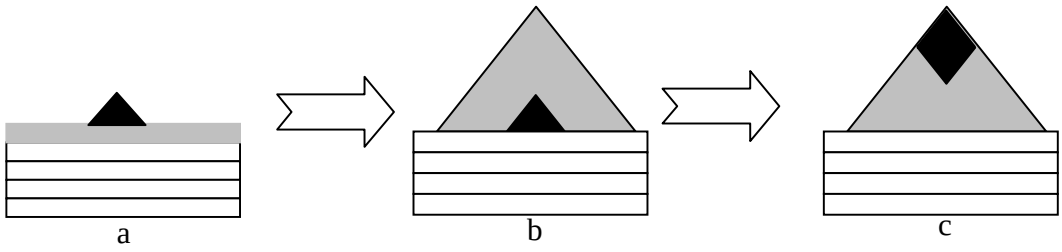

Figure 2.21: Self-capping of In-core QD: a) In core b) self-capping c) In rich apex

Aside from increasing the nucleation rate, In segregation significantly alters the alloy composition of the QD. The initial In core model (Tersoff 1998) shown in **Figure 2.21a** relies on a self-capping process (**Figure 2.21b**) that results from an In depleted reservoir i.e. the WL.

However internal segregation effects cause evolution from this plausible starting composition pushing In toward the apex (**Figure 2.21c**). Capped QD imaged via XSTM (Liu et al. 2000) seemed to confirm this assumption, however the inability to distinguish

between compositional and electronic effects unpinned the validity of the results. The truncated pyramids reported an “inverted-triangle”, heralding an In rich apex and a In deficient base. A year later, high resolution transmission electron microscopy (HTEM) utilising energy-selected imaging (ESI) provided the first direct elemental mapping measurements of In composition, providing conclusive evidence of the In rich apex (Walther et al. 2001). Empirical inter-atom potential simulations used to obtain dynamic relaxation further validated the early works (Migliorato et al. 2002). QD formation during growth and alteration during capping remains an area of active interest.

2.5 References

S. Adachi (1992) Book: Physical properties of III-V Semiconductor Compounds **Chapter 1**.

Y. Androussi, A. Lefebvre, T. Benabbas, P. Francois, C. Delamarre, J.Y. Laval and A. Dubon (1996) J. Cryst. Grow. **169**(2): 209.

Y. Androussi, A. Lefebvre, B. Courboules, N. Grandjean, J. Massies, T. Bouhacina and J.P. Aime (1994) Appl. Phys. Lett. **65**(9): 1162.

Y. Androussi, A. Lefebvre, C. Delamarre, L.P. Wang, A. Dubon, B. Courboules, C. Deparis and J. Massies (1995) Appl. Phys. Lett. **66**(25): 3450.

J.A. Appelbaum, G.A. Baraff and D.R. Hamann (1976) J. Vac. Sci. & Tech. **13**(4): 751.

J.R. Arthur (1966) J. Appl. Phys. **37**(8): 3057.

J.R. Arthur (1967) Journal of Physics and Chemistry of Solids **28**(11): 2257.

J.R. Arthur (1968) J. Appl. Phys. **39**(8): 4032.

J.R. Arthur (1974) Surf. Sci. **43**: 449.

A.R. Avery, H.T. Dobbs, D.M. Holmes, B.A. Joyce and D.D. Vvedensky (1997) Phys. Rev. Lett. **79**(20): 3938.

A.R. Avery, C.M. Goringe, D.M. Holmes, J.L. Sudijono and T.S. Jones (1996) Phys. Rev. Lett. **76**(18): 3344.

A.R. Avery, D.M. Holmes, J. Sudijono, T.S. Jones and B.A. Joyce (1995) Surf. Sci. **323**(1-2): 91.

A. Ballestad, B.J. Ruck, M. Adamcyk, T. Pinnington and T. Tiedje (2001) Phys. Rev. Lett. **86**(11): 2377.

M.C. Bartelt, S. Gunther, E. Kopatzki, R.J. Behm and J.W. Evans (1996) Phys. Rev. B **53**(7): 4099.

J.G. Belk, C.F. McConville, J.L. Sudijono, T.S. Jones and B.A. Joyce (1997) Surf. Sci. **387**(1-3): 213.

J.G. Belk, J.L. Sudijono, D.M. Holmes, C.F. McConville, T.S. Jones and B.A. Joyce (1996) Surf. Sci. **365**(3): 735.

G.R. Bell, J.G. Belk, C.F. McConville and T.S. Jones (1999a) Phys. Rev. B **59**(4): 2947.

G.R. Bell, M. Itoh, T.S. Jones and B.A. Joyce (1999b) Surf. Sci. **423**(2-3): L280.

G.R. Bell, T.J. Krzyzewski, P.B. Joyce and T.S. Jones (2000) Phys. Rev. B **61**(16): 10551.

D.K. Biegelsen, R.D. Bringans, J.E. Northrup and L.E. Swartz (1990) Phys. Rev. B **41**(9): 5701.

D.J. Bottomley (1998) Appl. Phys. Lett. **72**(7): 783.

D.J. Bottomley (1999) J. Vac. Sci. & Tech. B **17**(2): 259.

Boyce et al. (1982) Phys. Rev. Lett. **49**: 1412.

V. Bressler-Hill, S. Varma, A. Lorke, B.Z. Nosho, P.M. Petroff and W.H. Weinberg (1995) Phys. Rev. Lett. **74**(16): 3209.

V. Bressler-Hill, M. Wassermeier, K. Pond, R. Maboudian, G.A.D. Briggs, P.M. Petroff and W.H. Weinberg (1992) J. Vac. Sci. & Tech. B **10**(4): 1881.

L. Broekman, R. Leckey, J. Riley, B. Usher and B. Sexton (1995) Surf. Sci. **333**: 1115.

L.C. Cai, H. Chen, C.L. Bao, Q. Huan and J.M. Zhou (1999) J. Cryst. Grow. **197**(1-2): 364.

D.J. Chadi (1987) J. Vac. Sci. & Tech. A **5**: 834.

L.L. Chang, L. Esaki, W.E. Howard, R. Ludeke and G. Schul (1973) J. Vac. Sci. & Tech. **10**(5): 655.

Y. Chen and J. Washburn (1996) Phys. Rev. Lett. **77**(19): 4046.

A.Y. Cho (1971) J. Appl. Phys. **42**(5): 2074.

A.Y. Cho (1976) J. Appl. Phys. **47**(7): 2841.

V.R. Coluci, M.A. Cotta, C.A.C. Mendonca, K.M.I. Landers and M.M.G. de Carvalho (1998) Phys. Rev. B **58**(4): 1947.

A.G. Cullis, D.J. Norris, M.A. Migliorato and M. Hopkinson (2005) Appl. Surf. Sci. **244**(1-4): 65.

A.G. Cullis, D.J. Norris, T. Walther, M.A. Migliorato and M. Hopkinson (2002) Phys. Rev. B **66**(8): 081305

A.G. Cullis, A.J. Pidduck and M.T. Emeny (1995) Physical Review Letters **75**(12): 2368.

A.G. Cullis, A.J. Pidduck and M.T. Emeny (1996) J. Cryst. Grow. **158**(1-2): 15.

A.G. Cullis, D.J. Robbins, A.J. Pidduck and P.W. Smith (1992) Journal of Crystal Growth **123**(3-4): 333.

J.E. Davey and T. Pankey (1968) J. Appl. Phys. **39**(4): 1941.

L. Daweritz (1993) Cryst. Res. Tech. **28**: 813.

L. Daweritz and R. Hey (1990) Surface Science **236**(1-2): 15.

O. Dehaese, X. Wallart and F. Mollot (1995) Appl. Phys. Lett. **66**(1): 52.

T. Dietl and H. Ohno (2001) Physica B **9**: 185.

H.T. Dobbs, D.D. Vvedensky and A. Zangwill (1998) Appl. Surf. Sci. **123**: 646.

H.T. Dobbs, D.D. Vvedensky, A. Zangwill, J. Johansson, N. Carlsson and W. Seifert (1997) Phys. Rev. Lett. **79**(5): 897.

C.B. Duke (1993) Appl. Surf. Sci. **65/66**: 543.

C.B. Duke (1996) Chem. Rev. **96**(4): 1237.

D.J. Eaglesham and M. Cerullo (1990) Phys. Rev. Lett. **64**(16): 1943.

H.H. Farrell and C.J. Palmstrom (1990) J. Vac. Sci. & Tech. B **8**(4): 903.

P.N. Fawcett, B.A. Joyce, X. Zhang and D.W. Pashley (1992) J. Cryst. Grow. **116**(1-2): 81.

C.T. Foxon and B.A. Joyce (1975) Surf. Sci. **50**(2): 434.

C.T. Foxon and B.A. Joyce (1977) Surf. Sci. **64**(1): 293.

F.C. Frank and J.H. Van der Merwe (1949) Proc. Royal. Soc. Lon. Series A **198**(1053): 205.

D.J. Frankel, C. Yu and J.P. Harbison (1987) J. Vac. Sci. & Tech. B **5**: 1113.

Y. Fukunishi and H. Nakatsuji (1993) Surf. Sci. **291**(1-2): 281.

I. Furman and O. Biham (1997) Phys. Rev. B **55**(12): 7917.

J.M. Garcia, J.P. Silveira and F. Briones (2000) Appl. Phys. Lett. **77**(3): 409.

K.P. Giannakopoulos and P.J. Goodhew (1998) J. Cryst. Grow. **188**(1-4): 26.

S. Guha, A. Madhukar and K.C. Rajkumar (1990) Appl. Phys. Lett. **57**(20): 2110.

W.A. Harrison (1980) Book: Electronic Structure and Properties of Solids **Chapter 1**.

Y. Hasegawa, H. Kiyama, Q.K. Xue and T. Sakurai (1998) Appl. Phys. Lett. **72**(18): 2265.

T. Hashizume, Q.K. Xue, A. Ichimiya and T. Sakurai (1995) Phys. Rev. B **51**(7): 4200.

T. Hashizume, Q.K. Xue, J. Zhou, A. Ichimiya and T. Sakurai (1994) Phys. Rev. Lett. **73**(16): 2208.

C. Heyn (2001) Phys. Rev. B **64**(16): 165306

C. Heyn, T. Franke, R. Anton and M. Harsdorff (1997a) Phys. Rev. B **56**(20): 13483.

C. Heyn and M. Harsdorff (1995) J. Cryst. Grow. **150**(1-4): 117.

C. Heyn and M. Harsdorff (1997b) Phys. Rev. B **55**(11): 7034.

G. Hollinger, M. Gendry, J.L. Duvault, C. Santinelli, P. Ferret, C. Miossi and M. Pitaval (1992) Appl. Surf. Sci. **56-8**: 665.

Y. Horikoshi and M. Kawashima (1989) J. Cryst. Grow. **95**(1-4): 17.

A. Ichimiya, Q.K. Xue, T. Hashizume and T. Sakurai (1995) J. Cryst. Grow. **150**(1-4): 136.

M. Itoh (2001) Prog. Surf. Sci. **66**(3-5): 53.

M. Itoh, G.R. Bell, A.R. Avery, T.S. Jones, B.A. Joyce and D.D. Vvedensky (1998) Phys. Rev. Lett. **81**(3): 633.

M. Itoh and T. Ohno (2001a) Surf. Sci. **493**(1-3): 430.

M. Itoh and T. Ohno (2001b) Phys. Rev. B **63**(12): 125301

A. Jayaraman, W. Klement and G.C. Kennedy (1963) Phys. Rev. **130**(2): 540.

D.E. Jesson, S.J. Pennycook, J.M. Baribeau and D.C. Houghton (1993) Phys. Rev. Lett. **71**(11): 1744.

M.D. Johnson, C. Orme, A.W. Hunt, D. Graff, J. Sudijono, L.M. Sander and B.G. Orr (1994a) Phys. Rev. Lett. **72**(1): 116.

M.D. Johnson, J. Sudijono, A.W. Hunt and B.G. Orr (1994b) Appl. Phys. Lett. **64**(4): 484.

F. Jona (1965) IBM J. Res. & Dev. **9**(5-6): 375.

B.A. Joyce (1985) Rep. Prog. Phys. **48**(12): 1637.

B.A. Joyce, P.J. Dobson, J.H. Neave, K. Woodbridge, J. Zhang, P.K. Larsen and B. Bolger (1986) Surf. Sci. **168**(1-3): 423.

B.A. Joyce and D.D. Vvedensky (2004) Mat. Sci. & Eng. R **46**(6): 127.

B.A. Joyce, D.D. Vvedensky, G.R. Bell, J.G. Belk, M. Itoh and T.S. Jones (1999a) Mat. Sci. & Eng. B **67**(1-2): 7.

B.A. Joyce, D.D. Vvedensky, T.S. Jones, M. Itoh, G.R. Bell and J.G. Belk (1999b) J. Cryst. Grow. **202**: 106.

P.B. Joyce, T.J. Krzyzewski, G.R. Bell, T.S. Jones, S. Malik, D. Childs and R. Murray (2000) Phys. Rev. B **62**(16): 10891.

P.B. Joyce, T.J. Krzyzewski, G.R. Bell, B.A. Joyce and T.S. Jones (1998) Phys. Rev. B **58**(24): R15981.

D. Kandel (1997) Phys. Rev. Lett. **78**(3): 499.

P. Kratzer, C.G. Morgan and M. Scheffler (1999) Phys. Rev. B **59**(23): 15246.

P. Kratzer, E. Penev and M. Scheffler (2002) Appl. Phys. A **75**(1): 79.

P. Kratzer, E. Penev and M. Scheffler (2003) Appl. Surf. Sci. **216**(1-4): 436.

T.J. Krzyzewski and T.S. Jones (2004) J. Appl. Phys. **96**(1): 668.

T.J. Krzyzewski, B.A. Joyce, G.R. Bell and T.S. Jones (2002a) Surf. Sci. **517**: 8.

T.J. Krzyzewski, P.B. Joyce, G.R. Bell and T.S. Jones (2001) Surf. Sci. **482**: 891.

T.J. Krzyzewski, P.B. Joyce, G.R. Bell and T.S. Jones (2002b) Phys. Rev. B **66**(12): 121307.

T.J. Krzyzewski, P.B. Joyce, G.R. Bell and T.S. Jones (2003) Surf. Sci. **532**: 822.

J.A. Kubby and J.J. Boland (1996) Surf. Sci. Rep. **26**(3-6): 61.

L. Kuipers and R.E. Palmer (1996) Phys. Rev. B **53**(12): R7646.

V.P. LaBella, D.W. Bullock and C. Emery (2001a) Appl. Phys. Lett. **79**: 3065.

V.P. LaBella, Z. Ding, D.W. Bullock, C. Emery and P.M. Thibado (2001b) Int. J. Mod. Phys. B **15**: 2301.

V.P. LaBella, M.R. Krause, Z. Ding and P.M. Thibado (2005) Surf. Sci. Rep. **60**(1-4): 1.

V.P. LaBella, H. Yang, D.W. Bullock, P.M. Thibado, P. Kratzer and M. Scheffler (1999) Phys. Rev. Lett. **83**(15): 2989.

P.K. Larsen and D.J. Chadi (1988) Phys. Rev. B **37**: 8282.

H. Lee, R. Lowe-Webb, W.D. Yang and P.C. Sercel (1998) Appl. Phys. Lett. **72**(7): 812.

S.H. Lee, W. Moritz and M. Scheffler (2000) Phys. Rev. Lett. **85**(18): 3890.

F.K. Legoues, M.C. Reuter, J. Tersoff, M. Hammar and R.M. Tromp (1994) Physical Review Letters **73**(2): 300.

D. Leonard, M. Krishnamurthy, C.M. Reaves, S.P. Denbaars and P.M. Petroff (1993) Appl. Phys. Lett. **63**(23): 3203.

B.F. Lewis, F.J. Grunthaner, A. Madhukar, T.C. Lee and R. Fernandez (1985) J. Vac. Sci. & Tech. B **3**(5): 1317.

N. Liu, J. Tersoff, O. Baklenov, A.L. Holmes and C.K. Shih (2000) Phys. Rev. Lett. **84**(2): 334.

C. Lynch, E. Chason and R. Beresford (2006) J. Appl. Phys. **100**(1): 013525.

J. Mayer and S.S. Lau (1990a) Book: Electronic Material Science **Chapter 14**.

J. Mayer and S.S. Lau (1990b) Book: Electronic Material Science **Chapter 6**.

J.M. McCoy, U. Korte, P.A. Maksym and G. Meyerehmsen (1993) Phys. Rev. B **48**(7): 4721.

M.R. Melloch, J.M. Woodall and N. Harmon (1995) Ann. Rev. Mat. Sci. **25**: 547.

M.A. Migliorato, A.G. Cullis, M. Fearn and J.H. Jefferson (2002) Physica E **13**(2-4): 1147.

J.M. Moison, F. Houzay, F. Barthe, L. Leprince, E. Andre and O. Vatel (1994) Appl. Phys. Lett. **64**(2): 196.

N. Moll, A. Kley, E. Pehlke and M. Scheffler (1996) Phys. Rev. B **54**(12): 8844.

P.D. Moran, D.M. Hansen, R.J. Matyi, J.G. Cederberg, L.J. Mawst and T.F. Kuech (1999) Appl. Phys. Lett. **75**(11): 1559.

M.V.B. Moreira, M.A. Py and E. Tuncel (1991) J. Cryst. Grow. **112**(1): 14.

F. Much, M. Ahr, M. Biehl and W. Kinzel (2001) Euro-Phys. Lett. **56**(6): 791.

F. Much and M. Biehl (2003) Euro-Phys. Lett. **63**(1): 14.

Mullin et al. (1976) J. Appl. Phys. **47**: 2585.

K. Nakajima (1999) J. Cryst. Grow. **203**(3): 376.

J.H. Neave, B.A. Joyce, P.J. Dobson and N. Norton (1983a) Appl. Phys. A **31**(1): 1.

J.H. Neave, P.K. Larsen, J.F. Vanderveen, P.J. Dobson and B.A. Joyce (1983b) Surf. Sci. **133**(1): 267.

J.E. Northrup and S. Froyen (1993) Phys. Rev. Lett. **71**(14): 2276.

J.E. Northrup and S. Froyen (1994) Phys. Rev. B **50**(3): 2015.

S. Ohkouchi, N. Ikoma and I. Tanaka (1994) J. Vac. Sci. & Tech. B **12**(3): 2030.

H. Ohno (1993) Phys. Rev. Lett. **70**: 631.

H. Ohno, A. Shen and F. Matsukura (1996) Appl. Phys. Lett. **69**: 363.

T. Ohno (1996) Thin Solid Films **272**(2): 331.

A. Ohtake and M. Ozeki (2002) Phys. Rev. B **65**(15): 155318

C. Orme, M.D. Johnson, K.T. Leung and B.G. Orr (1995a) Mat. Sci. & Eng. B **30**(2-3): 143.

C. Orme, M.D. Johnson, K.T. Leung, B.G. Orr, P. Smilauer and D. Vvedensky (1995b) J. Cryst. Grow. **150**(1-4): 128.

C. Orme, M.D. Johnson, J.L. Sudijono, K.T. Leung and B.G. Orr (1994) Appl. Phys. Lett. **64**(7): 860.

M.D. Pashley (1989) Phys. Rev. B **40**(15): 10481.

M.D. Pashley and K.W. Haberern (1992a) Ultramicroscopy **42**: 1281.

M.D. Pashley, K.W. Haberern and R.M. Feenstra (1992b) J. Vac. Sci. & Tech. B **10**(4): 1874.

F. Patella, S. Nufris, F. Arciprete, M. Fanfoni, E. Placidi, A. Sgarlata and A. Balzarotti (2003) Phys. Rev. B **67**(20): 205308.

G. Patriarche and E. Le Bourhis (2001) Appl. Surf. Sci. **178**(1-4): 134.

C. Priester and M. Lannoo (1995) Phys. Rev. Lett. **75**(1): 93.

G.-X. Qian, R.M. Martin and D.J. Chadi (1988) Phys. Rev. B **38**(11): 7649.

T.R. Ramachandran, R. Heitz, P. Chen and A. Madhukar (1997a) Appl. Phys. Lett. **70**(5): 640.

T.R. Ramachandran, R. Heitz, N.P. Kobayashi, A. Kalburge, W. Yu, P. Chen and A. Madhukar (1997b) J. Cryst. Grow. **175**: 216.

C. Ratsch, P. Smilauer, D.D. Vvedensky and A. Zangwill (1996) J. De Phys. I **6**(4): 575.

C. Ratsch, P. Smilauer, A. Zangwill and D.D. Vvedensky (1995) Surf. Sci. **329**(1-2): L599.

C. Ratsch and A. Zangwill (1993) Surf. Sci. **293**(1-2): 123.

K. Reginski, J. Muszalski, V.V. Preobrazhenskii and D.I. Lubyshev (1995) Thin Solid Films **267**(1-2): 54.

B.P. Rodriguez and J.M. Millunchick (2004) J. Cryst. Grow. **264**(1-3): 64.

S. Ruvimov and K. Scheerschmidt (1995) Phys. Stat. Solid A **150**(1): 471.

A. Sasaki (1996) J. Cryst. Grow. **160**(1-2): 27.

W.G. Schmidt, S. Mirbt and F. Bechstedt (2000) Phys. Rev. B **62**(12): 8087.

R.L. Schwoebel and E.J. Shipsey (1966) J. Appl. Phys. **37**(10): 3682.

V.A. Shchukin and D. Bimberg (1999) Rev. Mod. Phys. **71**(4): 1125.

T. Shitara, D.D. Vvedensky, M.R. Wilby, J. Zhang, J.H. Neave and B.A. Joyce (1992) Phys. Rev. B **46**(11): 6825.

P. Smilauer and D.D. Vvedensky (1993) Phys. Rev. B **48**(23): 17603.

C.W. Snyder, B.G. Orr, D. Kessler and L.M. Sander (1991) Phys. Rev. Lett. **66**(23): 3032.

M. Sopanen, H. Lipsanen and J. Ahopelto (1995) Appl. Phys. Lett. **67**(25): 3768.

B.J. Spencer, P.W. Voorhees and S.H. Davis (1991) Phys. Rev. Lett. **67**(26): 3696.

B.J. Spencer, P.W. Voorhees and S.H. Davis (1993) J. Appl. Phys. **73**(10): 4955.

M. Tamura, A. Hashimoto and Y. Nakatsugawa (1992) J. Appl. Phys. **72**(8): 3398.

I. Tanaka, S. Ohkouchi, T. Kato and F. Osaka (1991) J. Vac. Sci. & Tech. B **9**(4): 2277.

J. Tersoff (1998) Phys. Rev. Lett. **81**(15): 3183.

J. Tersoff and F.K. Legoues (1994) Physical Review Letters **72**(22): 3570.

E.S. Tok, J.H. Neave, J. Zhang, B.A. Joyce and T.S. Jones (1997) Surf. Sci. **374**(1-3): 397.

E. Tournie, O. Brandt, K.H. Ploog and M. Hohenstein (1993) Appl. Phys. A **56**(1): 91.

Y. Uchida, H. Kakibayashi and S. Goto (1993) J. Appl. Phys. **74**(11): 6720.

W.N. Unertl (1996) Book: Handbook of Surface Science **Chapter 1**.

J.H. Van der Merwe (1991) J. Elec. Mat. **20**(10): 793.

J.A. Venables, G.D.T. Spiller and M. Hanbucken (1984) Rep. Prog. Phys. **47**(4): 399.

D.D. Vvedensky, M. Itoh, G.R. Bell, T.S. Jones and B.A. Joyce (1999) J. Cryst. Grow. **202**: 56.

T. Walther, A.G. Cullis, D.J. Norris and M. Hopkinson (2001) Phys. Rev. Lett. **86**(11): 2381.

J.F. Whitaker (1993) Mat. Sci. Eng. B: 61.

Q.K. Xue, Y. Hasegawa, T. Ogino, H. Kiyama and T. Sakurai (1997a) J. Vac. Sci. & Tech. B **15**(4): 1270.

Q.K. Xue, T. Hashizume and T. Sakurai (1997b) Prog. Surf. Sci. **56**(1-2): 1.

Q.K. Xue, T. Hashizume and T. Sakurai (1999) Appl. Surf. Sci. **141**(3-4): 244.

H. Yamaguchi and Y. Horikoshi (1995) Phys. Rev. B **51**(15): 9836.

H. Yamaguchi, M. Kawashima and Y. Horikoshi (1988) Appl. Surf. Sci. **33-4**: 406.

J. Zou, D.J.H. Cockayne and J.J. RussellHarriott (1997) Appl. Phys. Lett. **70**(23): 3134.

Chapter 3: Experimental Methods

This chapter introduces the experimental methods used during this work. Rather than develop a detailed history of the devices in question, this chapter introduces the general principles and discusses the specific idiosyncrasies of the Omicron combined MBE and STM utilised. Section **3.6 Concurrent MBE-STM** explores the well established Si/Ge *in situ* MBE-STM work and the current III-V status.

3.1 Molecular Beam Epitaxy

3.1.1 Overview

Molecular Beam Epitaxy (MBE) is basically a refined vacuum evaporation process (Joyce 1985). Neutral thermal atomic and molecular beams are directed toward a heated substrate held under ultra high vacuum (UHV). The apparatus used in this work is shown in **Figure 3.1**.

Briefly, samples enter the system through the Fast Entry Lock (FEL) to the rear (not shown) and the FEL is turbo pumped down to 10^{-9} mBar in approximately 30 minutes. Samples are then transferred to the manipulator stage, vacuum quickly recovers to 10^{-10} mBar ensuring an environment where high quality films can be manufactured. The FEL and MBE chambers are isolated via an interlock valve.

Molecular beams are created in Knudsen effusion cells, for Ga and In sources the crucible within the cell is manufactured from Pyrolytic Boron Nitride (PBN). Beam fluxes are given by (Joyce 1985):

$$J_i = \left[\frac{a p_i}{\pi d^2 (2\pi m_i kT)^{1/2}} \right] \cos\theta \qquad \textbf{Equation 3.1}$$

Where J_i is the flux per unit area at a distance d from the source, a is the orifice area, atoms/molecules have a mass m_i and a beam equivalent pressure (BEP) of p_i at temperature T K and θ is the angle between the source and the sample surface.

Group III elements produce monatomic beams, whilst group V sources are more complex (see below). Three cell variants are employed in this work.

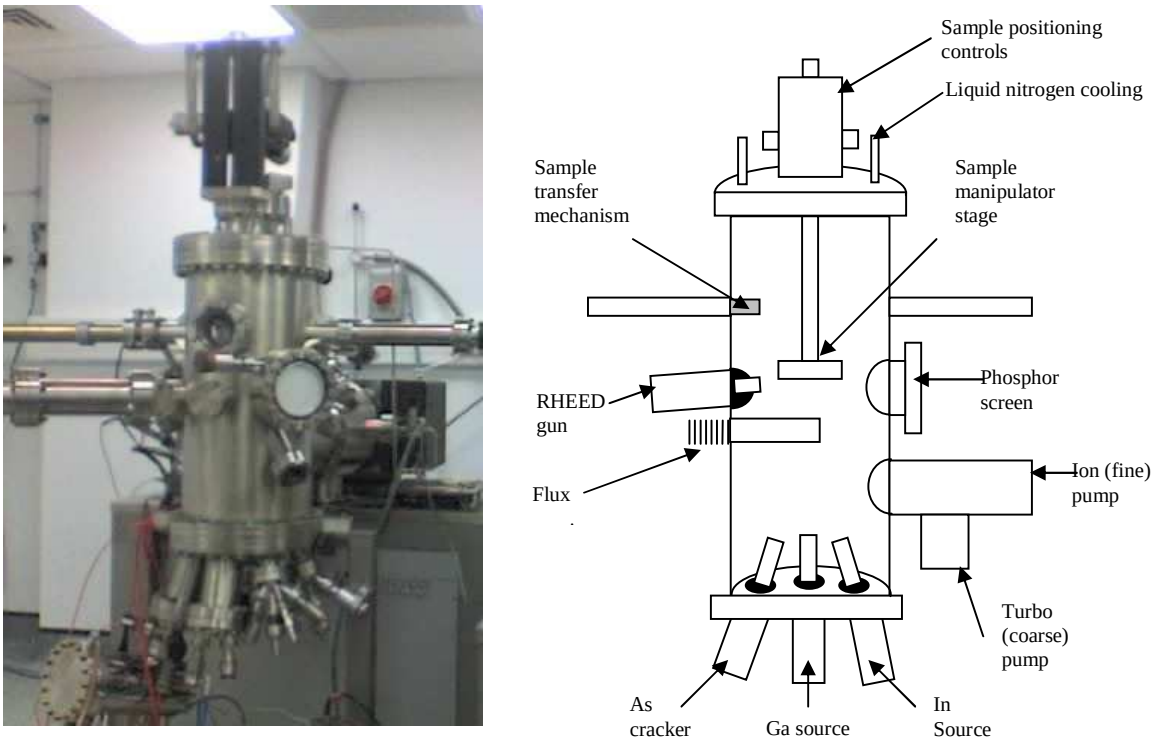

Figure 3.1: Image and schematic diagram of MBE chamber components

Firstly the Ga source is a simple Knudsen cell (MBE Komponenten GmBH: WEZ-40-10-KS) with an integrated cooling shroud to maintain a stable cell temperature and a shutter to regulated the flux that can be either mechanically or hand operated. An ion gauge head is employed as a flux monitor with growth rates calibrated from SEM observations of a patterned substrate.

The second source is a two-zone Knudsen cell As cracker. A tetramer flux is generated in the first zone from the evaporation of bulk As at 380 - 450 °C. This is then passed through an optically baffled high temperature stage producing dimers when operated above 800 °C. Cooling shrouds stabilize temperatures of operation and a needle-valve allows the flux to be altered from 1 - 100 % by a hand operated mechanism. The flux is calibrated with an ion gauge extended into the beam.

The third model is an electron beam (e-beam) source employed chiefly to reduce heating effects whilst operating within the STM chamber (see section **3.6 Concurrent MBE-STM**). Crucible material is chosen in respect of evaporation material, in order to provide a stable source. Whilst In, Ga and As can be created with e-beam sources, the applicability to As evaporation is reportedly poor, due to high vapour pressure at low temperature. The fluxes of the e-beam cells are calibrated with integrated flux monitors that simply require calibration to BEP (see section **7.3 E-beam cells for MBE**).

Cell alignment allows a focal point for the multiple beams upon the sample surface. Larger samples are often rotated within the flux (at a frequency greater than the duration to grow a single ML) to achieve uniform composition (Cho et al. 1981) though for the small samples used in this work this is superfluous. Liquid Nitrogen cooling plates within the system help reduce the chamber pressure by allowing a sink for the background flux.

Epi-ready substrates arrive with a volatile surface oxide created in the etching and cleaning process. Removal of this oxide at T_s = 580 - 620 °C under an As flux produces relatively smooth surfaces with deformation heights of 5 - 20 nm (see **section 6.3.1**). A 0.5 – 1.0 µm GaAs buffer layer grown at Ts = 580 - 620 °C restores an atomically flat surface. Growth can subsequently be performed at T_s = 350 - 520 °C for InAs (or InGaAs) and T_s = 480 - 620 °C for GaAs.

The great interest in MBE as a means of device fabrication initially arose due to the necessity for sub-ML deposition control to realise super lattice and quantum well structures. The same sub-ML depositional accuracy has allowed the investigation of kinetic processes for both homo- and heteroepitaxial III-V compounds via *in vacuo* STM. The invention of concurrent STM and MBE (see **section 3.6**) further expands the potential of this method.

3.1.2 Temperature Measurement

Samples can be heated by 3 different methods:

1. Radiative Heating (RH)

2. Direct Heating (DH)
3. Pyrolytic Boron-Nitride Radiative Heating (PBNRH)

RH is the common mechanism employed in MBE whereby a filament is placed close to the sample plate (typically molybdenum (Mo) or tantalum (Ta)). In this apparatus, wafers up to 15 x 15 mm^2 can be mounted and are adhered via a small In droplet.

DH and PBNRH utilise specially developed sample plates shown in **Figure 3.2a** and **b**, respectively. For DH, heating is achieved by passing a current through the sample via the contact bars, with one side being electrically isolated from the plate with ceramic washers. For PBNRH, current is passed through a pyrolytic graphite (PG) track encapsulated in the PBN plate, where again one contact bar is electrically isolated. Furthermore, the sample is grounded at both ends, which simplifies high temperature STM (see **section 7.4**). Achieving repeatable and accurate substrate temperature (T_s) is essential for MBE. Samples for the latter two heating methods have a typically surface area of 9 x 1.4 mm^2 for DH and 11 x 3.9 mm^2 for PBN though clamping procedures reduce the active length to 5.5 mm.

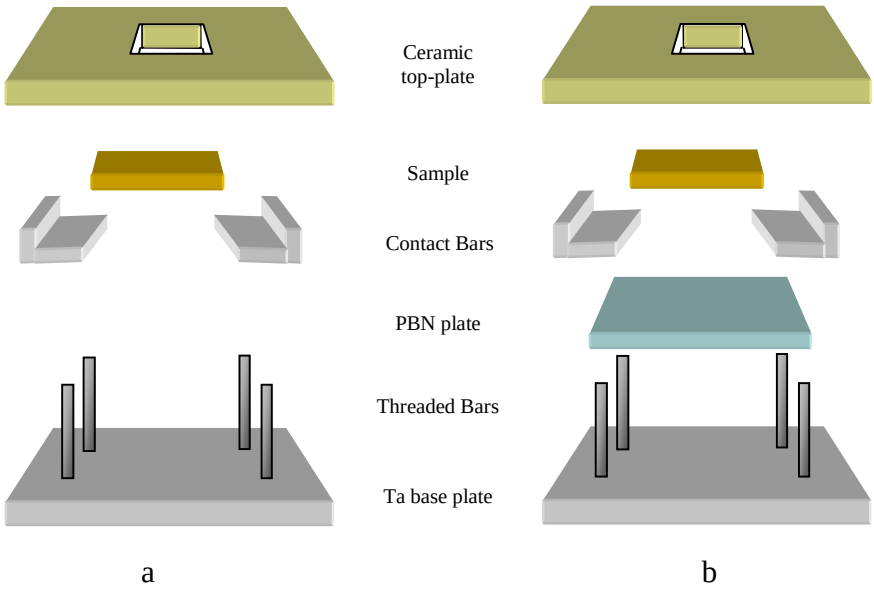

Figure 3.2: Exploded schematic of a) DH and b) PBNRH sample plates

Temperature monitoring is provided through a thermocouple mounted on the manipulator stage close to the sample plate. This provides reasonable correlation with the sample for RH, but a more accurate means of measurement is required to facilitate DH and PBNRH operation.

The original DH and PBNRH plates are incompatible with RHEED, due to the depth of the ceramic top plate and the glancing angle (1 - 3°) of the RHEED beam to the sample surface. A RHEED compatible alteration of the DH plate enables sample mounting on top of the ceramic plate (**Figure 3.3**). Principally RHEED can be used to attain two useful sample reference points at ~480 °C and ~580 °C as describe in section **3.2 Reflection High Energy Electron Diffraction**. RHEED is only available in the MBE chamber, hence without an alternative method sample heating in the STM chamber must reply on applying identical heating power as during the initial RHEED observations and assuming the temperature reached coincides in each case with reasonable accuracy (see **Chapter 4: Direct Heating**).

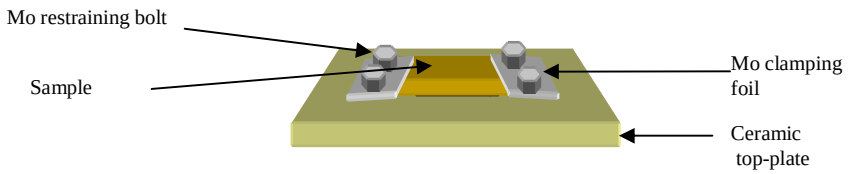

Figure 3.3: RHEED compatible alteration of DH top plate

A thermocouple attached at the centre of the sample can be implemented to provide temperature measurements. The quality of the connection will significantly alter the results, to this end RHEED temperature measurement can be used to verify two set points enabling a certain calibration. The thermocouple cannot be attached to the sample during growth and hence power-temperature curves generated from such results can only be used as a approximate guide for heating in the STM chamber. Remote thermocouple (i.e. located at a fixed position in close proximity to the sample) is notoriously inaccurate (Bracker et al. 2000) due to changes in radiative heating during growth.

Accurate optical pyrometery suffers from a requirement to know the exact emissivity of the material, a value that changes markedly over the growth regime 350 - 580 °C. This makes the technique extremely inaccurate in the first instance and limits its accuracy even following a reference temperature (Bracker et al. 2000).

Band-gap thermometry and transmission spectroscopy utilise the phenomenon that the band-gap energy of semiconductors decreases with increasing temperature (Foxon et al. 2007), hence changes of wavelength of the absorption edge of GaAs can be used to predict temperature (Hellman et al. 1987):

$$Eg(T) = 1.519 - \frac{5.409 \times 10^{-4} T^2}{(T + 204)} eV \qquad \textbf{Equation 3.2}$$

where T is the temperature. Whilst this method is applicable to GaAs (Sacks et al. 2005), an ~ 6 Å epilayer of a small bandgap semiconductor (such as InAs) would tend to absorb most of the source light (Bracker et al. 2000). Such a problem can be overcome by inserting a reflective epilayer into the structure and employing transmission spectroscopy in the reflectance mode (deLyon et al. 1997). This technique utilises direct radiative heating of the substrate, using the absorption of the light of the heating element to determine the temperature. Hence it is only applicable to PBNRH, with the ability to use the technique severely impaired by the small dimensions of the substrate.

DH of the substrate possesses the advantage of rapid quenching of >50 °C/s and hence effects of the quenching procedure can be observed. DH is governed by the power equation:

$$P_{electric} = P_{radiation} + P_{conducta\,nce} \qquad \textbf{Equation 3.3}$$

Where $P_{electric}$ is the electrical heating power ($= I(T)^2 R(T)$), $P_{radiation}$ is the power loss due to thermal radiation and $P_{conductance}$ is the power loss due to heat conductance. Whilst $P_{electric}$ is known from the power supply setting, $P_{radiation}$ can only be approximated and

hence $P_{conductance}$ and the heating curves generated are fraught with errors (see section **4.2 Power Equation**).

High temperature thermography (discussed in **3.3 Pyrometry**) can effectively be used to determine both the sample temperature and the gradient across the sample. This topic is discussed in detail in **Chapter 4: Direct Heating .**

3.1.3 Sample Preparation

Epi-ready wafers from the supplier are coated in a protective oxide that must be removed prior to growth. This oxide undergoes an aging process where the bulk reacts with the volatile As_2O_3 compound (Wasilewski et al. 2004):

$$2GaAs + As_2O_3 \rightarrow 4As + Ga_2O_3$$ **Equation 3.4**

Heating under UHV conditions below 400 °C results in an acceleration of the aging process where desorption of H_2O and the As-oxides are required to clean the surface. The observed roughening of the GaAs surface as discussed in section **2.3.6 Large Scale Mound Formation** is believed to result from a decomposition of the underlying bulk in order to produce a volatile Ga_2O oxide from the more stable Ga_2O_3:

$$Ga_2O_3 + 4GaAs = 3Ga_2O \uparrow + 2As_2$$ **Equation 3.5**

Hence the roughening could be lessened by supplying Ga externally by means of a Ga-flux at lower temperatures of around 440 °C, rather than relying on GaAs from the bulk at temperatures of 580 °C. The reaction would hence become:

$$Ga_2O_3 + 4Ga = 3Ga_2O \uparrow$$ **Equation 3.6**

However since the decomposition of the bulk is a random process with an activation temperature above 400 °C, the formation of micropits cannot be fully suppressed. Rather the surface roughness should be simply reduced. This principle is investigated in section **6.3 Clean-up Techniques (PBNRH)**.

3.2 Reflection High Energy Electron Diffraction

Reflection High Energy Electron Diffraction (RHEED) is utilised concurrently with MBE to determine:

1. Surface structure
2. Quality
3. Growth rate
4. Temperature.

The principle of RHEED involves an electron beam of 5 - 20 keV striking a crystal surface at an angle of 1 - 3°, the diffraction of which creates a pattern on a phosphor screen. The electrons only penetrate the first few monolayers due to the glancing angle, making RHEED extremely surface sensitive.

To identify the various surface reconstructions, three azimuths are required with 45° spacing ($[\bar{1}10]$, [010] and [110] (LaBella et al. 2005)). Patterns are classified by the number of spots, n, that appear in additional the primary spot. Hence (n + 1)×, where n can have any positive integer including zero. Additional spots correlate to a structural spacing (n + 1) times greater than the unreconstructed lattice. **Table 3.3.1** summarises the common surface reconstructions on GaAs(001) and their corresponding periodicities. An example of the pattern observed for diffraction from the GaAs(001)-(2 × 4) surface is given in **Figure 3.4**.

	$[110]$	$[010]$	$[\bar{1}10]$
c(4 × 4)	2×	4×	2×
(2 × 4)	2×	1×	4×
c(2 × 8)	2×	2×	4×
(2 × 1)	2×	1×	1×

Table 3.3.1: GaAs(001) Surface Reconstructions

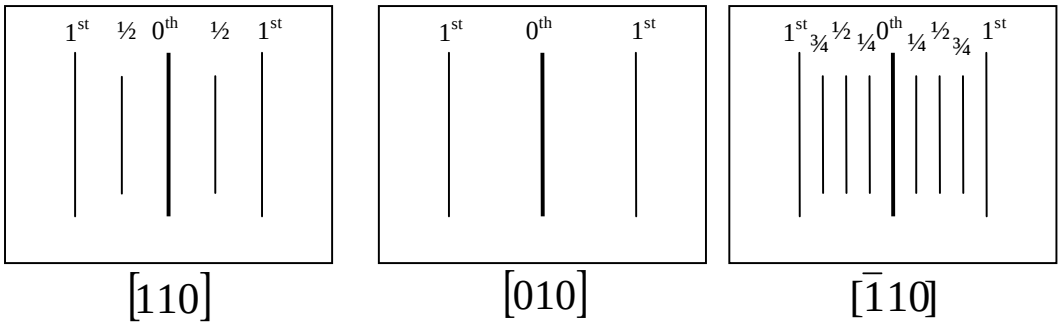

Figure 3.4: GaAs(001)-(2 × 4) diffraction patterns

Theoretically, if a surface is atomically flat with no ML steps, the long range surface order does not significantly effect the reciprocal lattice rods, and yields a "broken-streaky" RHEED pattern. (i.e. for an atomically flat surface, the reciprocal lattice rods are infinitely narrow and the intersections of the rods with the Ewald sphere will still be approximately points, hence the RHEED image will appear as a number of disassociated short streaks or oval spots).

If the rods have some width, however, the intersections broaden out into a "streaky" pattern, which then merge to form a continuous streak. (i.e. typical step edge roughness equates to broadening of the lattice rods, resulting in a "continuous-streaky" pattern). Further distinctions can be made for amorphous layers that appear as a "haze" and polycrystalline surfaces that exhibit "rings". Hence, RHEED gives a qualitative method for quickly checking the surface condition (LaBella et al. 2005).

The "spotty" (1 × 1) RHEED pattern is often associated with QD growth and is used to mark the transition. In this remark the spots correspond to scattering off the multiple facets of the surface.

The distance between adjacent streaks in a diffraction pattern corresponds to the lattice parameter (a) of the substrate. It can be shown that (Rioux 2006):

$$\frac{W}{L} \approx \frac{a * \lambda}{2\pi}$$ **Equation 3.7**

where W is the pattern spacing, L is the sample-screen distance, a^* is the reciprocal lattice rod spacing and λ is the electron wavelength. This fact has been utilised in heteroepitaxy of InAs/GaAs to monitor alloying in the epilayer.

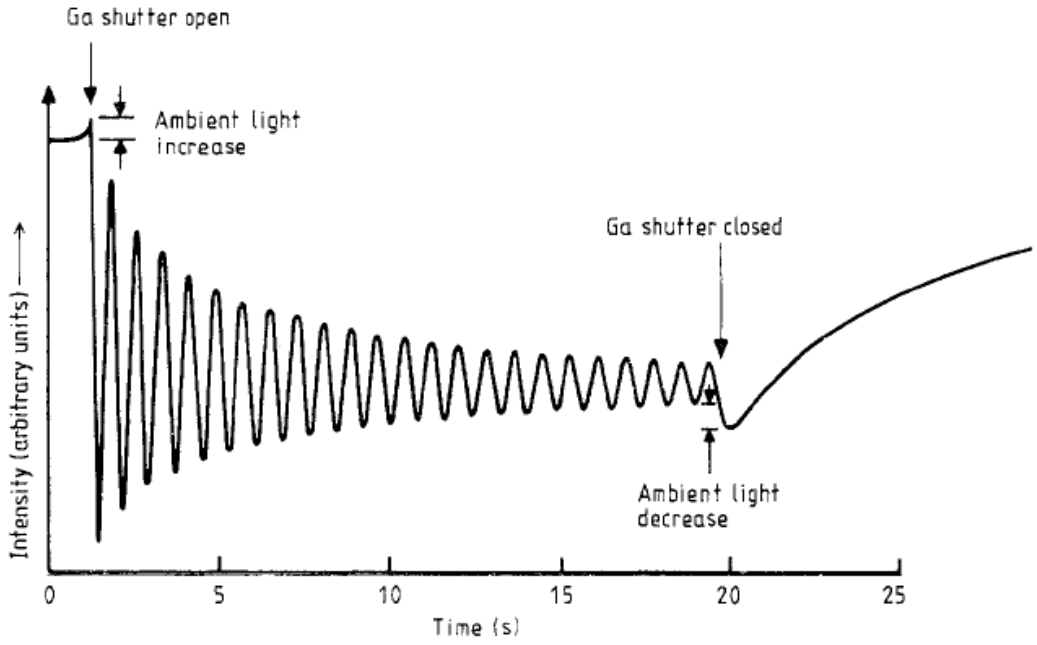

Figure 3.5: RHEED oscillation damping, taken from (Joyce 1985)

The spacing between neighbouring diffraction rods delineates the local spacing of the reconstruction domains on the surface. Chiefly noted in InAs/GaAs is an $a(1 \times 3)$ pattern, so called because the $^1/_3$ and $^2/_3$ order rods are closer to each other than the 1^{st} or 0^{th} order features (Bell et al. 1999). A possible cause is the overlap the twofold and threefold periodicity of the surface.

RHEED intensity oscillations provide a quick, accurate method for determining growth rates. Varying amplitude oscillation corresponds to film growth, with an entire amplitude cycle representative of a single ML. **Figure 3.5** shows a typical RHEED intensity variation with time. The damping of the oscillations corresponds to a subsequent roughening of the growth surface as discussed in section **2.3.3 Stoichiometry and Roughness**.

Transition	T / °C	As BEP / μTorr	Significance / Comment
c(4 × 4) to (2 × 4)	~500	3 - 5	Typical for InAs QD growth
(2 × 4) to (2 × 1)	~620	3 - 5	Buffer layer growth*
Rings to (2 × 4)	580	3 - 5	Oxide desorption and Clean-up
Haze to (1 × 3)	~290	3 - 5	As-cap desorption**
(2 × 1) to (4 × 2)	~680	3 - 5	High temperature reference***
c(4 × 4) to (2 × 4)	~400	0	Low temperature reference***

*higher quality buffer layers (reference)

**As-cap: amorphous As protective layer

***Used for reference only. Not typical growth regime.

Table 3.2: GaAs(001) RHEED transition temperatures

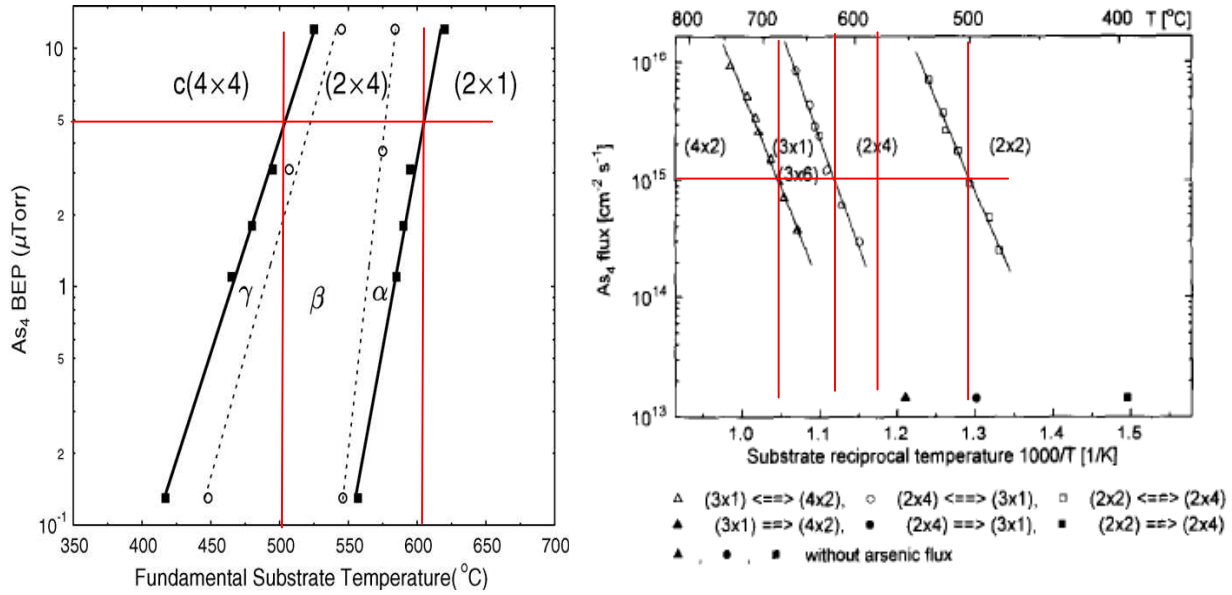

Figure 3.6: GaAs(001) Static Surface Maps a) from (LaBella et al. 2005) b) from (Reginski et al. 1995)

The GaAs(001) static surface map (**Figure 3.6**) plots the surface reconstructions as functions of both T_s and As_4 BEP. Consequentially the two reconstruction transitions can be utilised to predict T_s for a known BEP with relative accuracy, or vice versa. For

nominal As_4 BEP around 3 - 5 μTorr (**Figure 3.6**) the transition temperatures become of particular interest (**Table 3.2**). The utilisation of RHEED for temperature calibration is discussed in further detail in **Chapter 4: Direct Heating .**

To interpret **Figure 3.6**, it is important to relate the BEP to a molecular flux (**Equation 3.8**):

$$J(As_4) = \frac{BEP(As_4)}{\eta(As_4).T_{gauge}} . \sqrt{\frac{8.T_{source}}{\pi.k.m(As_4)}} \qquad \textbf{Equation 3.8}$$

Where $J(As_4)$ is the flux in mol cm^{-2} s^{-1}, $BEP(As_4)$ is the beam equivalent pressure in μTorr, $\eta(As_4)$ is the ion gauge sensitivity coefficient ~6.8, T_{guage} and T_{source} are the gauge and source temperatures of 300 K and 680 K respectively, k is the Boltzmann constant and $m(As_4)$ is the mass of a As-tetramer in grams. Hence a BEP of 5 x 10^{-6} μTorr equates to ~1 x 10^{15} mol cm^{-2} s^{-1}.

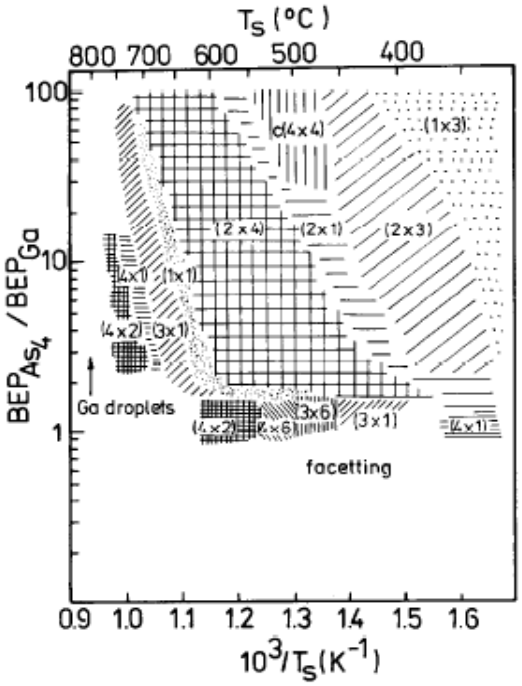

Figure 3.7: Dynamic Surface Map taken from (Daweritz et al. 1990)

The static surface diagram is merely a snapshot of dynamic surface diagram (**Figure 3.7**). This can be utilised to calibrate the As:Ga BEP for a known temperature, most notably the approximate 1:1 ratio for (2 × 4) to (1 × 1) transition at the clean-up temperature of 580 °C.

3.3 Pyrometry

Pyrometery is a well-known non-contact measurement of temperature utilising an object's emission and emissivity. Emissivity of a perfect emitter or black body is defined as 1, similarly an object that emits no radiation has an emissivity of 0.

The accuracy of pyrometery temperature relies on the accuracy of the emissivity. A problem in the case of semiconductors is that epilayers have significant effects on emissivity (Timans 1992; deLyon et al. 1997). Furthermore the doping density has a large effect on the emittance (and hence the emissivity) of a sample (Jordan 1980).

Accurately estimating the emissivity is a key problem for the Minolta/Land Cyclops 241 pyrometery camera used in this work, where the emissivity is set manually with an analogue dial. Attempts to do so can be found in Section **4.2.2 Total Hemispherical Emissivity.**

Emissivity corrected optical pyrometery (Anon 1972) claims to be an automated method for emissivity calibration, utilising a spherical light integrator having a reflective internal surface. Modulation of the light allows a reflected beam to be distinguished from the light source, emissivity is calculable from the reflected light. However such means were not available in this work.

3.4 Thermography

Thermography is a type of thermal imaging science that detects the radiation emitted by an object and produces an image based on that radiation. Two systems were considered in this work:

1. DeltaTherm from Stress Photonics, Inc.

2. Titanium Orion from Cedip Infrared Systems

Both systems comprise an infra-red camera and a digital signal processor (**Figure 3.8**). Originally developed for thermoelastic stress analysis (TSA), the DeltaTherm system has consequentially expanded into thermography.

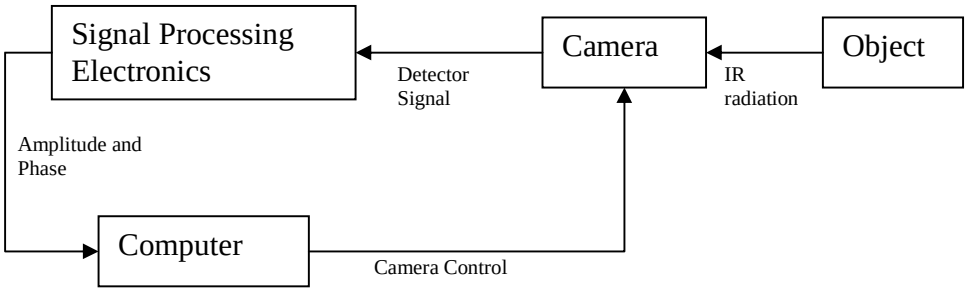

Figure 3.8: Block diagram of DeltaTherm System

The focal plane array (FPA) camera consist of thousands of InSb IR detectors, each measuring IR radiation at a specific point on the object's surface. The measured photon flux is converted to electrical charge and stored in a capacitor and read out at a specified frame rate. The pixel integration time represents the length of time allotted for capacitor charging.

The DeltaTherm instrument is particularly suited to measuring changing temperature, notably intent upon measuring small thermal changes caused by thermoelastic stress. Operation in AC mode enables thermoelastic stress to be monitored, whereas DC mode acquires data on absolute temperature values.

Data collected corresponds to photon hits and not temperature. Thus the DeltaTherm camera must be calibrated prior to use, producing a CAL file where a number of photon hits vs. temperature points are correlated and values between are estimated by linear approximation. The photonic range of the camera is set by the capacity of each capacitor, capable of storing 2^{14} or 16,384 bits. A trade off between range and resolution is required, where any change to the camera settings (shutter speed and pixel integration time) requires recalibration of the camera.

The Cedip Titanium has a number of calibration files for a range of objects, and hence calibration of the camera is somewhat simplified. The system was tolerant to changes in setup and automatically compensated shutter speed and pixel integration attenuations.

The accuracy of absolute values is hence governed by the accuracy of calibration temperatures, to which end the Cedip Titanium was chosen. However DeltaTherm does provide a 2D map of the sample surface displaying temperature variations in a colour contrast image, thus allowing the temperature variance as a result of both sample bending and current pinching to be investigated. This topic is discussed in detail in **Chapter 4: Direct Heating** and **Chapter 6: Sample Preparation for STM.**

3.5 Scanning Tunnelling Microscopy

3.5.1 Overview

Scanning Tunnelling Microscopy (STM) relies on the phenomenon of electron tunnelling. Where the classical physics principles require substitution for quantum theory. An exponential dependence of tunnelling current (I) on junction distance (s) is crucial to STM operation, the experimental observation of which in 1981 can be heralded as the birth of STM (Binning et al. 1982). Atomic resolution of Si(111)-(7 × 7) followed in late 1982 (Binnig et al. 1983).

The principle of operation involves bringing an ultra (atomically) sharp tip into angstrom separation from a (semi-)conducting sample. The experimental apparatus utilised in this work is given in **Figure 3.9**.

Samples are loaded into the flip stage from the MBE chamber via a transfer arm. The wobble stick is then used to manipulate the sample into the carousel for storage (12 in total) or insertion directly into the sample holder in the floating stage. The floating stage comprises a two-fold damping system, utilising springs and eddy current dampers. This low (approx. 1 Hz) stage resonance frequency combined with the high resonant frequency rigid STM unit body provides the overall system response. Under optimised conditions external vibrations can be reduced by a factor of 10^{-7}, which reduces the

typical 1 μm floor vibrations to 0.1 pm, in turn allowing vertical resolution of 1pm (0.01 Å) and hence high resolution atomic scale images.

In the absence of a heating element, sample heating can only be performed via Direct Heating (DH) or Pyrolytic Boron-Nitride Resistive Heating (PBNRH) as described in **3.1 Molecular Beam Epitaxy**, the application of which is discussed in detail in **Chapter 4: Direct Heating** . Additionally cooling can be achieved utilising liquid-He to produce temperatures down to 25 K.

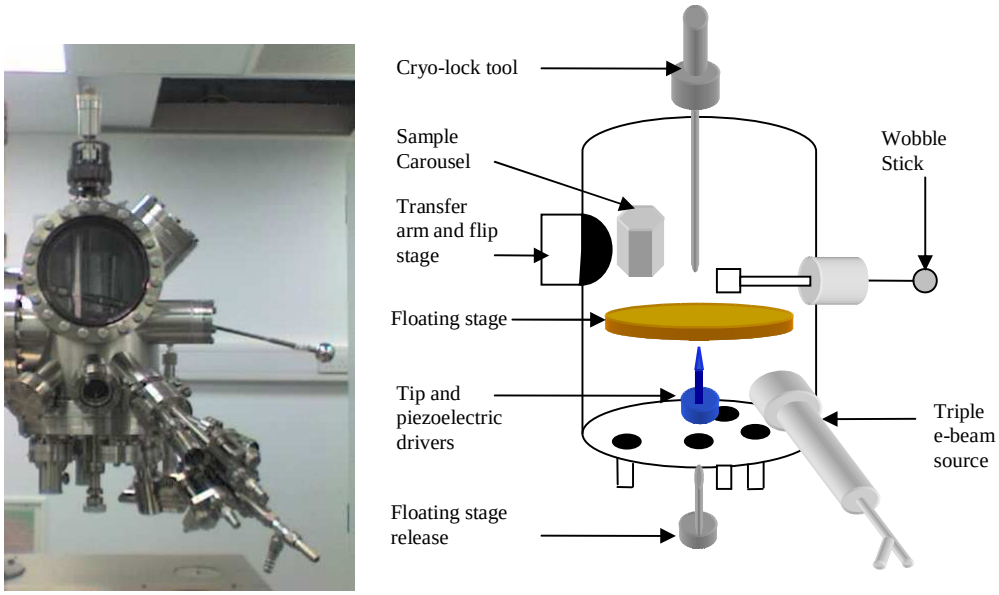

Figure 3.9: Image and Schematic of STM and components

The tip position is controlled by a single tube piezoelectric scanner shown schematically in **Figure 3.10**. A pair of outer electrodes allow "bending modes" realising x-y motion, whereas expansion of the tube provides z motion (Binnig et al. 1986). Applying equal and opposite voltages to the two outer electrodes provides deflection equated by:

$$\Delta x(\Delta y) = 2\sqrt{2}d_{31}\frac{l^2}{\pi Dh}U_{x(y)}$$ **Equation 3.9**

where D is the inner diameter of the tube, d_{31} is the piezo coefficient, $U_{x(y)}$ is the applied voltage, l is the length of the tube and h is its thickness (Chen 1992), whereas applying a voltage to a single electrode yields a deflection of exactly half that given in **Equation 3.9**. The tube has a maximum scan range of 12 x 12 μm^2 with 1.5 μm travel, however calibration has biased the scanner for use at atomic resolution and larger scale plots need careful interpretation or re-calibration.

End user control is facilitated through a software package named SCALA PRO developed by Omicron Nanotechnology GmBH [Omicron, SCALA PRO Software Manual, version 5.0 (2003)]. SCALA enables operation, data procession and analysis.

Operation covers controlling experimental parameters of gap voltage, V_{gap}, tunnelling current, I_{tunnel}, loop gain and scan speed. Analysis allows the selection of sub-areas within the current scan window and the application of Fourier transforms and autocorrelation functions. Processing accommodates background correction via interpolation and filtering and smoothing routines. Data can also be edited, magnified and the distortion corrected. Visualisation includes 3D renderings and line profiles.

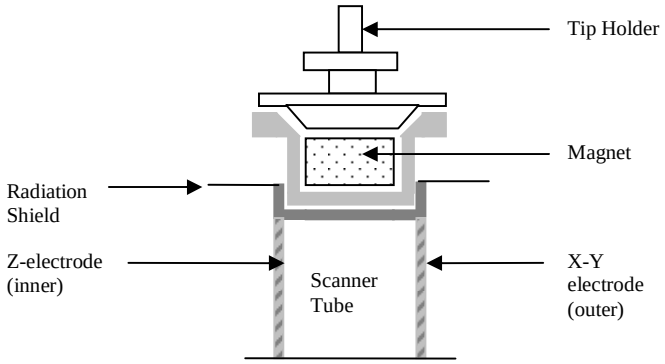

Figure 3.10: Scanner head and piezoelectric driver

3.5.2 Tip Fabrication

The STM tip is crucial to operation (Cricenti et al. 1994; Kubby et al. 1996). The required shape of an STM tip depends on its intended purpose. For imaging of flat

surfaces at atomic resolution the shape of the tip is inconsequential, provided it terminates on a single atom. Since the tunnelling current is exponentially dependent on tip-sample distance, only the atom at the apex contributes to the tunnelling current. Provided the next nearest atom is more than 3 Å removed, its contribution to tunnelling current can be considered negligible (~0.1 %). Unfortunately, if a cluster of atoms share a similar tip-sample separation distance then the contribution from said atoms is significant and this leads to multiple tip imagining artefacts or "ghosts" (Park et al. 1987).

For rough surface imaging, the shape of the tip becomes important. Cones with a broad angle fail to penetrate into deep, narrow topographic features leading to a smoothing of the observed surface (Musselman et al. 1990). Predicting the degree of roughening from scan speed and tip geometry (Keller 1991) is complicated by the fact that tunnelling current can switch between various atoms along the tip's side cone depending on its shape.

STM tip fabrication is a multistep process involving:

1. Electro-chemical etching
2. (Optional) *ex situ* preparation
3. *In vacuo* heating or ion bombardment
4. Maintenance

Electro-chemical etching can be separated into two broad categories:

1. In solution
2. Lamella

For in solution etching a length of wire is inserted into the solution (**Figure 3.11**) and whilst the meniscus concentrates the etching at the air-etchant interface the entire submerged section is effectively etched. Meniscus slipping (**Figure 3.11c**) can cause the etching area to move down the tungsten (W) wire, increasing the length of the tip.

For lamella etching the membrane concentrates the etching into a small area along the W wire (Melmed 1991; Klein et al. 1997) (**Figure 3.11b**). The fragile lamella

membrane is prone to multiple breakages during the etching process and the restoration of which involves "dipping" the ring back in the etchant, possibly moving the etching site. Additionally warping of the lamella around the wire can increase the initially concentrated etching area (**Figure 3.11d**). This technique requires constant supervision.

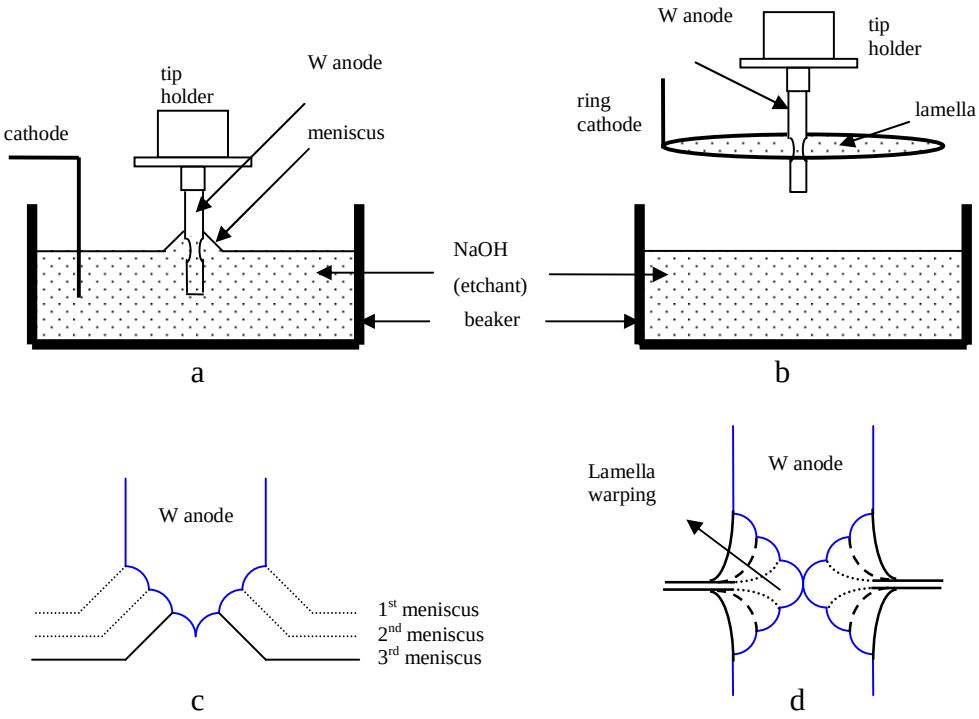

Figure 3.11: Etching procedures a) In solution b) lamella c) meniscus dropping d) lamella warping

Optimisation of tip etching is sought to produce sharp metal tips (small radius of curvature (ROC)) with low-aspect ratio shanks to minimise vibration noise (Bryant et al. 1987) and having a symmetrical shape to reduce convolution effects of the electronic wave function of the tip and sample (Oliva et al. 1996) (**Figure 3.12**). Where the lateral resolution (Δd) of a sinusoidal varying surface of amplitude (h_s) and periodicity (a) is given by (Stoll 1984):

$$\Delta d = h_s \exp\left\{-\pi^2 (r_t + d)/(\kappa_{00} a^2)\right\} \qquad \textbf{Equation 3.10}$$

where r_t is the radius of curvature, d is the tip-sample separation and $\kappa_{00} = \left(\phi 2m/\hbar^2\right)^{1/2}$, with ϕ = work function, m is the mass of an electron and $\hbar$ is Plank's constant divided by 2π.

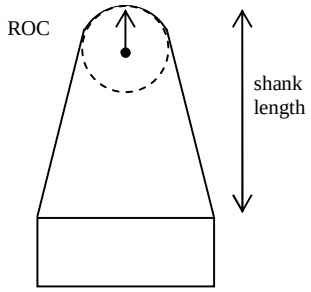

Figure 3.12: Schematic of tip apex highlighting radius of curvature (ROC) and shank length. Dimensions are distorted for clarity.

In initial work the etching current "cut-off" procedure adhered to a threshold current, below which the etch current cut. The subsequent electro-chemical polishing incident between tip drop and the current cut-off led to a relatively hemispherical tip with 0.1 - 1 μm radii (Bryant et al. 1987). The actual dropped section, being instantaneous cut from current when etched away does not suffer from this problem, and hence was utilised as a functional tip. Alternatively, a reverse chemical etch with a "fish hook" shaped anode utilises the same phenomenon (Fotino 1993). Other work has used a thin layer of etchant suspended atop a denser inert liquid (Lemke et al. 1990; Melmed 1991) and obtained ROC = 10 nm.

Enhanced electronic control has been implemented to reduce the cut-off time (Ibe et al. 1990). Good results were obtained via differential cut-off, where the current signal is constantly sampled and the cut-off event takes place after the rate of change of current falls below a pre-described value (Nakamura et al. 1999).

The refined differential etching method has a myriad of parameters:

1) Concentration of etchant
2) Immersion depth
3) DC etching voltage
    a. Constant
    b. Retarding
4) Differential value
5) Shielding effects
6) Cleaning / contaminants

The etchant concentration is nominally 2 - 3 M NaOH, with lower concentrations thought to increase oxide build-up (Kerfriden et al. 1998) whereas higher concentrations result in a non-ideal chemically active solution (Melmed 1991).

Immersion depth sets 1) the initial etching current, which depends on the etch length, and 2) the force on the thinned wire at drop-off (Oliva et al. 1996), with a longer insertion depth heralded as yielding a shorter tip.

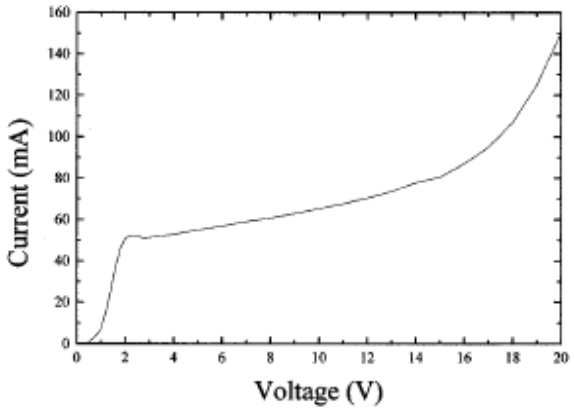

Figure 3.13: Voltagram of during etching of a 8 mm diameter rod taken from (Oliva et al. 1996)

Under normal conditions DC etching produces a sharp, short tip (Melmed 1991). The voltagram shown in **Figure 3.13** reveals etching times for voltages below 2 V are unfavourably long, whereas for high values, the ensuing violent reaction causes structural damage to the etching tip.

Shielding of the anode from the cathode is necessary at higher voltages due to the abundance of gas created and its adverse effect on the stability of the meniscus.

Cleaning involves the initial removal of NaOH crystals on the tip (sometimes ultrasonically) in distilled water, whereas removal of parasitic oxide from the tip surface requires an additional processing step.

Oxide removal techniques are notably varied. Perhaps the simplest technique documented involves oxide removal in hydrofluoric acid (Hockett et al. 1993), however the inclusion of fluorides into the vacuum system severely impair MBE growth. Focused Ion Beam (FIB) milling can be utilised to dually remove oxide and shape the tip apex (Vasile et al. 1991; Hopkins et al. 1995). Oxide removal by FIB typically proceeds in 30 - 40 minutes whereas tip shaping is a markedly lengthier process, limiting its use to only specialist areas. More frequently oxide removal is performed within the vacuum system, where the surface is cleaned with Ar+ ion bombardment with an ion gun (Zhang et al. 1996), annealed with an electron beam at ~1500 °C (Cricenti et al. 1994), self-sputtered ion process using a Ne background pressure (Albrektsen et al. 1994) or simply radiatively heated with a filament (Ekvall et al. 1999; Ding et al. 2005).

Optimisation of the etching procedure is more qualitatively than quantitatively documented, with results commenting on a single parameter of optimisation singularly rather than interactively with the other parameters. Hence a detailed investigation into tip manufacturing optimization has been undertaken in this work and is discussed in **Chapter 5: Tunnelling Tip Preparation.**

3.6 Concurrent MBE-STM

Initial STM semiconductor images were obtained *ex situ*, with transfer through air and subsequent ion bombardment prior to imaging (Bestwick et al. 1988), however the high level of damage introduced by the ion bombardment significantly impaired this technique's effectiveness. A much more viable solution comprised an MBE system (discussed in **3.1 Molecular Beam Epitaxy**) and an STM system (discussed in **3.5 Scanning Tunnelling Microscopy**) integrated into a closed system (Butz et al. 1990). So called *in vacuo* MBE-STM has been extensively used to investigate semiconductor

surfaces, though surfaces cannot be quoted to be *as-grown* as a result of the unknown effects of rapid thermal quenching to room temperature necessary before imaging. Integrating an MBE growth module into an existing STM chamber (MBSTM) or similarly integrating an STM unit into an MBE chamber (STMBE) has recently been achieved for group IV (Voigtlander et al. 1993) and III-V (Tsukamoto et al. 1999) semiconductors respectively.

The work of Tsukamoto to realise a functional STM module in an MBE system (Tsukamoto et al. 1999) overcame a number of noise related problems:

1. LN_2 bubbling noise
2. Vacuum Pump vibrational noise
3. Radiation noise from material sources

Furthermore, the chambers require careful design to ensure elimination of contamination of the electronics due to deposition fluxes (Tsukamoto et al. 2006a). Specifically, shielding of the piezoelectric drive is paramount (**Figure 3.14**). A custom-made heater module and STM stage allowed isolation from these unwanted influences. For high temperature STM, the advantage of performing STM in the MBE chamber centres around the ability to avoid quenching the sample between image and growth. However in the case of low temperature STM, any attempt at quenching would inevitably result in evaporation particulates adsorbing onto the cooled sample.

Further, contamination of the STM tip adversely effects image quality. Whilst the intimacy of the tip and sample during imaging makes this unavoidable, low deposition rates can reduce the necessary frequency of cleaning and maintenance. The cleaning procedure itself involves scanning at relatively high current and voltages resulting in tip heating and field desorption.

Deposition onto the tip implies that a degree of the sample is shaded by the tip, which has a typical radius of curvature of tens of nm. Optimisation of ROC and tip shape will reduce the shadowed area. The presence of As deficient structures would strongly suggest such an occurrence, and hence the absence of such domains implies that the

diffusion length of As is sufficiently large to compensate for the shading. (Tsukamoto et al. 2006a).

Sample heating is performed via either direct heating (DH) or pyrolytic pyrolytic boron-nitride radiative heating (PBNRH) as described in **3.1.2 Temperature Measurement**. For lightly doped wafers heated by DH, a sample bias correction must be applied to compensate for the voltage drop across the sample. Heating of any order generates thermal drift. Samples must be left to stabilize for several hours at a given heating current in order to minimize drift. Any residual drift can henceforth be corrected via SCALA's software correction tools.

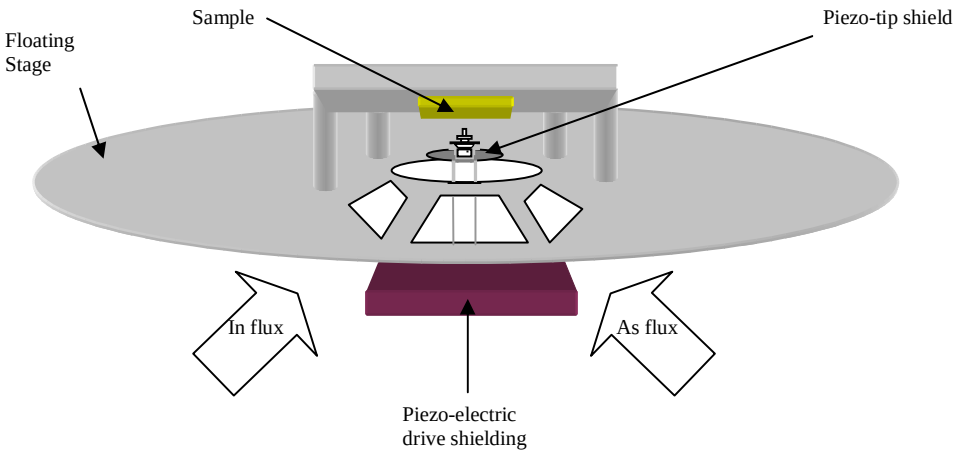

Figure 3.14: STM head and piezo shielding

Group IV MBSTM work is simplified with respect to III-V, as an overpressure of the group IV element is not necessary to stabilize the growth surface. Hence the sheer volume of atoms and molecules in the chamber for a given growth rate is higher for III-V MBE. The ability to resolve atomically during As-overpressure is severely limited (Tsukamoto et al. 1999; Tsukamoto et al. 2006a) though has been successfully attempted during growth. However III-V growth in the region 350 - 450 °C does not require constant As overpressure to stabilise the surface and hence offers an opportunity to commence simple studies of III-V MBSTM.

Data acquisition for an STM image has two key length scales. A resolvable length scale of 10^{-10} m allows for reconstruction and alloying investigation where as 10^{-7} m suits island and step-terrace observations. Typical acquisition times for such images are approximately 600 seconds, though can be reduced depending on data collection calibrations and image quality. Low growth rate MBE (0.013 ML s^{-1} or 77 s ML^{-1}) would clearly allow for only one tenth of an image per ML, hence there is a necessity to reduce the growth rates below what is considered low in conventional MBE terms, in order to extend the S-K transition over tens of images.

In situ III-V imaging commenced with growth then scanning, using As to stabilize the surface for imaging (Tsukamoto et al. 1999; Tsukamoto et al. 2000). This has the clear disadvantage of a pseudo-post-growth anneal and cannot be report as dynamic growth observations. Thus the (counter-) effects of quenching are still unresolved. More recently InAs/GaAs(001) growth has been observed with both group III and V fluxes (Tsukamoto et al. 2006a; Tsukamoto et al. 2006b), however imaging immediately upon the onset of growth is difficult due to the heating effect when opening the group III species cell shutter.

Thus the areas of expansion and investigation for InAs on GaAs are:

1. Identification of In bonding sites near S-K transition
    a. Atomic resolution imaging of mobile In near S-K transition
    b. In rich islands/reconstruction domains
2. Identification of quasi-stable structures (see **7.6.2 S-K Transition**)
3. Imaging with short growth interruption to investigate mobility and lifetimes
4. MEE growth (as discussed in Chapter **2.3 Homoepitaxy**)

For S-K transition observations under binary InAs/GaAs the critical thickness of interest is between 1.4 and 1.8 ML for T_s = 350 to 520 °C respectively. Clearly the inclusion of $In_xGa_{1-x}As$/GaAs, with x ~ 0.25 would delineate a greater critical thickness and hence "slow" the transition and allow more detailed observation.

Two viable MBSTM configurations are shown in **Figure 3.15**. The single sources have a maximum crucible capacity of 0.7 cc for As and 0.6 cc for In, where as the triple

source only permits 0.28 cc crucibles. Hence for In, Ga and As deposition the single source would be utilised for As overpressure whereas two crucibles of the triple source contain Ga and a single crucible contains In. Operation of the triple source is more complicated due to the required coalescence of three separate fluxes and the triple-control shutter mechanism. For simple first growth runs such complex alloyed layers are quite simply too complicated and hence work will begin with binary InAs on GaAs.

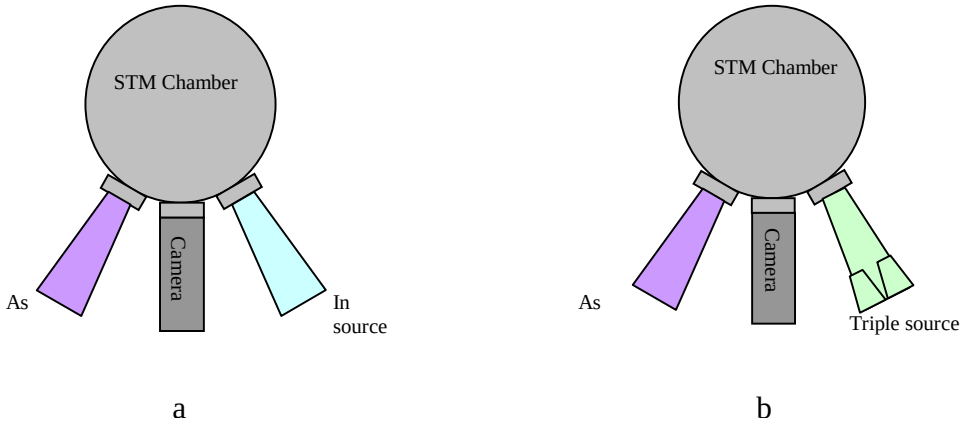

Figure 3.15: STM cell configurations: a) binary InAs two (single sources) and b) $In_xGa_{1-x}As/GaAs$ (one single and one triple source)

For MBSTM the issues relating to operation are inherently different. Ultimately the entire integration of MBE and STM is the goal. However with such small source capacities, long growth cycles are unattainable. Current MBSTM relies on a two stage preparation procedure whereby the sample is out-gassed, cleaned and has a buffer layer grown *in vacuo.* The sample preparation takes place in an MBE chamber fitted with RHEED and typical capacity As cracker and Ga effusion cells. After quenching (see **6.4 Quenching**) the sample can be transferred into the MBSTM chamber for further growth.

Whilst quenching complicates the growth procedure, high quality surfaces with 1 μm wide terraces and low vacancies can be attained with a careful algorithm (Yang et al. 1999). MBSTM does posses the advantage of negligible thermal variations when opening and closing the cell shutters, allowing stable imaging near the onset of growth.

3.7 References

O. Albrektsen, H.W.M. Salemink, K.A. Morch and A.R. Tholen (1994) J. Vac. Sci. Tech. A **12**(6): 3187.

Anon (1972) "Emissivity Corrected Optical Pyrometer" Patent: 3698813 USA

G.R. Bell, J.G. Belk, C.F. McConville and T.S. Jones (1999) Phys. Rev. B **59**(4): 2947.

T.D. Bestwick, M.E. Welland and R.B. Leane (1988) Vacuum **38**(8-10): 823.

G. Binnig, H. Rohrer, C. Gerber and E. Weibel (1983) Phys. Rev. Lett. **50**(2): 120.

G. Binnig and D.P.E. Smith (1986) Rev. Sci. Inst. **57**(8): 1688.

G. Binning, H. Rohrer, C. Gerber and E. Weibel (1982) Phys. Rev. Lett. **49**(1): 57.

A.S. Bracker, M.J. Yang, B.R. Bennett, J.C. Culbertson and W.J. Moore (2000) J. Cryst. Grow. **220**(4): 384.

P.J. Bryant, H.S. Kim, Y.C. Zheng and R. Yang (1987) Rev. Sci. Inst. **58**(6): 1115.

R. Butz and H. Wagner (1990) J. Elec. Mat. **19**(10): 1107.

C.J. Chen (1992) Appl. Phys. Lett. **60**(1): 132.

A.Y. Cho and K.Y. Cheng (1981) Appl. Phys. Lett. **38**(5): 360.

A. Cricenti, E. Paparazzo, M.A. Scarselli, L. Moretto and S. Selci (1994) Rev. Sci. Inst. **65**(5): 1558.

L. Daweritz and R. Hey (1990) Surf. Sci. **236**(1-2): 15.

T.J. deLyon, J.A. Roth and D.H. Chow (1997) J. Vac. Sci. & Tech. B **15**(2): 329.

H.F. Ding, J.E. Pearson, D.Q. Li, R.H. Cheng, F.Y. Fradin and S.D. Bader (2005) Rev. Sci. Inst. **76**(12): 123703.

I. Ekvall, E. Wahlstrom, D. Claesson, H. Olin and E. Olsson (1999) Meas. Sci. Tech. **10**(1): 11.

M. Fotino (1993) Rev. Sci. Inst. **64**(1): 159.

C.T. Foxon, R.P. Campion, V.A. Grant, S.V. Novikov, J.J. Harris, R. Thomson, C. Taylor and D. Barlett (2007) J. Cryst. Grow. **301-302**: 482.

E.S. Hellman and J.S. Harris (1987) J. Cryst. Grow. **81**(1-4): 38.

L.A. Hockett and S.E. Creager (1993) Rev. Sci. Inst. **64**(1): 263.

L.C. Hopkins, J.E. Griffith, L.R. Harriott and M.J. Vasile (1995) J. Vac. Sci. Tech. A **13**(2): 335.

J.P. Ibe, P.P. Bey, S.L. Brandow, R.A. Brizzolara, N.A. Burnham, D.P. Dilella, K.P. Lee, C.R.K. Marrian and R.J. Colton (1990) J. Vac. Sci. Tech. A **8**(4): 3570.

A.S. Jordan (1980) J. Appl. Phys. **51**(4): 2218.

B.A. Joyce (1985) Rep. Prog. Phys. **48**(12): 1637.

D. Keller (1991) Surf. Sci. **253**(1-3): 353.

S. Kerfriden, A.H. Nahle, S.A. Campbell, F.C. Walsh and J.R. Smith (1998) Electrochimica Acta **43**(12-13): 1939.

M. Klein and G. Schwitzgebel (1997) Rev. Sci. Inst. **68**(8): 3099.

J.A. Kubby and J.J. Boland (1996) Surf. Sci. Rep. **26**(3-6): 61.

V.P. LaBella, M.R. Krause, Z. Ding and P.M. Thibado (2005) Surf. Sci. Rep. **60**(1-4): 1.

H. Lemke, T. Goddenhenrich, H.P. Bochem, U. Hartmann and C. Heiden (1990) Rev. Sci. Inst. **61**(10): 2538.

A.J. Melmed (1991) J. Vac. Sci. Tech. A **9**(2): 601.

I.H. Musselman and P.E. Russell (1990) J. Vac. Sci. Tech. A **8**(4): 3558.

Y. Nakamura, Y. Mera and K. Maeda (1999) Rev. Sci. Inst. **70**(8): 3373.

A.I. Oliva, A. Romero, J.L. Pena, E. Anguiano and M. Aguilar (1996) Rev. Sci. Inst. **67**(5): 1917.

S.I. Park, J. Nogami and C.F. Quate (1987) Phys. Rev. B **36**(5): 2863.

K. Reginski, J. Muszalski, V.V. Preobrazhenskii and D.I. Lubyshev (1995) Thin Solid Films **267**(1-2): 54.

D. Rioux (2006) http://planck.phys.uwosh.edu/rioux/research.html.

R.N. Sacks, D. Barlett, C.A. Taylor and J. Williams (2005) J. Vac. Sci. & Tech. B **23**(3): 1247.

E. Stoll (1984) Surf. Sci. **143**(2-3): L411.

P.J. Timans (1992) J. Appl. Phys. **72**(2): 660.

S. Tsukamoto, G.R. Bell and Y. Arakawa (2006a) Micro-elec. J. **37**(12): 1498.

S. Tsukamoto, T. Honma, G.R. Bell, A. Ishii and Y. Arakawa (2006b) Small **2**(3): 386.

S. Tsukamoto and N. Koguchi (1999) J. Cryst. Grow. **202**: 118.

S. Tsukamoto and N. Koguchi (2000) J. Cryst. Grow. **209**(2-3): 258.

M.J. Vasile, D.A. Grigg, J.E. Griffith, E.A. Fitzgerald and P.E. Russell (1991) Rev. Sci. Inst. **62**(9): 2167.

B. Voigtlander and A. Zinner (1993) Appl. Phys. Lett. **63**(22): 3055.

Z.R. Wasilewski, J.M. Baribeau, M. Beaulieu, X. Wu and G.I. Sproule (2004) J. Vac. Sci. & Tech. B **22**(3): 1534.

H. Yang, V.P. Labella, D.W. Bullock and P.M. Thibado (1999) J. Vac. Sci. & Tech. B **17**(4): 1778.

R. Zhang and D.G. Ivey (1996) J. Vac. Sci. Tech. A **14**(1): 1.

Chapter 4: Direct Heating Characterisation

This chapter discusses the problem of obtaining reliable and accurate sample temperatures for use within the STM chamber. The STM mounting stage permits solely direct heating (DH) achieved by passing a current through the sample, or through the pyrolytic boron-nitride resistive heating plate (PBNRH) discussed in **Chapter 6: Sample Preparation for STM**). No internal temperature monitoring apparatus is available.

4.1 Argument: Direct Heating

All samples discussed herein are 8.5 x 1.4 x 0.3 mm^3 with resistivity 1.2 x 10^{-2} Ω.mm. These are resistively heated as discussed in **Chapter 3.** The use of identical samples results in a single heating curve that can be referenced throughout future experiments without the need for constant temperature measurement. This method has an inherent error of the order of ± 30 °C, hence as a second measure RHHED analysis must be performed to more accurately estimate the sample temperature before growth commences.

4.2 Power Equation

The theoretical temperature of a directly heated sample is governed by the equation:

$$P_E = P_R + P_L \qquad \textbf{Equation 4.1}$$

Where P_E is the electrical heating power, P_R is the power loss due to radiative heating and P_L is the power loss due to conduction and convection, the latter of which can be considered negligible in a UHV system.

The electrical heating power can be expressed simply in terms of the input current (I) and the temperature-dependent sample resistance ($R(T)$) in the equation:

$$P_E = I^2 R(T) \qquad \textbf{Equation 4.2}$$

The radiative heating power for a grey-body is given by the equation:

$$P_R = \varepsilon_T(T)\sigma A(T - T_0)^4 \qquad \textbf{Equation 4.3}$$

where $\varepsilon_T(T)$ is the temperature-dependent total hemispherical emissivity, σ is the Stefan-Boltzmann constant, A is the sample surface area, T is the sample temperature in K and T_0 is the ambient temperature in K.

Heating loss due to conduction is governed by the equation:

$$P_L = \frac{\kappa A \Delta T}{d} \qquad \textbf{Equation 4.4}$$

where κ is the thermal conductivity of the barrier, A is the cross sectional area, ΔT represents the temperature difference across the barrier and d is the thickness of said barrier. However the shape of the barrier in question is not simple nor regular.

Hence, in order to calculate the heating response of the GaAs sliver a number of variables need definition, namely:

- $R(T)$
- $\varepsilon_T(T)$
- P_L

4.2.1 Resistance vs. Temperature

Using highly doped n-type GaAs with doping density, N_d = 2.1 x 10^{18} cm^{-3} and hence ambient resistivity, ρ_0 = 1.2 x 10^{-3} Ω.cm the sample resistance at room temperature given by:

$$R_0 = \frac{\rho_0 l}{A} \qquad \textbf{Equation 4.5}$$

where all symbols have their usual meanings. Hence with an average sample length of 6.5 mm and a cross-sectional area of 0.42 mm^2 the ambient sample resistance is 0.18 Ω, which makes it of the same order of the resistance of the contacts in the sample plate, around 0.3 Ω.

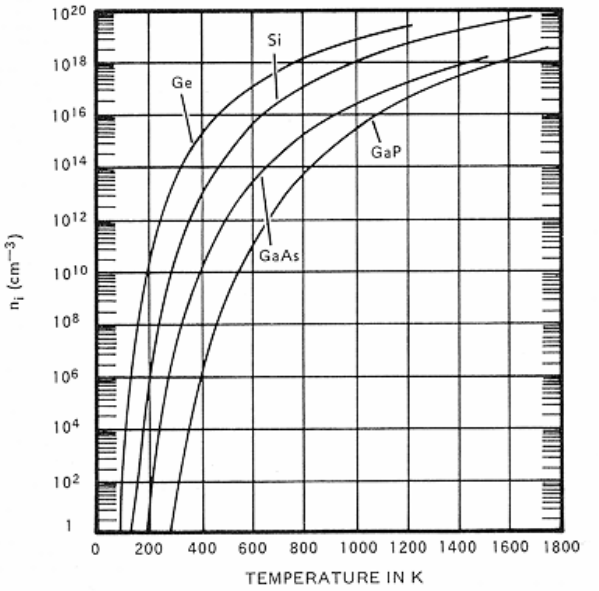

Figure 4.1: Intrinsic carrier concentration vs. Temperature, taken from (Thurmond 1975)

Hence the overall resistive response of the plate during heating will be a complicated function of both sample resistance falling and sample plate metal contact resistance rising. Additionally the metal-semiconductor contact resistance will significantly alter the resistive response during the first heating cycle.

The high doping level however offers the advantage that the sample resistance is relatively stable for moderate temperatures. **Figure 4.1** shows that the intrinsic carrier concentration of GaAs is two orders of magnitude smaller than the doping density at around 630 °C, which is already beyond the required range.

The resistivity varies due to a temperature dependence of mobility and free-carrier density (**Equation 4.6**). The n doping is such that *n(T)* is approximately constant in the required range, however the electron mobility, $\mu_e(T)$, falls by a factor of 3 between 25 °C and 630 °C for this doping level. Thus the effect of *p(T)* is more significant at lower

temperatures than the free-carrier curve would suggest. The hole mobility is nominally a factor of 10 less than the electron mobility, though it has a less strong temperature dependence.

$$\rho(T) = 1/[n(T)\mu_e(T) + p(T)\mu_h(T)] \qquad \textbf{Equation 4.6}$$

Substitution into **Equation 4.6** reveals a weak temperature dependence, hence for a first order approximation it is sufficient to assume R(T) is constant for all T.

4.2.2 Total Hemispherical Emissivity

The total hemispherical emissivity, ε(T), of pure GaAs changes significantly between 300 and 650 °C (Timans 1992), a fact that makes pyrometer reading inherently inaccurate. However the curve shown in **Figure 4.2** cannot be taken for highly n-type GaAs, for as pointed out by Jordan the emittance of GaAs has a strong dependence on doping level (Jordan 1980).

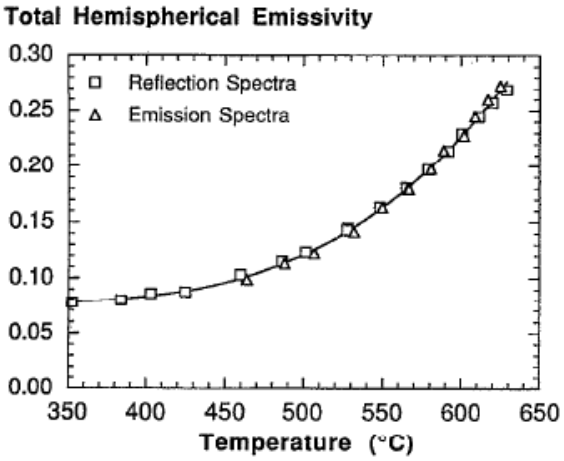

Figure 4.2: Total Hemispherical emissivity vs. sample temperature, taken from (Timans 1992)

For high doping levels (> 5 x 10^{17} cm^{-3}) the emittance is no longer a function of doping. Notably the profile shows a stark change at ~400 - 500 °C, where for large doping profiles the emittance (and supposedly the corresponding emissivity) saturates.

Hence the emissivity of N_d = 2.1 x 10^{18} cm^{-3} can be assumed to increase from a base between 0 and 400 °C, after which it becomes stable. The emittance displays a 3-fold increase from intrinsic to saturation doping at 25 °C, hence we can estimate a similar increase in base value of emissivity. The following region from 25 - 430 °C displays an asymptotic increase in emittance toward the saturation value 120 % greater. Thereafter the emittance is constant, yielding the estimated profile shown in **Figure 4.3**, with the asymptotic region given by:

$$\varepsilon(T) = 0.363 - 0.064 \times 0.995^{T} \qquad \textbf{Equation 4.7}$$

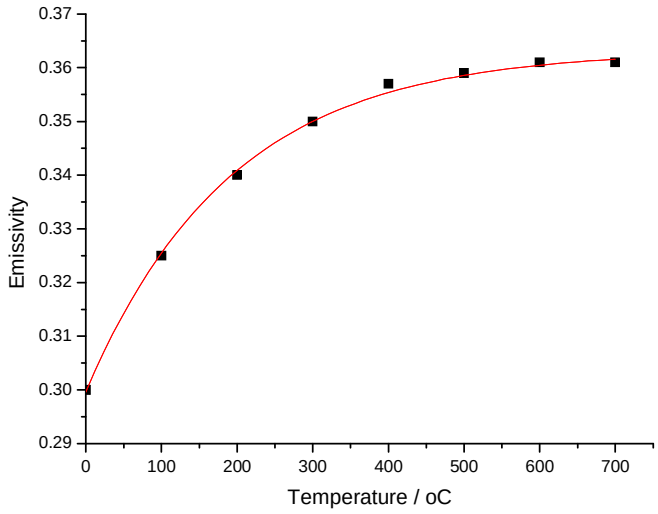

Figure 4.3: Deduced total hemispherical emissivity of n-type GaAs

4.2.3 Estimating Losses

The sample mounting is represented diagrammatically in **Figure 4.4**. The inner two circles representing the sample and the Mo-contacts are both subject to a heating current supplied externally. The outer two circles representing the sample plate bulk and the

manipulator stage are conductive heat sinks. The dashed line represents a premature termination to the system, ignoring higher levels.

The degree of accuracy when estimating losses depends on the level of complexity to which the system is taken. In a loss-less system only the inner-most circle is required. Assuming losses from 50 - 90 %, this simplistic model is too conservative. Estimation based upon the first two levels is a minimum requirement to obtain meaningful data.

The heating curve for the GaAs sample and the Mo-contacts without losses, derived from **Equation 4.3** is shown in **Figure 4.5**. Hence the Mo is approximately half the temperature of the GaAs sample across the entire range, except at temperatures < 200 °C where the difference is larger. Losses can be expected to be larger where the temperature difference between the two bodies is greater.

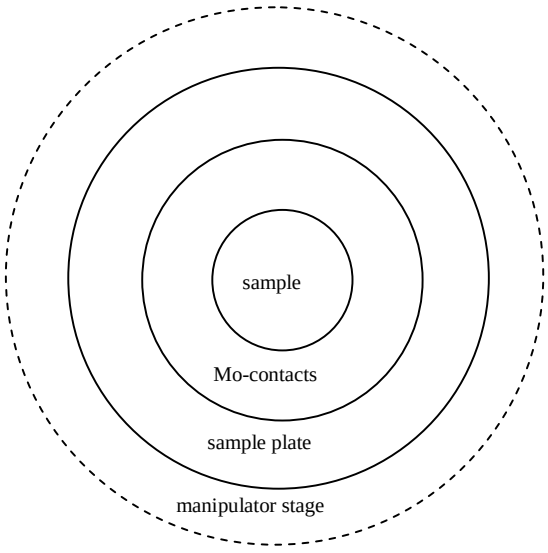

Figure 4.4: Diagrammatic representation of sample mounting

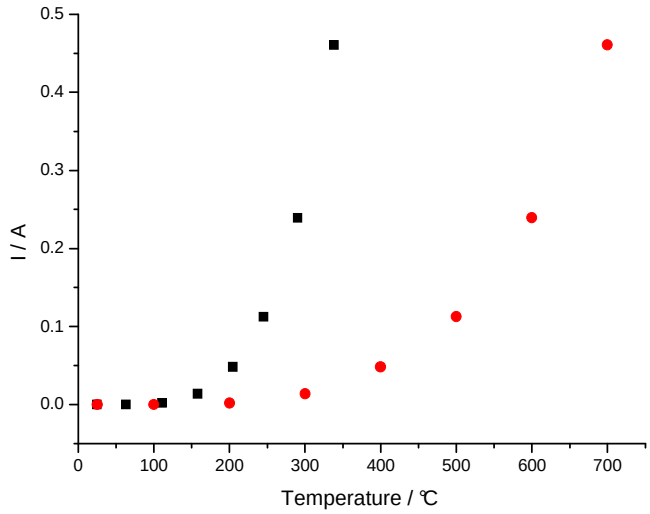

Figure 4.5: Loss-less heating curve
(red circles: GaAs, black squares Mo-contacts)

Considering the three components independently: sample, Mo-contacts, sample-Mo interface, the power necessary to compensate the losses at the interface can be calculated from **Equation 4.4**. Thus the power consumption of the three components has been calculated in the first instance. Hence the sum of the total power divided by the total resistance of the system yields a heating current based on a two component system.

4.2.4 Solution

Combining the three systems from **section 4.2.3** an overall system loss can be attained, as shown in the curve of **Figure 4.6**. This curve represents an over-estimate of temperature for a given heating current since the second and third boundary losses have been neglected. The curve will be referenced later in comparison to the other techniques.

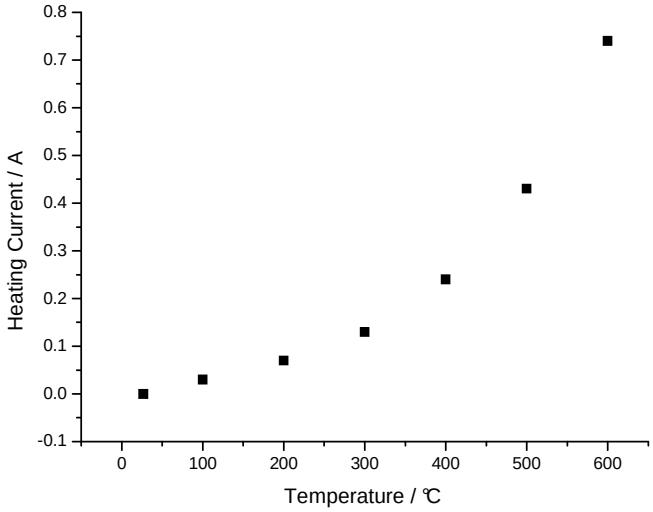

Figure 4.6: Three system heating curve estimation

4.3 Thermocouple

Thermocouple contact to the sample provides a first order means of estimating the sample temperature. The accuracy of the temperature measurement depends on the quality of the contact and the capacity of the wire as a heat-sink. Due to the inherent uncertainty of this contact method the results obtained were merely treated as a lower limit in the heating curve estimation band.

4.3.1 Method

Achieving a viable thermocouple contact is paramount for this method of temperature measurement. The thermocouple utilised in this work is commercially available k-type gauge 36 (ϕ = 0.125 mm), with an operation temperature -20 to 600 °C (suitable for flashing up to 850 °C).

Methods of directly affixing the thermocouple tip to the sample were regarded as suspect. Metallic contacts would offer an alternate current path and significantly alter the heating profile, whereas insulating contacts, such as ceramic cement, would increase the mass of the system and provide an additional heat sink. Thus, to minimise the effect of

contact the thermocouple end was merely affixed to the sample plate and held in physical contact with the sample.

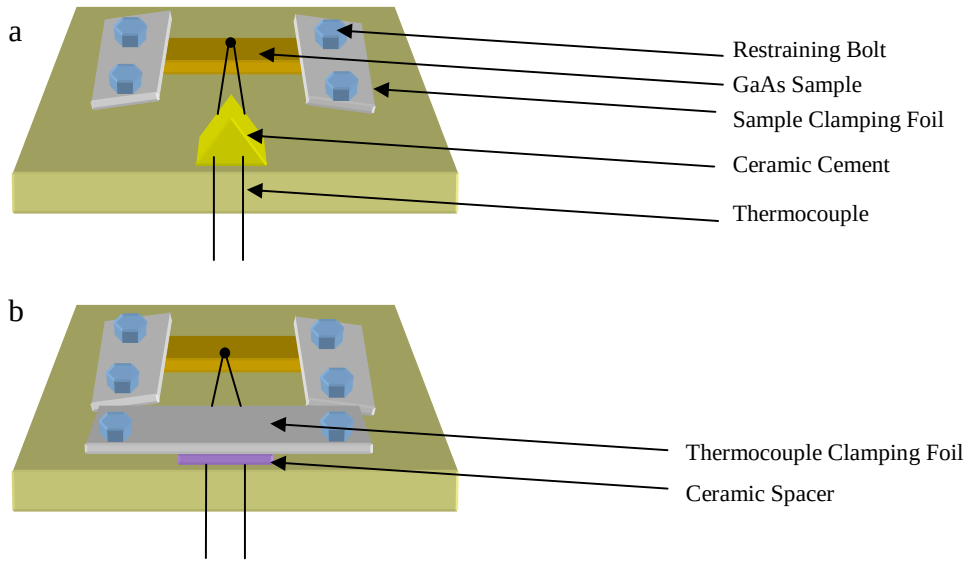

Figure 4.7: Thermocouple mounting methods a) Ceramic Cement b) Ta clamping foil

Two alternate methods of affixation were employed. One static clamping by means of ceramic cement (**Figure 4.7a**) and the second adjustable clamping employing Ta clamping foil (**Figure 4.7b**).

Heating power was then applied to the circuit and the temperature read from a digital meter. By monitoring the applied current and voltage and recording the sample temperature and heating stage temperature, a practical estimate can be given to the sample resistance and the heating losses of the system.

4.3.2 Results

The trends shown in **Figure 4.8** agreed with the initial supposition that the clamping foil, as a result of its greater positional precision, would allow more accurate temperature measurement. The similarity in curve shape in conjunction with an apparent offset in

values of around 50 °C suggest that the differences in the curves can be accounted by the poorer contact achieved by the ceramic cement.

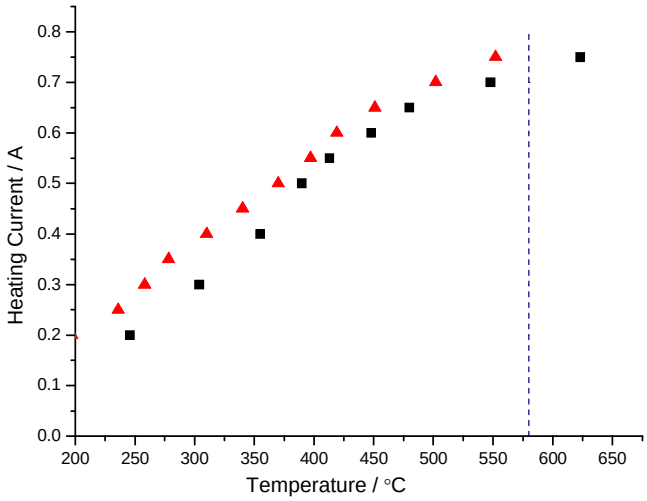

Figure 4.8: Thermocouple Heating Curve. Black squares: Clamping foil Red triangles: Ceramic cement. Dashed line shows clean up temperature.

Both samples exhibited a dull red glow visible in dim external lighting at 0.7A, suggesting a sample temperature $550 < T_s < 600$ °C. A result in close agreement with the clamping foil curve in which 0.7A corresponds to 548 °C, as read. The thermocouple can only be accurately rated at $T_s < 600$ °C, hence temperatures approaching this limit should be regarded as increasingly erroneous.

The "clean-up" temperature for RHEED that corresponds to oxide removal and the unveiling of a diffraction pattern (the dotted line in the figure) can be predicted to occur around 0.7A.

4.4 Optical Pyrometery

Optical pyrometery relies on sample emissivity for temperature measurement, as discussed in **section 3.3**. This sub-chapter utilises the Minolta/Land Cyclops 241 handheld pyrometery camera.

4.4.1 Method

The sample is loaded into the system and lowered so that it is visible through a quartz viewport. A louvered shutter is in place to minimise As contamination between measurements. Heating is performed in the current range 0 to incipient glow current, I_{glow}. The pyrometer has a lower limit of 250 °C.

The small sample surface area (8.5 x 1.4 mm^2) reduces the accuracy of the measurements. The targeting sight of the pyrometer is rastered over the visible heating stage area for 30 seconds during a measurement. The maximum temperature obtained during the cycle is taken to be the sample temperature.

Emissivity is estimated from the curve in **section 4.2.2** and has a permissible range $0.3 < \varepsilon < 0.36$. Temperature measurement is a recursive process intended to reduce initial emissivity errors by feeding back values associated with measured temperature.

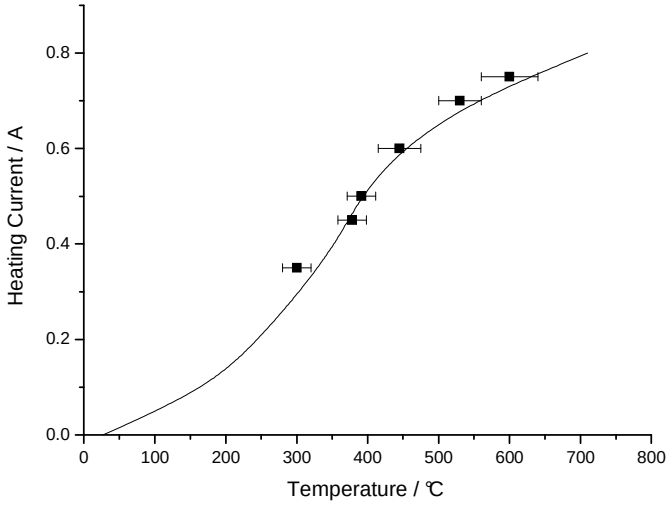

Figure 4.9: Optical Pyrometer Temperature Readings (black squares). Line represents the thermocouple results obtained previously

4.4.2 Results

Firstly it is worthy to note that the maximum temperature reading did not occur when the sample was in the cross-hairs of the pyrometer. The rather cumbersome sample targeting immediately poses a question concerning the validity of the results obtained.

The results as read are given in **Figure 4.9** and are overlain with the thermocouple results for ease of comparison. The results followed the general trend of the thermocouple curve, but the reproducibility was poor. The poor results are most likely caused by the small sample area, the large temperature gradient and the low resolution of the device.

Optical pyrometery is therefore not a suitable method for accurate temperature measurement in this instance.

4.5 RHEED Pattern Temperature Calibrations

The surface reconstruction of GaAs depends on both sample temperature and source BEP, as discussed in **Chapter 2**. The accuracy to which the former is known influences the accuracy to which the latter can be predicted, or vice versa. Hence in order to facilitate temperature measurement, first a flux calibration is required. This sub-chapter discusses the prevalent points pertaining to RHEED temperature calibrations.

4.5.1 Method 1: Flux Monitor

The MBE chamber has no designed flux monitor capabilities for the As-cracker or Ga Knudsen cell. However an accurate measurement of the As beam equivalent pressure is essential in order to determine an accurate temperature value from the surface reconstruction transitions. To this end a custom made flux monitor was fabricated from an ordinary ion gauge head.

The experimental setup is shown in **Figure 4.10**. The large aperture on the As-cracker gives a wide angle beam and hence a large area of coverage within the chamber, whereas the Ga cell has a narrow aperture and hence a comparatively small area of coverage. To successfully measure the fluxes, the ion gauge head needs inserting directly into the beams. However growth cannot commence with this configuration since the interruption of the beam has detrimental effects to the growth process.

By utilising a bellows flange, the head can be retracted 50 mm, allowing uninterrupted access from cell to sample. In order to facilitate flux monitoring two measurements are need, both “in” and “out of” the beam. These can then be correlated to attain the “in” beam flux from the “out of” beam flux to acceptable accuracy.

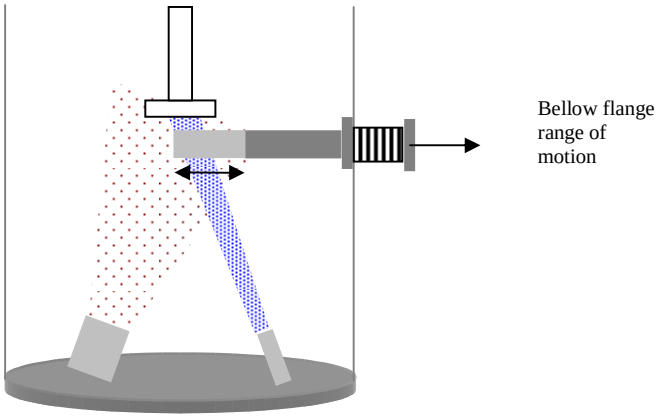

Figure 4.10: Ion Gauge Head for Flux Monitoring Schematic.
Red dots As flux, Blue dots Ga flux

4.5.2 Method 2: Sample Targeting

Initially the prospect of locating the visible sample area (5 x 1.4 mm^2) with a RHEED spot constituted a daunting challenge, a difficulty compounded by the absence of a RHEED pattern below the surface clean up temperature of approximately 580 °C. The actual emergence of a pattern further depends on azimuth and angle of incidence. Hence a range of variables require specifying:

- Manipulator position: M_x, M_y and M_z
- Azimuth location: M_r
- RHEED beam direction: R_x and R_y
- RHEED beam power parameters: I_R and V_R

M_x and M_y denote the lateral position of the manipulator stage within the MBE chamber. These are not aligned along the axis of the RHEED screen but at 45° to it and favour sample loading positioning. M_z corresponds to the positional height of the manipulator stage in the system. The top of the RHEED screen relates to a height of ~50 mm whereas the Ion Gauge head is located at ~10 mm, giving a 40 mm range of motion.

The samples have been sliced along the [110] azimuth and due to the interference of the sample plate only this azimuth ± 43 - 45° is available. Hence the value of M_r is restricted to a small range and will most commonly be selected so the at [110] azimuth is perpendicular to the RHEED screen. R_x and R_y denote the angle of the RHEED beam, where R_y is parallel to M_z and X_y operates on the plane depicted by $M_{x,y}$.

Finally I_R and V_R denote the current of the RHEED filament current and acceleration voltage of the RHEED beam, respectively. Nominal values are: $2 < I_R < 3$ A and $10 < V_R < 15$ kV. The beam power is a secondary consideration in order to fine tune the diffraction pattern, however without a sufficient initial power the emergence of said pattern is absent.

Testing the range of M_z led to a fortuitous discovery: The back of the ceramic plate is illuminated by the RHEED spot for a sufficient intensity, possibly due to diamond or metallic deposits residual from the slicing and fabrication process.

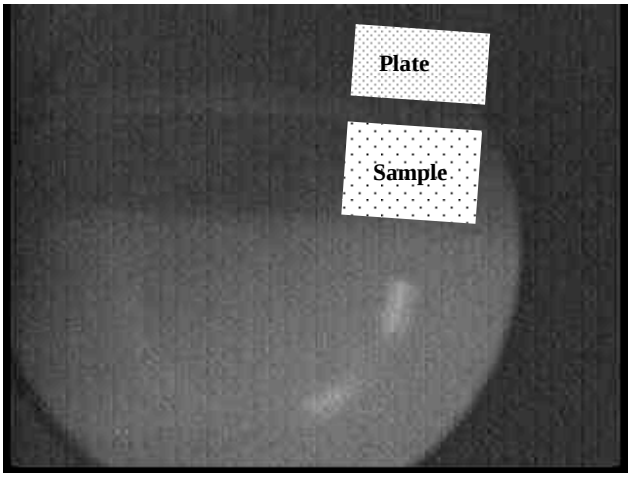

Figure 4.11: Intersection of RHEED spot by sample

Once the centre of the back of the plate has been located, R_y can be used to shift vertically along the direction of M_z. In doing so the RHEED spot will pass over the top of the plate and sample. The path of the beam to the screen is obstructed on one occasion, when the beam impinges on the 0.3 mm thick side-edge of the sample and the sample's shadow is cast forward onto the screen. The intersection of the beam is shown in **Figure**

4.11. The location of the sample top surface is just below the intersection with this side-edge.

To uncover the pattern and determine conclusively the location of the sample heating must be applied. Assuming the temperature curve obtained in **4.3 Thermocouple** are an under-estimate by the order of 50 °C a formula for reaching 580 °C can be applied.

4.5.3 Experiment 1: Flux Correlation Curves

Whilst this section is concerned with the static map, i.e. surface reconstructions without a Ga flux, the Ga flux is included here for completeness and as a reference for the following chapters. Firstly the As flux is controlled by a 2 stage effusion cell (bulk) and cracker. The bulk is operated at 380 - 450 °C typically depending on pressure requirements and charge contents. The cracker is further operated at 550 - 650 °C for As_4 or 800 - 1000 °C for As_2. This work concentrated on As_4 production with the cracker temperature at 600 °C and the bulk at 410 °C.

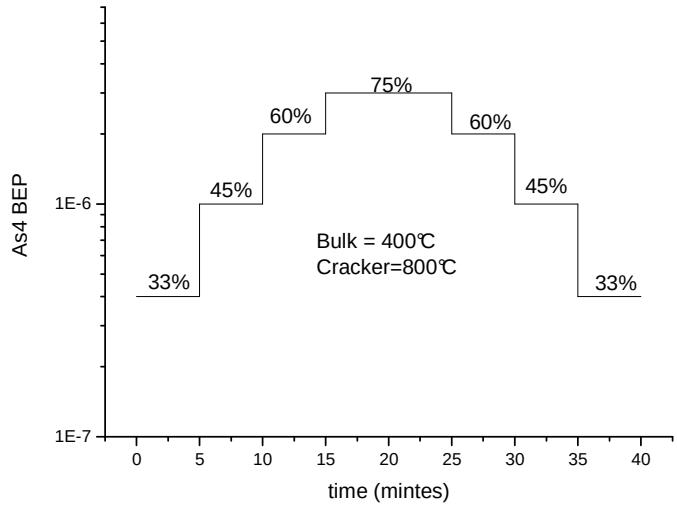

Figure 4.12: As_4 BEP for percentage openings of valve

When closed and with LN_2 cooling in effect the background pressure is 3.0×10^{-8} mBar with the As_4 beam equivalent pressure of the same value. The cracker valve is a micrometer controlled seal with 17 turns of precision from fully closed to fully open.

Figure 4.12 shows the As_4 BEP for a range of cracker valve positions. The As_4 pressure was highly reproducible and showed little change from week to week of operation.

The Ga cell is shuttered with a simple open and close rotating shield. The BEP can be altered solely by cell temperature and depends on cell occupancy. The As cell was ramped down to room temperature in order that flux leakage would not interfere with Ga measurements. **Figure 4.13** shows the typical Ga BEP for a charged cell. The curve shows an almost ten fold increase in BEP per 100 °C. The gradient gives the enthalpy of Ga at 2.2 eV, close to other experimentally obtained values (Honig et al. 1969; Kean et al. 1991). The coincidence of 2:1 As:Ga BEP ratio displays a RHEED pattern from As rich 4× to Ga rich 2× on the [110] azimuth at 520-580 °C.

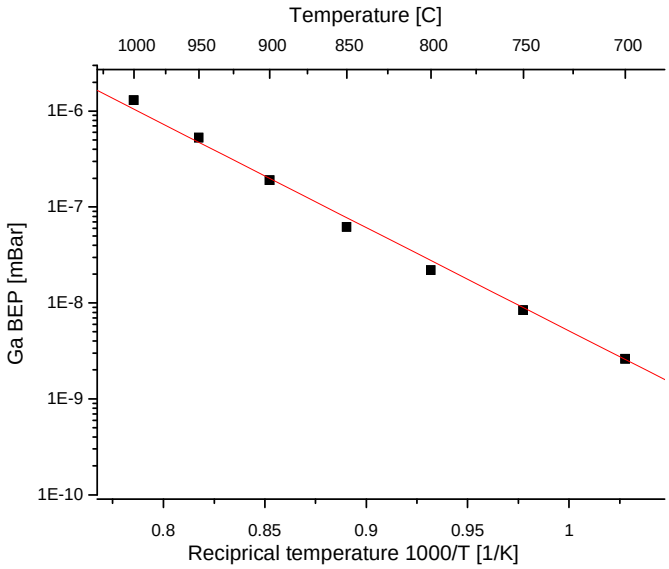

Figure 4.13: Ga BEP versus cell operating temperature

4.5.4 Experiment 2: Clean Up Temperature

It is well established that the protective oxide desorbs from GaAs at 580 °C (Neave et al. 1978). This first order point of reference can be attained by heating the GaAs sample under an incident RHEED beam. Unfortunately, with the added complication of sample targeting, the argument becomes a compound of the two cases where: a) a RHEED pattern will confirm sample targeting and b) a RHEED pattern will confirm clean up

temperature has been attained. Hence the reliability of the latter depends solely on the acquisition of the former.

Figure 4.14: RHEED pattern at 'Clean Up'

Extensive 'rastering' of the beam over the suspected target area allows a suitable search to be performed. However the search is complicated by the large range of M_z. The RHEED beam must have a specific incidence angle in order for a diffraction pattern to be observed. With no fixed angle the problem is 3D. Under this premise, it was observed that heating currents under 0.70A revealed no pattern. However with a transition to 0.72A a pattern emerged that grew in strength and clarity at a current of 0.73A (**Figure 4.14**).

The current range of 0.7 - 0.75 A corresponds to a temperature of approximately 550 - 600 °C from **4.3 Thermocouple**. Hence this correlates with a 30 - 50 °C error in the thermocouple reading, as expected in this case.

The sample begins to radiate visible red light in coincidence with the clean up temperature. This red light is only visible in the absence of all external sources, however the stray light from the RHEED gun filaments is not enough to mask its presence. Detectable red light occurs at ~600 °C, further supporting that the cleanup temperature of 580 °C has been reached.

Once the RHEED pattern is established, the c(4 × 4) to (2 × 4) and (2 × 4) to (4 × 2) transitions can be used to further estimate temperature values for known flux readings.

The RHEED pattern after cleaning is too weak to clearly identify the higher order diffraction lines. It is therefore necessary to grow a small buffer layer in order to restore surface order.

4.5.5 Experiment 3: Sample Reconstruction Transitions

The RHEED diffraction pattern reflects temperature-dependent reconstruction changes as discussed in **Chapter 3**. With direct heating only allowing access to a single azimuth the $[\bar{1}10]$ was chosen in favour of the [110] since the pattern changes most often along this azimuth for the reconstructions of interest.

After sample mounting heating is initially performed radiantly via the filament heater to degas the plate and to allow improved conductive contacts at the Mo-contact foils. Heating to 10W for 30 minutes is sufficient to enhance current flow. Subsequently DH is initiated for 1 hour at a low power 0.4 A (~350 °C) to further enhance and stabilise the contacts. The substrate now adheres to a repeatable heating cycle.

Firstly the clean-up temperature is approached in 30 minute stages from 0.69 A to 0.73 A with increments of 0.02 A. This result is in line with the clean-up temperature discussed in **section 4.5.4** and corresponds to 580 °C. Next a buffer layer is grown for 1 hour with a 3:1 As:Ga ratio until the 4× pattern corresponding to the (2×4) reconstruction along the $[\bar{1}10]$ azimuth is clearly visible (**Figure 4.15**).

Figure 4.15: 4× pattern along $[\bar{1}10]$ after 1hour buffer layer growth

The first transition corresponds to the $(2 \times 4) \rightarrow c(4 \times 4)$ at ~500 °C. Here the sample temperature is lowered by 0.02 A every 30 minutes until the 4× pattern transforms to a c4×, with is essentially a 2× comprising the 0^{th} and ½ diffraction spots folded above a ¼ and ¾ 2× pattern (**Figure 4.16**).

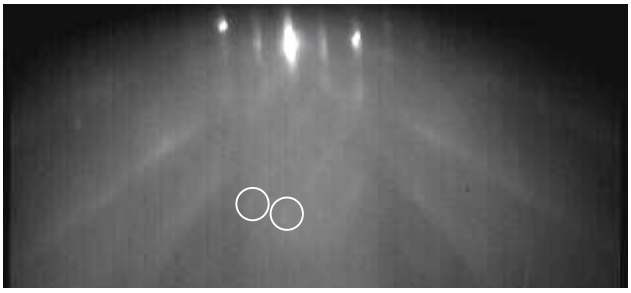

Figure 4.16: c4× pattern at ~500 °C. White circles depict composite 2× folded pattern.

The second transition involved freezing the c(4 × 4) pattern and ramping the As source to room temperature overnight, giving the system opportunity to purge background As from the chamber. The heating current was raised from 0.4 A in 0.02 A increments allowing 30 minutes settling time. The pattern consisted of mostly 2× and 3× hybrids until 0.54 A where the 4× pattern emerged corresponding to ~400 °C (**Figure 4.17**).

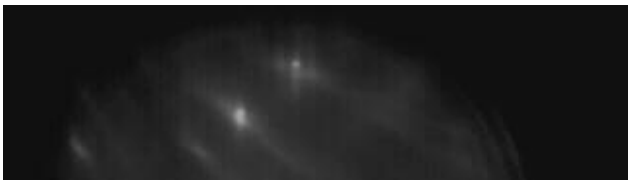

Figure 4.17: 4× pattern at 0.54 A with no As flux

For the third transition the temperature was raised to 580 °C and a buffer layer grown to repair the damage of heating without an As flux. Once the 4× pattern was strong the current was immediately ramped to zero and the flux left on for 12 hours. The As-cap prevented any RHEED pattern being imaged. Heating commenced at 0.2 A and was increased in 0.02 A increments of 30 minutes duration until the zero order spectral lines emerged at 0.30 A corresponding to ~295 °C.

Figure 4.18: As cap clean-up at 0.30 A

The fourth transition corresponded to the (2 × 4) → (2 × 1)/(3 × 1) at around ~620 °C. The actual 2× or 3× nature of the pattern is not important on the [110] azimuth where the 4× changes to a 1× in either case. The initial clean-up current of 0.75 A was increased by 0.01 A in 30 minute increments until the 1× pattern emerged (**Figure 4.19**) at 0.77 A.

Figure 4.19: 1× pattern at ~620 °C

Finally, the (2 × 1)/ (3 × 1) → (4×2) transition corresponding to ~680 °C was observed by further heating the sample in 0.01 A increments of 30 minutes duration until 0.84 A (**Figure 4.20**).

Figure 4.20: 2× pattern at ~680 °C

Comparing the three methods utilised in **sections 4.2, 4.3 and 4.5** it can be seen in **Figure 4.21** that the thermocouple and RHEED methods are in good agreement until around 600 °C where the reliability of the thermocouple is seen to fail. The theoretical treatment does not take account of sufficient losses to accurately predict the actual temperature of the substrate.

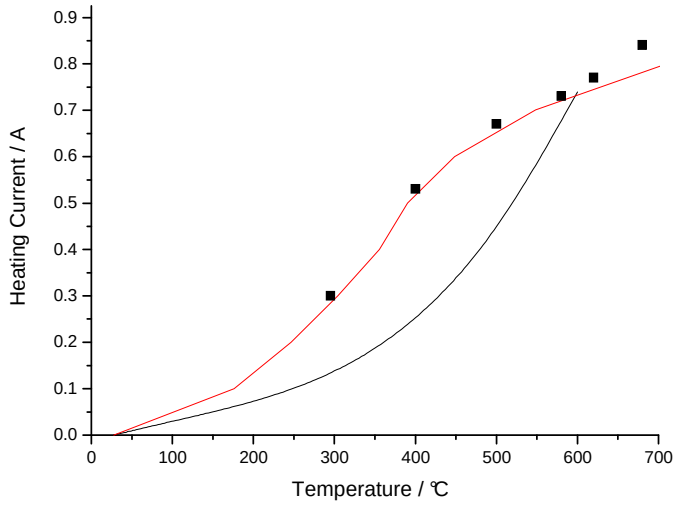

Figure 4.21: Graph of T vs. heating I showing correlation of Thermocouple (red line) theoretical (black line) and RHEED transitions (black squares)

4.6 Thermography

Thermography can be used to monitor both average surface temperature and temperature gradients across the sample.

4.6.1 Method

The Cedip Titanium Thermography camera utilised in this work required ad hoc calibration pertaining to the unknown sensitivity reduction whilst viewing through quartz glass. A heated sample was observed in the 250 - 600 °C temperature range both with and without a quartz viewport in place. The resulting correlation curve is shown in **Figure 4.22**. All further sample temperatures observed were translated via the simple function (**Equation 4.8**):

$$T_{comp} = (T_{read} + 1.337) / 0.8821$$ **Equation 4.8**

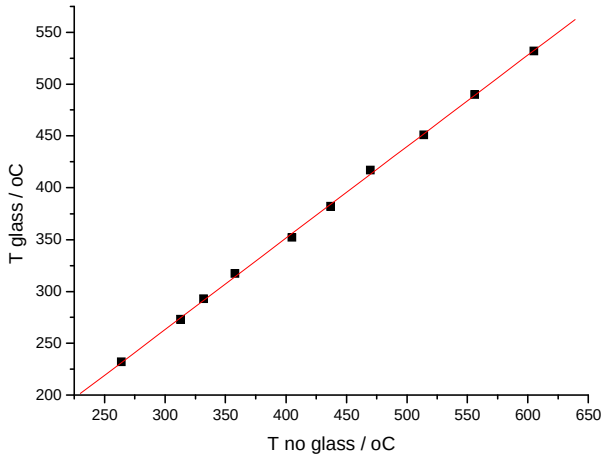

Figure 4.22: Quartz Glass Compensation Plot for Cedip Camera

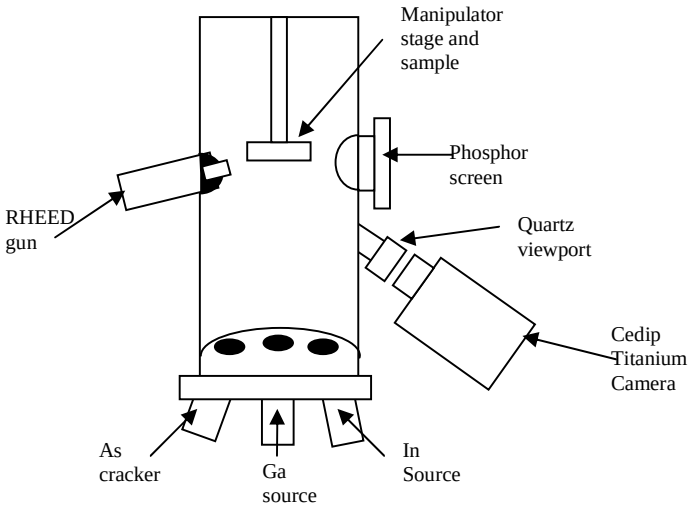

Figure 4.23: Cedip Thermography Camera Experimental Setup

The experimental setup is shown in **Figure 4.23.** The position of the viewport allows simultaneous access via both the Cedip camera and the RHEED gun. A sample-camera separation of ~300 mm supports the use of a standard 25 mm lens. Ideally a wide-angle zoom lens would have been implemented but was not available for this work. The quartz

viewport was protected via a simple shutter mechanism to reduce As contamination during growth cycles.

The stability of the sample temperature is crucial to successful MBE growth. DH sample heating is strongly susceptible to ramped heating temperature instabilities. Furthermore, the equilibrium temperature profile is of great importance as ultimately the quality of the growth surface depends on uniform sample heating. The following sections address these issues.

4.6.2 Results 1: RH Compensated Heating

Initially the plate is radiatively heated (RH) from the tungsten filament built into the manipulator stage to outgas the plate and condition the electrical contacts to support current flow. Typically the Mo of the plate reaches around 300 °C in this phase of the heating cycle and hence is significantly hotter than the actual sample. Since the plate is not acting as a heat sink, the temperature of the sample is relatively uniform, with a typical variation of 6 °C across the length.

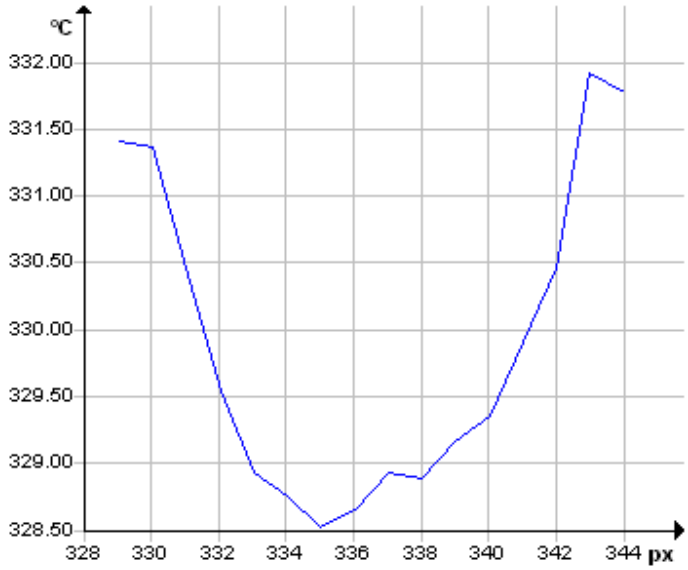

Figure 4.24: Temperature Profile average temperature 375 °C

This technique can be used for brief uniform sample flashing up to ~400 °C, beyond which the radiative heating require to enable stability becomes the limiting factor. **Figure 4.24** shows the sample temperature profile at 0.3 A heating current equating to an average sample temperature of 375 °C. This is higher than normal for 0.3 A heating because of the heat injected by the RH. Note that the outside of the sample are held at a higher temperature than the centre, caused by the extra heating in the sample plate. The uniform heating is transient and hence unsuitable for GaAs oxide removal applications. However for the purpose of evaporating an As capping layer at ~300 °C, this technique can be applied.

4.6.3 Results 2: Grounded Sample

4.6.3.1 Plate Design

The original RHEED accessible Direct Heat (DH) sample plate has the asymmetric clamping design shown in (**Figure 4.25**). The Ta clamping foils on the left of the sample couple into the grounding metal of the entire plate. The right-side comprises a substantially smaller heat sink path through the foil conduction bar and feed-through.

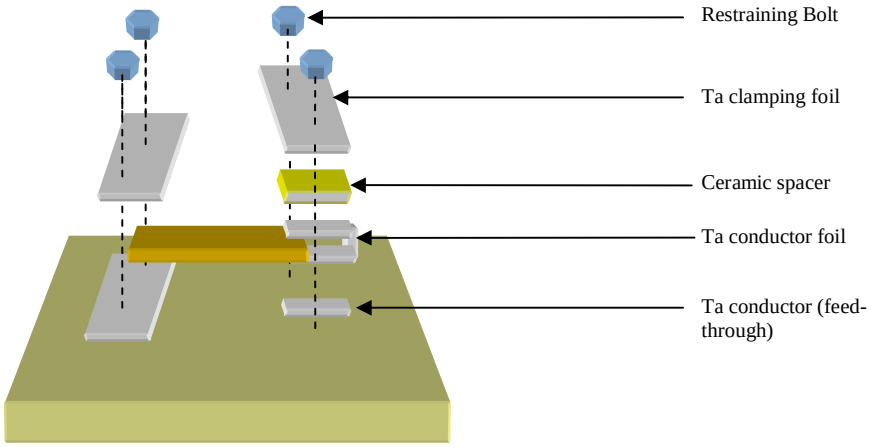

Figure 4.25: Asymmetric DH clamping design

The grounded end is strongly thermally coupled to the Mo of the plate, which in turn provides a path to ground and hence the manipulator stage. The Ta feed-through provides a conductive electrical path, which generates its own heat, however the bulk of the sample plate and the manipulator stage still constitute a heat sink. The high voltage end is naturally isolated from the grounded plate and manipulator. All the electrical conduction path generates heat, and losses are lower because of thermal isolation.

4.6.3.2 Dynamic Temperature Response

Dynamic heating corresponds to the sample plate's response to a step change in heating current. Unlike RH compensated heating, the sample conductively heats the sample plate, one side of which is strongly thermally coupled. Unsurprisingly the resulting temperature drop is large and varies from 30 °C at 300 °C to ~90 °C at 590 °C as shown in (**Figure 4.26**). (Note the temperature drop represents the transient response to an increase in current from 0.7 A to 0.75 A). Here the temperature value represents the raw data without applying the compensation for values taken through quartz. The compensated values are minimum = 530 °C , maximum = 630 °C and mean = 587 °C, which equates to a cross sample difference of 87 °C.

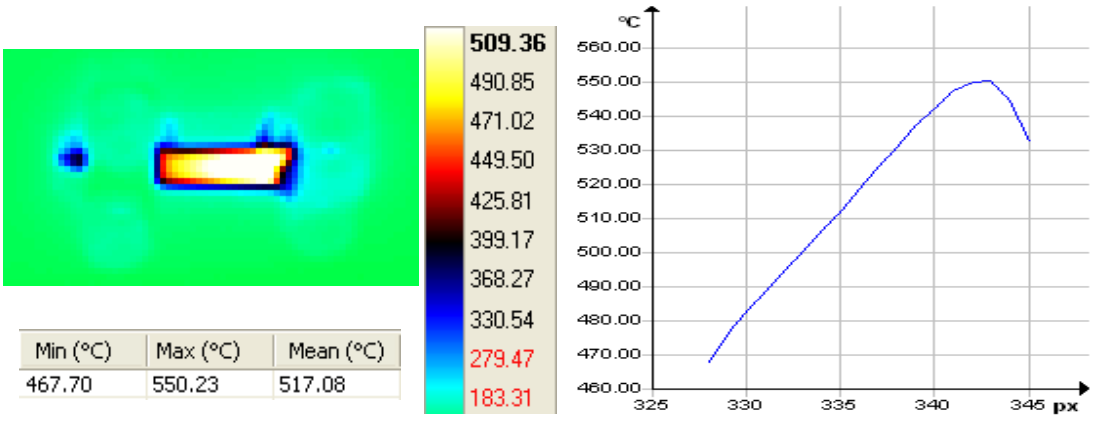

Figure 4.26: Thermography Image of Temperature Gradient at 87 °C

This effect is even more noticeably pronounced when viewing a sample in the STM chamber via the optical camera (**Figure 4.27**). Note the Ga droplets spread across half of the sample indicative of high temperature exposure (~700 °C) whereas the other end of the sample displays no sign of high temperature damage. In fact the resulting STM

imaging reveal 20 nm high topographic features that could result from roughness after clean-up.

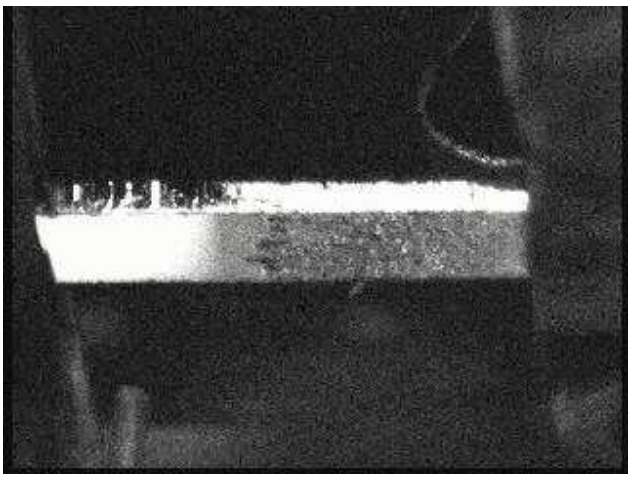

Figure 4.27: Optical Image of Ga Droplets on GaAs sample

The large temperature gradients are unsuitable for GaAs heating where care needs to be taken not to exceed ~620 °C to prevent damage to the surface.

4.6.3.3 Temperature Stability

In this instance the GaAs sample is heated from room temperature to 580 °C to perform oxide removal. The sample temperature was initially raised to ~475 °C in 50 °C per half hour increments with the sample temperature monitored throughout. The typical maximum temperature variation across the sample was 50 °C in this stage. After settling at 475 °C for an hour the equilibrium profile is as shown in **Figure 4.28**. The temperature drop across the sample is 30 °C.

However increasing the heating current by 0.1 A at this stage to approach 550 °C caused a massive temperature gradient across the sample. The actual maximum recorded temperature is 552 °C which is equivalent to an actual surface temperature of ~630 °C. Eventually the sample settled to an average temperature of 552 °C with the hottest region off centre toward the high-voltage end and a temperature variation of 35 °C across the sample.

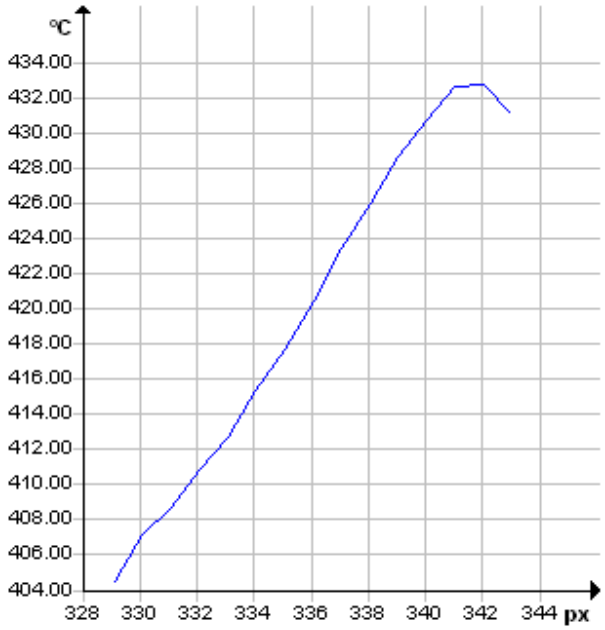

Figure 4.28: Equilibrium temperature profile at 475 °C

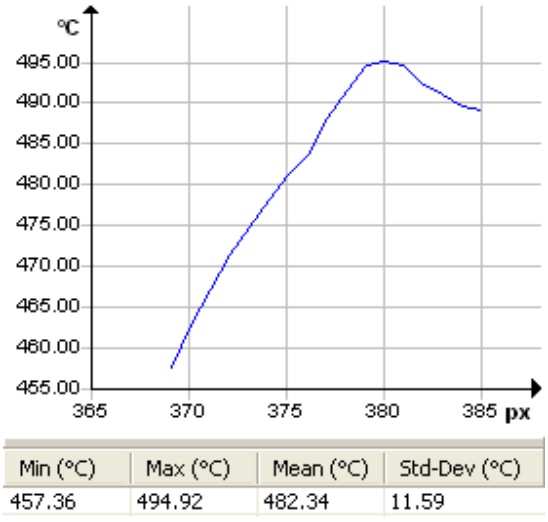

Figure 4.29: Equilibrium temperature profile at $T_{average}$ 550 °C

The temperature continues to wander for the following hour on average by 10 °C with a maximum change of the order of 40 °C. These temperature fluctuations are highly

undesirable, especially around 600 °C where sample damage can readily occur. The follow section discusses the response of a more compensated DH plate design.

4.6.4 Results 3: Compensated Grounding

4.6.4.1 Plate Design

To attempt to provide a more symmetrical heat sink the standard plate was modified as shown in **Figure 4.30**. The symmetric sample connector greatly improves linearity in heat loss conduction. The grounded-end is ultimately connected to the Mo plate metal and the manipulator stage bulk whereas the high voltage end is connected solely to electrically isolated conduction bars and connectors.

When the sample plate conduction path and the manipulator stage are both at room temperature, a ramp in heating current through the sample causes a heating profile across the sample surface. The origin of this heating profile can be attributed to the thermal conduction path across the terminals. Whilst the sample mounting has now been compensated, the feed-through paths are dissimilar. Hence the overall heating *loss* could never be symmetrical.

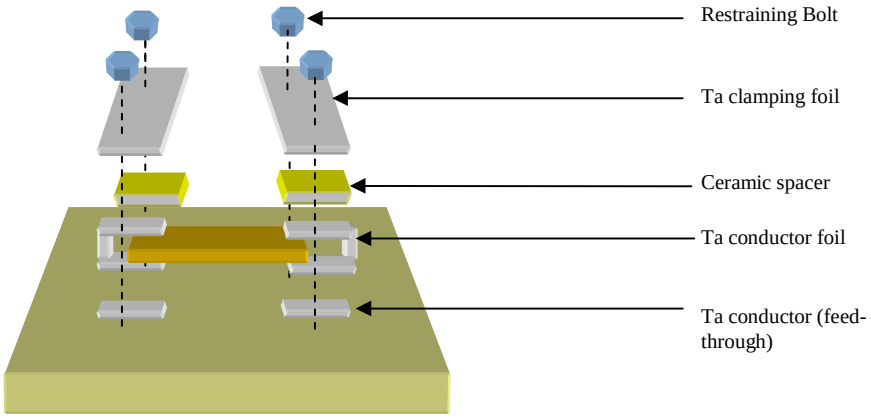

Figure 4.30: Modified RHEED DH plate

4.6.4.2 Dynamic Temperature Response

The new design in **section 4.6.4.1** exhibits a 20 °C drop across the sample at 300 °C which rises to a 30 °C drop at an average sample temperature of 525 °C (**Figure 4.31**). Again the temperature drop represents the transient response to a 0.05 A increase in heating current. Note that the temperature indicated on the figures is before the quartz glass compensation is applied, being of the order of 21 °C at 147 °C and 62 °C at 482 °C.

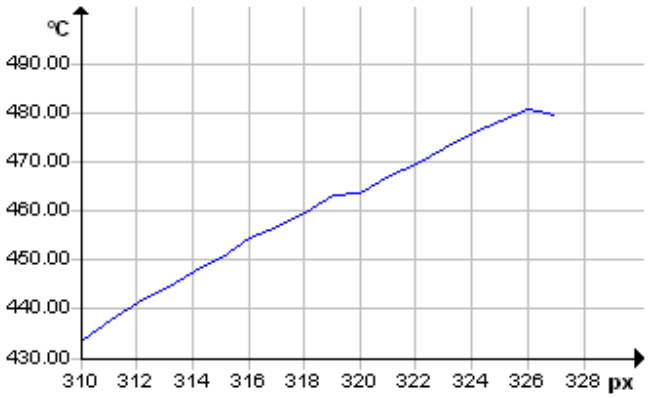

Figure 4.31: Improved sample mounting methodology at $T_{average}$ = 525 °C

4.6.4.3 Temperature Stability

Hence a step change in heating current from 0 to 0.3 A from cold generates an initial temperature drop of 30 °C where the heat sink on the grounded side is out of equilibrium. The temperature profile next undergoes a state of flux where the high voltage end maximum falls through conduction and the grounded end minimum rises due to thermal equilibrium between the bulk metal work and conduction path. The cycle repeats until an equilibrium state is entered after 30 minutes where the temperature drop is ~20 °C and the high voltage end maximum temperature is 30 °C lower than the initial overshoot. The temperature hence becomes stable at 300 °C with an expected temperature drop due to the asymmetric thermal conduction associated with the two ends of the sample.

Increasing the current to 0.35 A results in a net increase in the sample temperature, which initially adheres to the equilibrium temperature drop. However the thermal instability forces the system into another state of flux where a maximal 20 °C

minimal 12 °C drop appears across the surface with a periodicity in the order of 30 seconds. This state of flux is henceforth referred to as phase 1 (**Figure 4.32**).

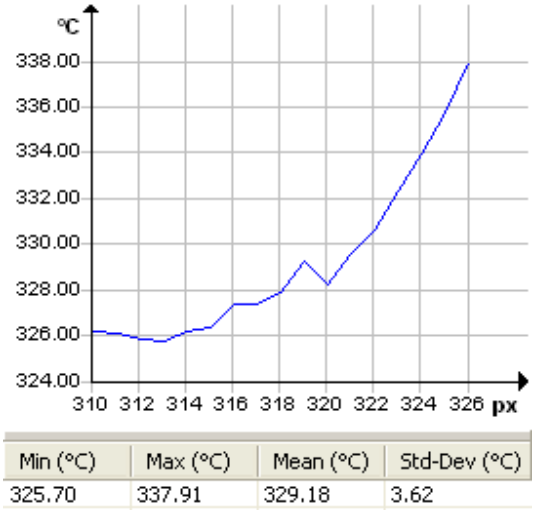

Figure 4.32: Phase 1: 12 °C Temperature Drop at 0.35 A

The sample and metal are held in electrical contact, however heating the system changes the quality of the contact. Hence either end of the bar can experience a temperature drop. Whilst this most frequently occurs for the grounded end, the system has entered a state where the sample has been hotter at the fringes than at the centre, presumably caused by the heating of the conduction path and the alteration of the electrical contacts resulting in current pinching at a certain point on the sample. This temperature variation is henceforth referred to as phase 2 (**Figure 4.33**).

A ramp change therefore induces initially a phase 1 temperature variation for the first 15 - 30 minutes, followed by a phase 2 variation. Note that in phase 2 the temperature profile shows a maxima at the grounded end, which is contrary to the initial argument of asymmetric losses. Furthermore the average recorded temperature is 25 °C lower for phase 2 at 0.35 A. The occurrence of these two states has the following ramification:

1. There is always an overshoot on increasing the current

2. Phase 1 has a temperature gradient from high to ground
3. Phase 2 has a 'U' shaped temperature profile.

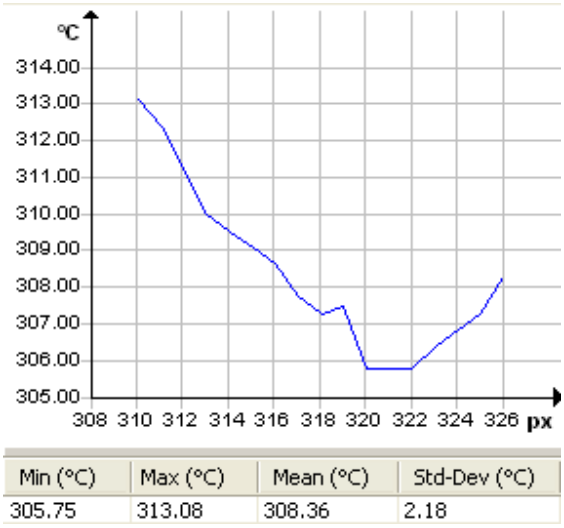

Figure 4.33: Phase 2: Edge heating effects

Phase 2 represents the final "equilibrium" state of the DH methodology. It is typically characterised by a higher voltage drop (4.0V) across the sample compared to a lower (3.2V) drop evident in stage 1. Phase 2 is relatively stable, with only ± 5 °C wander over the course of an hour and a temperature drop from 3 to 9 °C throughout.

A similar transition occurs for ramping down in power. For a sample cooled from 580 °C to 500 °C the original stable phase 2 stage gradually reduced to a phase 1 stage that exhibited general temperature fluctuations over a 30 minute period until the phase 2 state re-stabilised at the new temperature.

These results have 2 ramifications:

1. RHEED transitions unreliable
2. Lengthy heating cycles

The first ramification pertains to the overshoot and general flux like state of phase 1. This means that the RHEED transitions most likely occur because of transients in the surface

temperature rather than the stable states. The overshoot in most cases is around 25 °C and hence the inherent error is not substantial and can be accommodated.

The second ramification is in the interest of sample protection. In order to minimise overshoot, the heating current must be increased in small increments (ideally 0.01 A steps with 30 minute periodicity). Clearly, the temperatures are not of significance until around 600 °C. However an increase from 500 °C at 0.65 A to clean up at 580 °C and 0.72 A, could require several hours.

Investigations revealed that increasing the current in 0.02 A stages from 0.35 to 0.55 A with a 5 minute interim and stabilisation period allowed temperature increase without deviation from the phase 2 regime. However at 0.55 A the sample switched into a phase 1 stage. T_{max} increased by 50 °C and the $T_{average}$ by 30 °C giving the typical ~27 °C drop associated with phase 1 (**Figure 4.34**). Furthermore the sample temperature adhered to severe fluctuations during the following 30 minutes with maximal drops of 50 °C across the sample. After an hour the sample returned to a near phase 2 stage, with temperature drop of 14 °C and an average temperature of 378 °C as read.

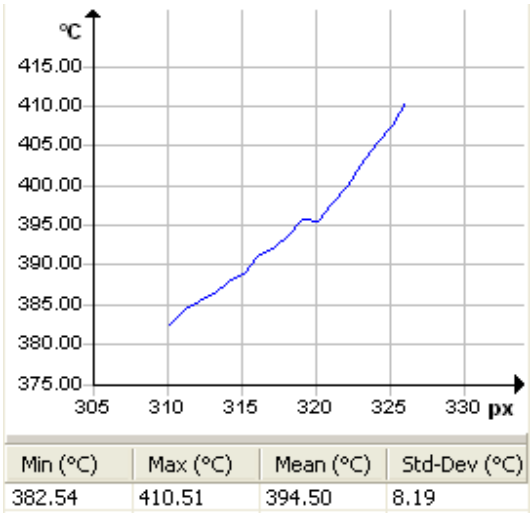

Figure 4.34: Phase 1: Temperature Profile at 0.55 A

Heating to 0.72 A to perform clean up proved equally problematic. The sample continued to experience large temperature fluctuations outside of equilibrium. Whilst the temperature drop across the sample was limited to less than 50 °C the maximum temperature of the sample varied by as much as 60 °C at the high voltage end. Hence a

PID control loop would be beneficial to prevent temperature surges. To eliminate these "surges", in the absence of such safeguards, increases in heating must be supplied in small increments, allowing an hour for stability before further increasing the heating.

The ability to identify the surface gradient is of chief importance for the use of DH sample preparation. The volatile nature of the GaAs surface requires careful heating control. The original purpose of the DH plate was to "flash" prepare Si(111)-(7 × 7) samples for STM imaging. Here the sample was heated to a stable 600°C, typically overnight, and then ramped to 1250 °C in 5 second cycles, intended to maintain the transient pseudo-phase 2 stage during heating. Whist the DH plate is applicable to this high temperature surface under rapid response, the suitability for low temperature GaAs applications is perhaps impractical.

Ultimately STM observations will be limited to the narrow band at the centre of the sample that appears to be immune from the large temperature fluctuations outside of equilibrium. The main advantage of this plate is the ability to rapidly thermally quench the sample post growth (**4.6.6 Results 5: Rapid Thermal Quenching**).

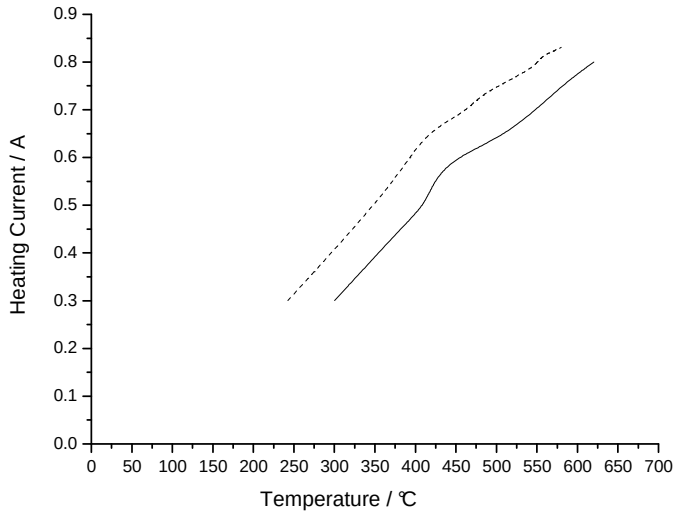

Figure 4.35: Sample temperatures observed via Cedip camera.
Dashed: LN_2 cooled Solid: No cooling

4.6.5 Results 4: Liquid Nitrogen Cooling

The effect of cooling must be considered for in the typical MBE chamber with an As cracker and Ga effusion cell the ambient temperature of the chamber and the background pressure must be controlled by a degree of liquid nitrogen cooling. The background pressure can be reduced by a factor of 10^2 provided sufficient cooling is supplied. Conversely the small e-beam cells utilised in the STM do not produce such a significant residual flux and hence cooling is neither required nor in this case available.

Appreciably the two methods will present a marked difference in ambient temperature and hence the conductive losses increase significantly in the presence of a LN_2 cooled chamber. As an aside, it is noted in section **4.6.4 Results 3: Compensated Grounding** the grounded side is thermally coupled to the manipulator stage, this is true for the MBE chamber only. In the STM chamber the high and low voltage connectors are isolated from ground. Hence the heating loss in the STM chamber should more closely adhere to the symmetric ideal.

Figure 4.35 plots the average sample temperatures against heating currents for a cooled and non-cooled sample. The two results differ by approximately 45 °C throughout. The temperature difference can be considered to be so large because of the small thermal volume of the sample (9 x 1.4 x 0.3 mm^3) in comparison to the thermal volume of the heat sink. Other heating methods, whilst susceptible to the cooling effect, are not so extremely influenced.

4.6.6 Results 5: Rapid Thermal Quenching

Sample quenching requires rapid temperature change in order to attempt to freeze the surface reconstruction. Additionally in the case of GaAs the As overpressure must be suitably reduced or "tuned" to maintain the reconstruction. As a prelude to quenching investigations it is necessary to observe the rate of sample cooling. The DH method offers the fastest cooling method in the absence of liquid N_2 enhanced cooling techniques.

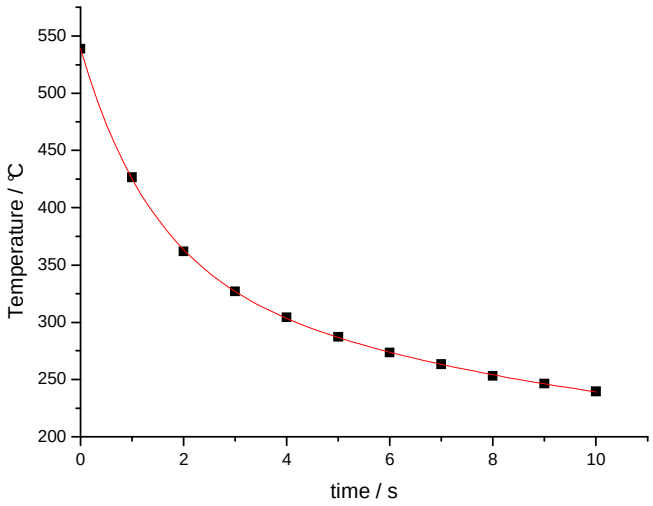

Figure 4.36: Rate of Cooling for DH sample T_0 = 540 °C

In the experiment the sample temperature is maintained at a steady 540 °C before the heating current is terminated. No attempt is made to compensate the As flux at this time, though it is worthy of note that the 4× RHEED pattern remained throughout the cooling cycle albeit at a reduced intensity.

The observed cooling curve is shown in **Figure 4.36**. There is a 112 °C drop in the first second, at which point the sample is in the phase 1 stage with a substantial temperature drop across the sample. A subsequent exponential decay reduces the sample temperature to 280 °C within 5 seconds. After a further 30 seconds of cooling the sample temperature is down to 140 °C.

The rapid cooling down to 300 °C is therefore offset by a more gradual cooling between 300 °C and ambient temperature. The slower cooler phase could have consequences for quenching investigations. However since the effects of quenching are in dispute it is not consistently proven what effect this would have. An investigation into the quenching capabilities of DH cooling by variation of As overpressure can however be conducted.

4.7 Sample Temperature Map

Evidentially directly heating the sample has a number of distinct phases resulting in a variety of responses to a given applied heating current:

1. Prior to initial radiative heating
2. Initial DH heating phase <600 °C
3. Uniform phase >600 °C

Stage one is a dynamic phase, incipient because of a requirement to heat the sample plate radiatively in order to encourage conduction through the sample and to degas the plate. Typically the sample and conduction path reach around 250 °C in this stage. Applying a low current (0.1 A) is sufficient to maintain a current path until the ambient temperature has reduced sufficiently to support the second phase of direct heating. Hence the first phase was not studied in detail.

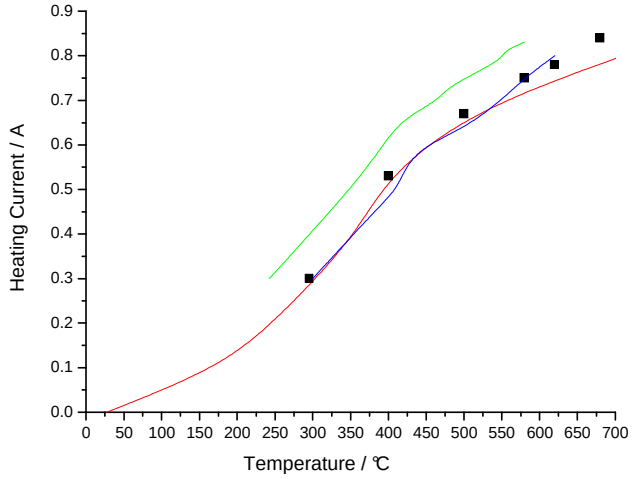

Figure 4.37: DH Temperature Map. Squares: RHEED, Red: Thermocouple, Blue: Thermography, Green: Cooling

Phase two is the essential phase as it is the semiconductor's response to the first DH cycle. The location of the clean up temperature at around 0.73 A is essential for sample preparation. The temperature map for this phase has been independently confirmed with

thermocouple, RHEED and thermography as is shown in **Figure 4.37**. The close correlation of the three methods support the argument that the system response is repeatable and predictable. The added complication of LN_2 cooling can alter the surface temperature by 45 °C, however, and hence RHEED is essential during growth in the MBE chamber.

Phase 3 requires further investigation, though only occurs for temperatures close to and beyond 600 °C. The sudden uniform temperature profile could be used to provide good buffer layer growth, however its applicability needs further investigation.

4.8 References

R.E. Honig and D.A. Kramer (1969) RCA Rev. **30**: 285.

A.S. Jordan (1980) J. Appl. Phys. **51**(4): 2218.

A.H. Kean, C.R. Stanley, M.C. Holland, J.L. Martin and J.N. Chapman (1991) J. Cryst. Grow. **111**(1-4): 189.

J.H. Neave and B.A. Joyce (1978) J. Cryst. Grow. **44**(4): 387.

C.D. Thurmond (1975) Journal of the Electrochemical Society **122**(8): 1133.

P.J. Timans (1992) J. Appl. Phys. **72**(2): 660.

Chapter 5: Tunnelling Tip Preparation

This chapter discusses the fabrication of the tunnelling tip, often quoted as the most crucial component of an STM system (Kubby et al. 1996). Tip fabrication is inherently a two step procedure, involving production of a fine point and then the inevitable cleaning of the tip before imaging can commence. The two procedures are systematically investigated and discussed herein.

5.1 Argument

5.1.1 Etching Detail

Electro-chemical etching is the most common method utilised for tip fabrication. Yet despite the importance of this crucial component, methods for production are relatively poorly documented and generally involve a small percentage of specifics and a high percentage of qualitative results.

The purpose of electrochemical etching is clearly to produce a sharp tip. The sharpness is reflected in the termination of the etching process immediately upon drop off (Bryant et al. 1987). The fact that both the etched electrode and the drop-off section constitute sharp tips has led to methods of protecting the fallen section of wire, the intention being to utilise this as a tip instead of the upper part, owing to the fact that clearly current was terminated to this section when it fell away from the upper part of the electrode.

Nevertheless, the sudden change in current at the point of drop off has inspired control circuitry based upon this finite-time singularity. A typical current-time plot is shown in **Figure 5.1**. Initial threshold control utilised the abrupt change in current to signify a termination to etching, with control depicted by a constant value. However due to the ever changing concentration and alteration of immersion depth from tip to tip this method proved ineffective.

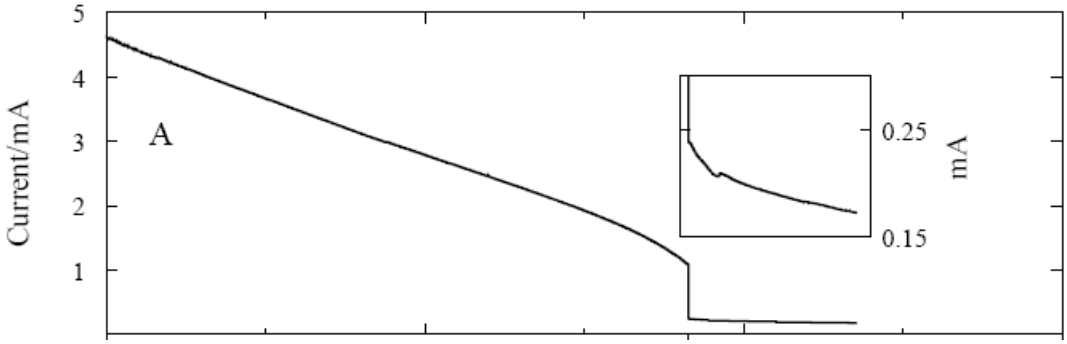

Figure 5.1: Current-time plot during etching process
From (Quaade et al. 2002)

An inspired alternative was to utilise the differential current or dI/dt (Chen et al. 1989; Ibe et al. 1990; Nakamura et al. 1999). The rate of change of current is relatively constant until the singularity, where an extremely rapid, if not vertical, rate of change is apparent.

One phenomenon evident from the etching process is that the wire actually snaps under the weight of the lower section before it is etched completely through (Quaade et al. 2002), a happenstance utilised to theorise an idyllic situation where the etching potential is ramped down alongside the current, resulting in a slow rate of etch at the point of breaking (Melmed 1991). Substantiation for this claim and any negative ramifications on the system dynamic require investigation.

For the apparatus in this work, an initial Voltagram can indicate the available bias range (Oliva et al. 1996; Kerfriden et al. 1998). The plateau in **Figure 5.2** depicts the most stable region for etching in terms of variable tolerances. Whereas at the higher potential etching would ultimately be faster and less reproducible, the relative importance of etch time, stability and reproducibility clearly needs to be addressed.

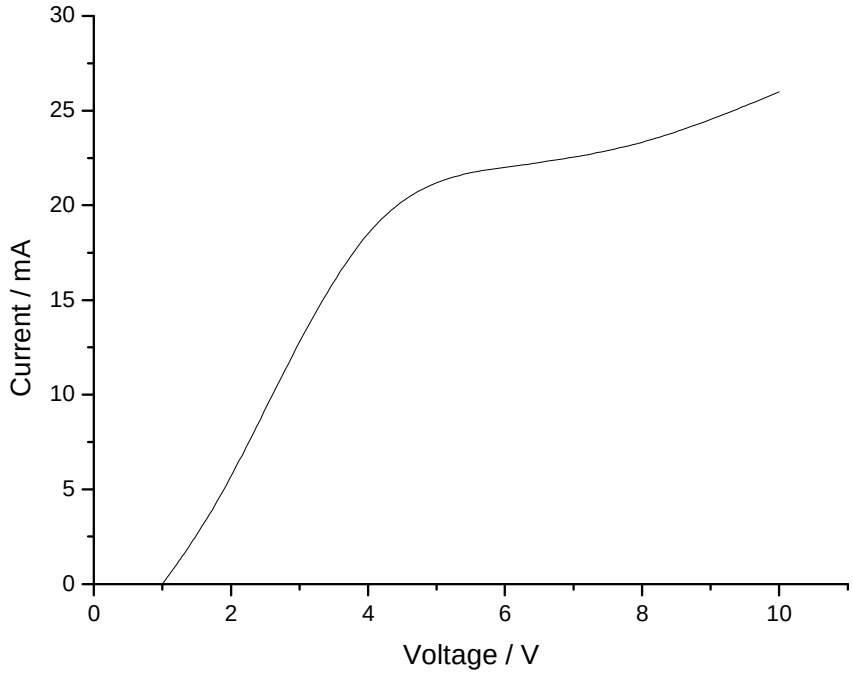

Figure 5.2: Voltagram obtained during tip preparation

Another variable thought to have significant effect on the shape of the final etched tip is the meniscus. A tip with a short, symmetrical shank terminating on a atomically sharp point represents the paragon for most applications. It has been postulated that the aspect ratio of the cone depends strongly on the shape of the meniscus during the etch (Ibe et al. 1990). Investigation into theory developing controllability of the aspect ratio requires work.

Moreover, the immersion depth is believed to affect the shape of the cone in two ways. Firstly the greater the length of the submerged part the shorter shank (Oliva et al. 1996). Whereas a heavier the drop-off section yields a greater the radius of curvature, ROC, (Ibe et al. 1990).

Electrode shielding of various guises has been heralded to minimise disturbances of the meniscus, due to protection from the bubbles formed at the cathode (Melmed 1991).

The final variable in the assembly, is the concentration of the solution. Intuitively the stronger the etchant the faster the etch, whereas lowering the concentration, whilst slowing the etching rate, has also been postulated to produce more parasitic oxide (Kerfriden et al. 1998).

The sheer myriad of variables discussed require lengthy and detailed analysis. The goal is to find a variable set that consistently yields the desired tip profile and, moreover, the factors that produce undesirable tips. Hence a complete map of the etching procedure can be developed that is independent of the specific apparatus and reflects purely the method.

5.1.2 Cleaning Detail

Regardless of the etching parameters, contamination with etching by-products, including native oxide, is unavoidable (Hockett et al. 1993; Cricenti et al. 1994). This native oxide is usually 5 - 20 nm thick and impairs the metallic behaviour of the tip. Many methods exist to remove the W-oxides. Perhaps the most simple involves heating the tip beyond the sublimation temperature of the W-oxides, which is inherently lower than the underlying W metal (3410 °C). The simplicity of this method is complicated by the thermally generated electron flux, which can lead to localised melting of the tip apex and significant increases in the ROC (Ekvall et al. 1999; Ding et al. 2005).

Tip shape is easily classified by scanning electron microscopy (SEM), with the ultimate apex requiring high-resolution transmission electron microscopy (TEM) and crude elemental mapping (Ekvall et al. 1999), though clearly the most obvious test involves performing STM upon the desired surfaces. In this work, the crucial parameters for both etching and e-beam cleaning that result in an atomically sharp STM tip, without the often detrimental effect of localised melting, are presented.

5.2 Differential Etching

Differential etching identifies the control mechanism for tip production only. The tip-solution interaction can be broadly classified into three categories. The simplest of

which is *in-solution* whereby the tip is lowered into the etchant, typically in a glass beaker, where the etching is performed. Methods to restrict the etch to a small area of wire involve either a *lamella* (Klein et al. 1997; Kerfriden et al. 1998) or a *floating layer* (Lemke et al. 1990; Melmed 1991). This work concentrated on the less convoluted *in-solution* variant. All further references to differential etching imply an *in-solution* configuration.

5.2.1 Tip Categorisation

Differential etching allows the control of four independent variables:

1. Immersion depth
2. Etching Voltage
3. Sensitivity (arbitrary units: defines $\Delta I/\Delta t$ at which cut off is detected)
4. Etchant Concentration

The relative combinations of these yield a finite number of tip types that allow simple categorisation. **Figure 5.3** depicts the 6 types of tip that occupy 4 generic categories.

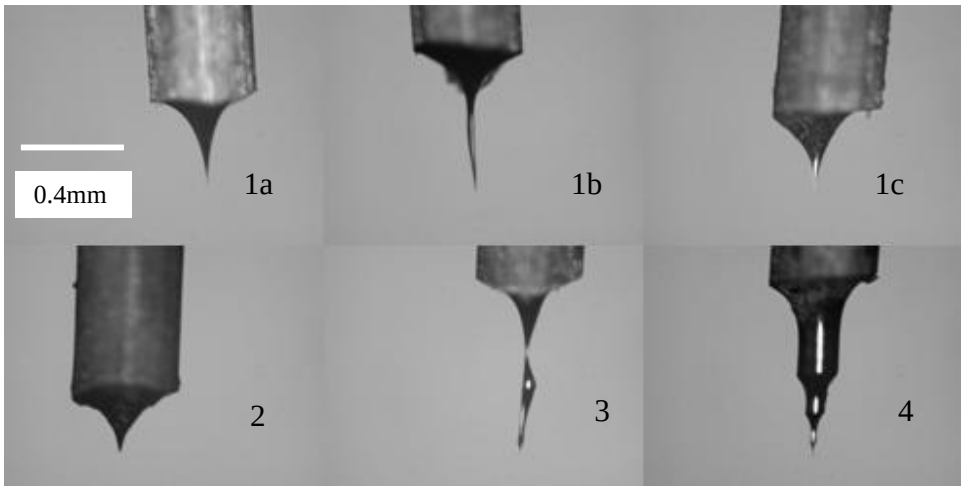

Figure 5.3: Light optical microscopy images of tip categories

Type 1a is often an idyllic tip with a sharp apex, short shanks and low aspect ratio. Whilst the radius of curvature (ROC) cannot be accurately estimated at the optical magnification given, the tips in this category pass a basic requirement. Type 1b is a variant of 1a with a larger aspect ratio. Whilst the sharp tip accommodates atomic scale resolution, the long shank introduces increased vibrational instabilities that can degrade image quality. Type 1c is a further variant of 1a having a short but asymmetric cone. Both meniscus shape and immersion depth are thought to influence cone shape. Investigation into the latter is performed in **section 5.2.4.**

Type 2 tips represent a late termination to the etching procedure, characterised by a rounding of the apex and a large ROC. Type 2's occur when the sensitivity is set to too low a value and are hence easily remedied. Strictly anything short of optimum cut off after drop off is a type 2 tip. The blunt apex does not always show under light optical microscopy. For purposes of classification anything greater than 10 nm ROC is considered type 2, however, this can only be determined by TEM imaging as discussed later.

Type 3 tips are the converse of type 2. Here the etching process terminated prematurely and hence the wire was not etched all the way through. Type 3's occur when the sensitivity is set too high and hence lowering the sensitivity is the remedy.

Type 4 tips occur as a result of meniscus drops and are characterised by ribs along the cone sidewalls. These inherently only occur for lengthy etches (greater than 30 minutes) or due to external instabilities discussed in **section 5.2.3.**

5.2.2 Etching vs. Polishing

The nature of the tip production process is often generalised as electrochemical etching. Specifically electrochemical *etching* entails employing a direct current through an electrochemical solution. An intermediate compound is formed on the etching surface (WO_4^{-2} in this case) which can be removed more easily than the W in its own right. For electrochemical *polishing* the metal is literally polished by a process removing microscopic amounts of the metal. Polish relies upon ion flow from the anode to the cathode and the finish is often planar. Clearly the distinction is a subtle one.

Electrochemical tip production inherently possess an enhanced etching rate at the upper part of the wire, yielding a necking-in effect. Classically this is describe by "enhanced etching near the meniscus", though it is perhaps more accurately described by a retardation of the etching process away from the meniscus. Dissolution of the W wire produces two species WO_4^{-2} and OH^- (Ibe et al. 1990; Zhang et al. 1996). The WO_4^{-2} ions travel down the length of the W wire, forming a shield against further etching whilst the less dense OH^- pockets move upward and outward, inevitably causing fresh NaOH to be drawn toward the etching site (**Figure 5.4**). Thus the etching process is enhanced.

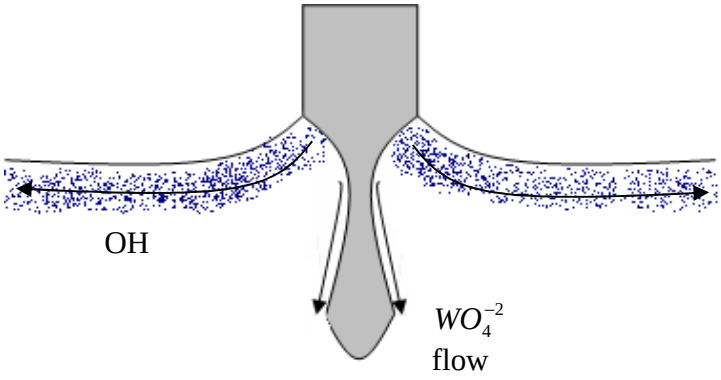

Figure 5.4: Ion Flow During Tip Etching

WO_4^{-2} flow down the anode is indicative of electrochemical polishing ion flow and is characterised by a bulbous formation in the lower end of the tip and should give a shiny finish. Etching would involve dissolution of the WO_4^{-2} and a dull, pitted surface.

To investigate the polishing-etching phenomenon 12 tips were etched: the first 6 at 1.5 mm immersion and the second at 5.0 mm. Of those 6: pairs were etched at 3.0, 6.5, and 10.0V with the etched terminating at 0.5 and 0.75 of the nominal etching time (t_{etch}) in each case. Selective results are given in **Figure 5.5.**

Progression from 3 to 10 V reveals an enhanced neck-in for increasing etching voltage, a phenomenon emphasised when the etching process is closer to termination. This indicates that polishing ion flow is being enhanced by increasing potential. Most notable is the rather dull appearance of the wire at 3 V and 5 mm insertion, indicating that

the conditions are such that polishing is no longer the driving mechanism and the process has resulted to a more passive etching. Increasing the etching voltage results in a restoration of the polishing mechanism.

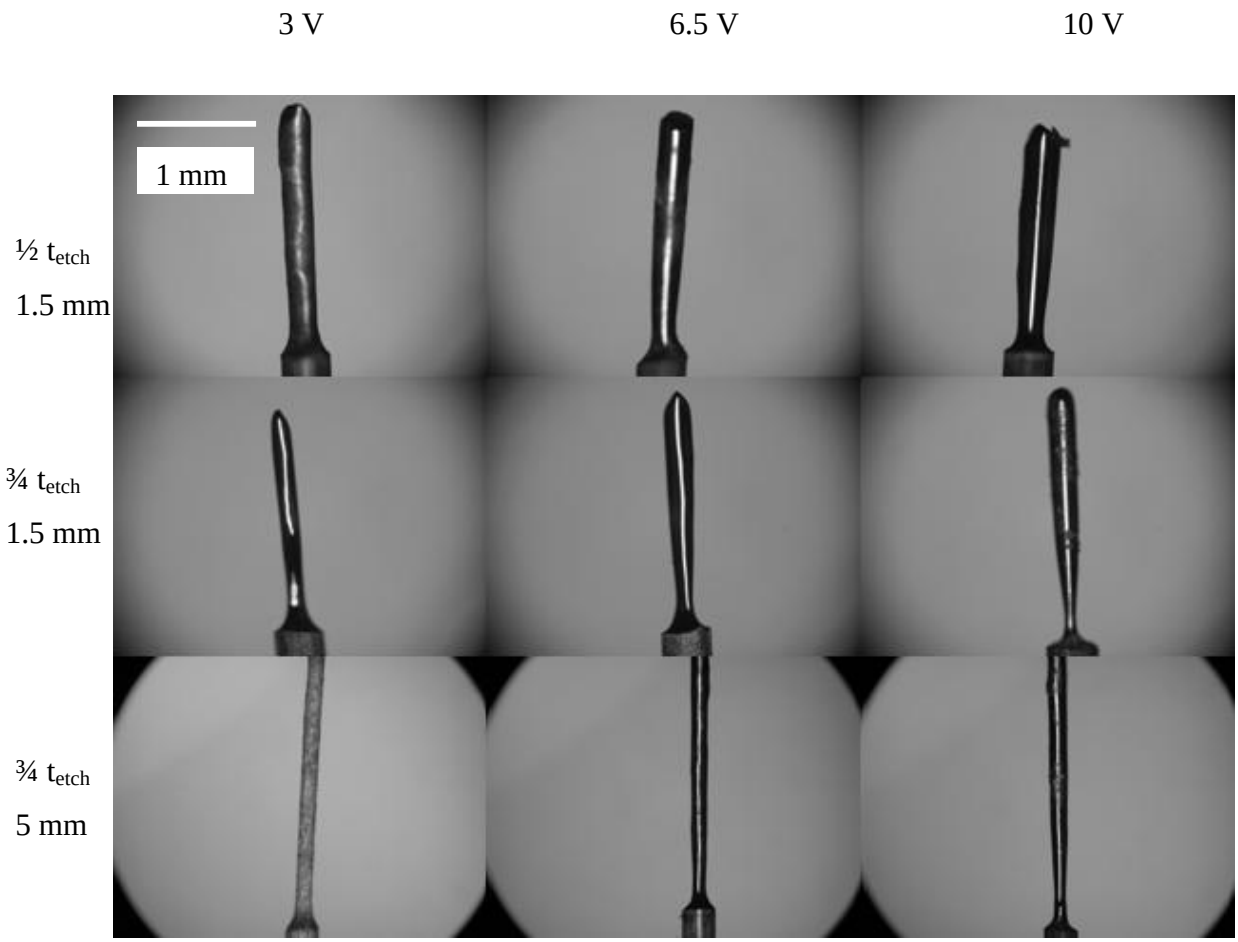

Figure 5.5: Light optical microscopy images of etched tips:
Columns: Voltages, Rows: time and immersion depth

5.2.3 Environmental Shielding

Stability of the etchant surface tension is essential during tip production. External and internal instabilities need to be minimised in order to ensure the etching procedure yields the desired tip shapes. It has been noted that type 4 tips habitually occur from alterations

in the meniscus during the etching procedure. Three types of instability have been identified throughout this work.

Firstly external vibrations, or floor vibrations, cause ripples in the etchant surface that are detrimental to the meniscus' stability. These can be eliminated by ensuring the etching apparatus stands in a low vibration environment and that the platform housing the etching apparatus is free from external (human) contact throughout.

Secondly fluctuations in the air above and around the etchant surface cause a similar effect. Air conditioning systems and air extraction systems are examples of sources. Shielding the etching apparatus in a box prevents air-source fluctuations from effecting the meniscus stability. The presence of this particular shielding commonly means the difference between a type 4 and a type 1 tip.

Finally the violent reaction occurring at the cathode causes H_2 bubbles to permeate through the etchant. These bubbles are again detrimental to the stability of the meniscus. Hence the anode requires shielding from the cathode. Inserting the cathode within a glass tube is sufficient to alleviate the problem (**Figure 5.6**).

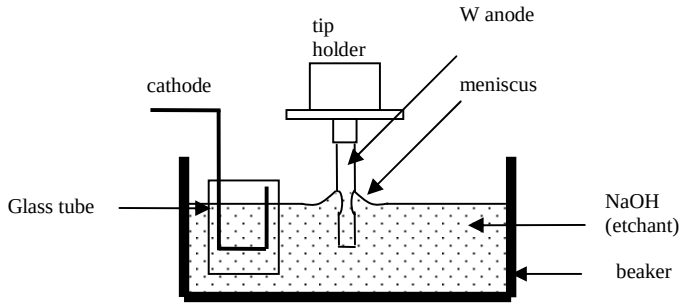

Figure 5.6: Tip etching apparatus showing cathode shielding tube

5.2.4 Experiment 1: Insertion Depth

To investigate the effect of immersion depth on tip quality a range of depths were investigated from 1 - 5 mm for the etching voltages 5, 8.5 and 10 V. All sensitivity values correlate to type 1a tips. The results are shown in **Figure 5.7**. The dashed lines represent a stable range around sensitivity = 6 within which the circuitry is optimised to detect drop off.

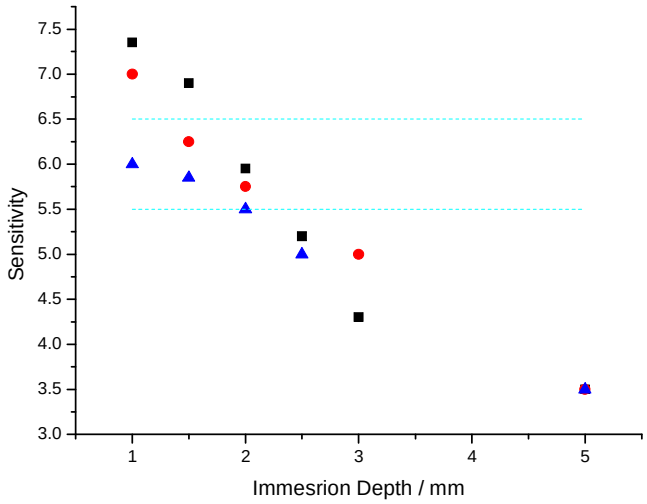

Figure 5.7: Graph of Depth vs. Sensitivity. Triangles = 5V, Circles = 8.5V and Squares = 10V. Dotted lines represent stable range

Clearly the stability is optimised for lower voltages, corresponding to the shape of the voltagram (**Figure 5.2**). All the voltages have reasonable stability around 1 - 2 mm immersion. Furthermore all curves coalesce at a common sensitivity value of 3.5 for immersion of 5 mm.

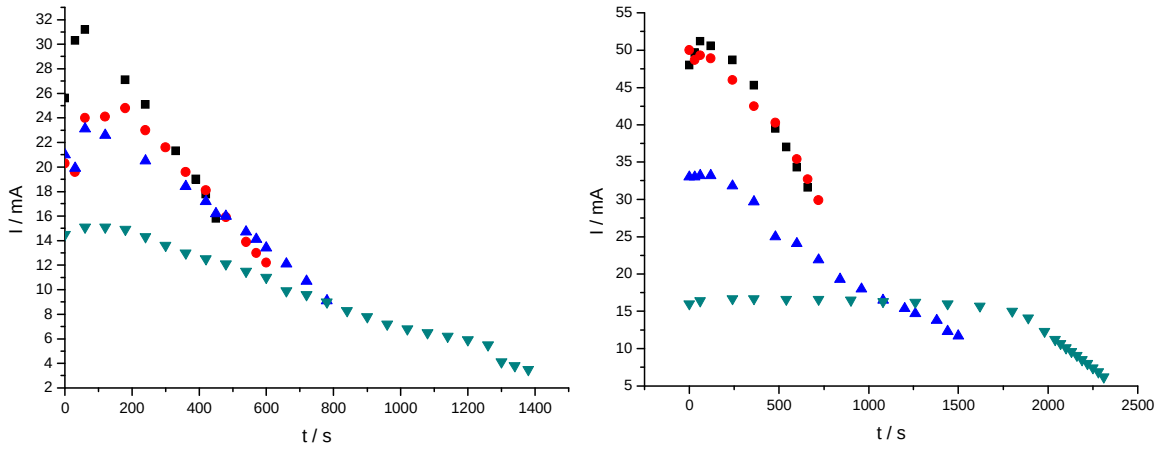

Figure 5.8: Etching current vs. time. Left: 1.5 mm immersion, right: 5.0 mm immersion. Square = 10V, Circles = 8.5V, Upright triangles = 5V, Inverted triangles = 3V.

To explore the nature of the etching procedure the etching current was mapped against etching time for 1.5 and 5 mm (**Figure 5.8**). At 1.5 mm immersion the curves collapse toward a common origin, implying a certain saturation of the etching current established from chemical concentrations within the etchant. Notice at around 1200 s there is a clear singularity event on the 3 V curve that is not large enough to stop the etching procedure. Such singularities are common for non-ideal parameters.

For 5 mm immersion it is cleat that 8.5 V and 10 V have almost identical responses, indicating a rate limit to the etching procedure at this immersion depth and solution concentration, perhaps caused by a passivity due to an OH population. Note that there is one obvious singularity event for 5 V at approximately 500 s. It is unlikely that the wire has etched to a degree that a premature drop off has occurred and more likely that an vibration or other disruption led to the singularity.

Initial extrapolation implies that etching is more stable at 1.5 mm immersion as opposed to 5.0 mm. Etching with large immersions requires greater potential differences, which in most circumstances will move beyond the desired 4 - 8V range indicated by the voltagram (**Figure 5.2).** Etching with large voltages at large immersions approaches a rate limit.

5.2.5 Experiment 2: Constant Bias Voltage

To investigate the effect of etching voltage on sensitivity and tip type, a range of voltages were chosen from 3 - 10 V. Expanding upon results from the previous section the immersion depth of 1.5 mm was chosen to enhance the stability of the procedure. All sensitivities were chosen to give type 1a tips.

Figure 5.9 shows the results obtained, providing an obvious similarity to the voltagram in **Figure 5.2.** Most notable is the plateau in sensitivity from 5 - 7 V. The stability of the circuitry has now been enhanced (if not optimised) for both immersion and etching voltage.

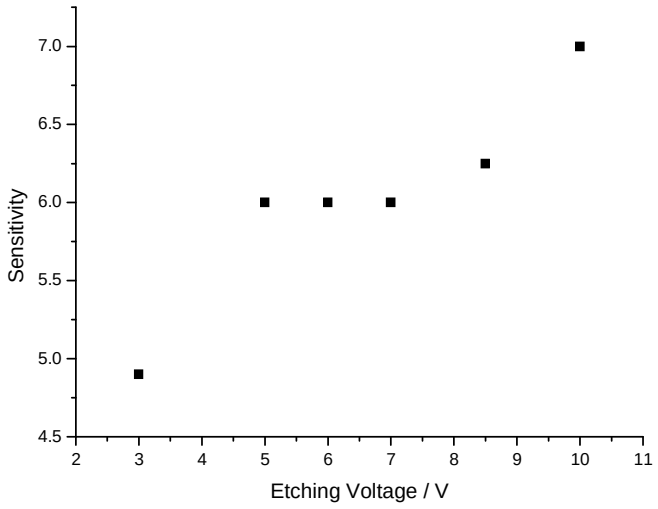

Figure 5.9: Etching Voltage vs. Sensitivity. Immersion depth =1.5 mm

Type 1a tips have hitherto been assumed to occupy a single sensitivity value, though it is apparent that under certain circumstances the type 1a category becomes broad and hence this anomaly allows the effect of varying the sensitivity close to the singularity to be investigated.

Applying an etching voltage of 6 V it is evident that a sensitivity of 4.5 gives a type 2 tip, implying that the sensitivity needs increasing, whilst a sensitivity of 8.0 gives a type 3 tip, implying that the sensitivity requires lowering. All tips produced with a sensitivity within this range are type 1a and 1c tips. Type 1c tips generally occurred when the wire was not perpendicular to the etchant surface.

It is intuitive to assume that the broadening of the type 1a category is required in this circumstance. In fact for this idyllic situation of a broad range of sensitivities it is perhaps more fitting to view the etching voltage vs. sensitivity as a range plot rather than a precise value (**Figure 5.10**). It is shown that the stability of operation around 6 V offers a large dynamic range in sensitivity values.

In order to analyse the type 1a tips more rigorously, Transmission Electron Microscopy (TEM) was undertaken to more accurately estimate a value for the radius of curvature, ROC, in each case. Choosing sensitivity values of 5.0, 6.5 and 7.0, three tips were fabricated at 6 V and imaged, with the results shown in **Figure 5.11**.

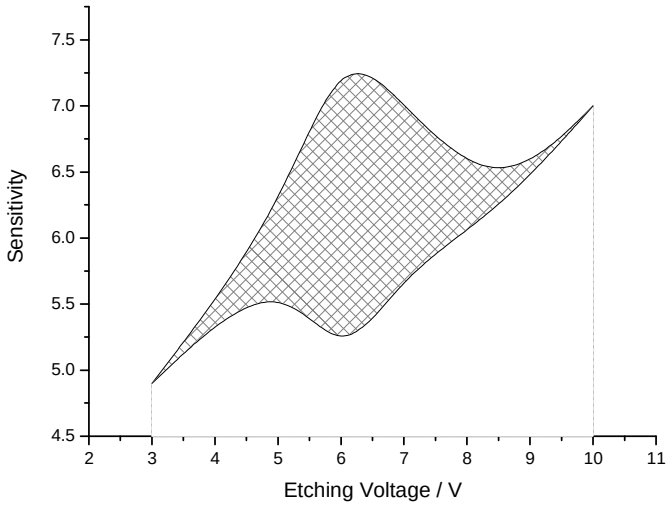

Figure 5.10: Etching voltage vs. sensitivity range plot

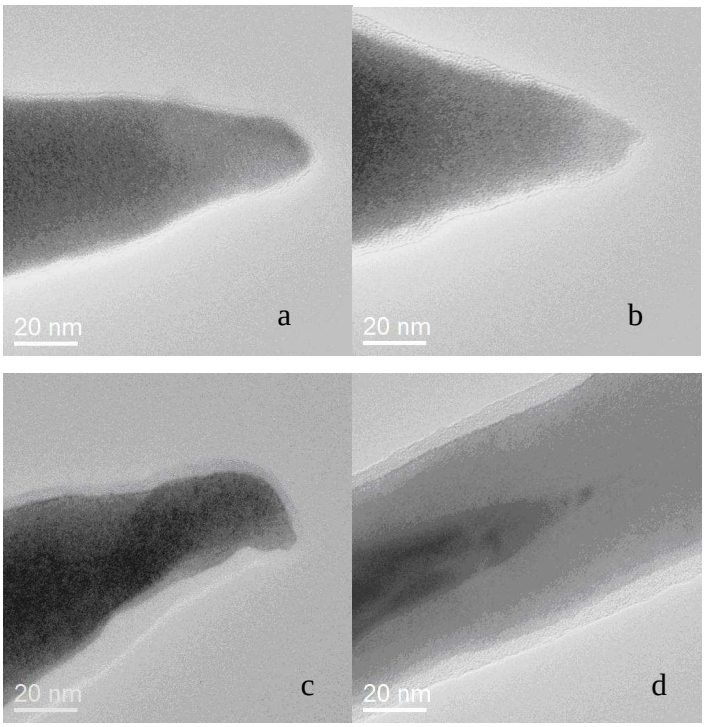

Figure 5.11: TEM tip images a) 5.0, b) 6.5 c) 7.0 d) 7.0 Tungsten core

Initial inspection shows an oxide coating on all the tips, with a ROC of approximately 20 nm in all cases. However, upon further analysis the 7.0 sensitivity revealed a W core with ROC ~ 1 – 2 nm. Without the ability to locate similar cores within the other images the effects of sensitivity are unknown. Regardless, a ROC of the order of 1 nm represents an ultra-sharp tip indicative of optimised parameters.

5.2.6 Experiment 3: The Cause of Asymmetry

Asymmetric STM tips are a commonly observed occurrence in differential etching. Logically the phenomenon can be traced to either non-perpendicular insert angle or electro-polishing effects.

Since the wire for the tips originates from a coil it is inherently curved and lengths must be taken to straighten it. To investigate the effects of this parameter two etches were performed, one intentionally bent at an angle to surface normal and the other nominally straight.

To investigate the effect of electro-polishing on the tip shape three tips were etched with inter-electrode distances of 45, 25 and 10 mm, with the intention of highlighting inter-electrode interactions and the dependence on distance.

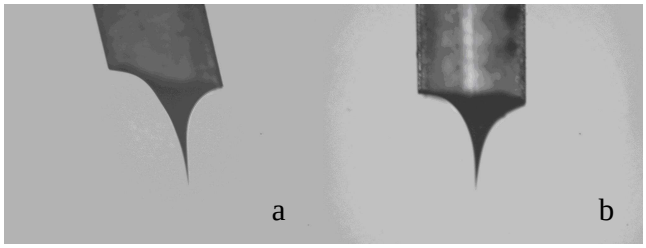

Figure 5.12: Asymmetric STM tips a) angle to surface normal, b) perpendicular. Both at nominal 25 mm inter-electrode separation.

For the former case of immersion angle, the results are given in **Figure 5.12**. Notably the two tips follow a similar shape, with the side closest to the cathode etching more quickly. However the off-surface-normal tip clearly accentuates the asymmetry present in the other tip.

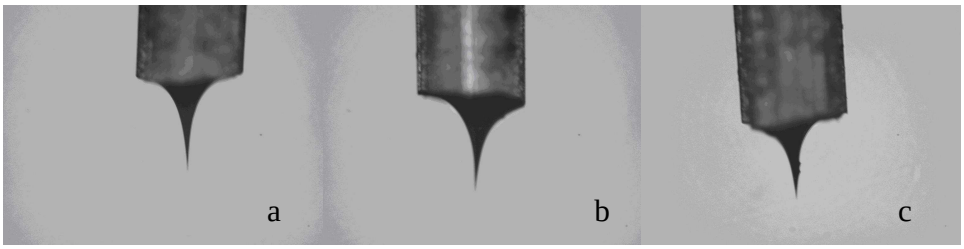

Figure 5.13: Asymmetric tips with inter-electrode separation:
a) 10 mm, b) 25 mm and c) 45 mm

For the latter case of inter-electrode separation, the results are given in **Figure 5.13**. The tips at 25 and 45 mm show significant asymmetry, whereas the tip at 10 mm exhibits notably less asymmetry, suggesting that the inter-electrode separation has an effect on the end tip shape, as would be expected from an electro-polishing action (c.f. **5.2.2 Etching vs. Polishing**).

Hence it can be assumed that both immersion angle and electrode separation effect the tip symmetry. The effect of the former can be minimised by straightening the wire before etching and the second can be reduced, but it cannot be overcome, whilst operating in the polishing regime, a regime proven to yield the sharpest tips in **5.2.5 Experiment 2: Constant Bias Voltage.**

5.2.7 Experiment 4: Solution Concentration

To investigate the effect of etchant concentration on the tip production procedure, three solutions were used. Namely: 2.5M, 3.75M and 5M NaOH. 1M being 40g / 1L with molecular masses of Na (22.99) + O (15.99) + H (1.01). The solution used in **5.2.4 Experiment 1: Insertion Depth** and **5.2.5 Experiment 2: Constant Bias Voltage** was the intermediate 3.75 M.

To compare the effectiveness of various etchant concentrations, the sensitivities yielding type 1a tips were sought through the 3 - 10 V range. The results are shown in **Figure 5.14**. Intuitively it appears that 3.75 M offers the best solution concentration, allowing the full range of etching potentials to be accessed. Furthermore, the 2.5 M curve

corresponds to the lower end of the 3.75 M curve, where the etching voltage is undesirably low. Naively it can be assumed that lowering the concentration has a similar effect to raising the etching potential, however the range of sensitivities accessed in **Figure 5.10** is not available for the 2.5 M case. Notably most of the tips etched in this range had longer shanks than the 3.75 M ones (**Figure 5.15c**). Similarly the 5 M curve corresponds to the upper end of the 3.75 M curve where the etching potential is undesirably high. A similar argument can be applied to the small range of sensitivities available for manufacturing type 1a tips. Converse to 2.5 M etching, the tips etched in 5 M solution have noticeably shorter shanks than those typically found for 3.75 M etching (**Figure 5.15a).**

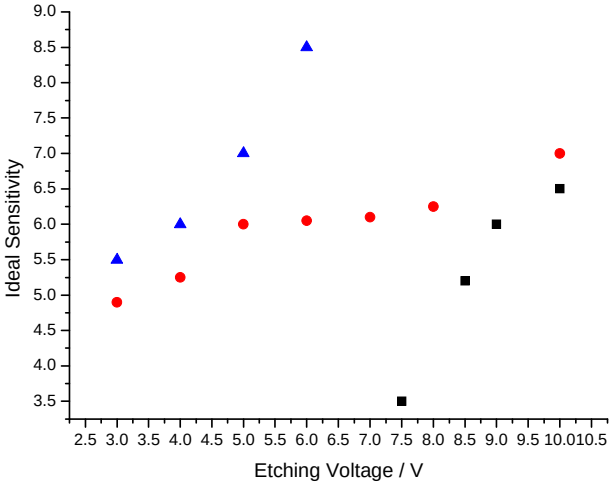

Figure 5.14: Etching voltage vs. sensitivity. Triangles = 5M, Circles = 3.75M and Squares = 2.5M

In order to decisively contrast the three type 1a tips, TEM was once again employed to estimate the ROC shown in **Figure 5.16**. Three tips were prepared all with 1.5 mm immersion: 2.5 M at 10 V, 3.75 M at 6 V and 5.0 M at 6 V. The ROC of the 2.5 M tip is strikingly large, even taking a conservative taper it is still in excess of 100 nm. Thus without optimising the parameters further, this tip is impractical for STM functionality. Two arguments can be made in defence of the 5.0 M solution: Firstly, the tip imaged showed an anomalous shape under lower magnification, implying that a random event may have effected the etching procedure. Secondly without further investigation,

non-optimum values for etching will seldom produce satisfactory tips. Hence this image is not a reflection solely upon the stronger solution but more enforces the requirement for optimisation. The 3.75 M tip shows a good shape, even accounting for the oxide, and the ROC is 20 nm in tune with those of section **5.2.5 Experiment 2: Constant Bias Voltage**. Without an image containing the W core, an actual ROC cannot be given. Finally the 5.0 M tip shows a large amount of amorphous oxide with an ROC of 90 nm, with a 10 nm ROC of the ultimate apex. Once more, the absence of a W core prevents proper analysis.

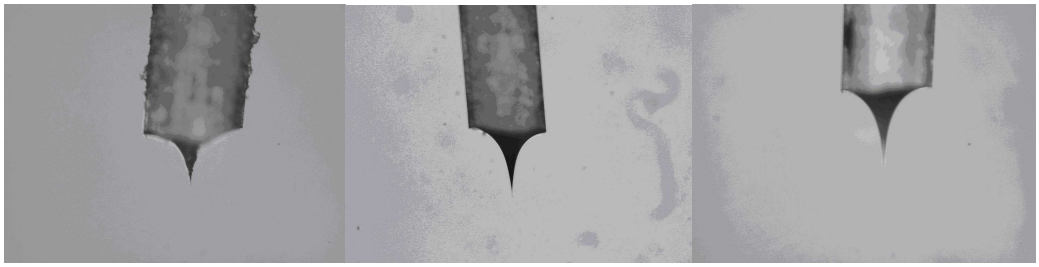

Figure 5.15: Typical tip for a) 5M, b) 3.75M and c) 2.5M

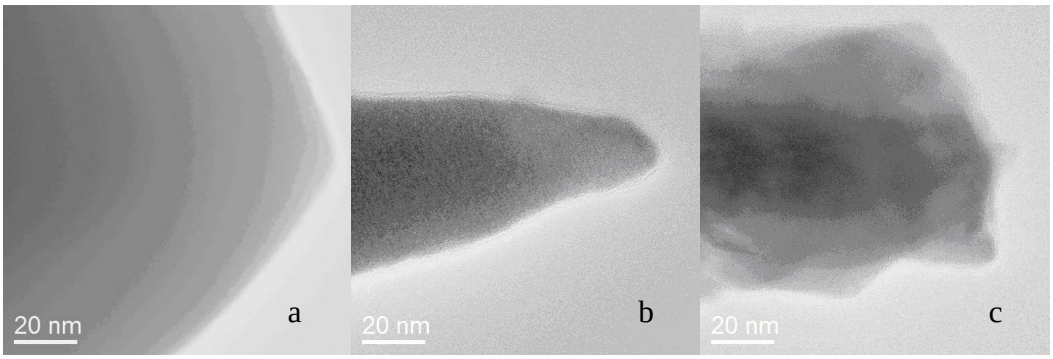

Figure 5.16: TEM tips a) 2.5M, b) 3.75M and c) 5.0M

Post-etch oxide removal is clearly an important next step and will be discussed in **5.3 Post-Etching Procedures**. From a practical perspective, the excessive oxide on 5.0 M tips makes them non-ideal as a result of the extra cleaning required.

5.2.8 Experiment 5: Ramped Bias Voltage

To explore the effects of reducing the etching rate close to drop off it is necessary to reduce either the etching voltage or the concentration of the etchant. Lowering the etching voltage is simpler to implement, with the ability to apply this change constantly throughout the etching processes without disruption to the meniscus.

Three tips were etched for direct comparison. The first two with a standard 10 V and 3 V respectively, whilst the third was etched for ¾ of the typical etching time at 10 V with a subsequent reduction to 3 V for the final duration before drop off.

Interestingly the 10 V type 1a tip and 3 V type 1a tip were generated with sensitivities of 7.0 and 4.9 respectively, whilst the reduced potential tip etched through with a sensitivity of 5.75, a value higher than can be accommodated for the typical 3 V etch.

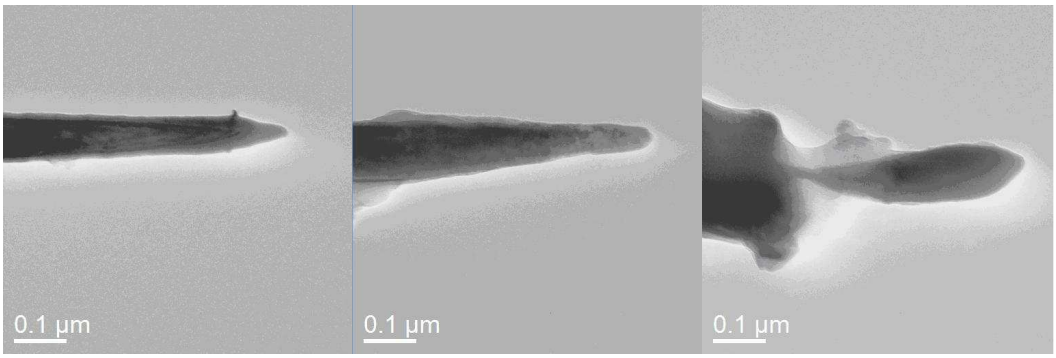

Figure 5.17: TEM tips a) 3.0V, b) drop from 10V to 3.0V c) 10V

The three tips appear virtually indistinguishable at optical magnification, however from the TEM images in **Figure 5.17** this is clearly not the case. The 3 V tip is rather long compared to those from previous sections, however the ROC of the oxide section is 17 nm and the W core around 7 nm, revealing both that the oxide is thinner for these parameters and that the ultimate W tip has a larger ROC than those optimised in **5.2.5 Experiment 2: Constant Bias Voltage**. The second image of the "voltage drop tip" is similar to the first, with a thicker oxide layer. However at larger magnification the ROC

can be estimated to be around 20 nm. Unfortunately the W core is absent and hence the ultimate ROC of the tip is irresolvable. Lastly the 10 V tip reflects a disturbance in the etching procedure, with an ROC of 60 nm. The large ROC is similar to that in **Figure 5.16a**, indicating that a similar effect may have caused the large ROC in that case also. It is assumed mechanical vibrations were present causing a meniscus drop and hence the irregular shape. Notably the necked-in section is approximately 20 nm across, and therefore would yield a ROC similar to that in the previous two cases.

Preliminary analysis indicates that for differential etching as described herein, a voltage drop has no noticeable advantages.

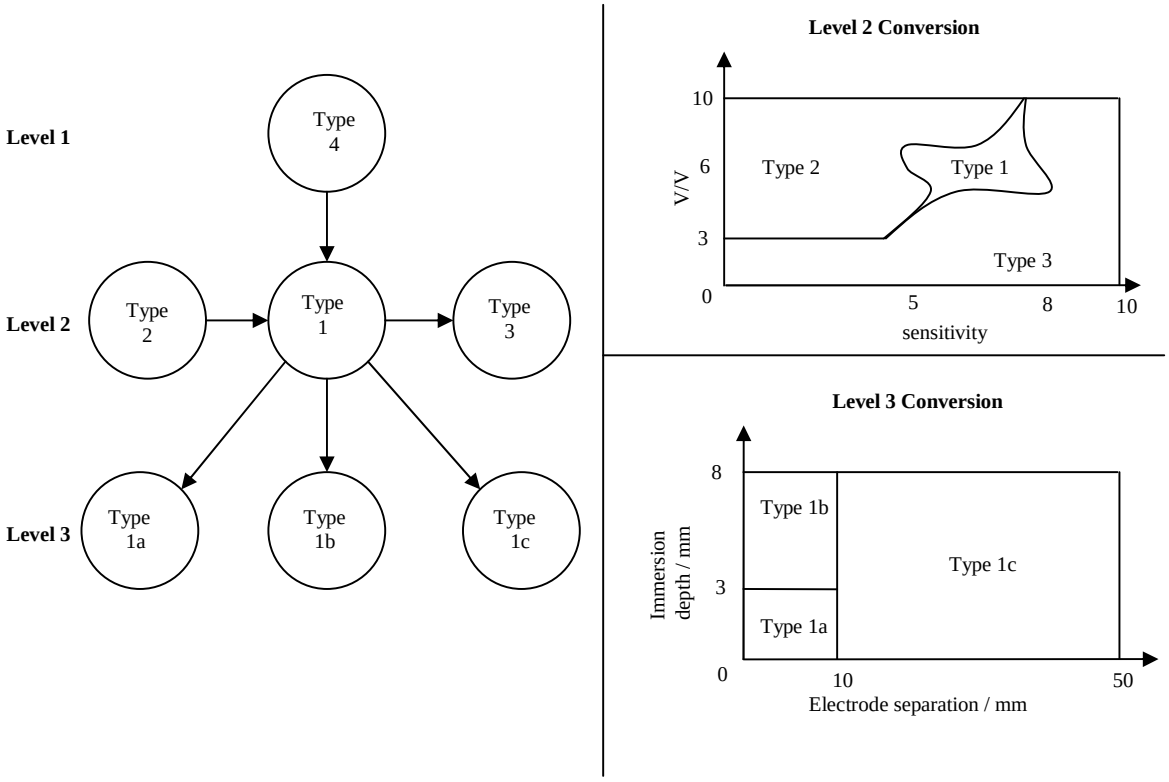

Figure 5.18: Tip type conversion diagram

5.2.9 Tip type conversion diagram

An overall conversion diagram of the results is given in **Figure 5.18**. Expressing the etching parameters as the variable function F(x, y, z) where x = voltage,

y = concentration and z = immersion depth, the shape and sharpness (ROC) are thus optimised for a given variable set F(x, y, z) operating at the type 1 → 2 transition point, a point set by the additional variables: a = immersion angle, b = electrode separation and c = systemic instabilities.

5.3 Post-Etching Procedures

Post-etching procedures concentrate on removing the amorphous oxide layer from the W tip (Mendez et al. 1992). With careful control of the etching parameters it is clear that the tip shape can be optimised, in terms of cone shape, ROC and the amount of oxide deposited. To ensure tips exhibit negligible oxide coating, two techniques are popularly employed: Ion Milling and Annealing. These will be discussed in the following sections.

5.3.1 FIB Milling

FIB milling can have a dual purpose. The 20 keV ion beam can both remove the oxide and re-shape the tip apex (Zhang et al. 1996). Re-shaping has been successfully utilised to create ultra-sharp probes from iridium and tungsten (Vasile et al. 1991; Hopkins et al. 1995). However the focus of this section is oxide removal from an optimised first step procedure.

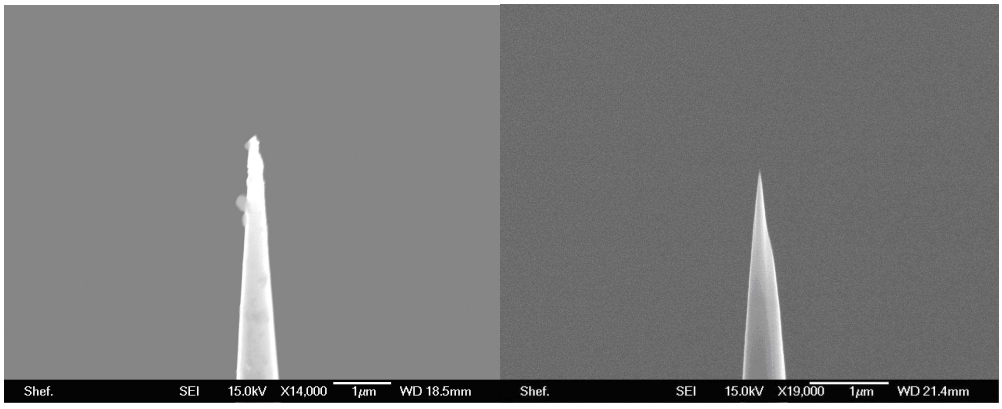

Figure 5.19: SEM of tip a) before and b) after milling

This work utilised a Jeol™ 'Fabrika' based upon a Jeol™ 6500F SEM with an Orsay Physics Ga+ ion column attached. Sample mounting inside the FIB chamber was a simple procedure, however vibrations inherent to the apparatus complicated the milling procedure, leading to the destruction of the first prototype.

Figure 5.19 shows the SEM images of the same tip before and after milling. The initial oxide layer is clearly significant in the first image, whereas, at the second image shows a significant reduction. Higher magnification reveals a ROC of the order of 10 nm, though this cannot be accurately quoted from SEM images with a resolution limit of this order.

FIB etching, whilst effective, is a time consuming process, the tip shown taking some 12 hours to fabricate. Furthermore, the ex situ nature of the FIB system requires fabricated tips to be transported through air between the two systems, ultimately resulting in further oxide contamination of the tip, though with rapid transition this effect is significantly reduced.

5.3.2 In vacuo Anneal

Heating of the tip is performed by the close proximity of a filament within the vacuum system. In this case, the heating procedure involves radiatively heating the tip which is in close proximity to a pair of tungsten filaments. With no high voltage bias, there will be a negligible flow of thermally generated electrons moving from the filament into the tip (Ekvall et al. 1999). The oxide (WO_3 and WO_2) sublimes at 800 °C in stark contrast to pure W at 3410 °C. Principally there should be no alteration to the underlying tip shape whist the oxide should be entirely removed. However, localised electron heating around the apex has reportedly caused necking in, warping and effective "melting" of the tip (Ekvall et al. 1999; Ding et al. 2005).

5.3.2.1 Method

To investigate the heating procedure, a tip heating plate was modified to support heating in a manner similar to that of Ding and Pearson et al. (Ding et al. 2005). The design was customised in the crucial matter of filament position to allow a more uniform heating and

lower currents. Further, the long ceramic spacers simplified the construction procedure. The tip transfer plate design is shown in **Figure 5.20**.

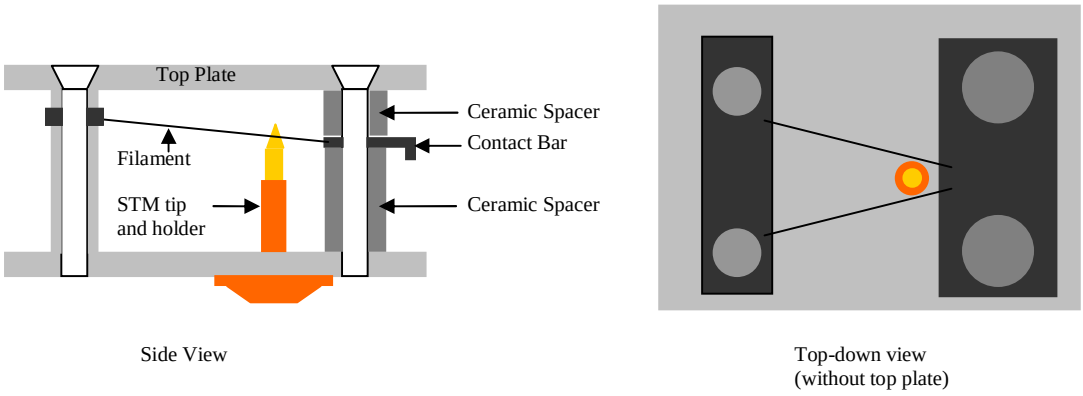

Figure 5.20: Tip Transfer Plate with 'V' shaped heating filament

5.3.2.2 Results 1: Thermocouple

Initially a thermocouple (diameter = 0.125 mm) was attached to the STM tip to record temperature during heating and estimate the desired heating current. The results are shown in Figure 5.21.

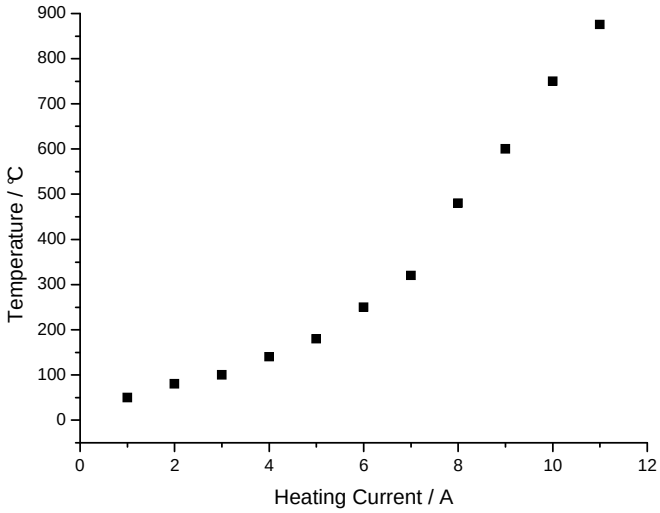

Figure 5.21: Tip Heating Curve as recorded by thermocouple contact

The general curve shows an exponential increase up to 8A heating current, whereto the temperature was allowed to settle for 10 minutes. The final points represent flash heating where the temperature was held for no further than 30 seconds. At a heating current of 10.5 A the thermocouple registered flash heating of 800 °C, suitable for the removal of oxide.

However the absolute temperature does not reveal the localised heating effects on the tip apex due to small electron bombardment and high current densities. The effects of this phenomenon have been shown to significantly reduce the required heating current (Ekvall et al. 1999).

5.3.2.3 Results 2: SEM of Progressive Heating Currents

In order to explore the effects of localised heating on the tips, all tips were manufactured using the optimised parameters in **5.2 Differential Etching**. To ensure that the heating is concentrated on a specific area, all tips were manufactured from a 4 mm length section of wire, which after 1.5 mm immersion leaves a 2.5 mm tip length protruding from the holder.

In order to examine the effect of heating on the tip shape a range of heating currents was applied to 'optically identical' tips before examination by SEM. Initially the tips were covered in a parasitic oxide as shown in **Figure 5.22a**.

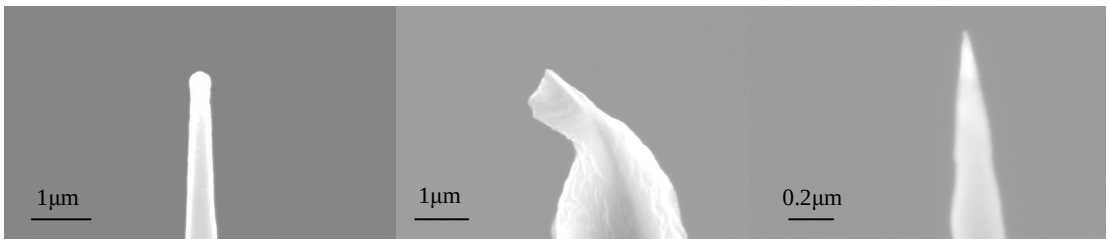

Figure 5.22: SEM images of STM tips a) Post-etch oxide,
b) 10 A for 30 seconds, c) 9.5 A for 30 seconds

Heating with 10 A for 2 cycles of 30 seconds (1 cycle = 10 A for 30 seconds followed by 5 A for 30 seconds) results in warping of the tip apex (**Figure 5.22b**). Notably there is a

bulbous formation and significant bending at lower magnification, thought to occur due to localised melting/strain (Ekvall et al. 1999). Since there is relatively negligible electron bombardment, the localised melting is probably caused by extremely large current densities created by such a microscopic apex. It is note worthy that the oxides appears to have been removed from the apex, so the heater is functioning in that regard. However, lowering the current to 9.5 A and applying the same 2 x 30 second heating cycles results in no bending or warping of the tip shape other than low amplitude sinuous perturbations along the side walls (**Figure 5.22c**). A similar experiment carried out at 9.0 A offered identical results.

5.3.2.4 Results 3: TEM of 9.0A and 9.5A

To investigate the extent of oxide removal, TEM was employed with 2×10^6 magnification. At this magnification the oxide, carbon and tungsten layers are usually resolvable. In continuation from the SEM pictures obtained in **Section 5.3.2.3** the heating current was restricted to less than 10 A to avoid warping of the apex.

Tips were heated to 7.0 A for 2 minutes followed by a 30 seconds flash under the maximum current and allowed to cool within the vacuum chamber. Following cooling in the vacuum system to < 40 °C, the tips were transferred through air into the TEM for analysis. Exposure time was of the order of 15 - 30 minutes, vacuum to vacuum. Whilst it is expected that such exposure will result in oxide re-growth the thickness should be markedly thinner than incurred from the etching procedure.

Figure 5.23a shows a high contrast image of the tip apex after 9.0 A heating. The tungsten core is clear visible within the outer oxide layer. It is worthy of note that there is significant thinning of the oxide 20 nm below the tungsten apex, most pronounced of all on the left side of the image where the localised removal presumably occurs. Furthermore, **Figure 5.23b** shows a tip after 9.5A heating. Note the significantly thinned oxide on the lower part of the image, close to 5 nm thickness.

The localised thinning of the oxide may be caused by asymmetric heating, specifically the difference in filament separation on either side of the tip. **Figure 5.24**

shows a lower magnification image of the same tips, note the significant change in shape along the shanks where local oxide has been removed.

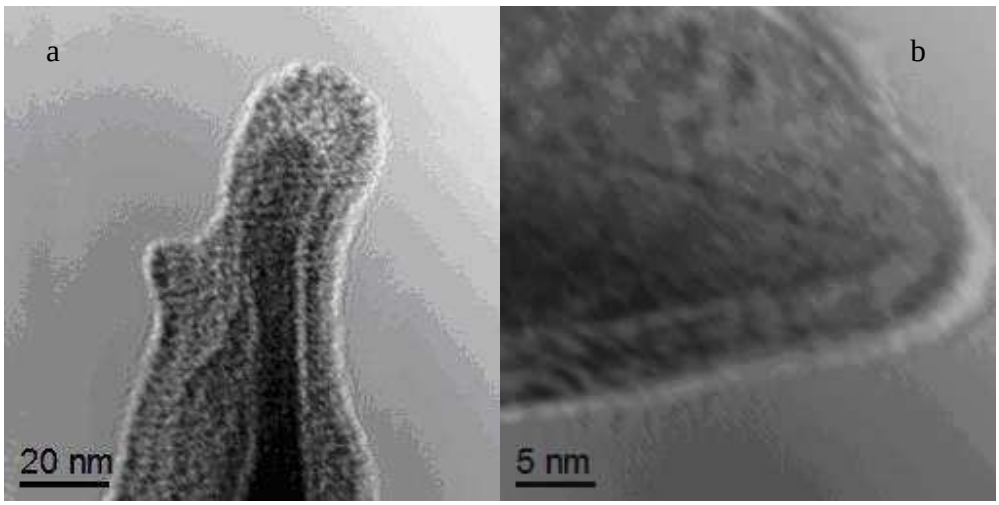

Figure 5.23: TEM images of Tip apex a) 9.0 A heating, b) 9.5 A heating

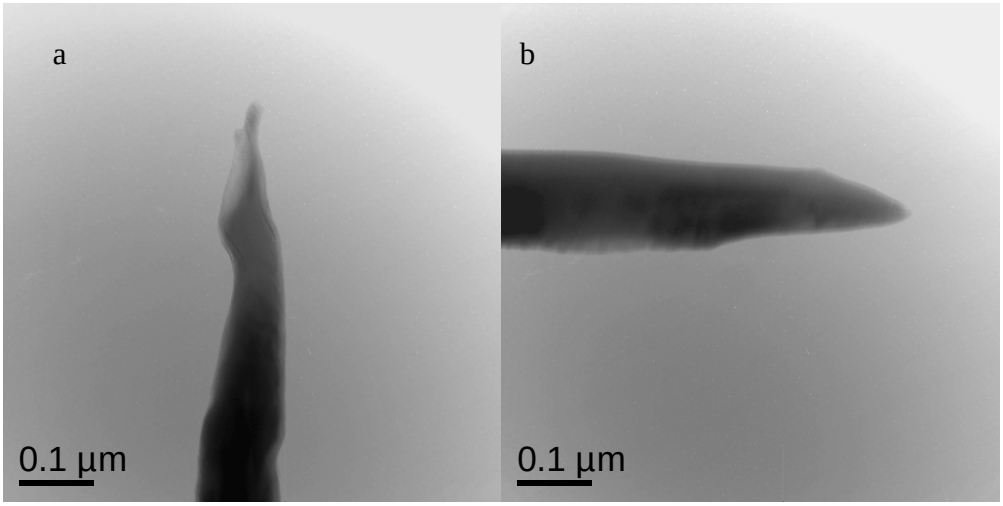

Figure 5.24: Low magnification TEM of Tip Apex a) 9.0A heating, b) 9.5A heating

These results indicate that oxide removal via radiative heating at temperatures below the melting point of the oxide has been achieved. To optimise the cleaning procedure it is

important to find the best tip-filament position set by the tip length and secondly to discover the time duration required for the heating cycle.

5.3.2.5 Results 4: TEM of Tips Made Using Varied Height

The precise tip-filament separation and geometry undoubtedly have an effect on the cleaning performance. In an attempt to identify the optimum geometry, three tips were cleaned with positions inline, beneath and above (as depicted in **Figure 5.25**). This experiment also emphasises the repeatability of the cleaning cycle and the tolerances of the positional variables.

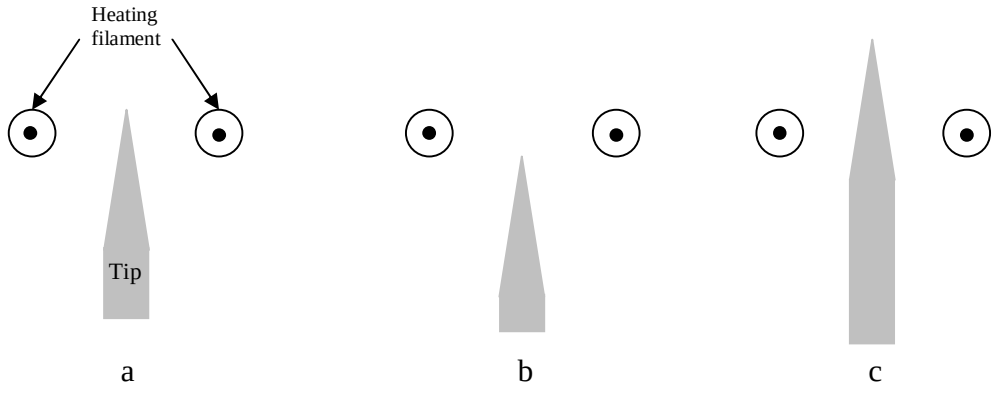

Figure 5.25: Tip-filament Geometries: a) in-line, b) beneath, c) above

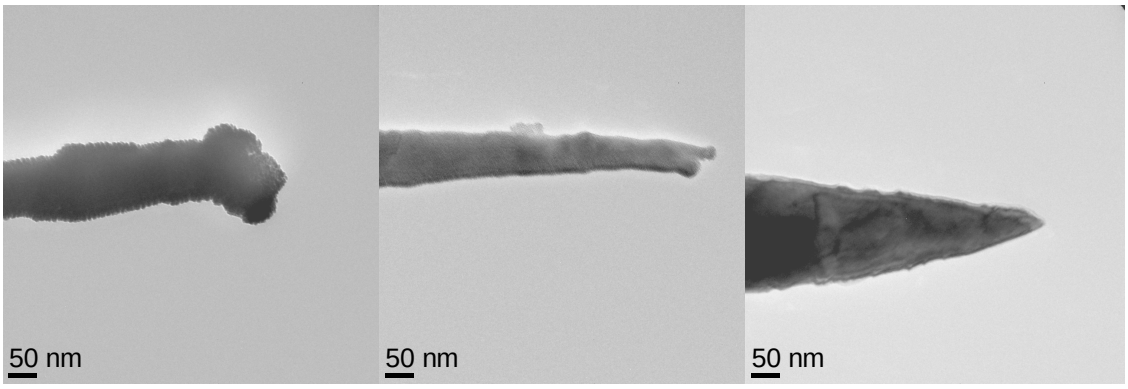

Figure 5.26: TEM images of tips heated with geometry: a) in-line b) beneath c) above

All tips were heated on the established cycle: 5 A for 120 seconds, followed by 7 A for 60 seconds followed by 9.5 A cycles 3 of 10 seconds before the heating current was immediately ramped to zero.

For heating in-line and below the filament, the shortest path to ground is through the apex of the tip, concentrating the heating and cleaning on this small locality. For the case where the apex is above the filaments, the path to ground is into the cone sidewalls. Hence the localised heating into the apex is significantly reduced.

The tip heated "inline" geometry offers the smallest apex-filament separation. Concentration of the electron flux into the apex can cause significant localised melting of the apex (**Figure 5.26a**). Whilst the separation is larger for the "beneath" geometry, the apex focal electron heating is sufficient to cause detrimental melting on a smaller scale (**Figure 5.26b**). However for the "above" geometry the focal point is not the apex hence melting of the tip is less problematic (**Figure 5.26c**).

These results reveal the ease with which a tip can be melted; an inherent problem with annealing (Ekvall et al. 1999). However in the "above" geometry localised melting was avoided. Repeated experiments confirmed the absence of melting in all cases. Furthermore oxide was significantly reduced to < 5 nm for 0.5 μm along the tip cone near the apex.

5.3.2.6 Results 5: Heating Cycle Optimisation

With the most favourable geometry identified in **section 5.3.2.5**, the final step remains to determine the optimum heating pattern. To concentrate solely on the implemented heating cycles, the transfer plate was degassed prior to tip insertion. Hence for subsequent tips, cleaning was achieved by ramping the current from 0 to 9.5A for n-cycles of 10 seconds. Where n = 3, 6, 9.

It should be noted that this is the first instance where the current is ramped from 0 to I_{max}, all other heating cycles have returned to a low value of 5A and ramping was more gradual. This had the two fold effect of, firstly, concentrating on the effects of electron heating rather than the slower ambient effect of the filament. Secondly, the reduced

ambient temperature offered protection for the small tip-lock magnet that can become demagnetised for lengthy exposures and high temperatures.

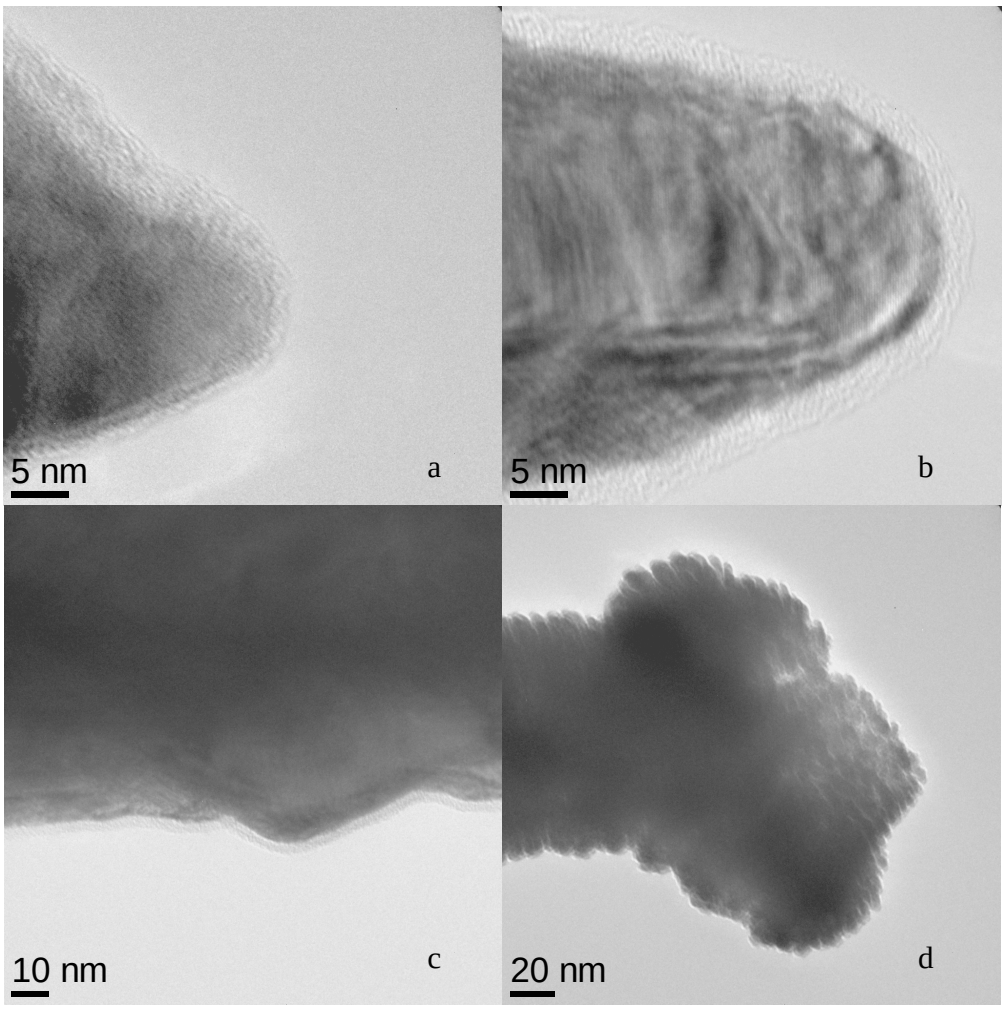

Figure 5.27: TEM images of cleaned STM tips: a) 3 x 10 second, b) 9 x 10 second, c) 9 x 10 second 0.75 μm from apex, d) melted tip for comparison of oxide thickness

TEM images of the tip heated for 3-cycles are shown in **Figure 5.27a**. The tip is ultra-sharp with an ROC of 5 nm and an oxide layer between 1.5 and 4 nm. The overall shape shows no evidence of melting and oxide is < 5 nm for > 1 μm of the tip length. Heating up to 9-cycles continued to show no evidence of melting. Oxide reduction was enhanced at 6-cycles with no noticeable change for increased cleaning. The tip shown in **Figure 5.27b** has a larger ROC of ~10 nm, a result of the etching process. The oxide is

< 2 nm across the whole apex and continues to be < 3 nm at 0.75 μm from the apex (**Figure 5.27c**). Oxide remains approximately < 5 nm until the contrast reduces to an extent where it is too poor to analyse. The large scale oxide removal is due to the tip-filament geometry, in contrast to the more apex focused cleaning usually observed (Ekvall et al. 1999).

All tips have a residual oxide layer, a result of the exposure to air when moving from vacuum to vacuum. Exposure is of the order of 15 minutes. The melted tip shown in **Figure 5.27d** was prepared with "inline" geometry and used to gauge the inter-vacuum oxide growth based on the principle that melting would remove all oxide during cleaning. Oxide thickness of 2 - 5 nm is apparent throughout the melted region. It is likely that the oxide present on the cleaned tips is due to the air exposure.

5.4 STM Imaging Verification

Perhaps the only definitive means of verifying the state of a tip is to utilise it for STM and judge on the results. Classically, atomic resolution of Si(111)-(7 × 7) is used to verify tip sharpness and ultimate performance, principally due to the flat terraces and well ordered pattern exhibited, whereas the more mountainous Au-on-Si tests the dynamic performance of the STM unit and the tip's suitability to varied topography. Both materials are investigated below.

5.4.1 Method

Tip production followed the two step optimisation procedures outlined above for electrochemical etching and *in vacuo* annealing. After cooling within the growth chamber to < 50 °C the tip was transferred to the STM chamber and loaded into the tip holder stage. Scanning was performed for Au-on-Si and Si(111)-(7 × 7) sequentially using the same tip in both cases. No cleaning cycle was used between experiments.

Si(111)-(7 × 7) was prepared by a three step temperature anneal. Firstly the sample plate was annealed to 250 °C by resistive heating (RH) for an hour to degas the plate. Secondly the sample was annealed via direct heating (DH) to 575 °C for 3 hours to degas the sample. Finally the sample was pulsed to 1200 °C in 5 x 1 second pulses in order to freeze the (7 × 7) reconstruction on the surface.

5.4.2 Au-on-Si

The image shown in **Figure 5.28** was captured with a scan speed (v_s) = 342 nm/s, gap voltage (V_g) = -2.0 V, a tunnelling current (I_t) = 0.15 nA and a gain ($g_{\%}$) = 5.13. The image topographically is typical of Au-on-Si with large height variations and structure sizes.

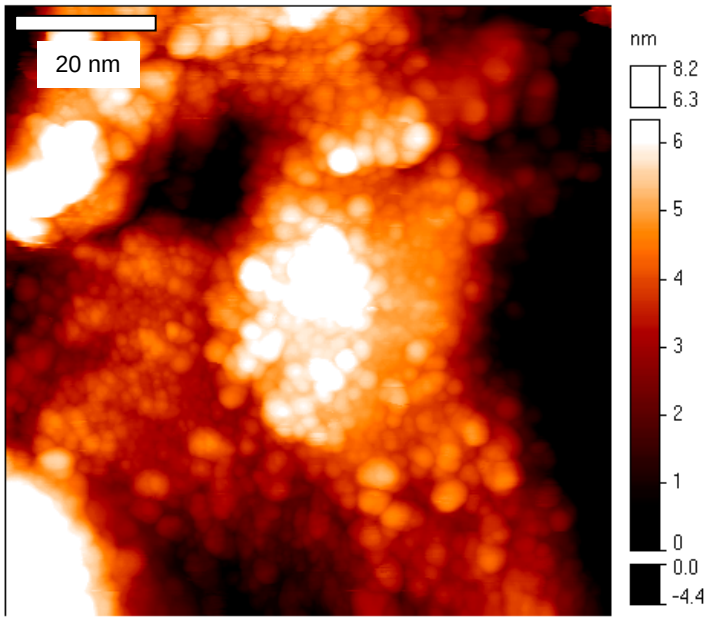

Figure 5.28: STM image of Au on Si

The ability to resolve the structures indicates this tip could be a good candidate for Si(111)-(7 × 7) atomic imaging discussed in the following section.

5.4.3 Si(111)-(7 × 7)

Atomic resolution on Si(111)-(7 × 7) is a step-wise process of area selection under increasing magnification. A typical initial scan area of 800 x 800 nm^2 is used to identify a flat terrace with few defects. At around 100 x 100 nm^2 the resolution of the STM is such that atomic (7 × 7) reconstructions can be seen (**Figure 5.29a**). The image parameters of this figure are: v_s = 396 nm/s, V_g = 1.74 V, I_t = 0.26 nA and $g_{\%}$ = 2.89. The drift of the STM is negligible at room temperature. The brighter deposits on the surface may be the

result of nickel contamination (Ukraintsev et al. 1997), possibly due to the high temperature heating of the stainless steel tip transfer plate (17 % chromium, 5 % nickel) during tip cleaning. Tip transfer plates manufactured from molybdenum would prevent such cross-contamination.

Figure 5.29b is a higher magnification of an area within **Figure 5.29a**. It was obtained with slightly altered scan parameters: v_s = 220 nm/s, V_g = 1.8V, I_t = 0.2 nA and $g_{\%}$ = 2.89. The image displays a small distortion and several missing LDOS that correspond to breaks in the regular pattern. Nickel contamination in the area is negligible.

Thus, atomic resolution has been attained for the 9.5 A tip. A small amount of voltage ramping in the 6 - 10 V range was initially required to stabilise the tip apex, such conditioning is typical for STM operation. The tip performed adequately during the next 6 hours for imaging before a further short burst spectroscopy was required to returned the earlier seen functionality.

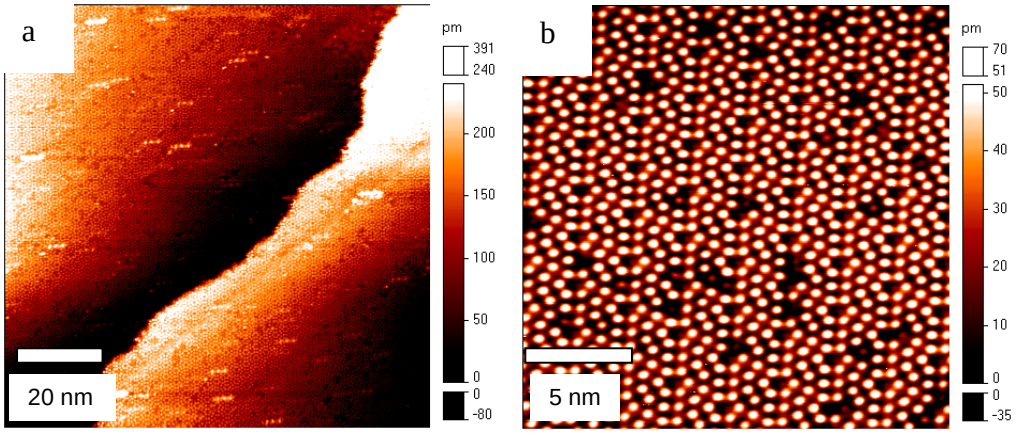

Figure 5.29: STM images of Si(111)-(7 × 7): a) Monolayer step, b) (7 × 7) reconstruction

5.5 Summary

Symmetrical, atomically sharp STM tip manufacture is a two step procedure involving electrochemical etching and parasitic oxide removal. In differential etching four primary parameters and three secondary parameters require consideration. Namely:

- Concentration of solution
- Differential Sensitivity
- Etching Voltage
- Immersion Depth

- Electrode separation
- Environmental Shielding
- Damping

The concentration of the solution in this work was optimised to 3.75 M (18 g per 120 ml of deionised water with a ± 0.5 g tolerance). Repetition indicates that the tolerance is not sufficient to yield identical results *ad infinitum* and hence that the concentration has a significant effect on the remaining parameters.

The sharpest tips were observed for an immersion depth of 1.5 mm and a moderate etching voltage of 6 V. At this voltage the differential sensitivity could be tuned over a wide range and the cut-off sensitivity optimised.

In addition to these primary parameters, three secondary parameters were identified to have a similarly significant effect on the tip shape. Electrode separation effected the asymmetry of the tip, due to etching within the electro-polishing regime. Hence a small electrode separation is essential for symmetric tips. Further environmental shielding is essential both in the case of anode shielding from the gases produced at the cathode and protection of the surface from air-conditioning or extraction system. Finally the system must be mechanically protected against vibrations to ensure meniscus integrity for the duration of the etch.

Once the etching procedure has been optimised and tips with < 10 nm ROC are routinely producible, the oxide layer must be removed to allow STM operation.

In the custom designed tip transfer plate *in vacuo* heater, the tip is brought into close proximity with a 'V' shaped heating filament. Results indicated that localised electron bombardment had a more significant effect on the cleaning procedure than the absolute temperature as measured by thermocouple.

A heating current of 9.5 A was chosen for maximal cleaning without the side effect of shape distortion found at higher currents. TEM analysis revealed a definite

thinning of the oxide at the tip apex and along the cone sidewalls. Tip-filament geometry is crucial to avoid melting, with the imperative that the heating must not be focused upon the apex.

Heating cycles of 3 x 10 seconds were sufficient to remove the oxide layer. Residual oxide of < 2 nm apparent on TEM images is attributed to air exposure when moving the tip from the STM to the TEM for analysis.

Nickel contamination of samples indicated that the high temperature annealing of stainless steel plates is sub-optimal. A side-effect that could be avoided in future by manufacturing a purely molybdenum tip transfer plate.

As a final measure, a *in vacuo* cleaned tip was used in STM analysis of Au-on-Si and Si(111)-(7 × 7). The images revealed good resolution and in the case of (7 × 7) atomic resolution was obtained with minor further spectroscopic cleaning.

STM tip fabrication has henceforth been extensively investigated and tips resolving atomic structure created routinely. Using the optimised parameters, tips display stable atomic resolution in 90% of cases following the recipe in this chapter, with an increase to 100% after more rigorous scanning and cleaning on Au-on-Si samples (large voltage and current cleaning) when necessary.

5.6 References

P.J. Bryant, H.S. Kim, Y.C. Zheng and R. Yang (1987) Rev. Sci. Inst. **58**(6): 1115.

Y. Chen, W. Xu and J. Huang (1989) J. Phys. E. **22**(7): 455.

A. Cricenti, E. Paparazzo, M.A. Scarselli, L. Moretto and S. Selci (1994) Rev. Sci. Inst. **65**(5): 1558.

H.F. Ding, J.E. Pearson, D.Q. Li, R.H. Cheng, F.Y. Fradin and S.D. Bader (2005) Rev. Sci. Inst. **76**(12): 123703.

I. Ekvall, E. Wahlstrom, D. Claesson, H. Olin and E. Olsson (1999) Meas. Sci. Tech. **10**(1): 11.

L.A. Hockett and S.E. Creager (1993) Rev. Sci. Inst. **64**(1): 263.

L.C. Hopkins, J.E. Griffith, L.R. Harriott and M.J. Vasile (1995) J. Vac. Sci. Tech. A **13**(2): 335.

J.P. Ibe, P.P. Bey, S.L. Brandow, R.A. Brizzolara, N.A. Burnham, D.P. Dilella, K.P. Lee, C.R.K. Marrian and R.J. Colton (1990) J. Vac. Sci. Tech. A **8**(4): 3570.

S. Kerfriden, A.H. Nahle, S.A. Campbell, F.C. Walsh and J.R. Smith (1998) Electrochimica Acta **43**(12-13): 1939.

M. Klein and G. Schwitzgebel (1997) Rev. Sci. Inst. **68**(8): 3099.

J.A. Kubby and J.J. Boland (1996) Surf. Sci. Rep. **26**(3-6): 61.

H. Lemke, T. Goddenhenrich, H.P. Bochem, U. Hartmann and C. Heiden (1990) Rev. Sci. Inst. **61**(10): 2538.

A.J. Melmed (1991) J. Vac. Sci. Tech. A **9**(2): 601.

J. Mendez, M. Luna and A.M. Baro (1992) Surf. Sci. **266**(1-3): 294.

Y. Nakamura, Y. Mera and K. Maeda (1999) Rev. Sci. Inst. **70**(8): 3373.

A.I. Oliva, A. Romero, J.L. Pena, E. Anguiano and M. Aguilar (1996) Rev. Sci. Inst. **67**(5): 1917.

U.J. Quaade and L. Oddershede (2002) Euro-Phys. Lett. **57**(4): 611.

V.A. Ukraintsev, Z. Dohnálek and J.T. Yates (1997) Surf. Sci. **388**(1-3): 132.

M.J. Vasile, D.A. Grigg, J.E. Griffith, E.A. Fitzgerald and P.E. Russell (1991) Rev. Sci. Inst. **62**(9): 2167.

R. Zhang and D.G. Ivey (1996) J. Vac. Sci. Tech. A **14**(1): 1.

Chapter 6: Sample Preparation for STM

This chapter discusses the techniques required for preparing a sample for high quality STM observations. **Chapter 4** concluded that Direct Heating (DH) sample preparation would be problematic when preparing GaAs samples for STM. This chapter briefly compares this technique with the alternative Pyrolytic Boron Nitride Resistive Heating (PBNRH) method. The sample preparation stages of cleaving, cleaning, growing and quenching are each discussed.

6.1 Ex-situ Sample Preparation

Most modern MBE machines accept full wafers which are heated via mounting free irradiation. In such cases sample storage and preparation is trivial, however when utilising 0.6 % of a 50 mm diameter wafer per sample for DH mounting or 0.9 % for PBNRH mounting the processes of sample preparation and storage become important.

6.1.1 Sample Cleaving

GaAs(001) samples as received from the manufacturer are epi-ready protective oxide coated wafers sealed in N_2 packaging. Each wafer has 2 strong cleavage planes along the [110] and $[\bar{1}10]$directions. Sample cleaving can easily be performed either:

1. by hand
2. by mechanical scriber

For hand cleaved samples, the main factor is reproducibility. Diamond scribing a short notch in the upper sample surface and then pressing the reverse provides an idyllic straight edge, however estimating sample size by hand leads to low precision. PBNRH is rather insensitive to 0.1 millimetre scale area errors, however DH requires more precise sample size control.

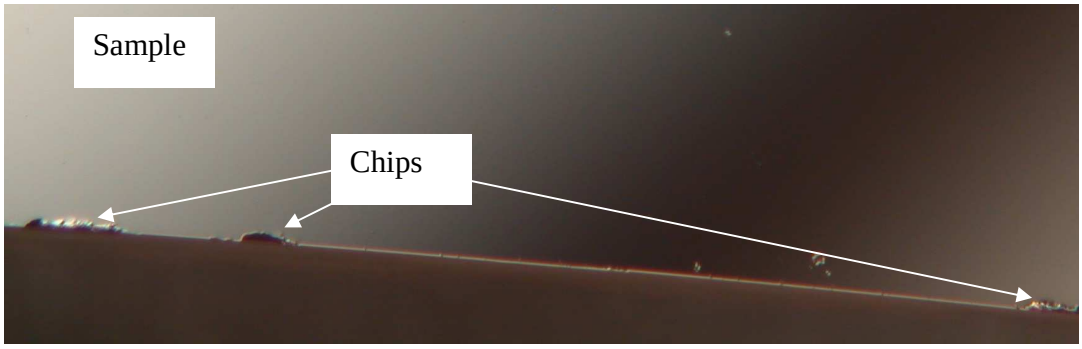

Figure 6.1: Mechanical scriber damage to cleavage plain.

Mechanically scribing the samples utilises a high precision micrometer for 0.05 mm accuracy. The diamond tip can adversely damage the surface (**Figure 6.1**) though this can be avoided by correct tip-sample height adjustment and the creation of a notch rather than drawing the tip across the full length of the wafer surface.

To protect the surface during scribing, the sample can be spin-coated with a layer of photo-resist. This has the advantage that any damage or debris caused by the scribing can be fully removed in an acetone bath before the sample is mounted. The main danger is that small quantities of photo-resist will persist after cleaning, reducing the quality of the growth surface.

Handling the small wafer pieces with tweezers can also cause damage similar to that of **Figure 6.1**. In this case surface debris can be removed via an acetone bath. The resulting surface is clean and debris free.

6.1.2 Sample Storage

A typical cleave will yield 10 PBN samples or 20 DH samples, constituting around 10 % of the wafer area. The samples then require storage prior to use. A simple desiccator can be used for short term storage of around a week duration. However the surface oxide becomes contaminated for lengthier storage times (**Figure 6.2**). Vacuum packaging the samples for storage >1 week is essential to maintain epi-ready substrates.

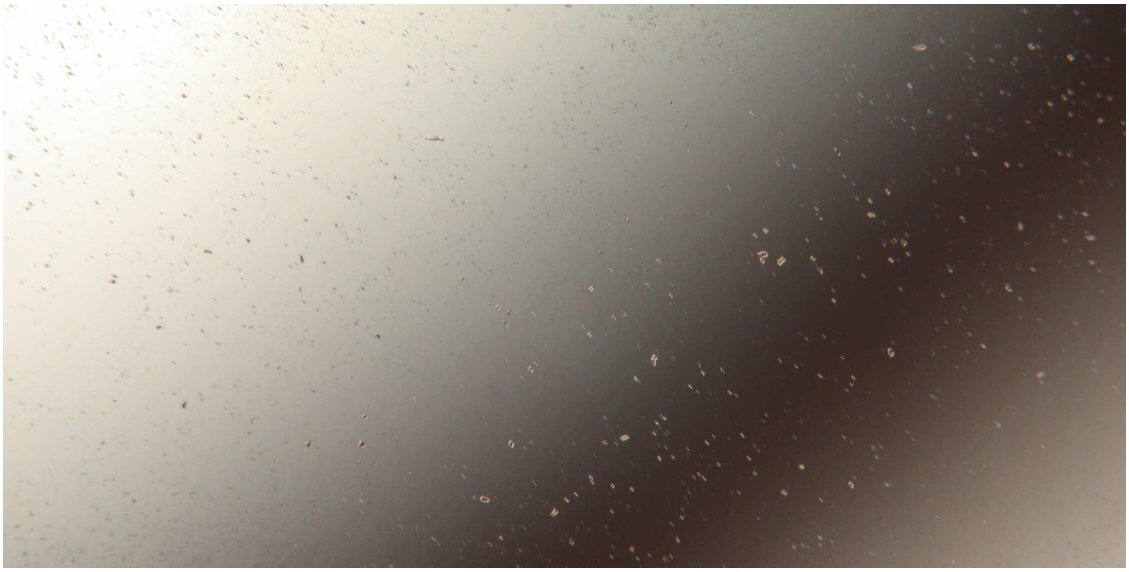

Figure 6.2: Contaminated oxide layer after 1 month desiccator storage.

6.1.3 Sample Mounting

For DH and PBNRH, the sample is mounted on the topside of the ceramic plate to allow RHEED access. DH sample mounting is discussed in **Chapter 4: Direct Heating Temperature Calibrations**.

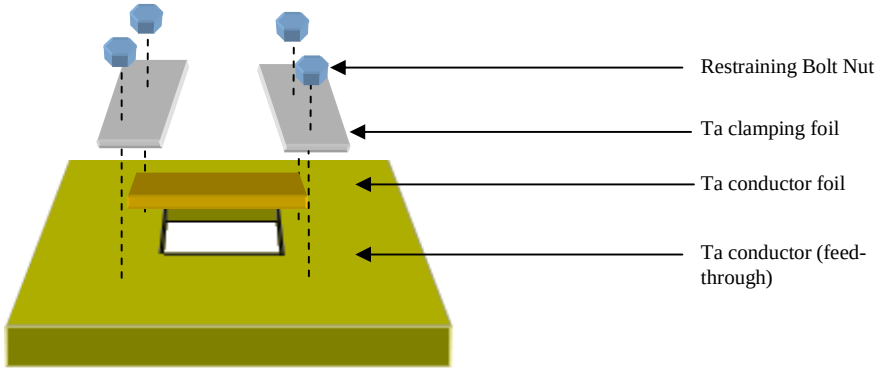

Figure 6.3: PBNRH Sample Mounting.

PBNRH samples are electrically grounded on both sides and hence the sample mounting is simplified (**Figure 6.3**). To prevent pressure damage to the sample the Ta basic clamping foils are 'n' shaped in the z-direction to accommodate the sample dimensions.

Otherwise the Ta-GaAs interaction points can insert damage to the wafer edges which ultimately manifests as debris on the sample surface.

A PBNRH sample accommodates much greater range of access to RHEED observations. Unlike DH mounting, PBNRH allows access to both [110] and $[\bar{1}10]$ azimuths by appropriate sample orientation.

The problems with this basic mounting methodology are two-fold. The first relates to the sample dimensions. The square shaped hole in the ceramic top plate is 5.5 x 5.5 mm^2, hence the maximal uniform heating area from the PBN is of this size. However the sample widths are limited by the spacing of the restraining bolts; which form the corners of a rectangle with 6.0 mm on one axis and 8.25 mm on the other. Hence for a nut of 2.75 mm maximal diameter and the clamping foil with 0.25 mm thickness, the maximum mounting sample width is hence 2.75 mm under standard orientation. This sample is relatively small and is difficult to locate with the RHEED spot, especially on the $[\bar{1}10]$ azimuth which is lengthwise across the sample.

The second problem is that the nuts cannot be completely secured at this theoretical maximum, due to angular displacement of the sample and the physical width of the nut adjustment tool. The various movements of the sample in the system, particularly the STM mounting where the ceramic top plate and not the Ta bottom plate is inserted into the clamp, can loosen the nuts. This hinders the ability to repeatedly move the sample from the MBE chamber to the STM chamber, since the nuts become loose after a single round trip and hence the sample must be ejected from the system. Samples can be covered in an As cap prior to removal to protect the surface, however this is far from ideal. The practical limit of sample width is therefore 2.25 mm.

Alternatively the sample can be mounted at right-angles to **Figure 6.3**, allowing an additional 2.25 mm to the theoretical width. For practical purposes however limiting the sample width to 4.0 mm is sufficient. The visible area has thus increased from 2.25 x 5.0 mm^2 to 4.0 x 4.0 mm^2 or by 42 %. The resulting decrease in sample length from 5.0 mm to 4.0 mm is due to the relative spacing between the threads and the square hole being dissimilar across the two axis.

The actual sample area accessible to RHEED is thus far relatively unchanged. In the [110] azimuth the separation of the restraining nuts is now 2.25 mm narrower,

reducing access along this azimuth. In the $[\bar{1}10]$ azimuth the clamping foils encroach an additional 1.0 mm onto the sample, increasing the difficulty of targeting the sample on this azimuth.

To circumvent this problem a 'c-shape' clamp was created in the xy-direction in addition in the 'n-shape' (**Figure 6.4**), exposing an additional 4.0 mm of the sample when employed as a pair. Note the visible sample is now larger than the heated portion, hence areas of the visible sample will always have oxide coating during growth. The heated sample is now 4.0 x 5.5 mm^2 with a wide area exposed for RHEED access to the $[\bar{1}10]$ azimuth.

Figure 6.4: Improved clamping foils. a: plan view and 'c-shape' section, b: side view and 'n-shape' section.

The 'c-shaped' clamping foils cannot be utilised with the original clamping method shown in **Figure 6.3** since they would encroach on the area of the ceramic required for mounting the sample in the STM chamber.

The final mounting methodology allows simplified RHEED access to both azimuth whilst enabling the restraining nuts to be adjusted to afford better stability. Samples can now be transferred ad infinitum from the MBE to the STM chamber without requiring adjustment.

6.2 PBNRH Sample Heating

Chapter 4: Direct Heating Characterisation presents a comprehensive analysis of DH sample heating. This sub-chapter provides a similar analysis of the more simplified PBNRH sample heating methodology.

6.2.1 PBNRH: Argument

The PBNRH can typically supply up to 30 W of radiant heating to a sample, in a similar means to basic MBE heating techniques. Heating is achieved by passing a current through a pyrolytic graphite (PG) track encased in PBN. Since the temperature of a large percentage of the plate exceeds that of the substrate, it is imperative to thoroughly outgas the plate to give optimum growth conditions. Initial out-gassing often creates carbon deposits on the ceramic and underside of the sample that would be detrimental to a clean, flat surface.

The area of the PBN heater is approximately 600 % that of the sample and held at a distance of 4.0 mm. The design supports uniform sample heating (discussed in **6.2.3 Temperature Map**) but the thermal inertia of the PBN prevents rapid cooling (discussed in **6.2.2 Temperature Dynamics**).

Optical pyrometery cannot be used for PBNRH for the high temperature PBN creates stray light that floods the sample space and masks the temperature of the sample. The thermography camera does not suffer from this problem, since the resolution of the camera is small enough to distinguish between the sample and the PBN and the temperature profile of the sample can be easily accessed by the software tools (**Figure 6.5**). The sample used in this experiment was 9.0 x 3.0 mm^2 and hence there was a sizable gap down either side of the sample through which the PBN could be seen. Hence, for curve two the high peak represents the temperature of the PBN plate, the lower peak represents the reflected heat from the Ta shielding of the plate interiors. Note that the sample temperature data corresponds to the orange curve in each case. Here the temperature drop is 5 °C across the length of the sample and 2 °C across the breadth.

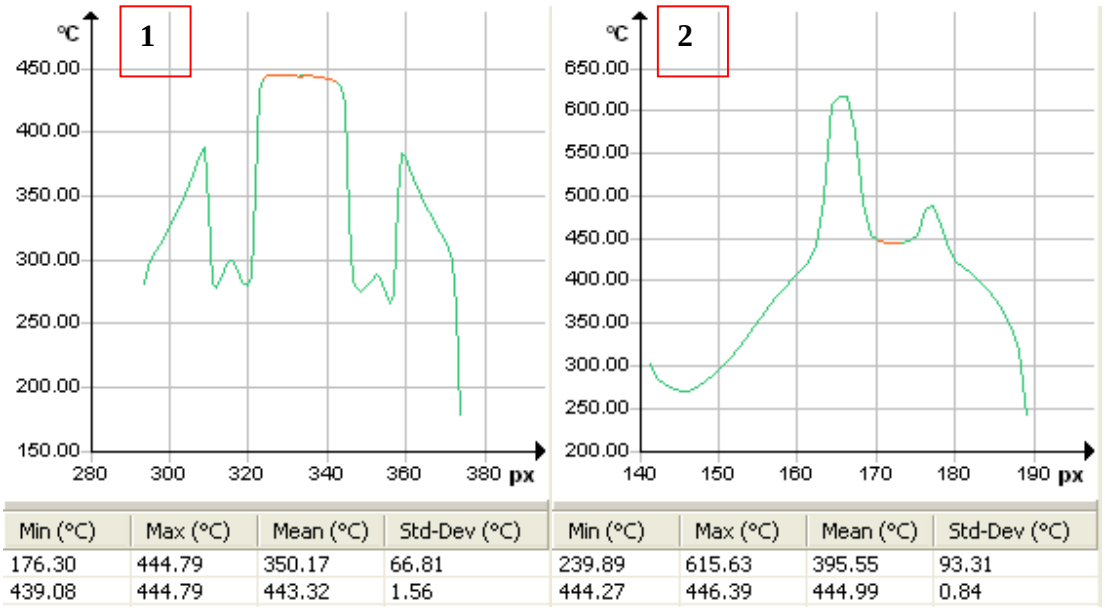

Min (°C)	Max (°C)	Mean (°C)	Std-Dev (°C)
176.30	444.79	350.17	66.81
439.08	444.79	443.32	1.56

Min (°C)	Max (°C)	Mean (°C)	Std-Dev (°C)
239.89	615.63	395.55	93.31
444.27	446.39	444.99	0.84

Figure 6.5: Cedip resolution test.

1: Green: length-wise profile of plate. Orange: Corresponding profile of sample

2: Top-to-bottom profile of plate. Orange: corresponding profile of sample.

6.2.2 Temperature Dynamics

To explore the heating dynamics a sample was heated from room temperature (25 °C) to 420 °C by applying a step change in power equal to 7.5 W (6.2 V at 1.2 A). The temperature increases with an initial drop of 15 °C across the sample which falls to around 8 °C when the temperature begins to stabilise. The temperature profile shown in **Figure 6.6** depicts a sharp increase in temperature over the first 200 seconds followed by a stabilising region that takes a total of 1200 seconds to reach equilibrium. Hence the complete cycle takes approximately 25 minutes at which point the temperature is stable and the drop is 5 °C across the sample.

Heating can be performed more swiftly by overshooting the power requirement and reducing the power when the sample begins to reach the desired temperature. Without the thermography camera to monitor the temperature dynamic during such a cycle, the sample could be easily damaged.

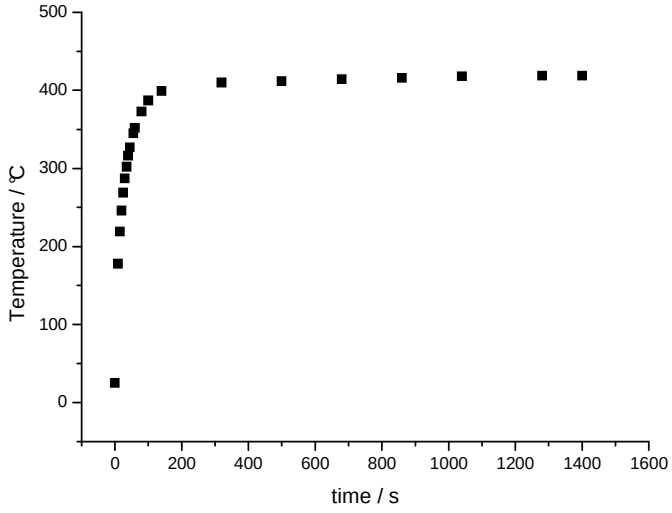

Figure 6.6: PBNRH Heating Cycle up to 420 °C.

Cooling on the other hand is much more sedate. Immediately stepping the heating power to 0 W yields the cooling curve shown in **Figure 6.7**. In the first 60 seconds the temperature falls by 126 °C. After 4 minutes the temperature is down to 124 °C which approaches the lower limit of the Cedip camera in the current range.

Cooling from 580 °C has an obviously swifter initial response (**Figure 6.7**), though the initial drop is only 57 °C in 10 seconds (c.f. 112 °C in 1 second for DH in **Chapter 4: Direct Heating characterisation**). The slower cooling cycle will have ramifications during quenching (**6.4 Quenching**).

6.2.3 Temperature Map

The PBNRH temperature is relatively unaffected by the influence of the As cracker elements or the LN_2 cooling. The sample shows stronger signs of external heating and cooling effects at lower temperatures, but unlike DH the sample temperature is only affected by ± 10 °C for the full possible combination of maximal heating with minimal cooling and maximal cooling with minimal heating. This is highly advantageous for transferring the sample into the STM unit where As evaporation is achieved via e-beam heaters that do not produce excessive heat and no LN_2 cooling is supported.

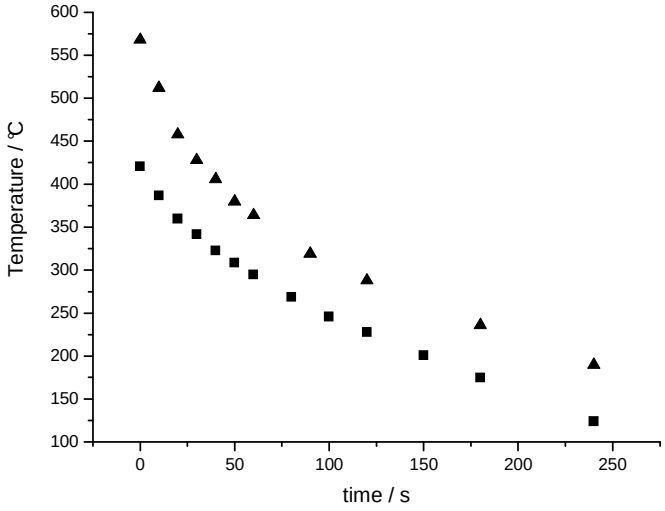

Figure 6.7: PBNRH Cooling.
Square from 420 °C. Triangles from 580 °C.

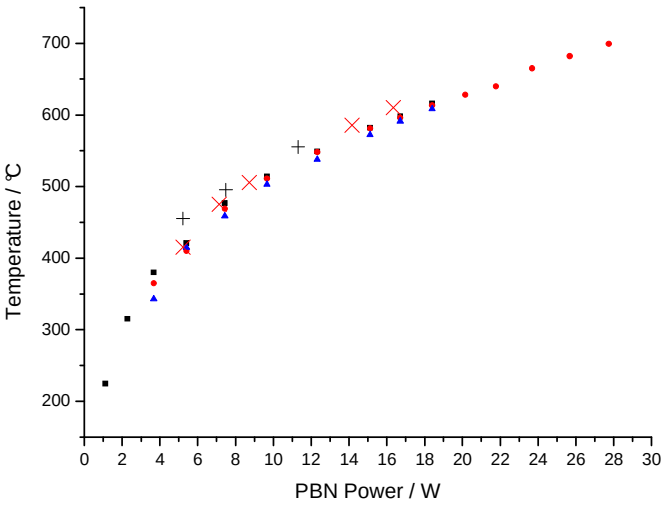

Figure 6.8: PBNRH Temperature map. Red circles: Cracker 930 °C (cooling).
Black squares Cracker 930 °C (no cooling). Blue triangles: Cracker 600 °C (no cooling).
Black crosses mark As rich reconstruction changes and clean up temperatures.
Red crosses mark Ga rich reconstruction change temperatures.

The sample temperature response was principally measured via the Cedip thermography used in **Chapter 4** for DH measurements. The observed temperature map is shown in

Figure 6.8. The maximum temperature variance across the sample was 6 °C during increases in power, though typically the maximum variance was 1 - 3 °C at equilibrium.

RHEED temperature mapping was performed under both static As- and dynamic Ga-rich conditions. With the As BEP set to 2.5×10^{-6} mBar the surface reconstructions were monitored by RHEED. Chiefly the (2 × 4) clean up at 580 °C, the (2 × 4) to (2 × 1) at ~600 °C and the (2 × 4) to c(4 × 4) at ~500 °C since they occupy the range of interest for GaAs growth. These are marked on **Figure 6.8** as red crosses ('×') slightly above the curve.

Further to this, two more (2 × 4) to c(4 × 4) transitions were taken with As BEP of 2.5×10^{-7} mBar and 1.0×10^{-8} mBar. The former corresponds to ~440 °C and the latter the negligible flux transition at ~400 °C. The discrepancy makes the thermography curve some 20 °C lower than the RHEED for a given power. The error could stem from As build up on the viewport during the experiment, though is more likely due to the inherent inaccuracy of RHEED transitions as temperature calibration points.

With the As:Ga ratio around 1:1, growth allowed access to the dynamic Ga-rich reconstructions. These were (4 × 2) to (4 × 6) at 550 °C, (4 × 6) to (3 × 6)/(4 × 3) at 500 °C and (3 × 6)/(4 × 3) to (3 × 1) at 460 °C. The transition points are marked as black crosses ('+') on **Figure 6.8**. Again there is a similar discrepancy in the order of 20 °C.

The curve is highly repeatable from sample to sample with only ±5 °C in temperature when sample width is varied from 2.5 to 4.0 mm.

6.3 Clean-up Techniques (PBNRH)

Classically native oxide is desorbed under an As-flux at 580 °C. The uncovered surface is substantially damaged, resulting in micro-pits that must be overgrown with a substantial buffer layer before they give the appearance of a flat surface with a degree of mounding (**2.3.6 Large Scale Mound Formation**). This section compares the traditional As oxide desorption with the newly discovered Ga oxide desorption, heralded to significantly reduce micro-pits and hence suppress mounding.

The STM images in this and the following sections are quantitatively compared via the RMS roughness of the frame:

$$RMS = \sum_{n} \sqrt{z_n - \bar{z}} \qquad \textbf{Equation 6.1}$$

Where z_n is the number value of the nth pixel and $\bar{z}$ is the average value. Images are 400 x 400 pixels giving an average over 1.6 x 10^5 values.

6.3.1 Arsenic overpressure oxide desorption at 580 ℃

The protective oxide sublimes from GaAs wafers at ~580 °C under an As flux. After initial sample out-gassing at 400 °C for 1 hour the sample temperature is raised to 450 °C in the absence of an As flux. At this point an As overpressure is supplied. From 450 °C to 550 °C the amorphous "haze" on the RHEED pattern, customarily attributed to the oxide, begins to weaken. The thinning of the oxide coincides with the emergence of kikuchi lines (Kikuchi 1928) which will underpin the diffraction pattern after "clean up". In the final stage between 550 °C and 580 °C the diffraction spots appear in the form of broken streaks. After ten minutes at the clean up temperature the higher order diffraction streaks are dimly represented on the [110] and [$\bar{1}$10] azimuths. Heating beyond 580 °C introduces more roughness to the sample observed as chevrons in the RHEED pattern along the [$\bar{1}$10] azimuth.

The clearest is the 2× pattern on the [110], though the pattern is slightly wavy which is characteristic of a degree of surface roughness. On the [$\bar{1}$10] azimuth the 1st and 4th order streaks can be seen dimly when the sample is rotated slightly off [$\bar{1}$10]. This could be attributed to a weak 4× reconstruction or possibly faint chevrons which would imply evidence of some surface roughness.

The sample was left to anneal for an hour before being cooled by the method utilised in **6.4.1 Compensation cooled (2 × 4) (PBNRH).** A low resolution 1.5 x 1.5 μm^2 image was then captured (**Figure 6.9)**. Three surface features were identified. The first is the roughened upper surface in speckled white-and-orange. The height profile of the upper surface is 1 – 3 nm constituting ~3 - 10 ML of roughness. High resolution imaging showed no evidence of a stepped surface.

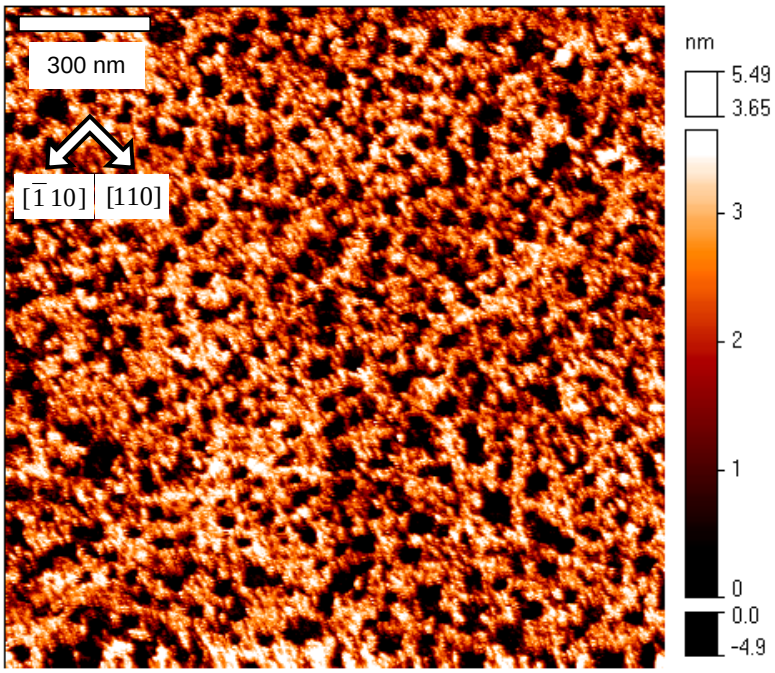

Figure 6.9: µpits formed on GaAs(001) during As-oxide desorption at 580 °C.

The second and third is a nano-pit and a micro-pit (µ-pit) respectively. Micro-pits are large surface roughening features caused when large amounts of $GaAs_{bulk}$ are removed from the surface in order to create volatile oxide from stable Ga_2O_3 (for details of the reaction see **section 6.3.2.6**) These large pits are typically >100nm in diameter and 5 - 20 nm deep. Many of the µ-pits coalesce to form arrays of holes with the upper surface forming ridges between. The smaller pits (term "nano-pits" by the author) vary in size, though typically they have depth profiles between 1 - 3 nm and diameter of 40 - 70 nm. The term precipice is used, for they are actually a small pits (1 - 3 ML) with a steep back edge, where the steps have bunched. This is easier to identify after 2 nm of growth has planarized the surface somewhat. **Figure 6.10** shows a 250 x 250 nm^2 image of the surface, where arrow a points to a shallower nano-pits and arrow b points the first micro-pit in a larger array.

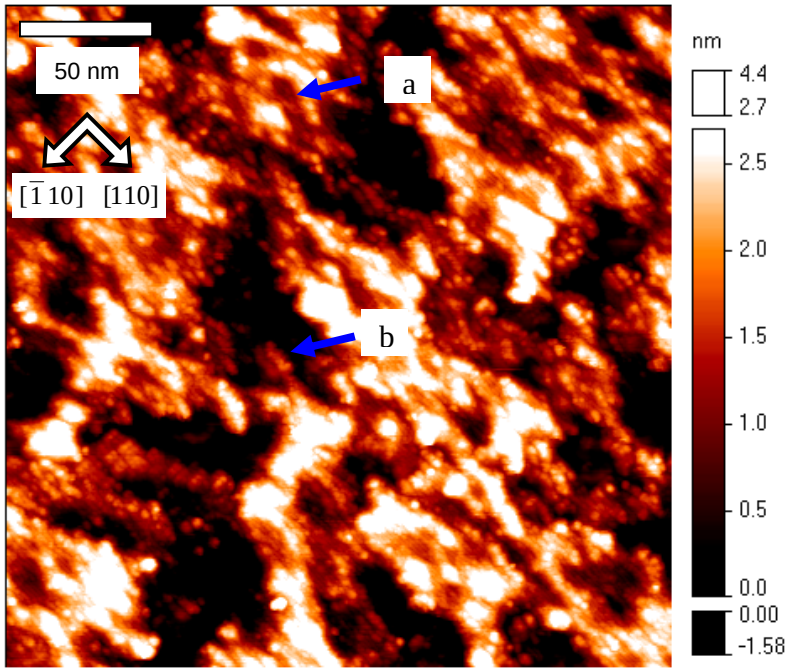

Figure 6.10: Pits on As-oxide desorbed surface.
Arrow a: nano-pit. Arrow b: micro-pit.

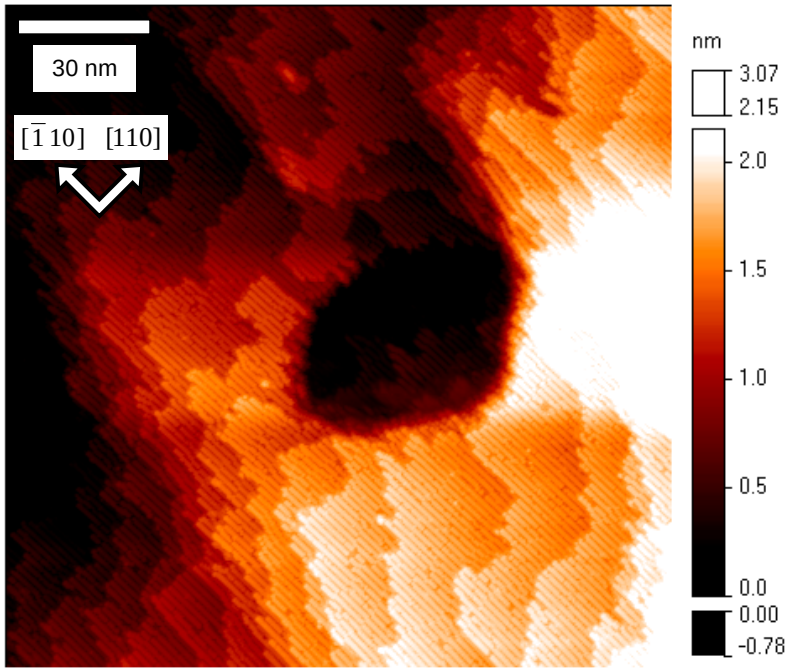

Figure 6.11: μ-pit after 10 nm of growth. Note that good (2 × 4) reconstruction is visible around the perimeter and across the pit floor.

Figure 6.11 shows a μ-pit after 10 nm of growth and a 30 minute anneal at 580 °C. The μ-pit in the image is currently 3.7 nm deep and around 20 nm in diameter. Interestingly, whilst the surface has planarized around the μ-pit the pit itself has not yet healed over. The actual (2 × 4) dimer rows of the surface can be seen within the pit, which may result in stacking defects and dislocations once the pit has healed.

This surface can be considered typical of samples prepared by thermal desorption of oxide under As flux at 580 °C. Hence the surface provides a benchmark for comparison in the following experiment on Ga oxide desorption.

6.3.2 Gallium enhanced oxide desorption at 400 - 500 ℃

6.3.2.1 Method

Samples of undoped GaAs wafer with 2° ± 0.05° off cut, were cleaved to the desired dimensions and immediately inserted into the UHV chamber without further *ex situ* preparation. Each sample was heated to 400 °C for one hour to degas volatile constituents before being heated to ~440 °C and held for 30 minutes.

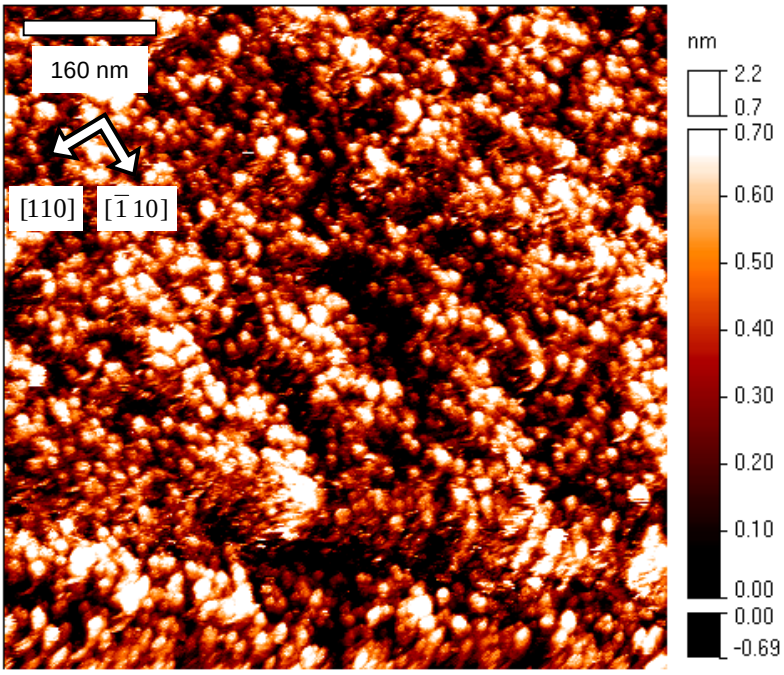

Figure 6.12: Out-gassed GaAs 001 sample.

The sample was exposed to a Ga flux of 8.0 x 10^{-8} mBar calculated to produce a growth rate of 0.05 MLs^{-1}. Each exposure of 10 seconds duration was monitored by RHEED throughout. After each exposure the sample was cooled and transferred to the STM chamber for imaging.

Sample heating and cooling times of 30 minutes were chosen to allow temperature stabilisation in each instance. The As cracker was ramped to room temperature during the experiment and a background pressure of 1.0 x 10^{-10} mBar and a background flux of 2.3 x 10^{-10} mBar was recorded under these conditions.

6.3.2.2 Results 1: Surface Evolution 0 - 8 ML of Ga flux

The initial out-gassed surface shows small areas of reconstruction amidst larger areas of amorphous oxides (**Figure 6.12**). The surface exhibits a nominal 1.75 nm height difference at this resolution. The surface is difficult to image in standard filled state STM imaging, largely due to the Ga-oxides atop the As layers. In contrast to typical GaAs STM, more stable imaging conditions are obtained with empty state imaging, tunnelling directly through the oxide and into the underlying Ga density of states. Furthermore, the presence of small amounts of oxide on the surface can contaminate the tip, resulting in a lower quality image, especially at high resolution.

After exposure to Ga the surface begins to flatten. After 60 seconds of exposure an equivalent to 3 ML of Ga has been deposited, roughly 37 % of the expected oxide coverage. The surface now displays more obvious reconstruction features, with the appearance of donut-like structures aligned along the step edges (**Figure 6.13**). Average height differences of 0.9 nm confirm the smoothing of the surface at this time.

Continued exposure up to 120s results in 6 ML of Ga being deposited and hence 72 % of the expected oxide coverage. The surface now exhibits strong As-rich domains and evidence of the (2 × 4) reconstruction (**Figure 6.14**). Average surface roughness of a line scan is now 0.75 nm and represents the minimum observed.

RHEED patterns obtained after 170s Ga exposure are shown in **Figure 6.15**. The $[\bar{1}10]$ azimuth displays ½ and ¾ order spectral streaks together, implying some degree of

As-rich 4× reconstruction exists on the surface. The [110] azimuth displays ½ order rods with relatively high intensity, indicating the presence of As-dimers.

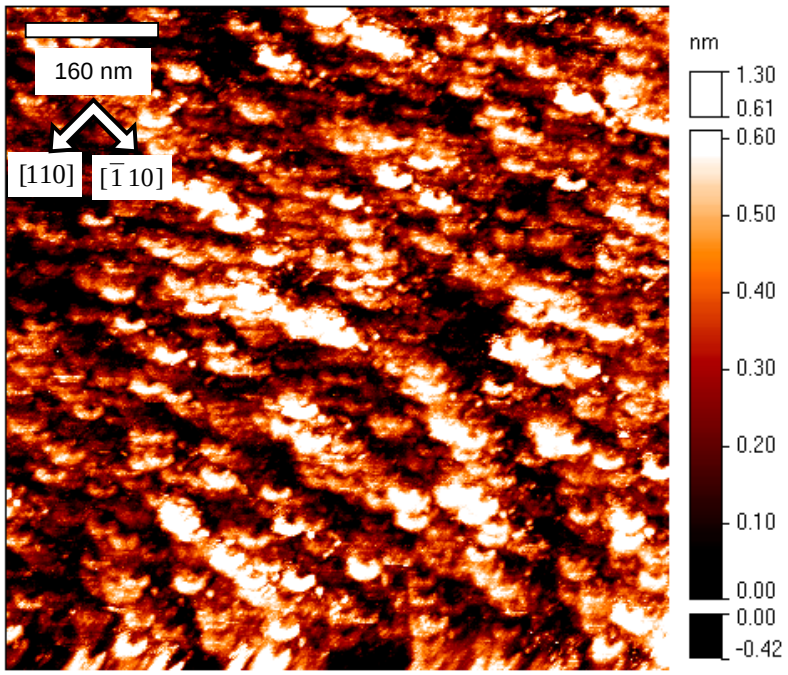

Figure 6.13: GaAs surface after 60s of exposure to Ga flux.

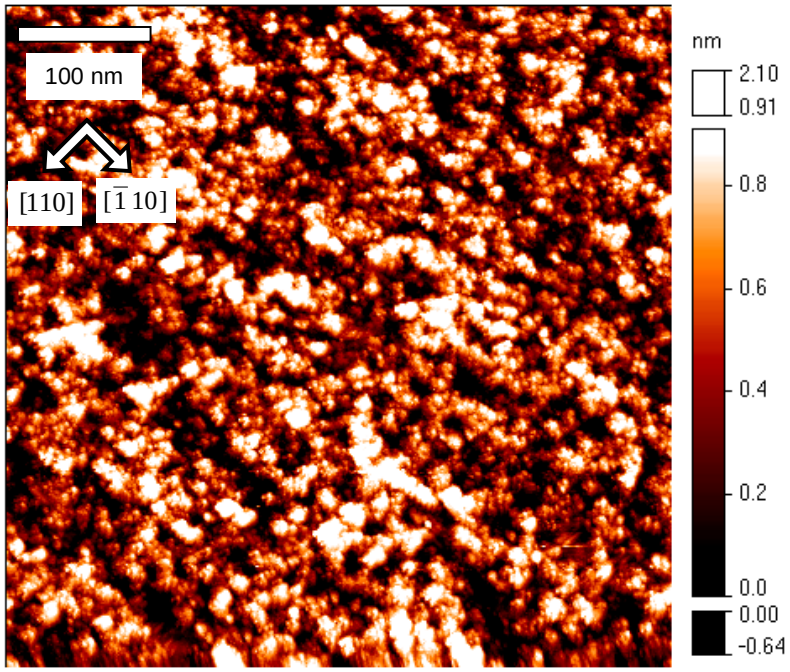

Figure 6.14: GaAs 001 surface after 120s Ga flux.

The sample is left to anneal at this deposition stage for an hour. The RHEED pattern depicted is a As-rich (2 × 4) with faint signs of Ga-rich (3 × 1). STM reveals well ordered As-rich (2 × 4) reconstruction domains (**Figure 6.16**). The surface roughness is now 0.9 to 1.1 nm per line scan correlating to approximately 3 - 4 ML.

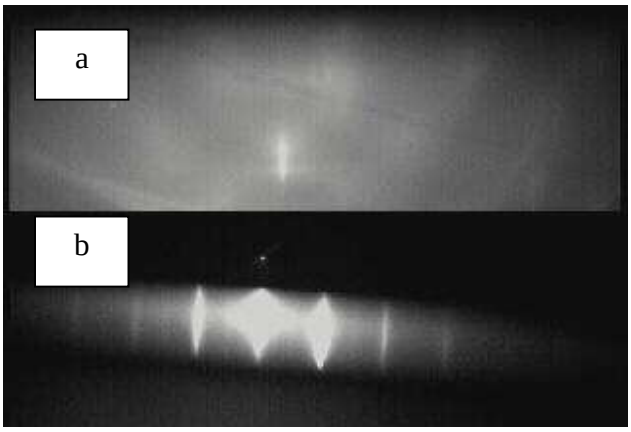

Figure 6.15: RHEED images at 170s deposition. A: $[\bar{1}10]$ **azimuth displaying 4× and B:** $[110]$ **azimuth displaying 2×.**

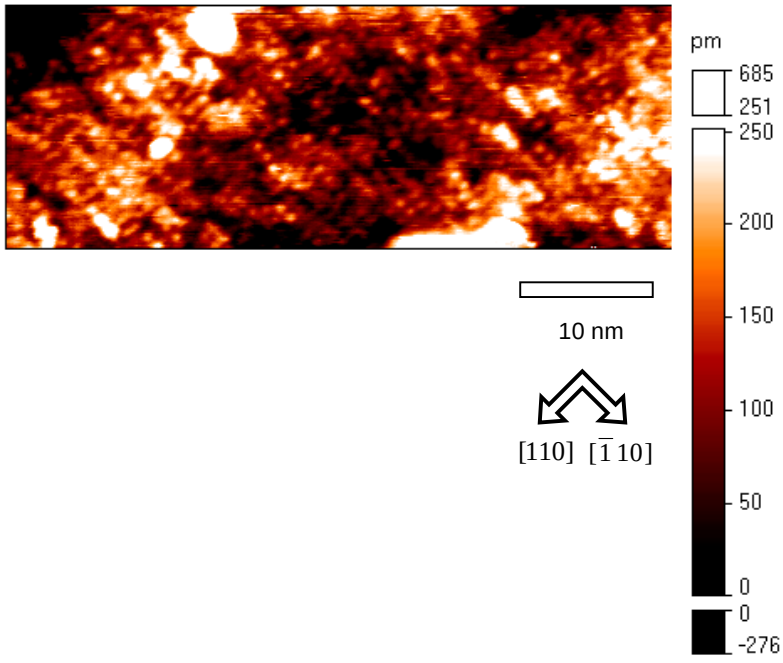

Figure 6.16: GaAs(001)-(2 × 4) reconstruction after 170s Ga flux.

6.3.2.3 Results 2: Clean-up optimisation

The critical deposition amount is therefore 8 ML of Ga for an epi-ready wafer. In order to optimise the oxide removal procedure, a further study was performed varying the sample temperature from 380 °C to 530 °C.

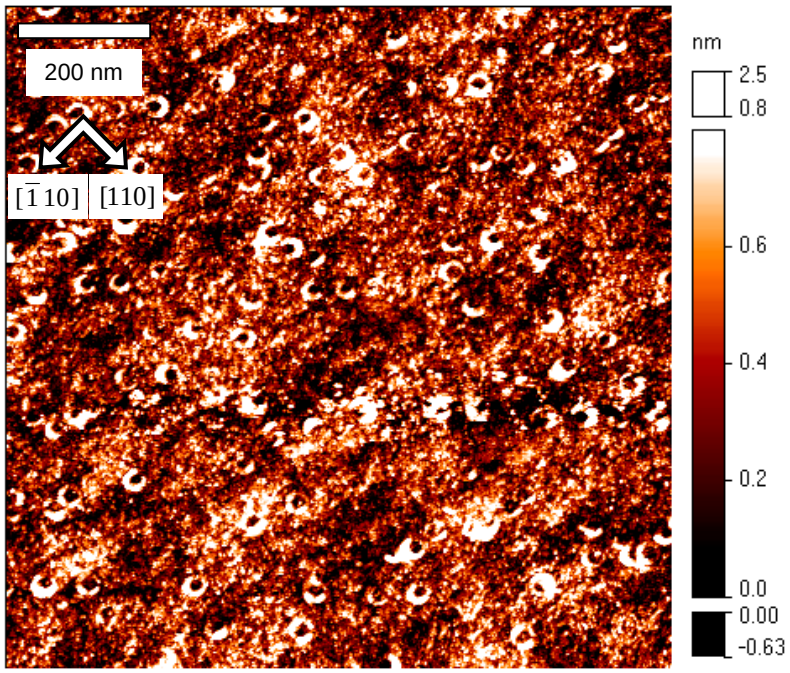

Figure 6.17: Clean-up surface at 460 °C after Ga assisted oxide removal.

For sample temperatures below 400 °C, Ga droplets form on the surface. This indicates that this is below the activation temperature for Ga assisted oxide removal. Hence, the stable Ga_2O_3 does not breakdown into volatile Ga_2O until sufficient thermal energy is supplied.

As the temperature is raised, the thermal activation barrier is broken and Ga assisted oxide desorption commences. In the temperature range between 400 °C and 500 °C the typical clean-up surface is shown in **Figure 6.17**. The surface is covered with 'volcano' nano-pits that typically have a 0.5 nm lip above a 1.0 - 2.0 nm dip. The white lip on the volcano-nano-pit cannot easily be identified by STM, though it is plausible to be either residual metallic Ga or residual Ga-oxide. After over-growing the sample with 10 ML of GaAs at 520 °C the surface healed, and whilst the pits were still evident the lips

had disappeared. This indicates that the lips are Ga deposits that combined with the As flux during the growth cycle.

A sample temperature between 440 °C and 460 °C is frequently reported in the recent AFM studies of Ga assisted oxide removal (Asaoka 2003; Wasilewski et al. 2004; Lee et al. 2006). All parties reported Ga deposits when the sample was over-supplied, however there was a simultaneous dimming of the RHEED pattern in all cases. In the present work the RHEED pattern does not diminish, indeed the As-rich (2 × 4) becomes clearly visible at the point of cleanup. It is clear from this work that a very low deposition rates (≤0.05 ML/s) are necessary to fine tune the Ga supply based on RHEED intensity.

For a sample prepared between 500 °C and 530 °C, the surface cleans up in a subtly different manner. The RHEED pattern evolves to a clear As rich (2 × 4) after 7.5 ML of has been Ga deposited. A further 0.25 ML invokes a shift to Ga rich (3 × 1)/(3 × 6) which then remains stable. A final 0.25 ML invokes a further change to Ga rich (4 × 2)/(4 × 6). The 4× pattern on the [110] azimuth can revert to a 3× pattern after a 15 minute break, indicating that Ga that had contributed to the reconstruction change has diffused into oxide and has been consumed. In such cases a further 0.25 ML can be supplied to the surface without fear of over supply, resulting in 8.25 ML of Ga in total. The resulting (4 × 2)/(4 × 6) pattern remains stable. This procedure is much more tuneable and reliable than the RHEED pattern investigation at lower temperatures.

The resulting surface after 8 to 8.25 ML of Ga is shown in **Figure 6.18**. The sample shows isotropic nano-pits that no longer exhibit the 0.5 nm lip found at lower temperatures. The pits display elongation in the [110] direction, likely a result of Ga diffusion from step edges (Atkinson et al. 2008). Pits have a depth of 0.5 - 1.5 nm and a similar density to that of the lower temperature sample (**Figure 6.17**). This sample is 2° off-cut, with an average step length of 8.6 nm, and hence the pitting distribution may follow the hidden step edge profile of the sample.

High resolution imaging on the sample shown in **Figure 6.18** revealed the presence of the disordered step structure shown in **Figure 6.19**. Aside from the ragged step edges across the sample, there is also evidence of both Ga-rich and As-rich reconstructions. This means that whilst the (4 × 2) remains dominant on the RHEED pattern, the (2 × 4) patches are still present across the surface. The presence of both

step-edges and reconstruction indicates that Ga-assisted oxide removal at 520 °C significantly reduces damage and preserves the flat epi-ready prepared surface.

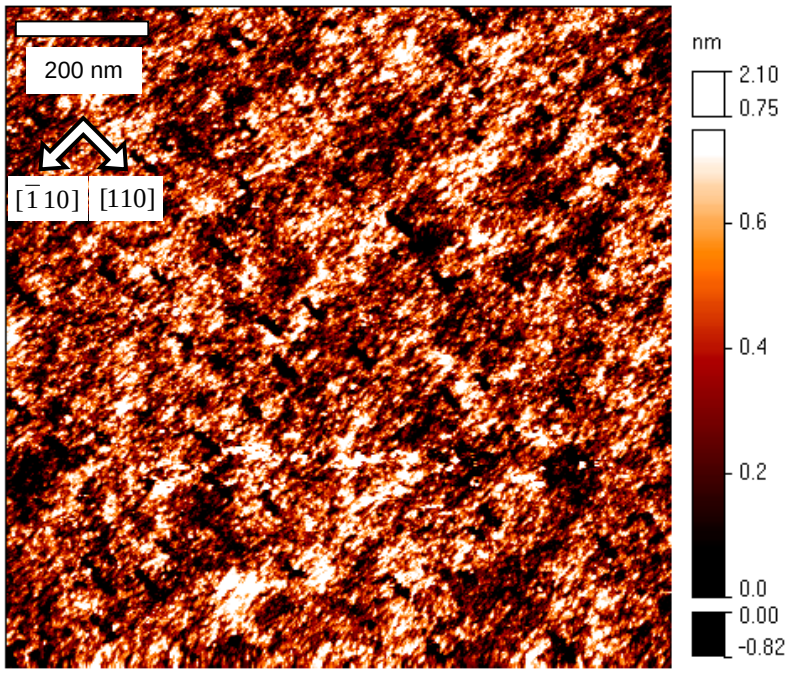

Figure 6.18: Clean-up surface at 520 °C after Ga assisted oxide removal.

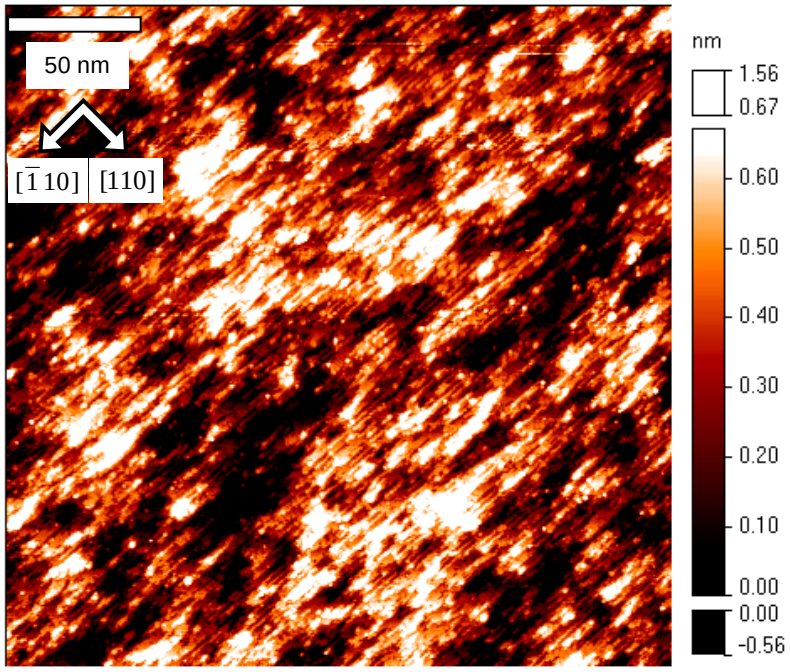

Figure 6.19: High resolution image after clean up at 520 °C under Ga flux.

6.3.2.4 Results 3: Anneal under As Overpressure

To ensure 100 % of the oxide is removed and to compare the sample to conventional cleaning, the sample temperature was raised to 590 °C in the presence of an As flux and held at this temperature for 1 hour before slow quench to room temperature and STM imaging. A low resolution image of the sample is shown in **Figure 6.20**. Immediately it is noticeable that pits have changed shape, primarily they appear rounder or in other cases to be rotated by 90°, this is probably caused by attachment of As-adatoms to the favoured steps 90° from the Ga-favoured steps in the previous stage.

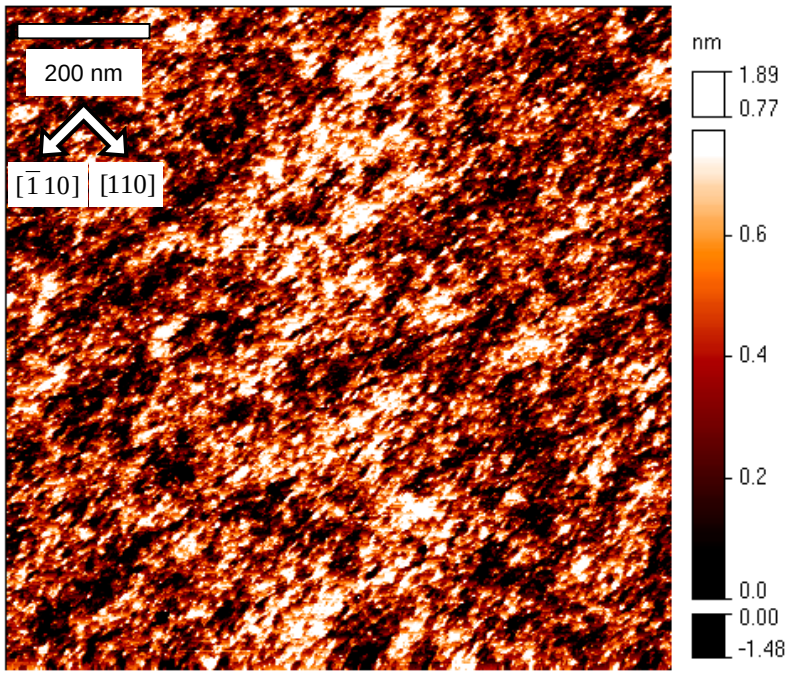

Figure 6.20: Low resolution image of Ga assisted oxide removal sample after high temperature anneal under an As flux.

Aside from the pit shape change, there is a clear planarization of the surface and a reduction in roughness by ~0.25 nm per line scan. The RHEED pattern changed from Ga-rich to a strong As-rich (2 × 4) pattern during the anneal. The reconstruction change can clearly be seen in the high resolution image in **Figure 6.21**. A strong

(2 × 4) reconstruction before buffer layer growth is not achieved in the conventional clean up method, due to the damage induced. Whilst there is now 0.9 - 1.25 nm of roughness across a 1000 x 1000 nm^2 image (0.28 nm RMS roughness) this is far less than damage induced in the conventional method (1.25 nm RMS roughness).

6.3.2.5 Results 4: 10 nm Buffer Layer Over Growth

It is customary to grow a 1 μm thick buffer layer to ensure the surface is suitably flat with well ordered steps and to heal μpits that form during the As oxide anneal (Orme et al. 1994). The surfaces usually exhibit large scale mounding, thought to result from the healing of said μpits.

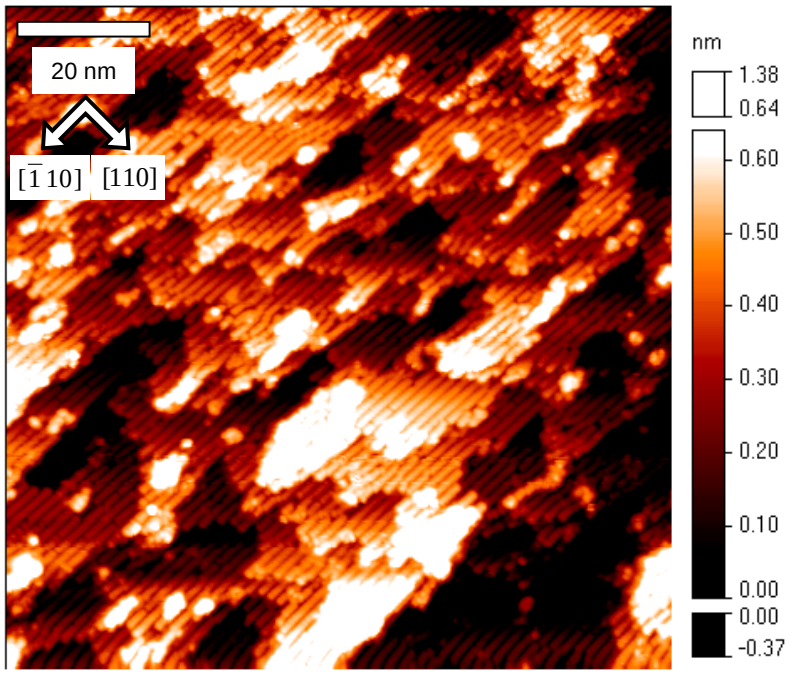

Figure 6.21: High resolution image of Ga-assisted oxide desorbed sample after high temperature anneal under As. Present on the surface are a number of well defined ML steps, small GaAs islands and As-rich (2 × 4) reconstruction dimer rows.

In this case, since the μpits have not formed, such a thick buffer layer should not be necessary and the large scale mounds should not form. Since the STM typically

concentrates on relatively small areas of the sample surface, the ability to image large scale mounds is hindered. However, in continuous images across the sample covering an area of 10 x 10 μm^2 no evidence of a change to the well-ordered step progression was found.

The state of the surface after a 10 nm buffer layer without an ensuing anneal is shown in **Figure 6.22**. The nano-pits have now healed into triangular wedges, that are formed from step bunches. Their typical depth is of the order of 0.56 - 1.12 nm in keeping with a depth of 2 - 4 ML. The step train is now clearly visible and a single step can be followed across the length of the image. On closer investigation of the triangular step-bunches, the well ordered As-dimer rows are clearly visible **Figure 6.23**.

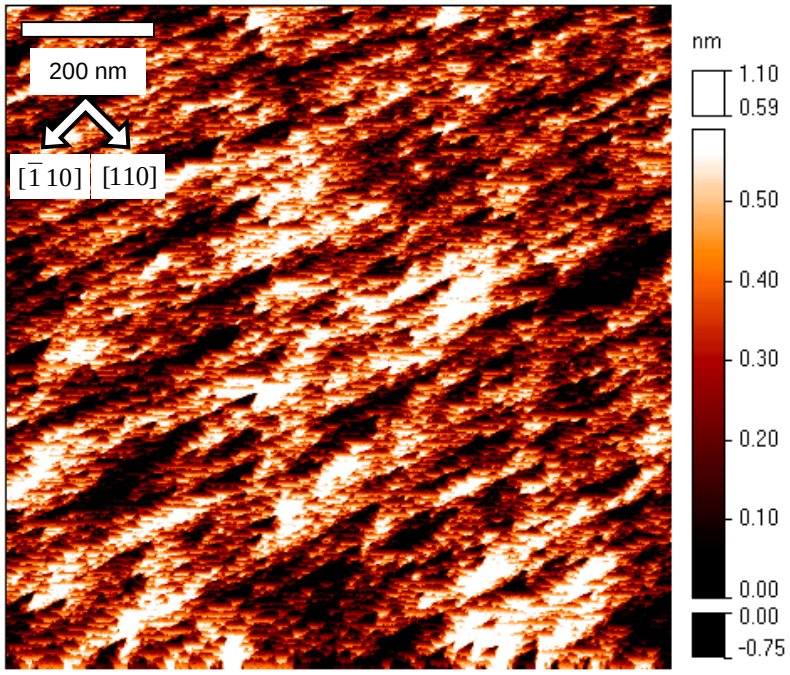

Figure 6.22: Low resolution image of Ga-assisted oxide desorbed sample after a 10 nm buffer layer has been grown. The pits have healed into triangular features where there is a high step density.

After an additional 10 nm buffer layer, the surface is much more planar. The RHEED pattern displayed a strong (2×4) reconstruction throughout. **Figure 6.24** shows the surface immediately after growth and a short anneal. The triangular step-bunches have now largely planarized, resulting in an ordered step train with 8 - 20 nm terraces. The surface has <1 nm of roughness across a 1 x 1 μm^2 image (0.18nm RMS roughness).

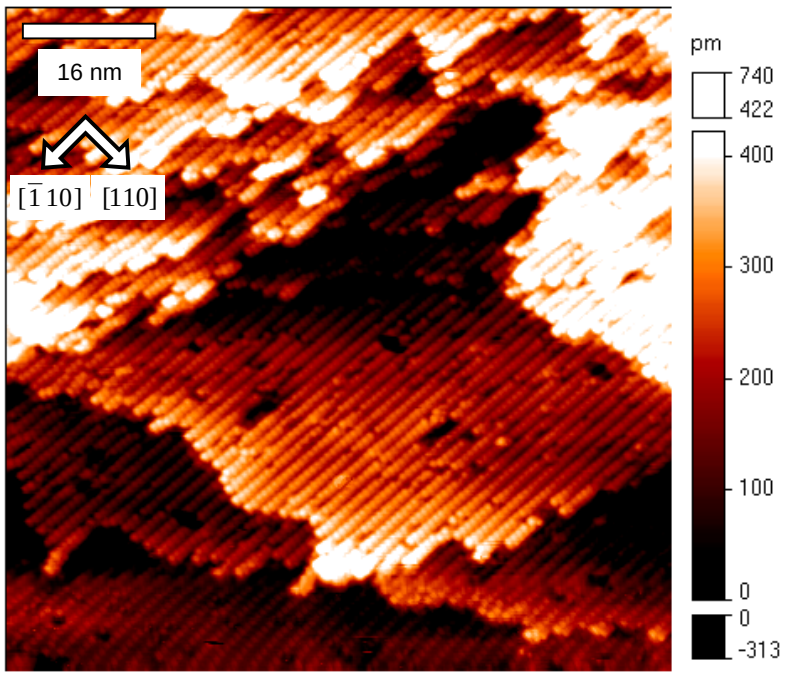

Figure 6.23: High resolution image of Ga-assisted oxide desorbed sample showing the high step density around a healed pit.

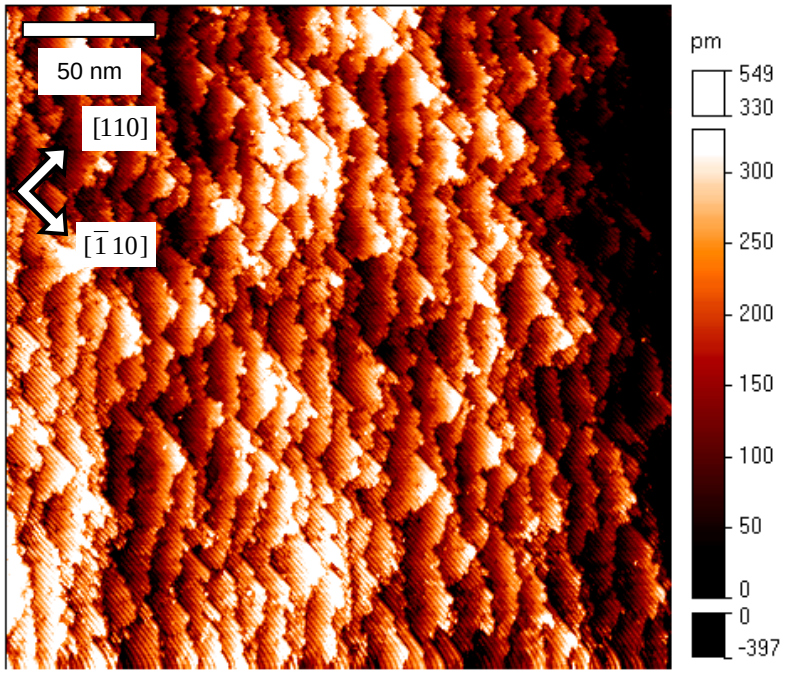

Figure 6.24: Medium resolution image of a 10 nm buffer sample after subsequent "growth interruption" anneal at 590 °C in order to planarize the surface. The surface is now an ideal progression of 10 nm ML terraces as expected from a 2° off cut sample.

6.3.2.6 Discussion

The first image taken after the initial outgas, represents a surface from which the H_2O and As_2O_3 have been removed. Hence the surface is composed mainly of amorphous Ga_2O_3 and exposed areas of GaAs substrate. The exposed areas are liable to be present due to the random thermal desorption of Ga_2O_3 into Ga_2O as described in section **3.1.3: Sample Preparation**. The roughness at this stage is of the order of 1.75 nm or 6 ML per line scan. This clearly indicates that the oxide coverage is inhomogeneous and exists at various thicknesses across the surface.

After exposure to 3 ML of Ga, the surface exhibits donut-like structures, primarily aligned along step edges, these are liable to be the precursor of the volcano-nano-pits seen in **Figure 6.17**, however oxide interference is limiting the resolution. It is postulated that these represent patches of Ga_2O_3 from which the centre region, after forming a transient Ga_2O, has been removed. Close up images reveal reconstruction within the centre hole, implying that the centre exposes the underlying substrate or at least a thinned oxide region. The donuts are all aligned in the same direction, supporting the theory that they are Ga-rich structures.

The total RMS roughness is now approximately half the original value and of the order of 3 ML per line scan. A clear indication that the group III flux has reduced the surface oxide. The presence of Ga-rich domains are either exposed GaAs substrate or Ga-oxide domains aligned to the underlying substrate.

After a total of 6 ML of Ga the surface consists of a greater proportion of GaAs than Ga_2O_3. Assuming the surface has ~8 ML of oxide, this state represents a 75 % oxide reduction. The exposed GaAs has a clear As-rich reconstruction, possibly accounted for by assuming that the Ga-rich surface layer was consumed in the oxide removal process, a fact that would ultimately leave a residual As-presence on the surface.

At this stage the roughness reaches a experimental low of 0.75 nm or 2.5 ML per line scan. The height difference is accounted for in both the residual amorphous patches and the small trenches or pits. These pits can be explained by the random thermal oxide removal that causes the micropits in the As-thermal oxide desorption at 580 °C. Hence it would appear that the pits formed in Ga-oxide desorption at 440 °C are much smaller,

indicating that the external Ga-flux suppresses the requirement for "digging" for Ga in the underlying substrate.

At 8 ML of Ga deposition the surface exhibits a good RHEED pattern indicating an As-rich (2 × 4) presence on the surface. The localised (2 × 4) domains, of which an example is shown in **Figure 6.16**, are separated by relatively large areas of roughness of up to 1.2 nm or ~4 ML. The large roughness makes atomic resolution difficult. The cause of such roughness can be attributed again to the thermal desorption of Ga_2O_3 by "digging" into the substrate. The image represents the state of the surface after an hour long anneal at 440 °C. Assuming the thermal desorption is a random process, for every moment that a Ga-flux is not supplied a patch of Ga_2O_3 can potentially desorb into Ga_2O by taking Ga from the substrate. Hence the exact conditions for preparing a flat surface revolve around the sample temperature and Ga deposition time at this crucial point of ~8 ML.

For deposition beyond ~8 ML the surface continues to display a RHEED pattern, but the increase in noise in the STM images indicate that Ga droplets have begun to form and are interfering with the tip-sample interface. Images can be captured with low gap V_{gap} (+2.0V) and I_{tunnel} (0.05 nA), implying that tunnelling is occurring into a metallic surface. Attempts to image at higher gap voltages (2.5 - 4.0V) or negative bias result in a saw-toothed waveform. It is worthy of note that areas of (2 × 4) domains can be located, though at this stage the peak-trough roughness of a line scan has increased to around 1.5 nm for 500 x 500 nm^2 scan areas.

A strong, stable RHEED diffraction pattern is crucial to identify the clean up point. Below 500 °C, the 1× RHEED pattern continued to grow in brightness throughout the experiment, even after such a time that Ga droplets were believed to form. Above 500 °C, the RHEED pattern provides greater detail on the degree of cleanup (progressing from 2x → 3x → 4x → spots), indicating that this is the preferred temperature of operation. Indeed, subsequent attempts at optimisation supported evidence that increasing the sample temperature has positive effects on the surface, resulting in shallower albeit fractionally larger isotropic pits.

After annealing, the surface displayed a morphology in the nano-pits shape and size, liable to be caused by the As adsorption and desorption of the weakly bound step

atoms. These nano-pits are lower in frequency and volume compared to those formed during thermal oxide desorption under As flux, implying that the Ga oxide desorption process suppressed the formation of such structures. This is to be expected since the extra Ga required by the Ga_2O_3 oxide in order to sublime has primarily been supplied externally.

No micro-pits were identified in the area considered in this study. Several $10 \times 10\ \mu m^2$ areas were investigation, implying that they μpits are either absent or rarely occur.

Since the Ga-assisted oxide desorption is performed at 520 °C, the process is susceptible to random thermal oxide desorption, which will inherently increase surface roughness. Further, it seems possible to remove all the oxide from the surface without the side-effect of Ga droplet formation, so long as the sample temperature is sufficiently high and hence the Ga diffusion length sufficiently large. At 520 °C it is possible that both thermal desorption and Ga-assisted desorption of Ga_2O_3 are active, however the low RMS roughness implies that the larger proportion of the oxide is removed via in Ga-assisted mode. At lower temperatures (400 - 500 °C), since the number of oxide-bonding sights for each Ga adatom is of an order with the Ga-bonding sites for low oxide coverages, Ga droplets have a high formation probability. Hence some surface oxide will always remain.

Hence, with sufficient care and optimisation, the surface can possess a semblance of the appearance of those prepared under hydrogen flux (Khatiri et al. 2004). The strong (2×4) reconstruction and ordered step edges after an As anneal at 590 °C prove that the surface damage induced by this technique is significantly reduced. It is, therefore, evident that the use of Ga, which is always present in GaAs MBE system, can be used to suppress the surface roughness inherent to the typical oxide removal technique.

6.4 Quenching

Quenching involves attempting to freeze the growing surface for STM observations. Whilst DH is inadequate for GaAs heating requirements (**Chapter 4: Direct Heating Characterisation**) the heating profile perfectly lends itself to rapid thermal quenching. In

contrast, the slower rate of cooling for PBNRH heating (**6.2.2 Temperature Dynamics**) cannot support this technique. The two techniques of rapid and compensated quenching are compared herein.

6.4.1 Compensation cooled (2 × 4) (PBNRH)

Compensation cooling involves lowering the As-flux in line with the substrate temperature in order to preserve the original reconstruction. This method can preserve both As-rich c(4 × 4) and (2 × 4) reconstructions. The method outlined by Yang (Yang et al. 1999) has four distinct phases after initial buffer layer growth:

1. Anneal at 600 °C under a 10^{-6} Torr As BEP to eliminate step bunching and produce large terraces.
2. Anneal at 570 °C under a 8 x 10^{-7} Torr As BEP to eliminate adatom and vacancy islands on the terraces.
3. Ramp from 570 °C to 450 °C. This phase sets the reconstruction. The correct amount of As must be applied to the surface during the temperature ramp to ensure a (2 × 4) reconstruction persists after the As needle valve is closed.
4. Anneal at 450 °C whilst background As is pumped out of the system
5. Exodus to the STM stage and finally cooling from 450 °C to ambient temperature.

In order to facilitate compensated cooling with the PBN heating plates, the various reconstructions were mapped against temperatures whilst monitoring the As BEP. **Figure 6.25** shows the resulting reconstruction chart plotted against heating current.

For the preparation of a β2(2 × 4) surface, it is important to maintain the correct reconstruction throughout, otherwise the regular dimer rows begin to kink and vacancies form in the pattern. This is more important with the c(4 × 4) to (2 × 4) boundary where the planarity of the surface is affected by boundary hopping back and forth from c(4 × 4) to (2 × 4) during cooling (**6.4.2 Compensation cooled c(4 × 4) (PBNRH)**).

For (2 × 4) the method is complicated by the fact that As adsorbs on to a (2 × 4) surface to produce a c(4 × 4) reconstruction for all temperatures between 300 °C and ~410 °C. Interestingly once the c(4 × 4) pattern has established in this range, removing

the As is not sufficient to revert to the (2 × 4) pattern until the temperature is raised to ~420 °C. Hence a method of producing either (2 × 4) or c(4 × 4) is established at 400 °C.

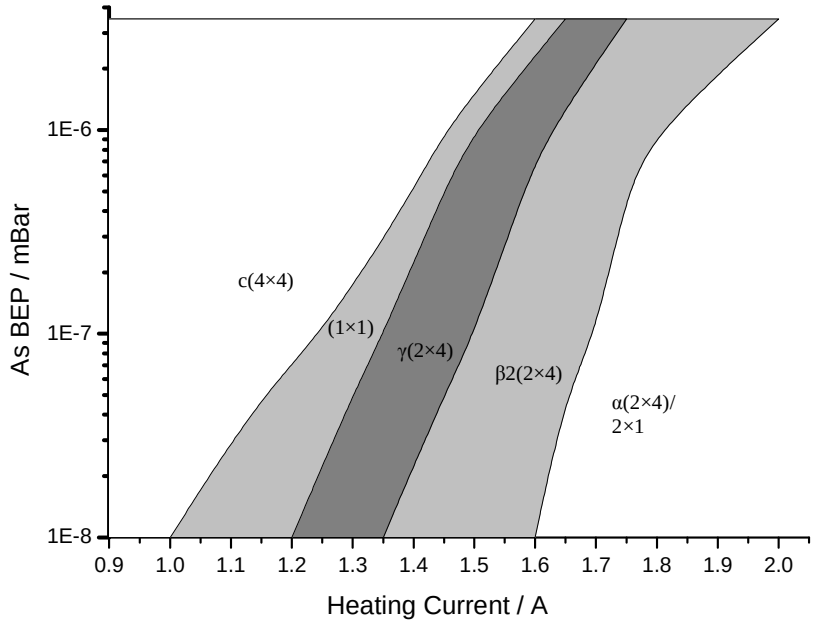

Figure 6.25: Reconstruction cooling chart.

In order to preserve the (2 × 4) pattern grown at 580 °C, the As BEP is reduced in line with the sample temperature until ~460 °C, where the needle valve is fully closed (Step 3). A leakage pressure of $<1 \times 10^{-8}$ mBar exists under such conditions. The sample temperature can then be lowered to ~430 °C without significant alteration of the RHEED pattern. Below 400 °C background As adsorbs onto the surface creating a "hazy" ×c4 pattern with the ×4 still being prominent on the $[\bar{1}10]$ azimuth. Continued cooling results in the two patterns being overlaid until ~300 °C where the ×4 begins to fade and the ×c4 becomes prominent. The end result is a "hazy" c(4 × 4) pattern at room temperature.

To prevent the reconstruction change it is necessary to ramp the As cracker down to <300 °C whilst the sample is held at ~440 °C. Once the chamber is vented of background As, the sample can be immediately ramped to room temperature. The (2 × 4) pattern persists after 8 hours implying that the sample has been adequately quenched.

Evidently it is not the cooling cycle, but the adsorbed As that alters the reconstruction. Hence to reduce adsorption the method was altered to involve a swift exodus into the STM chamber. The method involves holding the sample at 440 °C whilst moving it into position to be collected by the linear transfer mechanism. Once in place, the sample power is removed and the sample is transferred immediately into the STM chamber. The normal time for the event is <5 seconds. This method ensures that very little background As adsorbs, but does not have the benefit of monitoring the surface with RHEED.

The compensation quenching presented four As adsorption regimes, for maximum BEP of 5.0×10^{-6} mBar:

1. amorphous As adsorption under 300 °C
2. irreversible (2 × 4) to c(4 × 4) between 300 °C and 410 °C
3. reversible (2 × 4) to c(4 × 4) between 410 °C and 580 °C
4. constant (2 × 4) between 580 °C and 620 °C

The actual precise temperature of the transition point depends on the As BEP as discussed in **Chapter 3: Experimental Methods**. However the point of significance is the irreversible range between 300 °C and 410 °C where the (2 × 4) pattern will persist indefinitely for small ($<1 \times 10^{-8}$ mBar) BEP. Whereas the c(4 × 4) pattern will persist, once established, under the same conditions.

Hence for a constant temperature, a shuttered As source can induce a stable reconstruction change from (2 × 4) to c(4 × 4). This premise underpins the *in situ* experiments presented in **Chapter 7: In situ STM**.

6.4.2 Compensation cooled c(4 × 4) (PBNRH)

The c(4 × 4) surface reconstruction can be created for temperatures between 570 °C and ~350 °C, depending on the As BEP (**Figure 6.25**). Similarly the (2 × 4) pattern can be reverse engineered from the c(4 × 4) pattern down to ~410 °C.

Hence, superficially, surface reconstruction preparation is a simple process. However maintaining a single ML surface in the reconstruction is not a simple process when crossing the c(4 × 4)/(2 × 4) boundary. The presence of a (1 × 1) reconstruction in **Figure 6.25**, represents a hazy pattern when the two reconstructions share similar occupancy and hence neither pattern is dominant. The problem exists as a result of the c(4 × 4) reconstruction forming both above and below the (2 × 4) reconstruction. This disturbs the μm long steps formed due to the high temperature anneal and results in 2D islanding.

Three types of surface can be prepared based upon this presumption:

1. c(4 × 4) prepared at 570 °C
2. c(4 × 4) prepared on (2 × 4) at 430 °C
3. (1 × 1): c(4 × 4) and (2 × 4) in similar occupancy

The general technique is identical to that undertaken in **6.4.1 Compensation cooled (2 × 4) (PBNRH).** The optimum c(4 × 4) preparation methodology and the effects of the (1 × 1) range upon the sample surface is investigated via STM imaging in section **6.5.2 c(4 × 4) PBN Resistive Heating**.

6.4.3 Rapid cooled (DH)

Rapid cooling involves quenching the sample to room temperature within the order of several seconds in order to preserve the as-grown reconstruction. Due to the practical limitations of the MBE-STM system utilised in this work two concessions are required:

1. In the absence of LN_2 sample cooling in the growth chamber, samples can only be rapidly quenched to ~150 °C. The exponential decrease from 600 °C to 150 °C is in the order of 10 seconds, whereas the exponential segment from 150 °C to room temperature takes many minutes.
2. Rapid cooling is only accessible to DH sample plates, since the large thermal mass of the PBN plate prevents the rapid cooling cycle.

Despite the difficulties presented in **Chapter 4: Direct Heating Characterisation**, a (2 × 4) buffer layer can be successfully grown on a DH sample. In order to quench the sample, the heating current is simply ramped to zero and the As needle valve immediately closed. However due to the background pressure it is imperative to remove the sample from the growth chamber, otherwise As adsorption adversely effects reconstruction preservation (Yang et al. 1999).

After removing the sample from the MBE chamber, the sample was allowed to cool in the STM chamber overnight whilst the As cracker was cooled in the MBE chamber. Upon re-insertion a weak (2 × 4)/c(4 × 4) hybrid was observed, similar to that described in **6.4.1 Compensation cooled (2 × 4) (PBNRH)**. The change in the RHEED pattern occurred as a result of the adsorption of background As between initial termination of the sample power and removal from the chamber, an operation which took around 30 seconds.

6.5 STM Imaging

6.5.1 (2 × 4) PBN Resistive Heating

Low resolution images of a non-annealed GaAs sample revealed a high density of anisotropic islands aligned along the $[\bar{1}10]$ direction (**Figure 6.26**), consisting of long chains of As dimers which produce the 2× periodicity in the [110] azimuth (Pashley et al. 1988). The actual islands varied in length from 200 nm down to several dimers and had an average 3:1 length to width ratio. The step density was relatively high, with plateau widths ranging between 50 and 250 nm. Step edges displayed much wandering with many “bays” and “fingers” along their length. Macroscopically the surface was not flat. The high density of islands after annealing suggest that the As flux was too low to allow the formation of an ordered flat surface (LaBella et al. 2005). This disordered flat surface (DOF) is characterised by the high 2D island density atop step terraces.

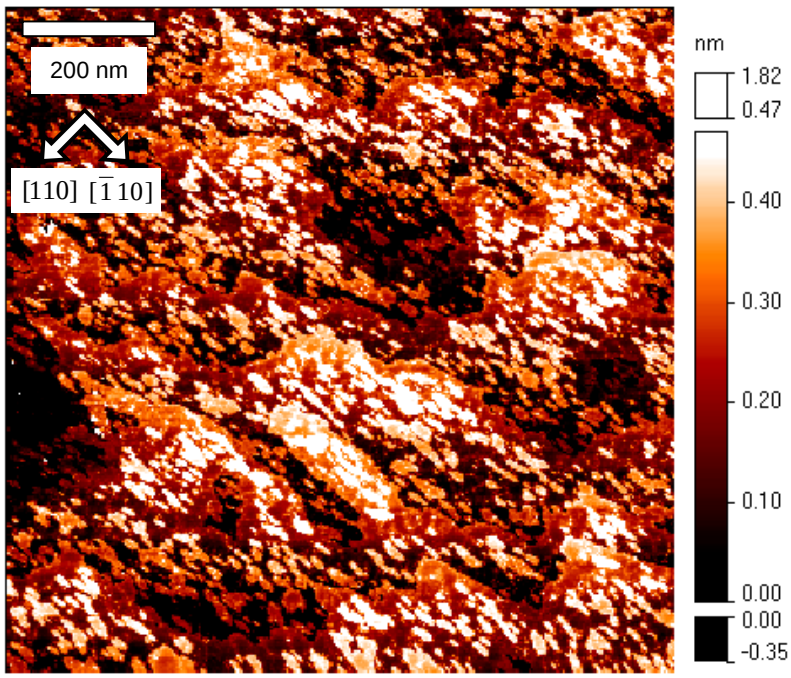

Figure 6.26: 1 x 1 μm^2 GaAs 001 image showing dense islands structures.

Higher resolution imaging revealed the atomic structure of the surface (**Figure 6.27**). The reconstruction is clearly not the diagonal As-dimer-pair lines of β2(2 × 4) in this case, but a combination of (2 × 4) (arrow) and more common c(4 × 4) domains (that appear like a cross-hatch pattern). The high disorder in the reconstruction is liable to result from the unknown flux and temperature ratios used in the cooling phase (step 3) to freeze the reconstructed surface.

Dimer strings are visible on many areas of the sample, implying that small islands still exhibit (2 × 4) reconstruction whilst the larger islands and the wide plateau regions have begun to revert to c(4 × 4). Image analysis revealed 0.4 nm spaced peaks that can be attributed to adjacent dimer spacing. These structures usually occur 2-a-breast indicating the β2(2 × 4) dimer rows, thought they also occur occasionally 3-a-breast indicating a β(2 × 4) surface. The low frequency of the 3-dimer rows indicates they are most likely to be unstable island growth sites rather than surface reconstructions.

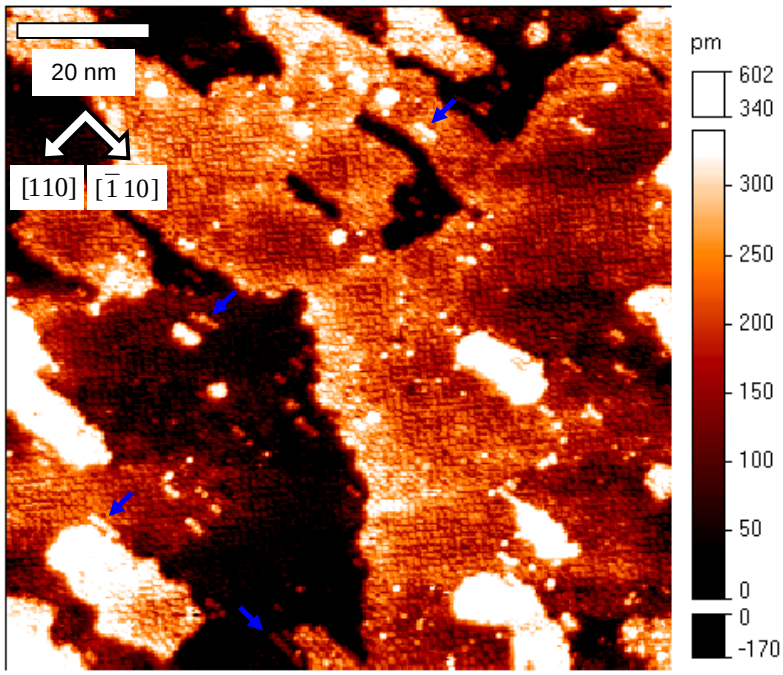

Figure 6.27: 100 x 100 nm^2 GaAs image revealing reconstruction. Arrows indicate residual (2 × 4) domains.

A line profile across the image reveals high disorder, in keeping with speculation from **Figure 6.27**. The ideal dimer rows with 0.4 nm spacing between dimers and 1.6 nm spacing between unit cells is broken by dimer vacancies. It is possible that these single sided resolved dimers are Ga-As dimers as speculated by Ohtake and Nakamura (Ohtake et al. 2004). Hence the Ga atom appears as a vacancy in the empty site image.

Additionally, many of the dimers imaged with 0.4 nm spacing had a As capping dimer twisted at 90 °C. This γ(2 × 4) structure is thought to emerge as a precursor state to the c(4 × 4) structure. Indeed the surface at this stage is a mixture of disordered (2 × 4) and c(4 × 4) phases.

Unfortunately the As cracker needle valve became damaged at this point in the work, hence the cracker was replaced by a As_4 effusion cell with integral shutter. The new operating conditions allowed a As_4 BEP of 1.2×10^{-6} mBar for As crucible

temperature 324 °C. This setting were used for clean up and growth with a Ga BEP of 4 x 10^{-8} mBar, giving a As:Ga BEP ratio of 30:1.

After initial oxide removal at 580 °C, a buffer layer was grown for 1 hour after which the surface was annealed for a further hour to produce an ordered flat (OF) surface (LaBella et al. 2005). OF is defined as displaying > 100 nm wide terraces and a low density of 2D islands. After annealing, the power of the As cell is set zero. The BEP falls from 1.2 x 10^{-6} mbar to 5.0 x 10^{-9} mBar over the course of 30 minutes. During which time the sample temperature is lowered whilst attempting to maintain a bright 2nd order RHEED rod, indicative of the β2(2 × 4) RHEED intensity (Hashizume et al. 1994).

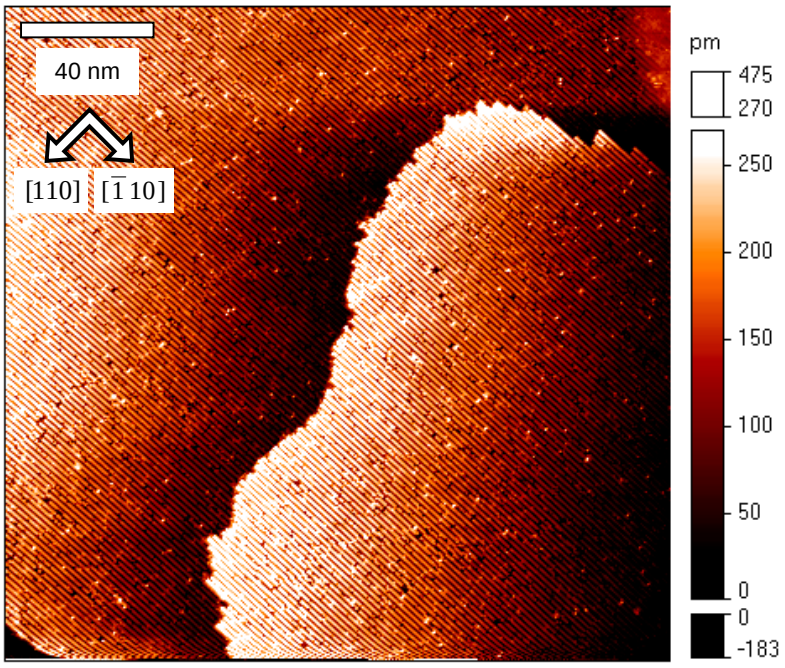

Figure 6.28: 200 x 200 nm^2 STM image: As dimer rows of an As-rich (2 × 4) reconstruction.

Ultimately the temperature and As flux are never truly synchronised. As an initial caution the temperature was lowered slightly ahead of the As flux, hence the reconstruction traverses the β2(2 × 4) and γ(2 × 4) boundary, revealed in the RHEED pattern with the

dimming of the 2nd order rod for γ and a subsequent increase in intensity when the β2 phase re-emerges.

Once the RHEED is established at 420 °C, the sample is held at this temperature for 5 minutes to ascertain whether the reconstruction is stable, at which point the sample heating power is set to zero and the sample is immediately transferred into the adjoining STM chamber. Actual sample transfer times are of the order of 20 seconds.

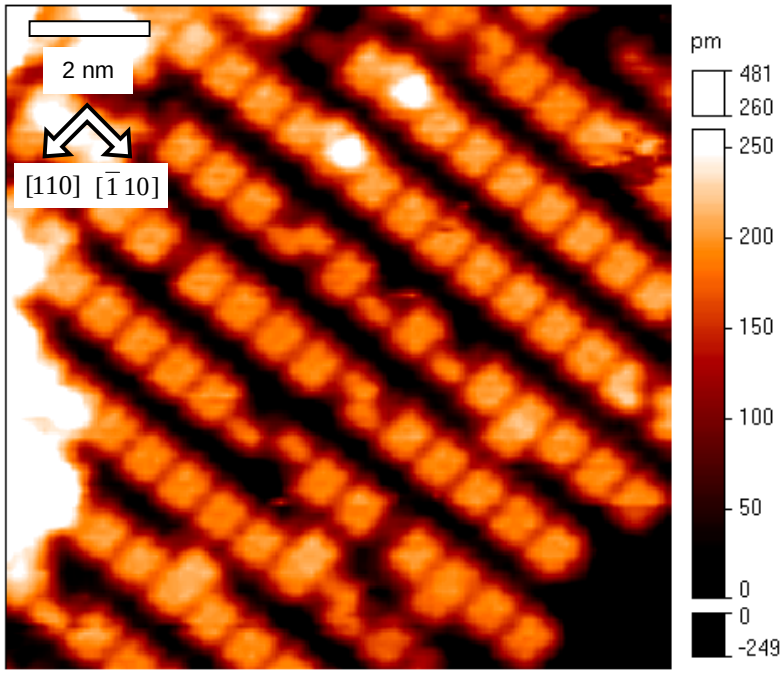

Figure 6.29: As dimer rows showing disordered As-rich reconstruction.

This second method to produce a OF-β2(2 × 4) GaAs(001) surface proved more successful. The terraces were up to 500 nm wide with suppression of 2D islands, the surface only displaying the occasional 2D island and these little more than a string of As-dimers or an As-As cluster.

At 200 x 200 nm^2 scan size the rows of As-dimers can begin to be resolved. This is particularly prevalent at step edges that give a good contrast for images. **Figure 6.28** shows a high resolution (2 × 4) image revealing clear lines of dimer rows running from

top-left to bottom-right along the [$\bar{1}$10] direction. The brighter clusters randomly scattered across the image are believed to be As-dimers atop the β2(2 × 4).

It is however at < 100 x 100 nm^2 that the dimer rows are best imaged. At 12 x 12 nm^2 the presence of dimers becomes strikingly apparent. The image in **Figure 6.29** shows the disorder in the (2 × 4) pattern with various missing dimers evident in the small vacancies formed on the surface. The dimerization is shown clearly with small rectangular sections aligned along [110] representing a pair of As-dimers making up a (2 × 4) unit cell

6.5.2 c(4 × 4) PBN Resistive Heating

When preparing a c(4 × 4) sample, the ultimate starting point is the β2(2 × 4) buffer layer grown at 580 °C. Once annealed at 600 °C the surface has been proven to consist of up to 1 μm wide terraces. Hence any islanding on the surface is primarily a result of the c(4 × 4) surface forming above the β2(2 × 4) surface and any trough formation is a result of the c(4 × 4) forming below the β2(2 × 4). This is illustrated in **Figure 6.30** which conclusively depicts the point. The sample was prepared by annealing a β2(2 × 4) and then allowing a brief period in the 1 × 1 transitional phase. Arrow (a) points to the original β2(2 × 4) reconstruction, arrow (b) points to a c(4 × 4) island above the original β2(2 × 4) and arrow (c) points c(4 × 4) below the original β2(2 × 4).

This implies that without a degree of annealing the surface will always exhibit single ML islanding. This theory is reinforced in **Figure 6.31** which shows a c(4 × 4) surface prepared from a β2(2 × 4) reconstruction at 425 °C. The sample was left to anneal for 30 minutes after initial emergence of the c(4 × 4) RHEED pattern. The actual reconstruction is not resolvable until the scan area is reduced to ~100 x 100 nm^2 (**Figure 6.32**).

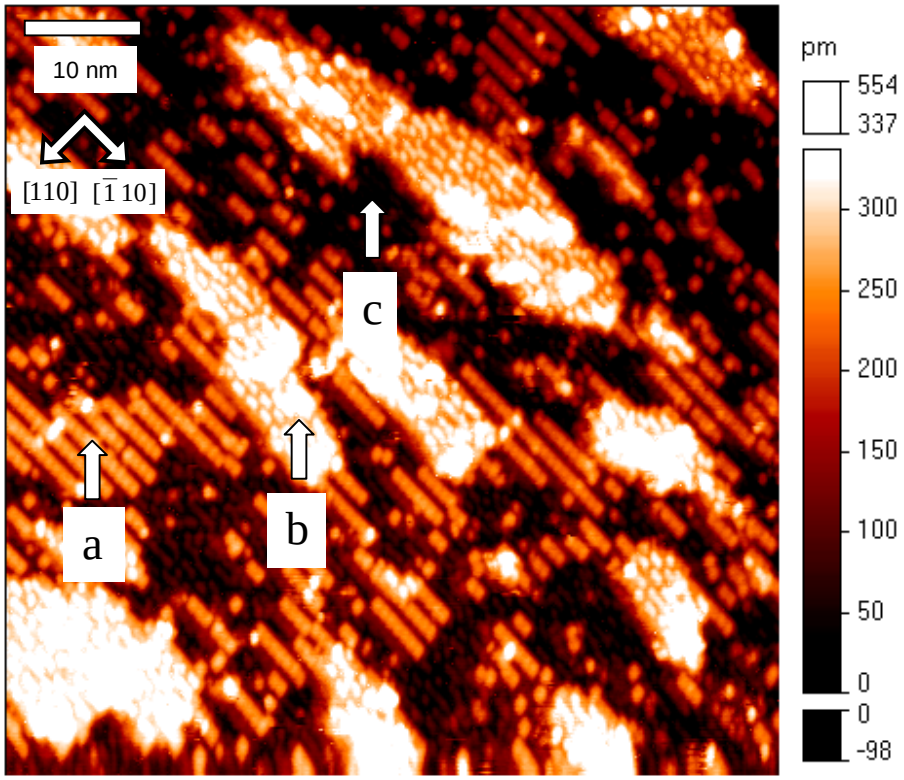

Figure 6.30: in vacuo prepared sample showing a mixture of c(4 × 4) and (2 × 4) domains. Arrow (a) indicates original (2 × 4) domain. Arrow (b) indicates c(4 × 4) forming above original (2 × 4). Arrow (c) indicates c(4 × 4) forming below original (2 × 4).

In the high resolution image the "brick-work" c(4 × 4) pattern is clearly resolvable. A number of white rectangles are visible that are liable to be adsorbed As dimers or remnants of the previous (2 × 4) configuration.

To planarize the surface and eliminate islanding, the initial β2(2 × 4) surface was cooled to 500 °C under a 2.0 x 10^{-6} mBar As BEP pressure and the c(4 × 4) was allowed to stabilise for an hour prior to compensation cooling through the c(4 × 4) domain. The resulting surface is shown in **Figure 6.33**. The brick-like c(4 × 4) appears like a cross-hatched pattern under this resolution. The surface is free from islands that form above the original β2(2 × 4) pattern and hence the surface can be assumed to have formed below.

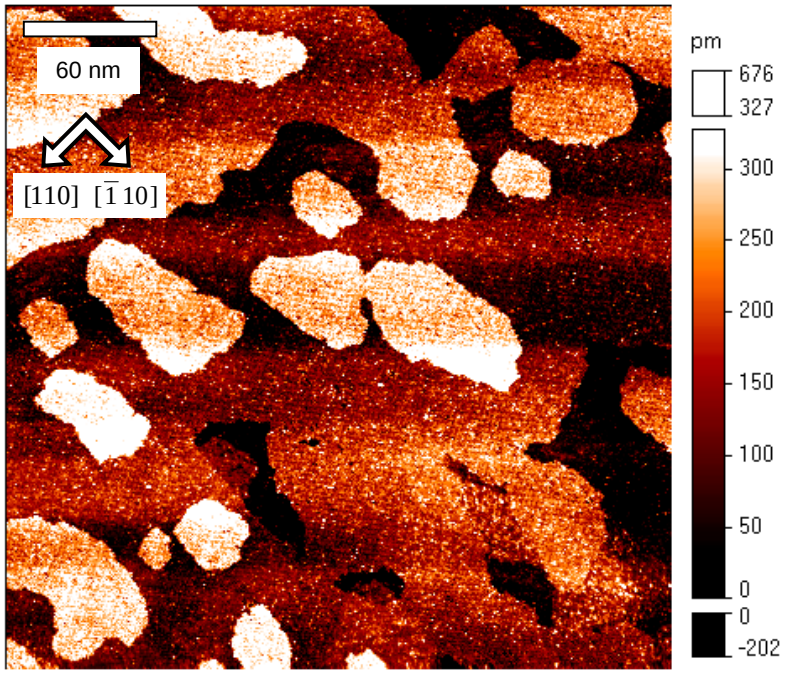

Figure 6.31: 300 x 300 nm^2 STM image of c(4 × 4) 300 nm.

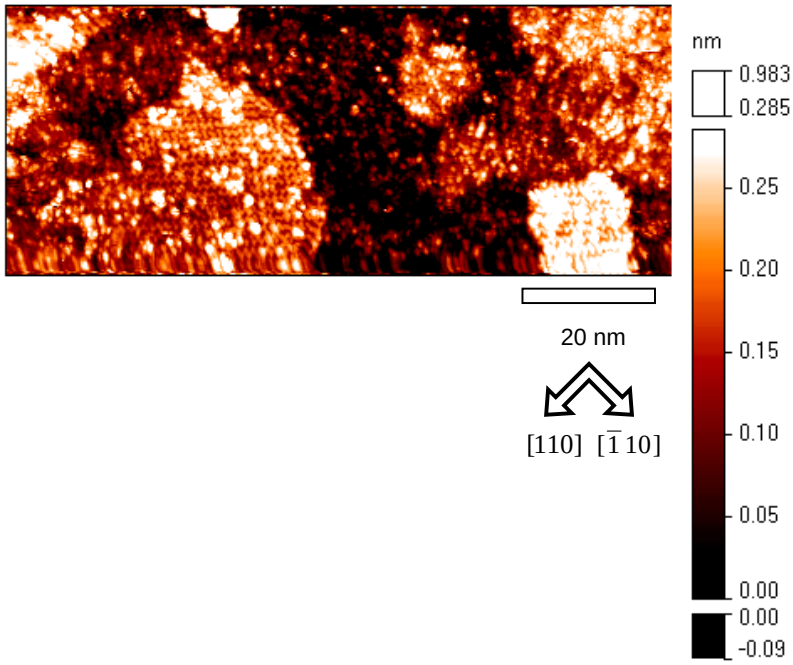

Figure 6.32: 100 x 40 nm^2 STM image of c(4 × 4).

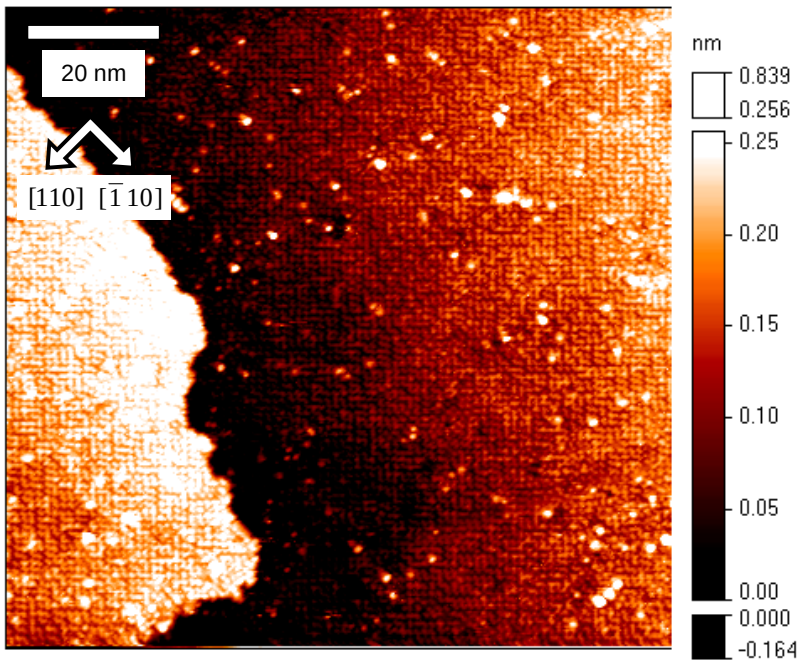

Figure 6.33: 100 x 100 nm^2 STM image of planar c(4 × 4) surface prepared at 500 °C.

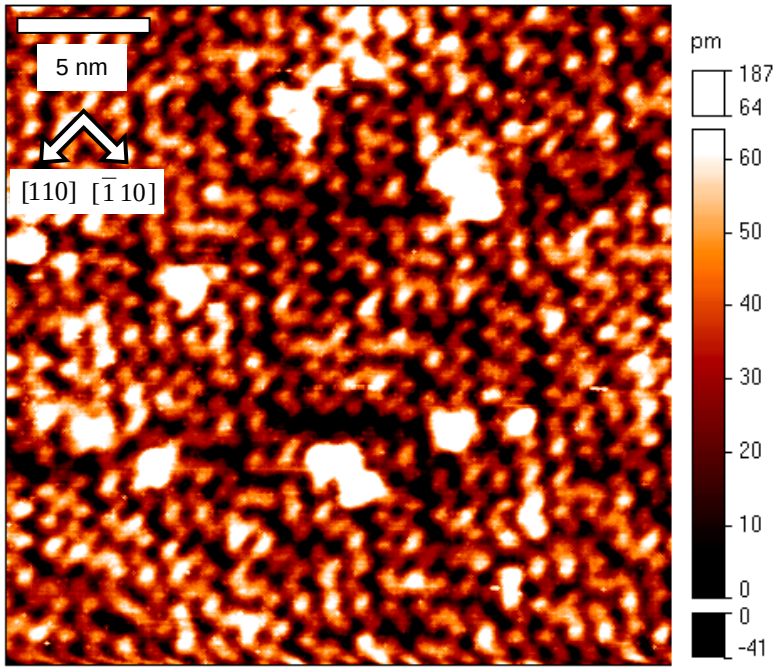

Figure 6.34: High resolution c(4 × 4) surface prepared at 500 °C.

The white spots visible on **Figure 6.33** and the higher resolution image of **Figure 6.34** are a result of compensation cooling and background flux adsorbing onto the surface. Adsorption of As on c(4 × 4) makes preparation of a perfect c(4 × 4) surface difficult. The surface in **Figure 6.34** shows some vacancies to the regular brick-like pattern, that would imply that As has been under-supplied slightly on initial reconstruction change at 500 °C.

6.5.3 Direct Heating

The DH sample did not present the expected ML island domains, but rather a large degree of surface roughness (**Figure 6.35**). No steps could be identified at 1 x 1 μm^2. The height of the structures varied by up to 7 nm across the image, equivalent to 25 ML of roughness. It is hypothesised that the step terraces and 2D islands attributed to normal GaAs growth are hidden by short order 3D roughness, resulting in 3 ML height difference within 5 nm of lateral distance.

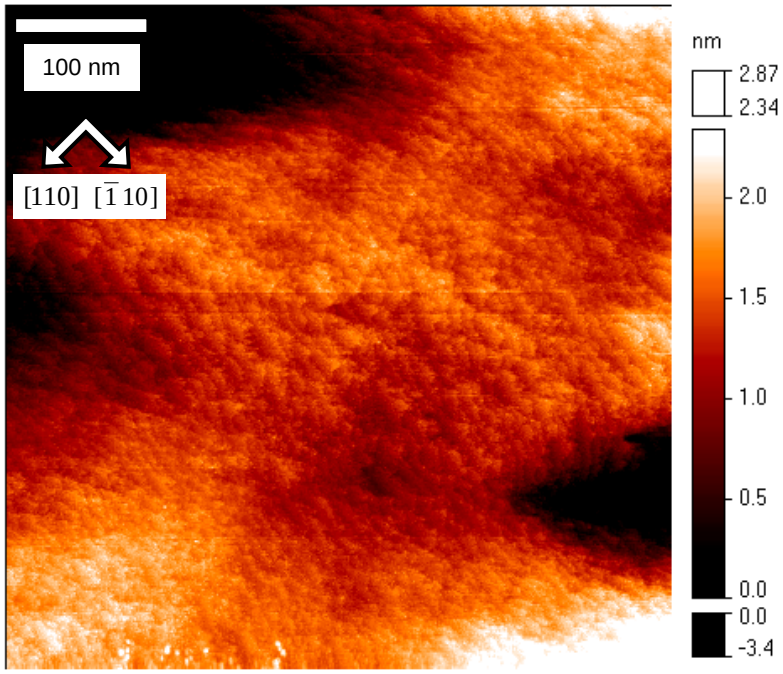

Figure 6.35: DH GaAs 001 sample with surface roughness.

The poor surface quality is liable to be a direct result of the clean-up procedure outlined in **Chapter 4**, here the temperature fluctuations of the sample resulted in high temperature spikes that could easily have caused the damage observed.

Despite the poor large scale growth, the reconstruction is accessible under high resolution imaging (**Figure 6.36**). The spacing between the diagonal rows is consistent with the 1.6 nm As-dimer spacing of the 4× unit cell. The brighter regions toward the centre of the image appear to be As clusters with partial c(4 × 4) reconstruction and exist 0.5 ML in height above the disordered β2(2 × 4) .

The presence of β2(2 × 4) domains even on the poor growth surface implies that whilst the initial clean up is insufficient for GaAs growth the quenching is an effective means of freezing the reconstruction during growth.

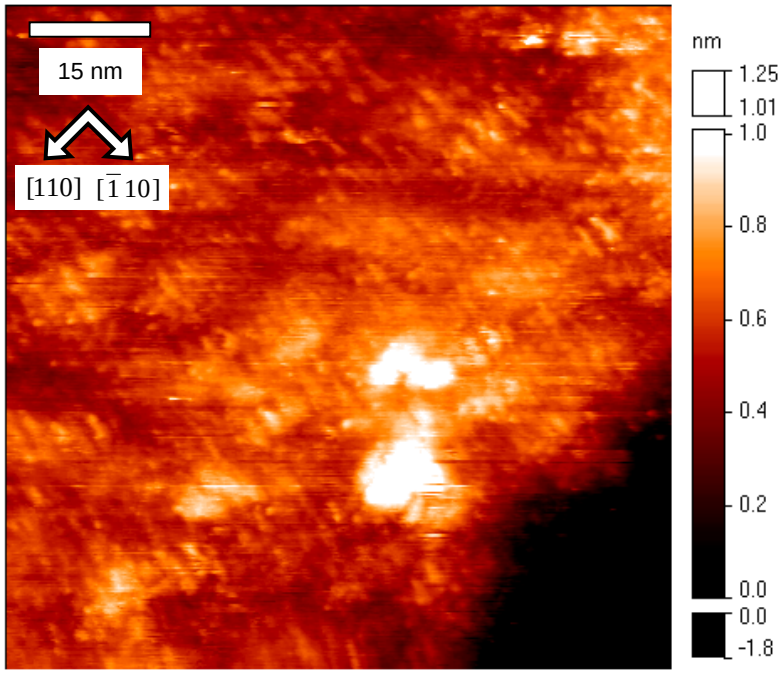

Figure 6.36: 82 x 82 nm ^{2} GaAs 001 image showing reconstruction.

The high resolution disorder in **Figure 6.36** is similar to that observed in **Chapter 7** for high temperature STM, where the sample temperature was taken to between 460 and 500 °C at which point As desorbs from the surface. Since the sample was prepared in the

MBE chamber where a resident background flux was incident it is unlikely that the damage occurred at 460 - 500 °C. More likely the sample temperature increased above 620 °C during cleanup and growth and the resulting damage could not be recovered.

6.6 Summary

This chapter introduced PBNRH and compared it with the alternative DH methodology. The larger PBNRH samples are easier to cleave and mount than the smaller DH counterparts. The simplified *ex situ* sample preparation helped to improve sample quality and reduce accidental handling and mounting damage.

The PBNRH heating characteristic was examined in an identical manner to DH in Chapter 4. The heating curve produced by thermography was repeatable to within ± 2.5 °C from sample to sample. Additionally the heating profile across the sample showed high uniformity with typical variation less than 3 °C across the sample. Cross referencing the temperatures with RHEED reconstruction analysis provided good confirmation of the curve shape, though involve ~ 30 °C of error. The cause could be related to As on the viewport or flux estimation errors resulting in discrepancies in the RHEED transition points.

It is well established that thermal oxide removal under an As flux at 580 °C causes the formation of μpits and general surface roughness. It has been proven in this work that externally supplying Ga to desorb Ga_2O_3 significantly reduces the formation of μpits and helps reduce nanometre scale surface roughness.

Rapid thermal quenching on DH samples was compared to compensation quenching on PBNRH samples. RHEED diffraction pattern analysis was used to confirm that a β2(2 × 4) pattern can be frozen at ~450 °C on PBNRH samples. The final ramping stage from 450 °C to room temperature requires absence of As in order to prevent adsorption. Hence in either case the best method is to swiftly remove the sample from the growth chamber for the final part of the cooling cycle.

Low resolution imaging of quenched samples revealed that the PBNRH surface was of a higher quality that the DH counterpart. The PBNRH displayed ML islands and regular, albeit high density steps. The DH sample displayed 3D damage and roughness which prevented the 2D features from being clearly identified.

After identifying PBNRH as the stronger candidate, optimisation attempts were made to freeze the As-rich β2(2 × 4) and c(4 × 4) reconstructions for STM imaging. An recipe was developed to enable both ordered flat and disordered flat β2(2 × 4) reconstruction to be produced after buffer layer growth. The c(4 × 4) surface produced suffered from adsorbed As interfering with the regular "brick-like" pattern. The preserved surface reconstructions, whilst suffering small scale disorder, are largely maintained. The ability to preserve the surface reconstruction and prepare high quality buffer layers means that PBNRH is highly favourable for surface preparation in this work. With these prerequisites established, the final step is to perform MBSTM growth.

6.7 Reference

Y. Asaoka (2003) J. Cryst. Growth **251**(1-4): 40.

P. Atkinson, S. Kiravittaya, M. Benyoucef, A. Rastelli and O.G. Schmidt (2008) Appl. Phys. Lett. **93**(10): 101908

T. Hashizume, Q.K. Xue, J. Zhou, A. Ichimiya and T. Sakurai (1994) Phys. Rev. Lett. **73**(16): 2208.

A. Khatiri, J.M. Ripalda, T.J. Krzyzewski, G.R. Bell, C.F. McConville and T.S. Jones (2004) Surf. Sci. **548**(1-3): L1.

S. Kikuchi (1928) Jap. J. of App. Phys. **5**: 83.

V.P. LaBella, M.R. Krause, Z. Ding and P.M. Thibado (2005) Surf. Sci. Rep. **60**(1-4): 1.

J.H. Lee, Z.M. Wang and G.J. Salamo (2006) Appl. Phys. Lett. **88**(25): 252108.

A. Ohtake, J. Nakamura, N. Koguchi and A. Natori (2004) Surf. Sci. **566-568**(Part 1): 58.

C. Orme, M.D. Johnson, J.L. Sudijono, K.T. Leung and B.G. Orr (1994) Appl. Phys. Lett. **64**(7): 860.

M.D. Pashley, K.W. Haberern, W. Friday, J.M. Woodall and P.D. Kirchner (1988) Phys. Rev. Lett. **60**(21): 2176.

Z.R. Wasilewski, J.M. Baribeau, M. Beaulieu, X. Wu and G.I. Sproule (2004) J. Vac. Sci. Technol. B **22**(3): 1534.

H. Yang, V.P. Labella, D.W. Bullock and P.M. Thibado (1999) J. Vac. Sci. & Tech. B **17**(4): 1778.

Chapter 7: In situ STM

This chapter represents the culmination of the previous chapters in order to realise functional MBE operation during STM imaging. The experiment expands upon early work by Tsukamoto (Tsukamoto et al. 2002) performed in a custom made STMBE machine to explore As-rich reconstruction changes from β2(2 × 4) to c(4 × 4) observed via STM during simultaneous As overpressure. Finally both In and As are applied in order to fully utilise the MBSTM capabilities.

7.1 Argument

In vacuo MBE-STM of the growth surface relies on one of the quenching methods described in section **6.4 Quenching** to obtain snap-shots of the surface. However all the growth dynamics are lost since imaging is performed at room temperature to suppress adatom mobility. Recently work by Tsukamoto (Tsukamoto et al. 2002) has observed surface site hopping for As atoms on c(4 × 4) surfaces imaged in a custom made STM built inside an MBE growth chamber.

The ability to observe reconstruction changes *in situ* is complicated by the fact that alterations in sample surface temperature require suitable stabilisation time in order to accommodate subsequent STM. However holding a surface at around 400 °C and inciting a reconstruction change via As flux changes can be accommodated via simple constant drift correction.

Radiant heating from source cells is minimised by the use of e-beam cells as opposed to standard hot filament effusion cells. To monitor reconstruction transformation only a single cell producing As_4 is necessary.

7.2 Method

Samples are cleaved from epi-ready substrates into 3.9 x 11.0 mm^2 segments, mounted on PBNRH heating plates and loaded into the fast entry lock (FEL) with no further *ex situ* processing. After pump down, samples are transferred into the MBE growth chamber

where they are heated to 400 °C for an hour. Once out-gassed, an As BEP of 5.0×10^{-6} mBar is applied before clean-up of the sample at 590 °C. The sample temperature is then lowered to 580 °C and a 300 nm buffer layer is grown under 30:1 As:Ga BEP ratio. A $\beta2(2 \times 4)$ surface is observed via RHEED throughout growth. The sample temperature is then lowered to ~ 440 °C over the course of an hour with subsequent reduction of the As BEP to a final value of 1.2×10^{-9} mBar. Heating power is then terminated and the sample is swiftly removed from the chamber and transferred to the STM chamber for imaging. This method is similar to that outlined by Yang (Yang et al. 1999) used to produce regularly order $\beta2(2 \times 4)$ dimer rows on wide ML step terraces.

STM sample heating is supplied via current contact, in the same method as in the MBE chamber. The As e-beam cell is maintained between 5×10^{-9} and 1×10^{-8} mBar BEP with the shutter closed. The background chamber pressure is 5×10^{-9} mBar throughout.

Ultimately the methodologies for Molecular Beam Scanning Tunnelling Microscopy (MBSTM) and Scanning Tunnelling Molecular Beam Epitaxy (STMBE) have subtle but significant differences. The latter concerns operating an STM unit inside a pre-existing MBE chamber, as performed by Tsukamoto (Tsukamoto et al. 2002; Tsukamoto et al. 2006). The former involves inserting MBE sources into a pre-existing STM chamber. Hence in the former case the vibrational damping issues and STM orientation and operation have been resolved, and it is the operation of the sources that requires consideration.

7.3 E-beam cells for MBE

To enable MBE to be performed in the STM chamber, the system is fitted with a pair of e-beam UHV evaporation cells. These were initially intended for low deposition rates of metals, but can be extended to As deposition. The cells have a built in ion collector that serves as a flux monitor, giving a flux current directly proportional to the number of atoms. Hence the only necessary requirement is to establish a BEP for a given flux current.

7.3.1 In e-beam Evaporation

In the case of In evaporation, emission sets in at high voltage (HV) = 800 V with a filament current = 1.80 A and reaches operational values for HV = 950 V, where 1000 V is the maximum supported by the cell. Once moderate emission is established, either the HV or the emission current can be used to regulate the flux. In this case the emission current was used.

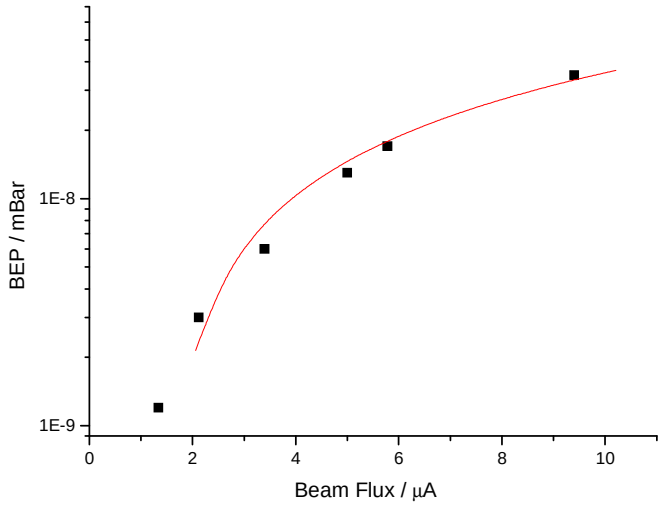

Figure 7.1: Plot of Flux vs. BEP for In e-beam cell.
Triangles show data points, line represents linear best fit

Figure 7.1 shows the BEP as measured from an ion gauge head at 150 mm from the orifice and the corresponding flux in μA. The BEP grows linearly with flux current (distorted in the log plot). The errors are thought to occur due to degassing and hence fluctuations in background pressure and also the required settling time in order to stabilise the BEP reading. The orifice-sample distance is slightly smaller when operating in the STM chamber, and hence BEP recorded here is liable to be an underestimate.

Low BEP is easily attainable and sustainable for e-beam cells, however for a BEP > 2.5 x 10^{-8} mBar, the cell must first undergo an hour of degassing and this consumes much of the small quantity of material. To this end it is perhaps better to operate in the 1.0 x 10^{-9} to 2.5 x 10^{-8} mBar range and deposit with growth rates much lower than for normal MBE growth.

7.3.2 As e-beam Evaporation

Operation of the As e-beam cell is slightly complicated by the fact that for low filament currents of around 1.5 A the bulk As begins to evaporate by radiative heating without HV e-beam stimulation. The actual recorded fluxes are ~10 nA. This rises to 400 nA at 1.8 A, indicating that the temperature of the crucible is reaching ~300 °C by the radiant heating of the filament . Hence stimulating emission at 1.68 A at HV = 300 V already produces a flux of 1 μA and corresponding BEP of ~ 2.0 x 10^{-8} mBar.

The As cell must therefore be operated at low currents, which further complicates the degassing procedure, which would normally allow the cell to be heated to 250 - 300 °C without cooling to ensure all the contaminants from the bake out procedure are evaporated. However to perform such a degas would inevitably evaporate the As in the crucible as well. Hence the cell must be degassed carefully after bake-out and further degassed whist stimulating emissions with high flux immediately before operation.

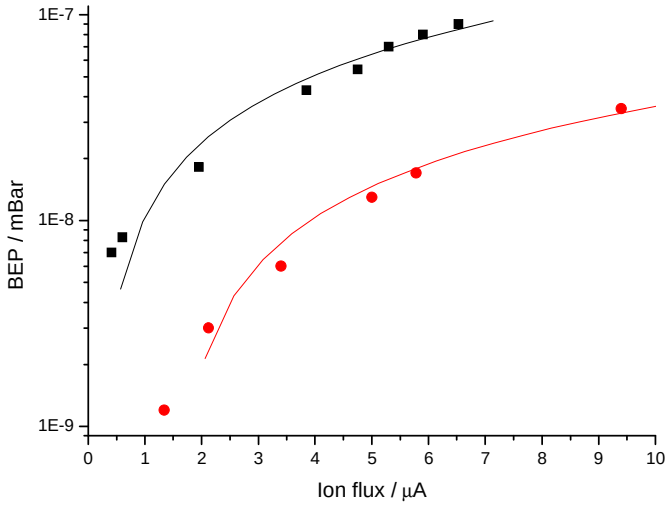

Figure 7.2: Flux vs. BEP for As e-beam cell.
Squares and black line are As data and linear fit respectively.
Circles and red line are corresponding In cell data.

The flux vs. BEP plot for As is shown in **Figure 7.2**. It can clearly be seen that the BEP for a corresponding flux is higher for the As than for the In. This is probably due to the

ionising potential of As_4 molecules (947.0 kJ mol^{-1}) being larger than for In monomers (558.3 kJ mol^{-1}). Notably the high voltage (HV) at which the cell is operated 300 V for As and 950 V for In would also effect the ratio of ionised to non-ionised molecules in each case.

From this data it can be argued that operating the cells with BEP up to 1.0×10^{-8} mBar is liable to yield the most reliable and reproducible results. This BEP is around 100 times less than conventionally used for MBE and hence growth will have to be performed below 500 °C in order not to damage the surface. In addition it is worthy of note that a full charge of As lasted around 12 hours.

7.4 Results 1: High Temperature STM

The results described below follow a systematic progression from those described in **Chapter 6** at room temperature. Samples were prepared with a 300 nm buffer layer and were then quenched as outlined in **section 6.4** to preserve a $\beta2(2 \times 4)$ surface.

In order to preserve the growth surface, high temperature STM was performed for samples up to 450 °C in the absence of an As flux. The aim of this experiment was to:

1. explore the effects of high sample temperatures on the STM head and imaging quality
2. confirm the samples are stable below 400 °C
3. verify that the reconstruction can be imaged.

7.4.1 Introduction to High Temperature STM

At high temperature the effects of drift and tip instability are significantly increased. Drift can be up to 0.3 nm/s in the X and Y directions even after a sample has been given an hour to stabilise. XY-drift can however be compensated using the drift correction function of the software. However it is the Z-drift that becomes problematic. The tip slowly approaches the sample during imaging and cannot be automatically corrected.

The piezo feedback system allows 100 nm of vertical (z-wise) motion during image capture. All heights are referenced within this 100 nm scale and later are used to

plane the image to give height correlating contrast of image colours. However with Z-drift greater than 100 nm per image (equivalent to 0.25 nm/s) any image captured becomes segmented with the z-position having to be altered mid-image and hence the reference point moved.

Scanning within the first 4 hours of heating in the 0.8 A to 1.0 A range results in Z-drift of an order of 0.25 nm/s. Hence images captured are low quality and further more any heights referenced in the scan direction are spurious in nature. Each section of the image can be utilised to identify surface reconstructions within that time, provided that the XY-drift can be sufficiently compensated.

The problem with XY-drift is inherently caused by the Z-drift. A singe image takes 400 seconds to capture for the parameters utilised to give high quality images. After each image the tip moves toward the sample, and hence after an number of images the tip must be manually retracted. The process becomes a cyclic affair involving decreasing area selection and XY-drift correction. The typical starting area is $1 \times 1\ \mu m^2$, this provides a large enough area so that even for drift in the order of 0.5 nm/s a surface feature will not move significantly. Once the drift is correct over a process of 4 images the next area is selected. The process repeats for 500 nm, 250 nm, 100 nm, at which stage the image resolution is such that the reconstruction can be clearly identified (see section **7.4.2 Sample temperature < 300 °C**). Ultimately the drift alters when:

1. The scan area is altered
2. The scan area is laterally displaced
3. The z position changes

Thankfully the latter condition has a small effect when compared to the other two. Regardless, selection of a $100 \times 100\ nm^2$ area takes 12 images over a course of 1 hour. Hence the Z-drift must be small enough to allow an hour of scanning without manual tip retraction.

During manual tip retraction, scanning is halted and the coarse positional piezo is used to retract the tip several steps. During this z-movement, the x-y position is alter by several μm and hence the original scan area is lost.

After 4 hours of temperature stabilisation the Z-drift is below 0.1 nm/s and hence, whilst still problematic, imaging can be performed in a more convenient manner. The following 3 sections discuss high temperature STM in the 0.2 - 1.0 A PBNRH heating range covering temperatures from ~ 100 - 450 °C.

7.4.2 Sample temperature < 300 ℃

Sample heating was applied systematically between 0 and 0.6 A in 0.2 A stages. Images recorded in this range were comparable with those obtained at room temperature: after half an hour of scanning, Z-drift was negligible and XY-drift was of an order of 0.05 nm/s.

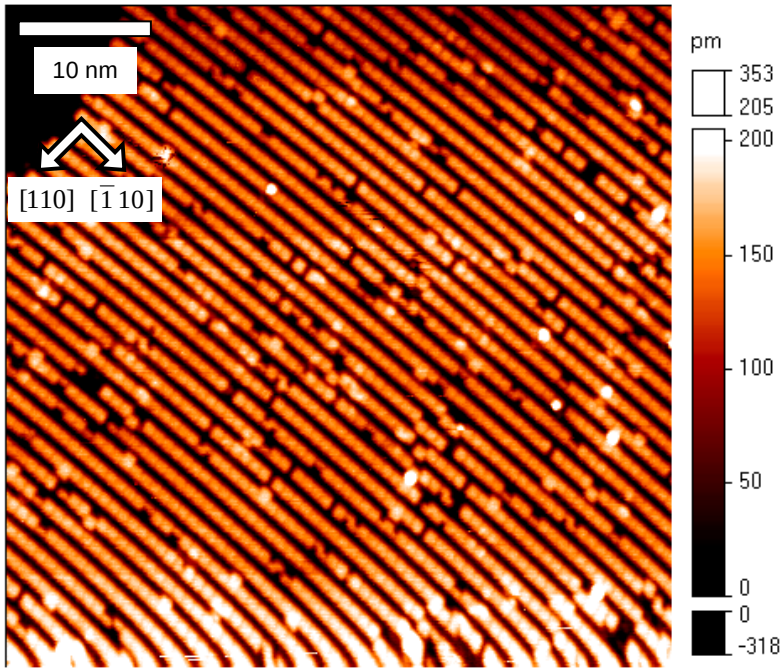

Figure 7.3: (2 × 4) As-dimers at 50 x 50 nm^2 resolution. T ~ 160 °C.

During stable temperature operation STM images from 1 x 1 μm^2 down to 15 x 15 nm^2 can be easily obtained with simple small order drift correction applied during a change in resolution. The As-dimer rows have a spacing of 1.6 nm and hence become resolvable at around 100 x 100 nm^2 (**Figure 7.3**). The dimer rows are aligned in the [$\bar{1}$10] direction. Vacancies in the reconstruction appear as small dark patches, whereas the bright dots are

adsorbed As atoms. The appearance of vacancies and adsorbates are a direct result of the quenching procedure, that, whilst adequate, is sub-optimal.

Imaging at 50 x 50 nm^2 allows the individual dimer pairs of the β2(2 × 4) reconstruction to be resolved. The dimer pairs appear as rectangular segments, affording the dimer rows an appearance akin to a stack of bricks (**Figure 7.4**). The segments have a spacing of 0.8 nm in correspondence to the 2× reconstruction in the [110] direction.

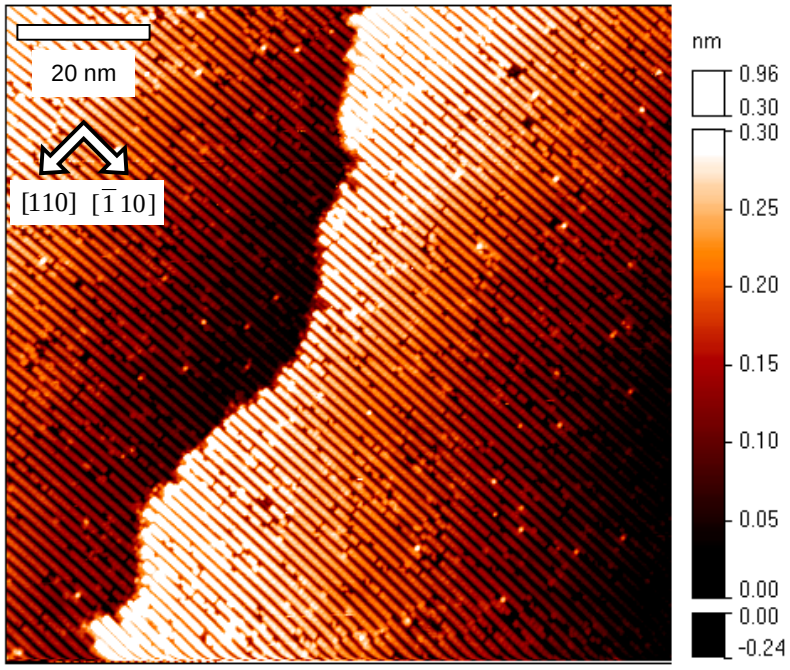

Figure 7.4: β2(2 × 4) As-dimers at 100 x 100 nm^2 resolution. T ~ 250 °C.

7.4.3 Sample temperature 300 – 350 ℃

The generally accepted stable (2 × 4) model, β2, is shown schematically in **Figure 7.5a** and in real-space in the STM image of **Figure 7.5d**. To establish c(4 × 4) half a ML beneath this reconstruction as observed (Orr et al. 1991; Kanisawa et al. 1997; Bell et al. 1999) requires the removal of 0.5 ML of As and 0.75 ML of Ga to produce a (1 × 1) surface, with finally the addition of 0.75 ML of As to produce the accepted c(4 × 4) model (**Figure 7.5c** and **e**). Hence the entire conversion requires the addition of 0.25 ML of As and the removal of 0.75 ML of Ga. Local disorder by the removal of dimers can

supply 0.25 ML of As, however the accommodation of 0.75 ML requires either hetero-dimers, Ga clusters or Ga-rich As-terminated domains. Possible sites for Ga incorporation are highlighted by arrows in the figures. These incommensurate reconstructions, such as the appearance of γ(2 × 4) (**Figure 7.5b**) when (2 × 4) and c(4 × 4) co-exist, can be detected by RHEED when they are in sufficient areal density. However, in the case of small local domains, STM is a far more powerful tool.

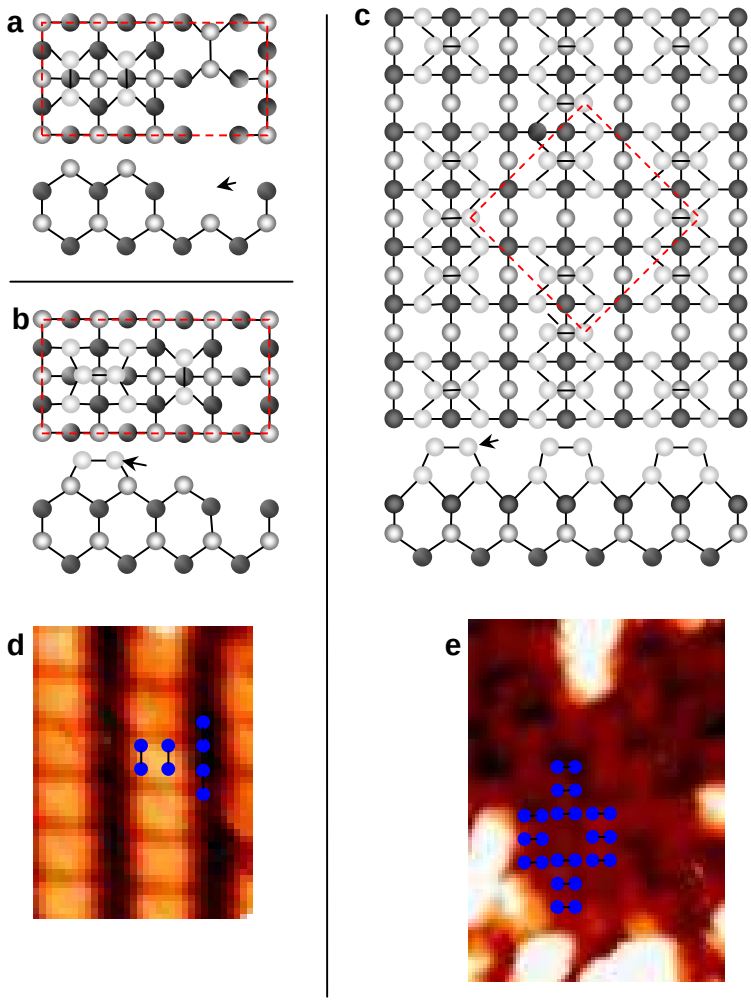

Figure 7.5: GaAs Schematic diagram of GaAs(001) As-rich reconstructions, As (white) and Ga (grey). (a) β2(2 × 4) (b) γ(2 × 4) (c) c(4 × 4). Arrows point to possible Ga adatom bonding sites. STM images: (d) (2 × 4) with blue circles marking As dimers (e) c(4 ×4) with blue circles marking As dimers in lines of three

As the temperature, and hence the thermal energy is increased, a small percentage of the As population becomes mobile. A greater frequency of missing dimers and atomic layer scale pit formation is observed at 320 °C (**Figure 7.6d**) when compared to **Figures 7.3** and **7.4**.

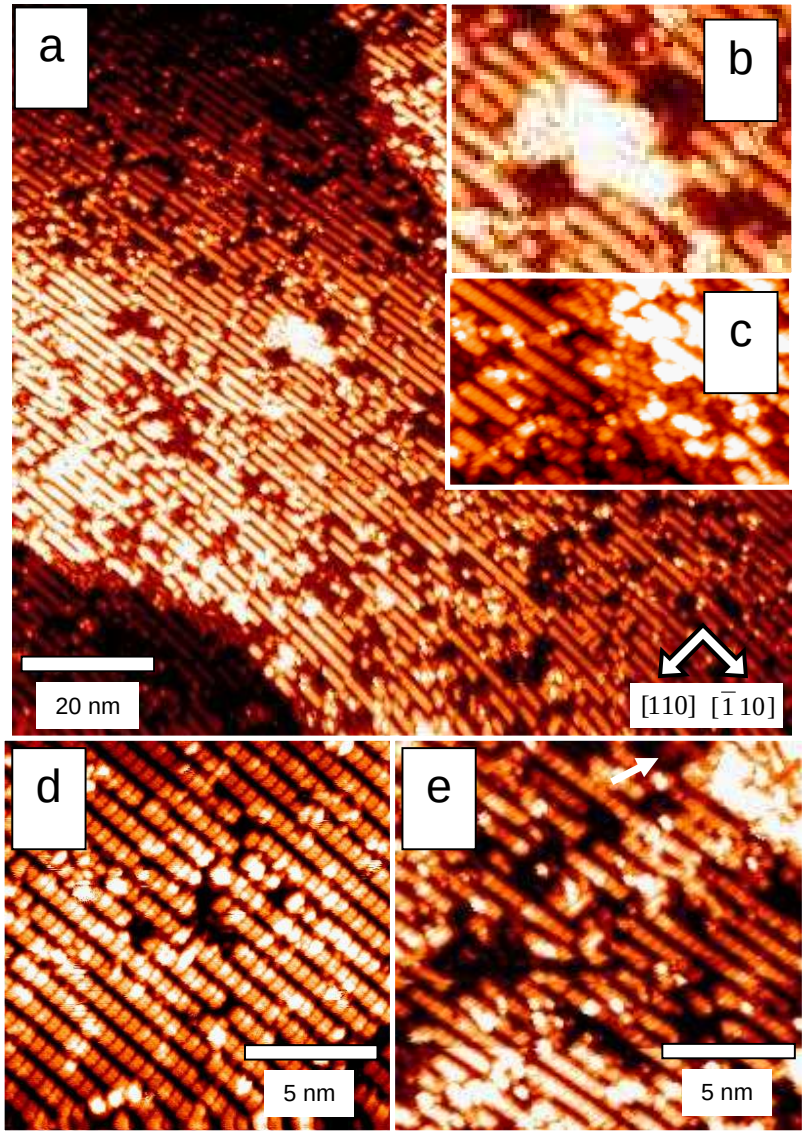

Figure 7.6: STM images of GaAs(001) sample a) 100 x 100 nm^2 after 10 hours at 350 °C. Whilst (2 × 4) is still dominant, c(4 × 4) is now clearly visible below along step edges and in troughs, and above in a 5 x 10 nm^2 island in the centre of the image. b) high resolution image of c(4 × 4) island. c) high resolution image of step edge with clear c(4 × 4) domains. d) 15 x 15 nm^2 after 10 hours at 320 °C, e) 15 x 15 nm^2 after 10 hours at 350 °C with white arrow point to Ga cluster at type B step

Upon increasing the temperature to the 320 - 350 °C range, a large enough percentage of the local As population is mobile to induce a fractional reconstruction transformation from the As-rich β2(2 × 4) to the As-rich c(4 × 4) surface (**Figure 7.6a**). The formation of c(4 × 4) islands on β2(2 × 4) requires a total of + 0.25 ML of Ga and +1.25 ML of As. Alternatively, a c(4 × 4) pit below β2(2 × 4) requires +0.25 ML of As and -0.75 ML of Ga. This means that whilst 3 islands would consume the Ga supplied by a pit of the same size, As will always be deficient, since either transformation requires As to be completed. In the absence of an external As flux, it seems intuitive that less islands would form than pits under this mechanism, and indeed from the figures this is the case.

The transformation from β2(2 × 4) to c(4 × 4) is thought to proceed through a stable γ(2 × 4) phase (Bell et al. 1999; LaBella et al. 2005). The γ(2 × 4) consists of an additional As-dimer back-bonded to the β2(2 × 4) unit cell, resulting in a larger As surface population (**Figure 7.5b**). The validity of the α(2 × 4) and γ(2 × 4) reconstructions are in dispute, strictly whether they are localized transients or surface wide phases.

Thermally generated mobile As adatoms/molecules are relatively few for this low temperature regime. Hence the reconstruction change is only on a domain-wise level and is not significant enough to alter RHEED patterns by more than a dimming of the 2nd order rods, indicating a transition from β2 to γ(2 × 4). The partial conversion from (2 × 4) to c(4 × 4) appears, therefore, to be limited due to As deficiency, causing multiple-adatom Ga cluster formation (**Figure 7.6e**).

Comparing the surface at 320 °C (**Figure 7.6d**) to the surface at 350 °C (**Figure 7.6e**) it is clear β2(2 × 4) rows, γ(2 × 4) and c(4 × 4) exist in close proximity in both cases, indicating that γ(2 × 4) is a transient reconstruction. In fact the γ(2 × 4) unit cells seem to fringe the c(4 × 4) pits. It seems, therefore, that the stable (2 × 4) and c(4 × 4) domains are ringed by local disorder. This juxtaposition, can be explain by the excess Ga and deficiency of As produced when forming c(4 × 4) below (2 × 4). This temporary store is highlighted in **Figure 7.6a** where bright spots are arranged atop the atomically resolved (2 × 4) rows. These spots appear larger than mere As-As dimers, and are likely adsorption sites for Ga-rich clusters. It is possible that the small white spots are in fact hetro-dimers (Ohtake et al. 2002; Wang et al. 2003) which would account for their

disordered appearance, since filled state imaging is sensitive to primarily As in this case. Further the excess Ga could be stored in the missing dimer row trenches of the (2 × 4) reconstruction, where it is know to cluster at low temperature (Itoh et al. 1998), which could be the feature noted in the **Figure 7.6c** near B-type step edges.

Notable in the inset of **Figure 7.6b** is the presence of a 5 nm x 10 nm c(4 × 4) island toward the centre of the image 0.5 ML above the underlying (2 × 4), initial thought was that this indicated that thermally mobile As has reconfigured in a more stable reconstruction, however analysis of the reconstruction shows (2 × 4) periodicity above the c(4 × 4) and hence this is merely an island not annealed out after buffer layer growth. This island, along with the adjacent step edges, presents a catalyst for the reconstruction transition, this is particularly prominent on the B-type step (**Figure 7.6c**). It is clear from the images that the reconstruction transition is not limited to the step edges, however, the c(4 × 4) is more ordered at these edges and the local disorder is less frequent. Presumably step propagation occurs in favor of the less energetically favorable disorder, and that disorder exists where adatoms do not possess enough thermal energy to reach step edges.

7.4.4 Sample temperature 350 – 410 ℃

After heating to ~0.9A for 10 hours the sample imaging became stable, displaying typical quantities of 2D drift and none in the Z direction. Images obtained were free from interference and showed very little disruption from the regular β2(2 × 4) dimer rows (**Figure 7.7**). White dots on the image are migrated As atoms, similarly dark holes are vacancies in the β2(2 × 4) pattern. It seems conclusive that β2(2 × 4) is stable for these heating parameters.

Small disruptions to the regular pattern are more easily identified at higher resolution. **Figure 7.8** shows a number of white clusters of adsorbed As atoms atop the regular pattern. The distorted sections appear as a merger between neighbouring rows. The regular spacing of the dimer “blocks” at this resolution make identifying the number of consecutive vacancies straightforward. Aside from the number of single dimers scattered across the image, there are several instances where 3 or 4 dimers are missing from a single row.

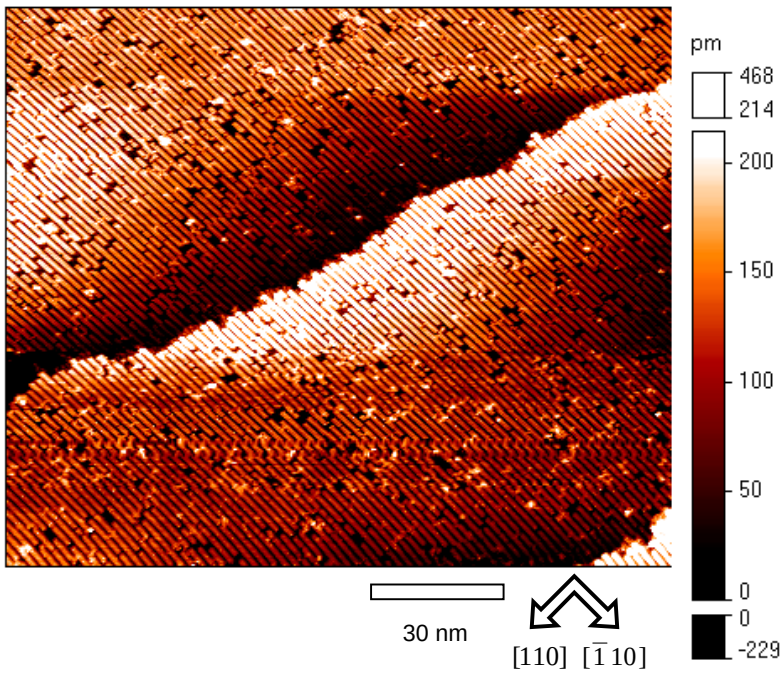

Figure 7.7: 150 x 125 nm^2 STM image of β2(2 × 4) dimer rows at 0.9 A heating.

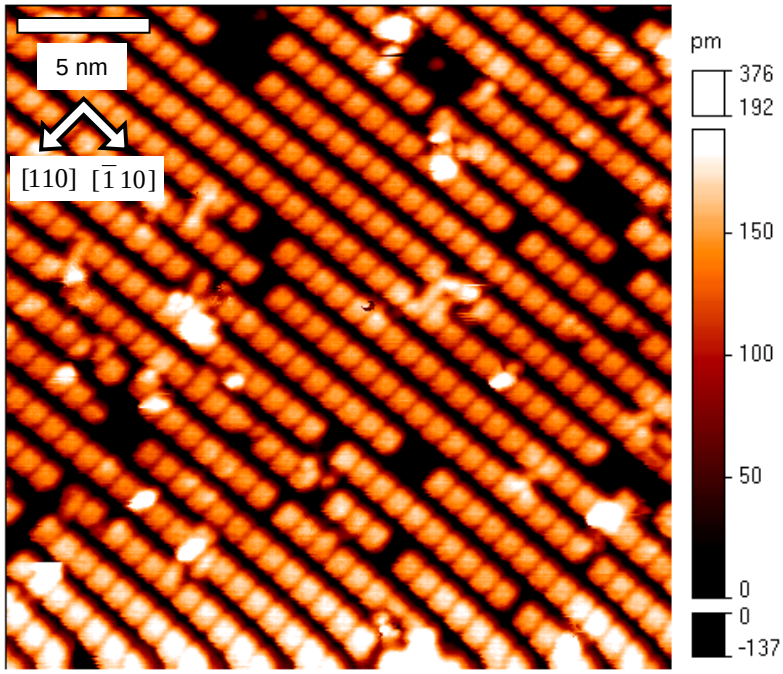

Figure 7.8: 25 x 12 nm^2 high resolution image of disruptions to β2(2 × 4) rows at 0.9 A.

Upon cooling back to room temperature the (2 × 4) pattern still persists. The vacancies and adsorbed As atoms are still clearly visible. Importantly this shows that heating to 0.9 A on this heating plate can be repeated without damage to the surface structure. This temperature range seems to represent a stable range for β2(2 × 4), this result is key for further MBSTM investigation, where a highly ordered β2(2 × 4) surface is required prior to growth in the STM chamber.

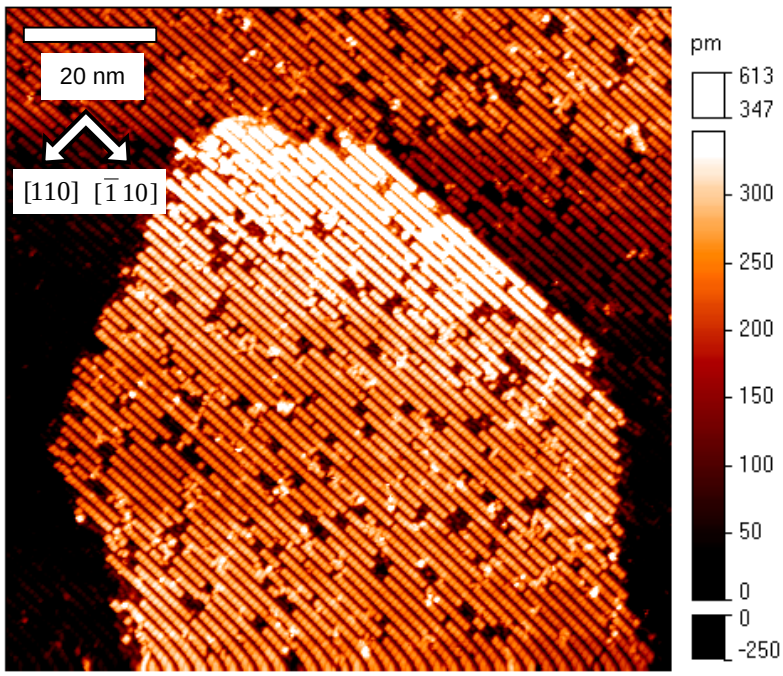

Figure 7.9: Dimer rows after cooling to room temperature.

7.4.5 Sample temperature > 410 ℃

In the InAs/GaAs(001) system, (2 × 4) to c(4 × 4) reconstruction changes are noted, before the InAs wetting layer is established and a (n × 3) reconstruction develops, similar to (1 × 3) shown in (**Figure 7.10**). Under this system, In is present is excess on the

surface, and it is equally plausible that it binds by a similar means, such as the hetero-dimers in the upper atomic layer of the figure.

By considering the local storage of excess Ga during homoepitaxy, parallels can be drawn between homo- and hetero-epitaxy. At temperatures > 410 °C, the As-rich β2(2 × 4) reconstruction is no longer stable (**Figure 7.11a**). The degree of roughening is to be expected from a surface where As sublimation is present. The As adatoms are now highly mobile, and frequently desorb from the surface into the vacuum. The result is a highly disordered surface with 2 ML of roughness resulting from islands and troughs. Short (2 × 4) domains are still visible on the surface, even after 10 hours of heating, however these brighter lines are relatively sparse compared to the darker pits beneath. The inset (**Figure 7.11b**) shows a high resolution image of a mid-terrace pit, whilst the (2 × 4) are visible nearby, there is much local disorder along the periphery, similar to that observed around c(4 × 4) pits at lower temperatures. The reconstruction in the pit is surprisingly ordered, displaying 3× periodicity in the [110] direction and either 1× periodicity along [$\bar{1}$10], with the occasional 2× periodicity attributed to a missing dimer.

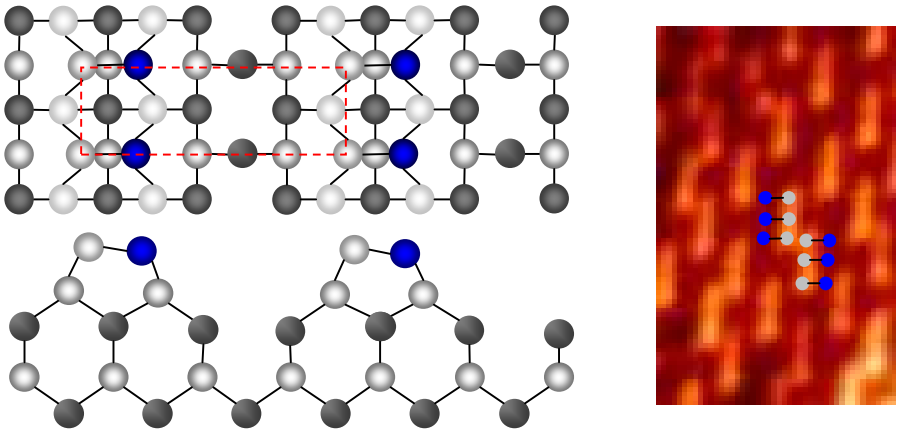

Figure 7.10: Schematic diagram of GaAs-(1 × 3) with hetero-dimers. STM images shows hetro-dimers on c(4 × 4), grey (blue) circles are As (Ga).

In the homo-epitaxial system, for (1 × 3) to form *below* (2 × 4) requires the initial loss of the dimer rows (0.5 ML of As) from the first atomic layer and the additional loss of ⅓ ML from the 3rd atomic layer. If the dimerization in the top-layer of (1 × 3) is assumed

to be pure Ga, then the Ga present in the 2nd atomic layer of the (2 × 4) is sufficient, with $^{1}/_{12}$ ML in excess. It is plausible from the filled-state images that the As-dimers of the 2nd layer are resolved, and the Ga dimers of the 1st layer are not visible, this would account for the narrow trenches and the wide dimer blocks. The dimers could also be As-Ga hetero-dimers (**Figure 7.10**), accommodating the excess As from the 3rd atomic layer of the original (2 × 4), but in this case the excess Ga, constituting $^{5}/_{12}$ ML must be stored elsewhere.

This (1 × 3) pattern for III-V is commonly observed during InAs/GaAs wetting layer growth. In hetero-epitaxy, the (1 × 3) reconstruction is believed to be strain driven, with In-In dimers in the upper atomic layer (Belk et al. 1996). A direct comparison between InAs/GaAs and the GaAs/GaAs observed here is infeasible due to the presence and absence of strain respectively. However, both systems possess excess group-III adatoms which require semi-permanent incorporation into the evolving epi-layer.

Figure 7.11c shows a high resolution inset of a highly disordered region. Several domains are notable. Line 1 marks another (1 × 3) reconstruction discussed previously. Line 2 marks 3 rows of a 2× periodicity, making a (1 × 2) domain. Line 3 marks one of the original (2 × 4) dimer rows. These 3 reconstructions, along with local roughness and disorder are present within the immediate 10 x 10 μm^2 area investigate by subsequent STM imaging. The small (1 × 2) and (1 × 3) domains are always bordered by remnants of (2 × 4) or As dimers 0.5 ML above, implying they only form temporarily due to desorption of the unstable (2 × 4). Analytical techniques that average a large surface area, such as RHEED, cannot detect these small domains.

It is interesting that there is not enough areal population of any one reconstruction to dominate the RHEED pattern, and a hazy (2 × 1) pattern actually is shown, presumably from the remaining As dimerization along $[\bar{1}10]$ (LaBella et al. 2005). The surface does not display any Ga-rich (3 × 1) or (4 × 2) domains, and hence it can be assumed that the As desorption is relatively slow and at an early stage, however, Ga is now in excess due to partial As desorption and the established domains are Ga-rich. What we observe is excess Ga binding in a (1 × 3) reconstruction similar to excess In binding during InAs/GaAs wetting layer formation. It can be speculated that the (1 × 3) provides temporary storage for excess group-III adatoms on a c(4 × 4)/(2 × 4) surface before other

Ga-rich domains dominate. The validity of this hypothesis for InAs/GaAs(001) requires further investigation.

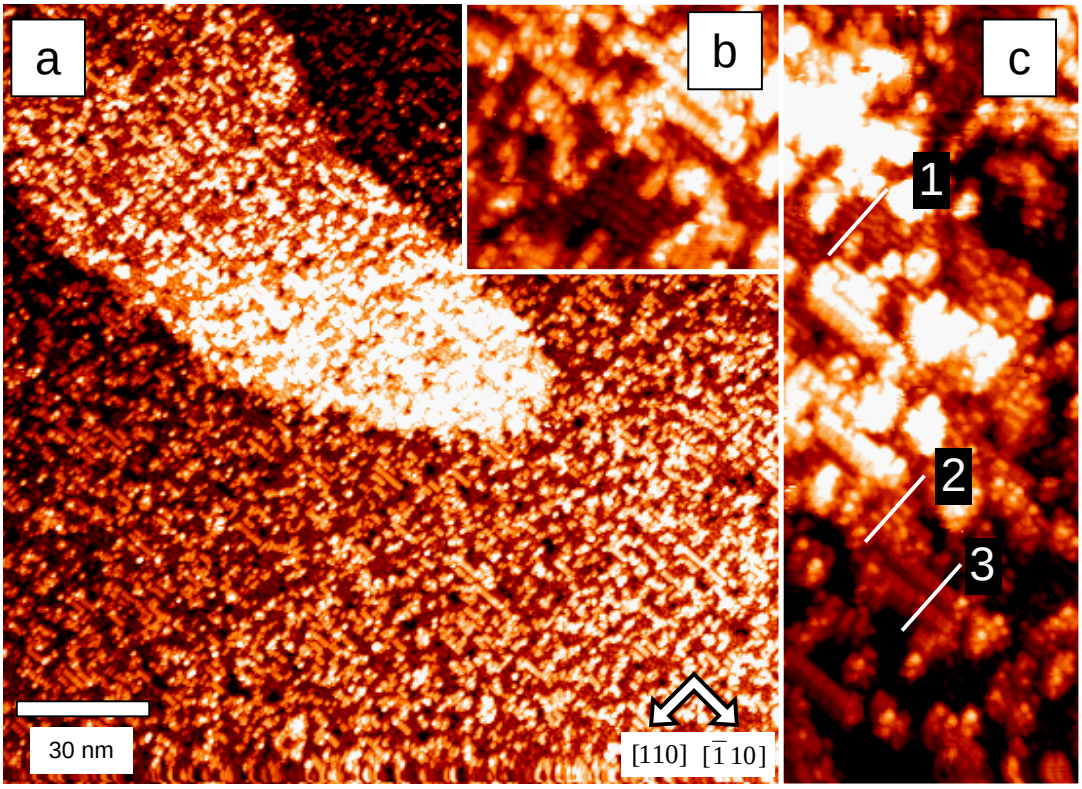

Figure 7.11: Roughening of (2 × 4) at 420 °C a) 150 x 150 nm^2 displaying areal coverage of original (2 × 4), b) inset showing a mid island pit and the (1 × 3) reconstruction within, c) inset showing (1) (1 × 3), (2) (1 × 2) and (3) (2 × 4)

7.5 Results 2: As overpressure at 400 ℃

This section relies on the premise that: *A surface stabilised to β2(2 × 4) reconstruction below 400 °C will remain β2(2 × 4) until irradiated by an As flux. The rate of change from β2(2 × 4) to c(4 × 4) depends on the size of that flux. However the transition is ultimately irreversible as observed by RHEED until the sample temperature is increased to ~ 400 °C.*

GaAs c(4 × 4) ultimately relies on an As overpressure to stabilise the growth surface for temperature in excess of ~ 400 °C. Achieving this prerequisite at ~ 400 °C

allows exploration of reconstruction changes under the presence of an As flux, discovering the effect of the flux on STM operation and the heated surface.

A heating current of 0.9 A was chosen in light of the results of section **7.4.4: Sample temperature 350 – 410 °C**. This provides a stable β2(2 × 4) reconstruction in the absence of As overpressure and should form a good basis for the c(4 × 4) reconstruction to form for small As fluxes.

7.5.1 Tip shadow: Scanning away from source

The tip-sample-source geometry is shown in **Figure 7.12a**. The default scan direction, at 0°, is from the source cell toward the back of the sample (**Figure 7.12b**). In this work the default direction has thus far been altered to 45°, allowing imaging of the dimer rows diagonally across the sample (**Figure 7.12c**). However the orientation scan window has potentially significant effects on the sample whilst under flux irradiation. In the default direction the tip effectively "shadows" the sample area *prior* to scanning it, hence any change to the sample surface is due to the effect of adatom diffusion and migration rather than direct exposure.

This is clearly illustrated in **Figure 7.13** which shows the sample before irradiation and **Figure 7.14** which shows the same sample after an hour of irradiation at 400 nA As flux and 0.9 A heating current. The two images form the start and end of a series of 9 pictures taken consecutively over the course of said hour.

Whilst there has been minor alteration to the β2(2 × 4) pattern, on the whole the pattern is still clearly visible. A number of small c(4 × 4) clusters have formed atop the existing (2 × 4) pattern (note the bottom-left of **Figure 7.14**). In addition there is an increased number of dimer vacancies with c(4 × 4) reconstruction revealed beneath. The relatively small change is assume to be a result of the afore mentioned shadowing and the migrating surface As.

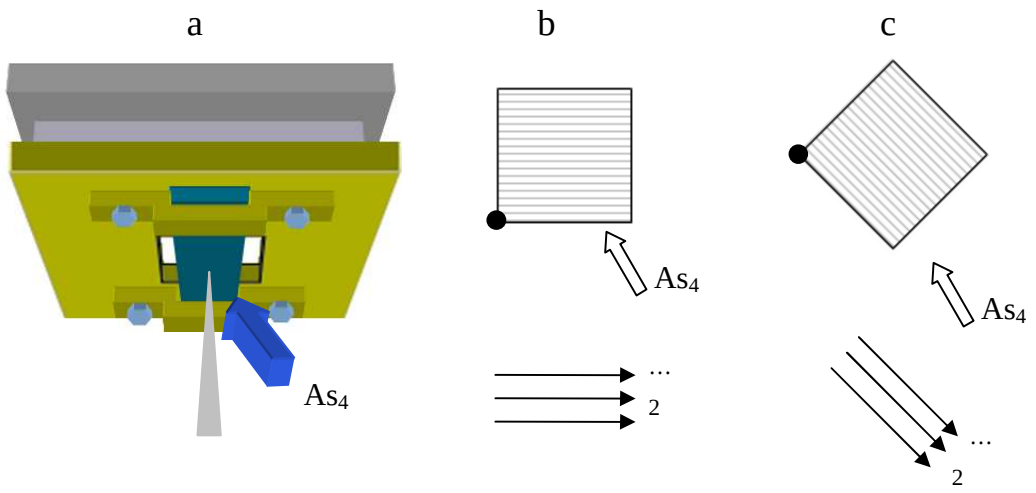

Figure 7.12: Tip scanning geometry, a) shows the tip and sample alignment within the STM chamber under As_4 irradiation, b) shows the default 0° orientation with the scan lines indicated by arrows, start point by the black dot and the cell flux direction labelled As_4, c) shows the standard scan direction in the work with the scan area rotated to 45°. From the flux direction is can be seen that the scanner is scanning into the flux.

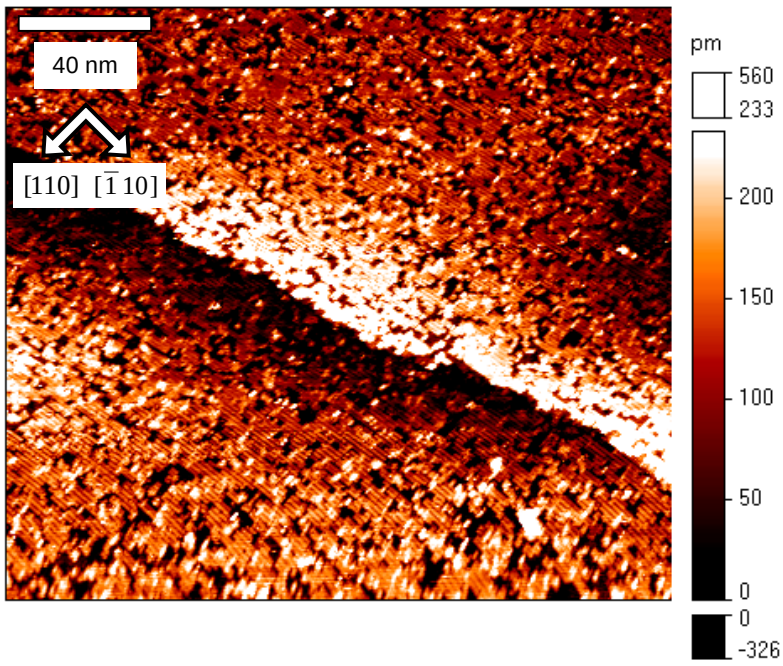

Figure 7.13: Pre-As flux sample.

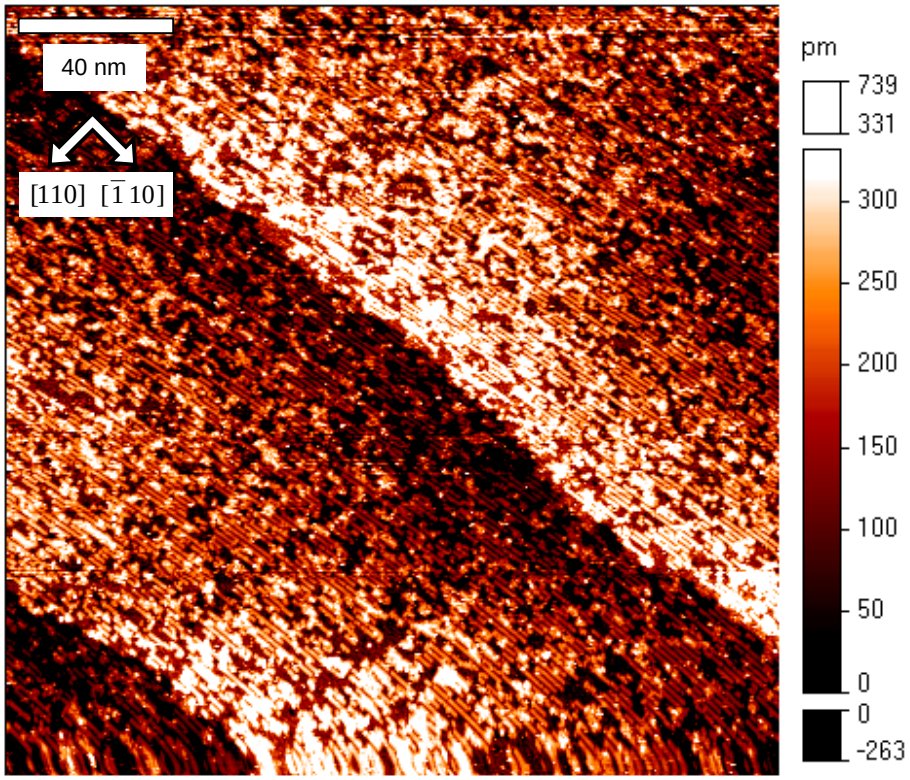

Figure 7.14: Post-growth As flux sample.

When moving away from the shadowed area by 2000 μm, the sample surface is wholly different (**Figure 7.15**). Here the c(4 × 4) reconstruction is clearly visible (on islands) above and (in troughs) below the initial (2 × 4) reconstruction. There are some dimer chains visible, however they occupy only a small fraction of the sample surface.

Evidently the migration at 400 °C is not sufficient to counteract the shadowing of the tip on the far side of the sample. Hence whilst this experiment shows that the e-beam source and PBNRH utilised are capable of transforming a β2(2 × 4) surface to a c(4 × 4) surface, the transformation cannot be observed by STM in this orientation.

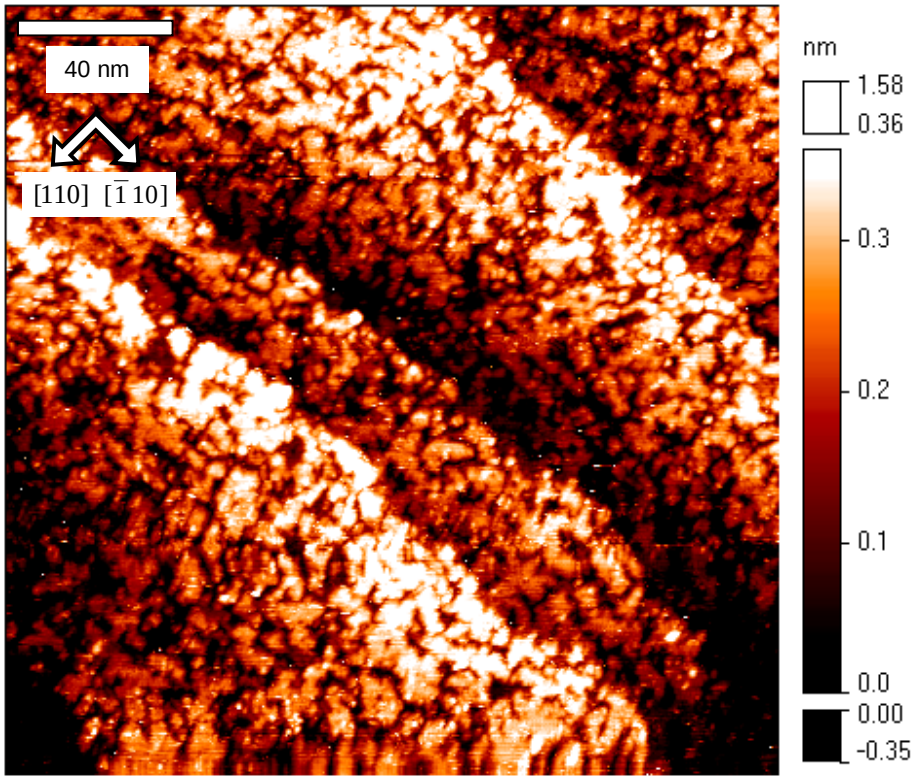

Figure 7.15: c(4 × 4) islands after As flux irradiation.

7.5.2 (2 × 4) to c(4 × 4): Scanning into source

Initially a β2(2 × 4) surface was prepared with the standard preparation technique used throughout. This was heated to 0.9 A (~ 400 °C) for 9 hours, after which STM imaging commenced and was allowed to settle for a further hour until drift was negligible at 150 x 150 nm^2 resolution. A flux of 500 nA (~1.0 x 10^{-8} mBar) was applied throughout.

Studies of the (2 × 4) to c(4 × 4) transformation have identified β2 as the generally accepted (2 × 4) model (**Figure 7.5a**) but the exact composition of the c(4 × 4) reconstruction is still under debate. The simplistic model of As-As dimers simply back-bonded upon the existing dimer rows of the (2 × 4) (**Figure 7.5b**) perhaps over simplifies the actual atomic binding configuration, for which Ga incorporation has also been speculated (Kanisawa et al. 1997; Wang et al. 2003).

The transition from β2(2 × 4) to c(4 × 4) normally takes place between 450 – 550 °C, depending on the applied As flux. At these relatively low temperatures, Ga surface atoms will be relatively immobile due to limited thermal kinetics. In density function theory (DFT) the motion of a single Ga adatom involves migration from an initial state (*i*) over a potential barrier to a final state (*f*). Hence the hopping rate for a Ga adatom in then assumed to obey a Arrhenius form (LePage et al. 1998):

$$r_{i,f} = \nu_0 \exp\left(\frac{-\Delta E_{i,f}}{kT}\right)$$ **Equation 7.1**

Where $\Delta E_{i,f}$ is the activation energy (i.e. the difference between the relative E_i and $E_{i,f}$ the saddle point between site *i* and *f*). ν_0 is a site independent constant approximated to $2kT/h$, where *k* is Boltzmann's constant, *h* is Plank's constant and *T* is the absolute temperature.

Potential energy surface (PES) gives the binding energy for a single Ga atom at each site in a given reconstruction. For from β2(2 × 4) the energy barriers for diffusion are 0.8 eV and 0.6 eV in the [110] and $[\bar{1}10]$ directions respectively, hence diffusion is anisotropic. This gives a typical Ga adatom hopping rate of ~10^7 to 10^{10} s^{-1} at 450 °C compare to ~10^8 to 10^{11} s^{-1} at 550 °C. Whereas for c(4 × 4) the barriers are 0.34 eV and 0.45 eV in the [110] and $[\bar{1}10]$ directions respectively, hence growth is more closely isotropic in this case. The lower energy barrier reduces the effect of the exponential term and creates a greater hopping rate that varies little from 450 to 550 °C, ~10^{10} to 10^{12} s^{-1}. However in all cases the effect of As must be included, which typically reduces the hopping rate of a Ga adatom to ~10^8 s^{-1} whilst it is trapped in a Ga-As_2 complex (Kley et al. 1997).

The transport of Ga would be expected to play a key role in the reconstruction transformation, with local-range Ga transport responsible for pit and island formation during the formation of a c(4 × 4) surface on a (2 × 4) and vice versa (Wang et al. 2003). Simplistically a single unit cell of β2(2 × 4) can be transformed into a (1 × 1) layer by

either the addition of 0.25 ML of Ga and 0.5 ML of As or the removal of 0.75 ML Ga and 0.5 ML As, allowing a (1 × 1) to be created either in line with the existing (2 × 4) or 1 ML below, respectively. The (1 × 1) layer forms the nucleus of the traditional c(4 × 4) model (**Figure 7.5c**) and would require an additional 0.75 ML of As to produce the reconstruction. Since islanding requires only a third of the Ga produced by the formation of an identical sized pit, it can be assumed that a two-level c(4 × 4) surface would exhibit a 3:1 island:pit ratio. It has been observed experimentally that this is not the case in section **7.4 Results 1: High Temperature STM**, so the question remains: where is the excess Ga incorporated?

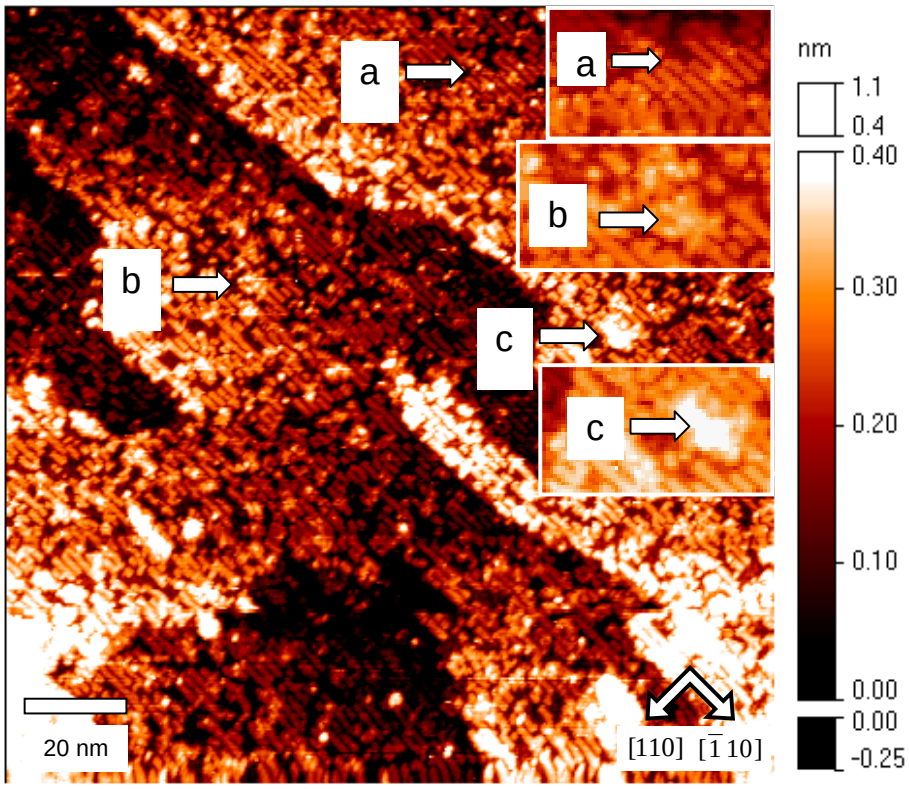

Figure 7.16: Image 00/37: (2 × 4) prior to As flux. Measurement parameters V = -4 V , I = 0.5 nA, Gain=2 %. The arrow (a) points to a number of (2 × 4) dimer rows with several back-bonded As dimers. Arrow (b) points a small c(4 × 4) island on the lower terrace, arrow (c) points to a similar island on the upper terrace. These features probably formed due to the low temperature anneal surface As migration or the background flux from the shuttered As source.

The presence of hetro-dimers (Ohtake et al. 2002; Wang et al. 2003) have been proposed to explain the excess Ga incorporation, a structure easily detectable with STM due to the sensitivity to empty and filled states (**Figure 7.10b**). Furthermore, the reported coexistence of (2 × 4) and c(4 × 4) (Avery et al. 1995) raises a question to the presence and stability of the theoretical γ(2 × 4) between the established β2(2 × 4) and the c(4 × 4).

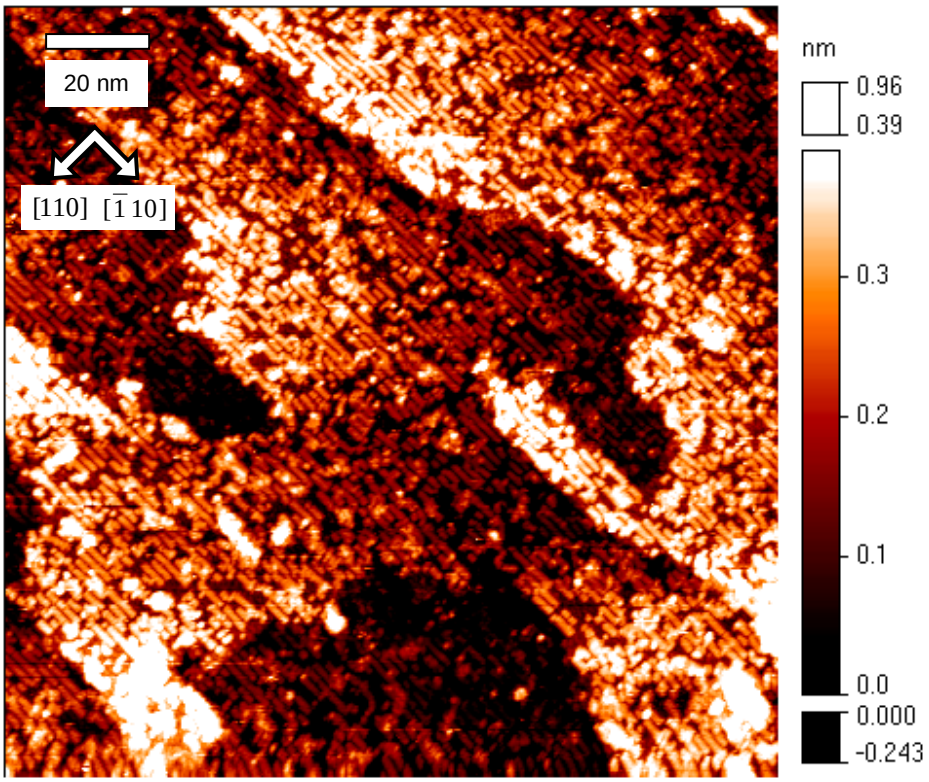

Figure 7.17: Image 02/37. Measurement parameters V = -4 V , I = 0.5 nA, Gain = 2 %.
All values in nm. Large number of scan lines across the image.
Note white dots (As dimers) on top of the original (2 × 4).

To accommodate the tip shadowing, the sample scan window is rotated by a further 180°. Hence the same sample area is imaged from the top down rather than the bottom up. This orientation means that the tip only shadows an area *after* it is imaged. **Figure 7.16** represents image #00 of the series. All images have the same orientation and hence upper-right receives the largest flux, whereas bottom-left is most in shadow. Hence whilst

the lower portion of the image will receive less flux than the upper portion, the entire scan area will receive a dose of As from image to image.

Figure 7.16 shows the GaAs surface prior to the onset of As flux at 400 °C. Notice that there are a number of white spots on the surface (e.g. arrows b and c), some of which are adsorbed As dimers formed from the sample quenching in the MBE chamber. Further, the reconstruction is broken as a result of the adsorption of background As during the outgas and initial heating of the e-beam cell before the steady state condition of normal operation was achieved. This random distribution of back-bonded As dimers is enough to contribute to a fractional dimming of the 2^{nd} order RHEED rods, in keeping with observances of the $\gamma(2 \times 4)$ surface. Regardless of the small contaminants, a strong (2×4) is present on the surface (arrow a).

What follows is a progression of 37 consecutive images captured under an As e-beam flux. Each image takes exactly 400 seconds to capture and hence progressive changes in the surface occurred within a 400 second window from the previous image.

The first image of note is #02 (**Figure 7.17**), representing the surface at time 400 - 800 s from initial As flux onset. Beside the increased number of scan lines present in the raw image (scan lines have been removed from image as presented using SCALA image processing features), a number of small white dots have appeared on the upper step. These appear to be initial $c(4 \times 4)$ dimer domains forming above the (2×4) structure, however at this stage the adsorbed As is still relatively small. The small number of adsorbed As_4 molecules after 800s raises a number of points. Firstly, the degree of tip shadowing present is brought into dispute, even after the advantageous configuration. An additional experiment exploring the rate of $c(4 \times 4)$ evolution away from the scanned region suggested that the effect is still present. The area presented in this series of images must be treat as receiving a relative flux, smaller that the BEP of the cell.

Whilst the sample temperature has been chosen to stabilise the growth surface, the very low BEP introduces the possibility of desorption of As species, especially in the presence of tip shadowing. In the series of images, As incorporation is small from image to image, but no notable evidence of As desorption is observed. The small flux is necessary to invoke near-dynamic conditions when considering a 400 s delay between subsequent images. Since multi-line rastering is inherent to STM imaging, any dynamic

observations are ultimately limited to the growth rate and image rate. In most cases multiple images are necessary to discern any significant alterations in the surface, suggesting that the image-to-image incorporation rate is small and adsorption dynamics are suitably observed.

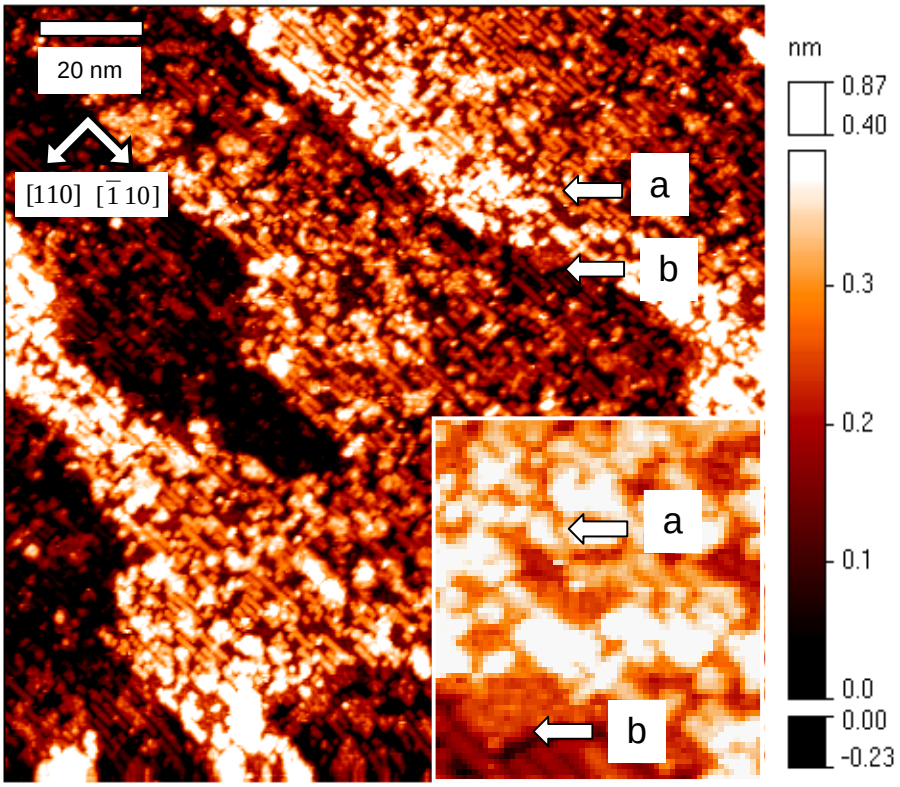

Figure 7.18: Image 06/37. Measurement parameters V = -4 V , I = 0.5 nA, Gain = 2 %. Small c(4 × 4) domains above and below. Arrow (a) points to one of the numerous small c(4 × 4) domains forming above the (2 × 4). Arrow (b) points to c(4 × 4) forming at the step edge where loosely bound As is more easily lost.

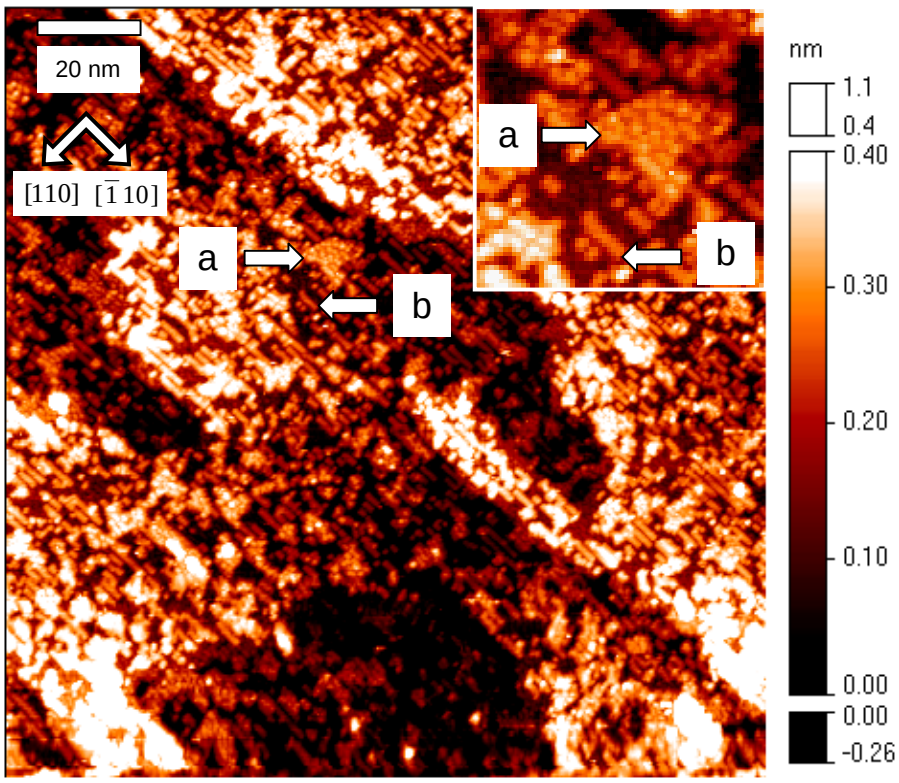

Figure 7.19: Image 17/37. Measurement parameters V = -4 V , I = 0.5 nA, Gain = 2 %. Large c(4 × 4) domains above and below. Desorbed As dimers. Arrows (a) point to a large, highly ordered c(4 × 4) formed above (2 × 4). Arrow (b) points to a small (2 × 4) domain and a darker c(4 × 4) domains forming below this original (2 × 4) reconstruction.

The next image of note is #06 (**Figure 7.18**). The c(4 × 4) islands have enlarged on the upper step (arrow a) and have also formed in relatively large size on the step below around the dark trough in the upper-centre of the image. It can also be seen that inside that larger pits the initial fractured dimer rows of image #02 have desorbed revealing a c(4 × 4) pattern beneath the (2 × 4). Most notable is the new highly-ordered c(4 × 4) domain on the step-edge (arrow b), which is known to be a catalyst for reconstruction change due to the extra dangling bonds at step edges creating loose atom bonding sites (Ouerghi et al. 2008). This domain marks a step-edge procession that can be followed through the later images. Evidence of, in the absence of an external Ga flux, a pseudo-

growth condition as a result of the excess Ga resulting from pit formation. The relatively high step density encourages step flow. However a similar argument could be applied to island growth synonymous to heteroepitaxy. This observation can only be made and strongly supported because successive imaging of the same features can be performed. Approximately 30 % of the (2 × 4) has begun to desorb and break up, though it is only on a small scale and can only been seen through careful point-by-point examination of the surface area and with comparison to earlier images.

The reconstruction transition continues in a similar manner through the following images. The change is somewhat subtle from image to image, due to the low flux rate. Concentrating on image #17 (**Figure 7.19**) the change with regard to image #06 (**Figure 7.18**) is marked and striking. The c(4 × 4) domains above (light) and below (dark) are now both obvious and clear under the current resolution. The (2 × 4) dimer rows are scattered across the surface but are significantly smaller in number (arrow b). Arrow a points to one of the larger islands, where the c(4 × 4) domain structure is clearly visible. It is plausible that this island, as with the nearby step edge, is growing as a result of Ga incorporation along its edge. Two c(4 × 4) domains are now apparent: firstly is the highly ordered domain on the larger islands and step edges and second is a more disordered, low range reconstruction. The former likely corresponds to the traditional c(4 × 4) with 3 As-As dimers in the upper atomic layer, whereas the latter, due to its disorder, is more likely a combination of As-Ga hetero-dimers and other non-uniformities. Clustering of Ga at B-type step edges has been previously observed for Ga deposition in the absence of an As flux (Tsukamoto et al. 1999), however in this image no Ga-rich clusters are observed since the impinging As flux would quickly create a disordered As-terminated Ga-rich c(4 × 4) like-reconstruction, as observed in the images. It is postulated here that disorder to the traditional c(4 × 4) pattern is injected in order to bond the excess Ga. Hence such a structure (disorder) should be transient and should be limited to smaller islands/atom sites close to step edges. Once established, islands grow and incorporate their excess Ga in preferred sites in the 3rd atomic layer and the ordered pattern emerges. This image can be compared directly to **Figure 6.30** which shows the termination of reconstruction change from (2 × 4) to c(4 × 4), exhibiting both domains in similar proportions. Both samples were prepared under the same temperature conditions,

however **Figure 6.30** was prepared *in vacuo* in the MBE chamber, and both images show ordered and disordered c(4 × 4).

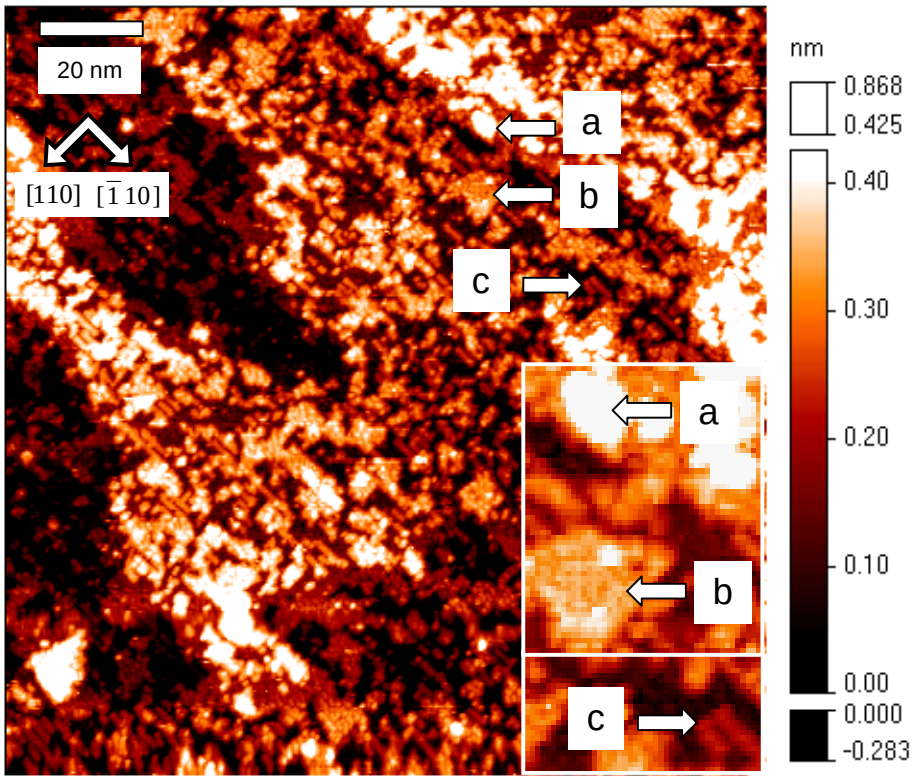

Figure 7.20: Image 25/37. Measurement parameters V = -4 V , I = 0.5 nA, Gain = 2 %. Upper step almost completely c(4 × 4). Arrow (a) indicates one of the many small c(4 × 4) island that has formed above the (2 × 4) on the upper-step. Arrow (b) points to a large, highly ordered c(4 × 4) island now common to the images. Arrow (c) points to a residual (2 × 4) cluster.

Moving ahead in time to image #25 (**Figure 7.20)** it can be seen that the c(4 × 4) reconstruction is dominant on the surface, especially on the upper terrace where almost no (2 × 4) remains (arrow a). The reconstruction gradient is due to the afore mentioned shadowing effect. Indeed, it is only the bottom-left corner that still has significant (2 × 4) structure, a fact due to the tip shadowing that portion of the sample for a significant proportion of the imaging time. The larger island (arrow b) remains highly ordered and has increased in diameter from the previous image, providing evidence of step edge

incorporation. The smaller islands have a variety of stoichiometries, some displaying hetro-dimers and As-As dimers in long chains, rather than the 3-in-a-row expected on the top atomic layer of c(4 × 4). The low temperature of this experiment hinders Ga mobility which may cause the high density of small islands.

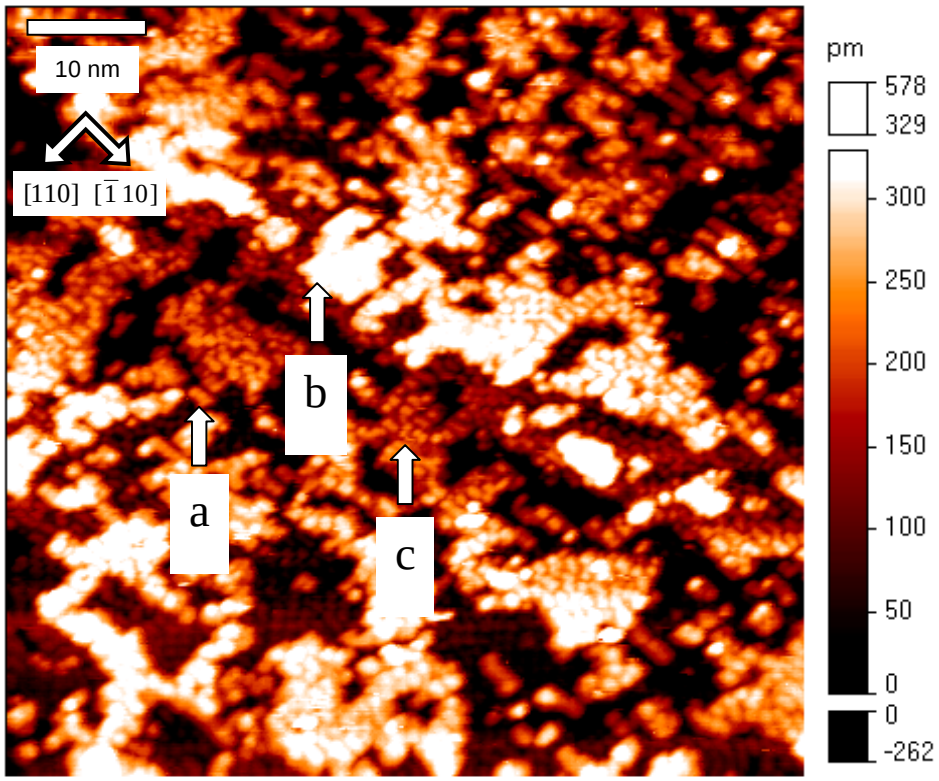

Figure 7.21: Image 37/37. Measurement parameters V = -4 V , I = 0.5 nA, Gain = 2 %. Complete conversion to c(4 × 4) 66 nm x 66 nm. Arrow (a) points to one of the small, residual (2 × 4) domains. Arrow (b) indicates coalesced larger c(4 × 4) islands formed above (2 × 4) on upper step. Arrow (c) indicates large c(4 × 4) islands coalescing with the step-edge.

The final image in the series shows the complete conversion from (2 × 4) to c(4 × 4) of a sample surface prepared in the STM chamber under an As flux during imaging (**Figure 7.21**). This shows the smaller islands coalesce with the larger islands and the ordered

c(4 × 4) reconstruction dominates (arrow b). The step edge toward the top of the image has begun to coalesce with the larger islands here (arrow c), where further Ga has incorporated. The planarization of the layer could result from Ga transport from weakly bound hetero-dimers and similar disordered binding, since very little (2 × 4) now remains to contribute to mass transport (arrow a).

Apart from random As dimers scattered across the surface, no evidence of γ(2 × 4) was identified. The transformation was suitably slow to allow time for a transient reconstruction to arise. This suggests that RHEED evidence of a transient reconstruction is due to either combinations of co-existing (2 × 4) and c(4 × 4) domains or the γ(2 × 4) reconstruction as observed by RHEED results not from an additional As dimer but from Ga incorporation into the β2(2 × 4) pattern. Such incorporation would provide temporary storage for the access Ga produced by pit formation.

The images were recorded under a very small As flux and hence conversion took place over a period of 4 hours. The actual conversion time for the sample may be shorter, as the tip still shadows the image area and hence slows the reconstruction change. Investigation of the surrounding sample area revealed similar c(4 × 4) surface structures, showing that the conversion was sample wide and complete.

7.6 Results 3: MBE at 400 ℃

The deposition of a thin film (~ 1.7 ML) of InAs on GaAs in the temperature range 350 - 500 °C results in a wetting layer with an evolution to S-K growth of small 3D islands commonly termed quantum dots (QD). The growth stage is discussed in full in **Chapter 2**, though can be generalised into two main areas of interest: wetting layer growth and quantum dot formation.

In the following section both In and As e-beam sources are employed in the STM chamber in order to observe the two areas in turn. **Section 7.6.1** reports the dynamic growth of the wetting layer from the initial GaAs (2 × 4) / c(4 × 4) to the formation of InAs (n × 3). Whereas **section 7.6.2** explores the evolution of the mature InAs wetting layer into the S-K regime that ultimately leads to 3D growth in the form of QDs.

7.6.1 Wetting Layer Formation

A GaAs(001)-(2 × 4) surface was prepared as outlined in **section 7.4**. After transfer to the STM chamber the sample was heated to 400 °C for 9 hours prior to scanning. The surface showed good (2 × 4) reconstruction as expected under these conditions from the results in **section 7.4.4**.

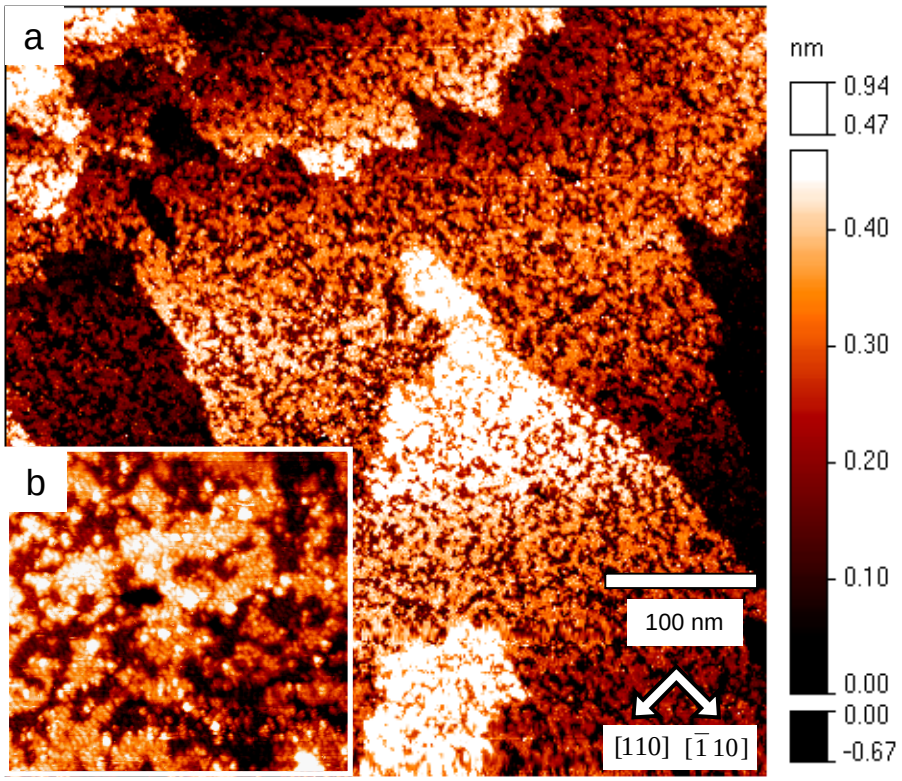

Figure 7.22: a) Image 00/46. Initial GaAs c(4 × 4) and (2 × 4) surface with <0.1 ML InAs. The surface displays a broken c(4 × 4) pattern, indicating the (2 × 4)/c(4 × 4) transition is incomplete, b) Image #00a/46. High resolution image of <0.1 ML of InAs on GaAs.

Initially the As source shutter was opened and the surface was scanned at low resolution where the emergence of c(4 × 4) islands and pits could be seen clearly on the (2 × 4) surface. Before the (2 × 4) to c(4 × 4) transition was completed the In source was opened. Imaging was hence performed in the presence of both source fluxes.

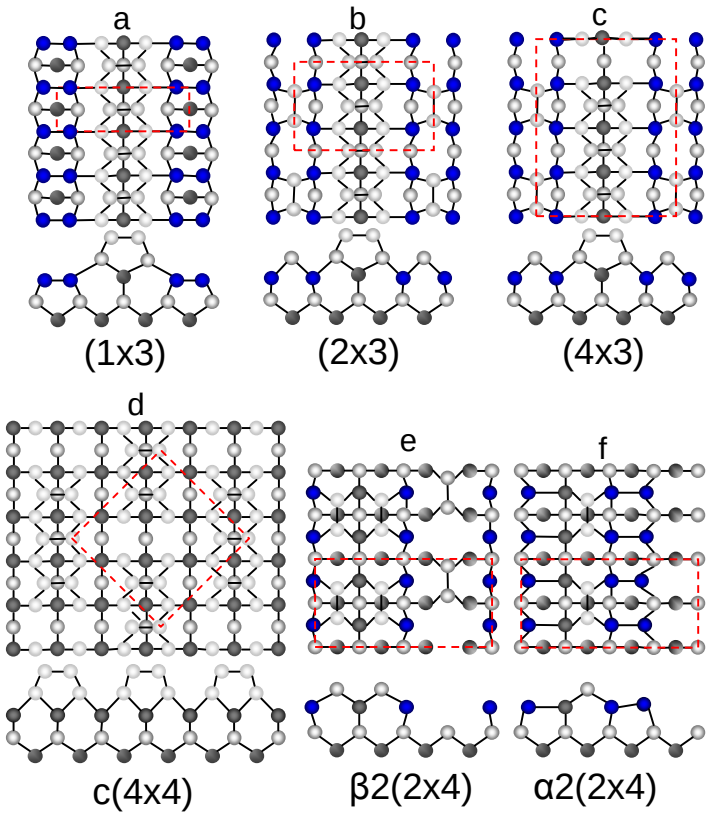

Figure 7.23: : InAs/GaAs(001) reconstructions showing additional In bonding, a) (1 × 3), b) (2 × 3), c) (4 × 3), d) c(4 × 4) e) In:Ga = 2:1 $\beta 2_{In}$(2 × 4) with relaxed ridges f) In:Ga = 3:1 $\alpha 2_{In}$(2 × 4) with excess In in the trenches. White: As, grey: Ga, blue: In.

Figure 7.22a shows image #00 of a series of 46 captured whilst the surface was under both an As and In flux. The only exception is image #00a (**Figure 7.22b**) which was taken directly after image #00 with only the As cell open. This was to investigate the surface reconstructions after a single image without altering the surface with further In flux. **Figure 7.22a** shows a 1 ML rough morphology commonly observed during a part-wise transformation from (2 × 4) to c(4 × 4) under an As flux (Bell et al. 2000). From the inset (**Figure 7.22b)** it is clear the surface is rough with a mixture of 2× (0.8 nm) and 4× (1.6 nm) along [110], spread over 3 atomic layers. The 2D islands of the establishing c(4 × 4) reconstruction are currently mostly isolated. The presence of alloyed (n × 3) is negligible at this stage, as expected for this surface and deposition (Belk et al. 1997).

There is the further consideration of the tip shadowing the sample and locally slowing growth as discussed in **section 7.5 Results 2: As overpressure at 400 °C.**

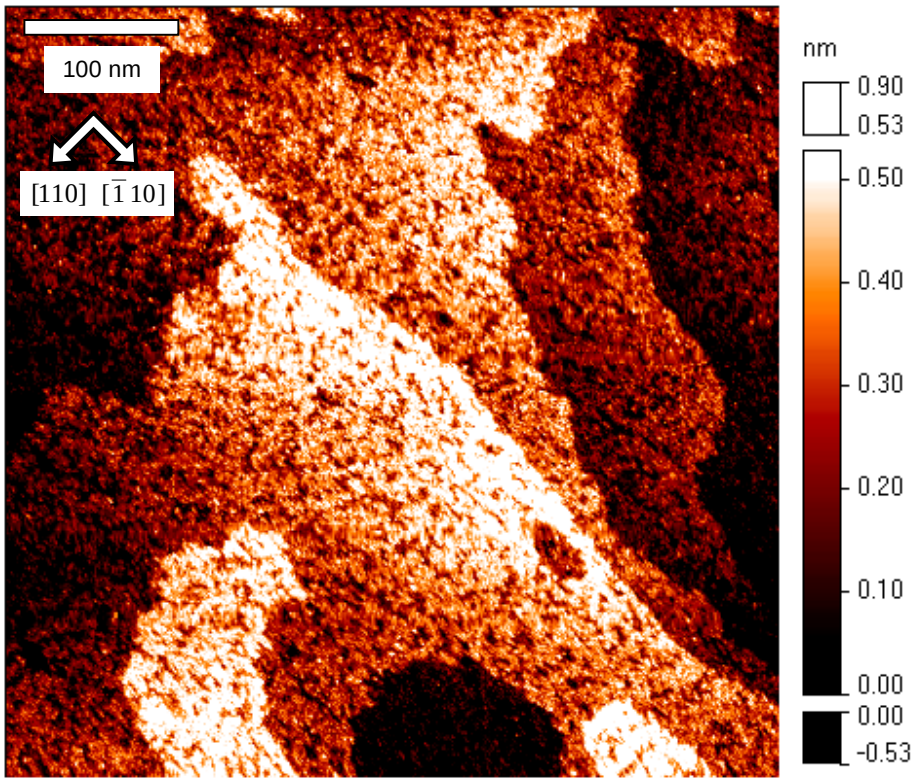

Figure 7.24: Image 24/46. 2D growth of InAs (n × 3) on same level as GaAs c(4 × 4). The surface has planarized from the initial rough state.

The order of the (n × 3) where n = 1, 2 or 4 (**Figure 7.23a-c**) cannot be ascertained from the current resolution. Theoretical works (Kratzer et al. 2002; Kratzer et al. 2003; Penev et al. 2004) have predicted that (2 × 3) is more energetically favourable with $In_xGa_{1-x}As$ composition: x = $^2/_3$. However, experimentally, the alloyed (n × 3) WL is disordered, incommensurate and possesses varied stoichiometry. Island height and coalescence can be analysed in order to understand the WL evolution from mixed (2 × 4)/c(4 × 4) up to initial 3D growth. It is worthy of note that the (n × 3) and c(4 × 4) shown in **Figure 7.23a-d** all form on the same atomic level and all have their upper most dimers aligned in

the [110] direction (Belk et al. 1996). Thus, the surface undergoes "healing" from the initial roughening caused by the (2 × 4) to c(4 × 4) transformation. This can be seen in the form of 2D growth from images #01-24. This is noted as the first stage in the formation of the wetting layer where the InAs adopts the homogenous growth model of GaAs (Heyn 2001). The isolated c(4 × 4) islands begin to coalesce and adopt alloyed InGaAs (n × 3) reconstruction.

At ~1 ML InAs, the surface is covered in coalescing 2D islands (**Figure 7.24**). A comparison with previous and following images shows that the surface is at its flattest stage. All islands are 1 ML in height and display disordered (n × 3) reconstruction. A point by point comparison of **Figure 7.22** and **Figure 7.24** can be used to determine the WL evolution from 0 to 1 ML. The most apparent surface feature from image #00 (**Figure 7.22**) and image #24 (**Figure 7.24**) is the absence of type-A step flow. The central "peninsula" feature and the longer steps in the right of the image exhibit only subtle change. Type-A steps, perpendicular to [110], have been observed to exhibit negligible or even negative growth (Gong et al. 2002); whereas type-B steps, parallel to [110] grow rapidly. The dominant type-B step at the top of the image has progressed around 10 nm from its original position. This progression is also evident in other surface features formed by type-B steps.

Two conclusions can be drawn from this anisotropic growth. Firstly, the low As:In flux ratio of 10:1 has not aided the step flow growth mechanism, even though the In diffusion length should be suitably enhanced. Most of the first ML has, therefore, grown via 2D island coalescence and (n × 3) integration into the existing c(4 × 4) atomic layer. The form of the alloy and the extent of c(4 × 4) dissolution is unclear. Secondly, whilst the islands have increased in areal size, some islands have decreased in width. This narrowing is caused by Ga detachment from type-A steps. If the (n × 3) reconstruction at 1 ML is assumed to possess composition: $In_{2/3}G_{1/3}As$, even with the deposition of pure InAs, intermixing must occur between the upper atomic layers (Kita et al. 2002). **Figure 7.24** shows many small InAs islands nucleating on top of the larger islands before they coalesce. These upper layer nucleation sites are therefore preferential to step edges on the atomic plane below. Perhaps formation of (n × 3) within the existing c(4 × 4) atomic plane is limited by Ga availability *and* In incorporation. The loosely bound Ga from step

edges provides a source for the Ga fraction in the (n × 3) layer, whilst the steps themselves provide low strain sites for In incorporation into the sub-surface layer at step edge sites. However once the entire step is In terminated, future step growth is strain limited. The upper two layers are assumed to experience segregation (Dehaese et al. 1995), it is possible In segregates out of these sites before the larger islands finally coalesce as observed in **Figure 7.25**.

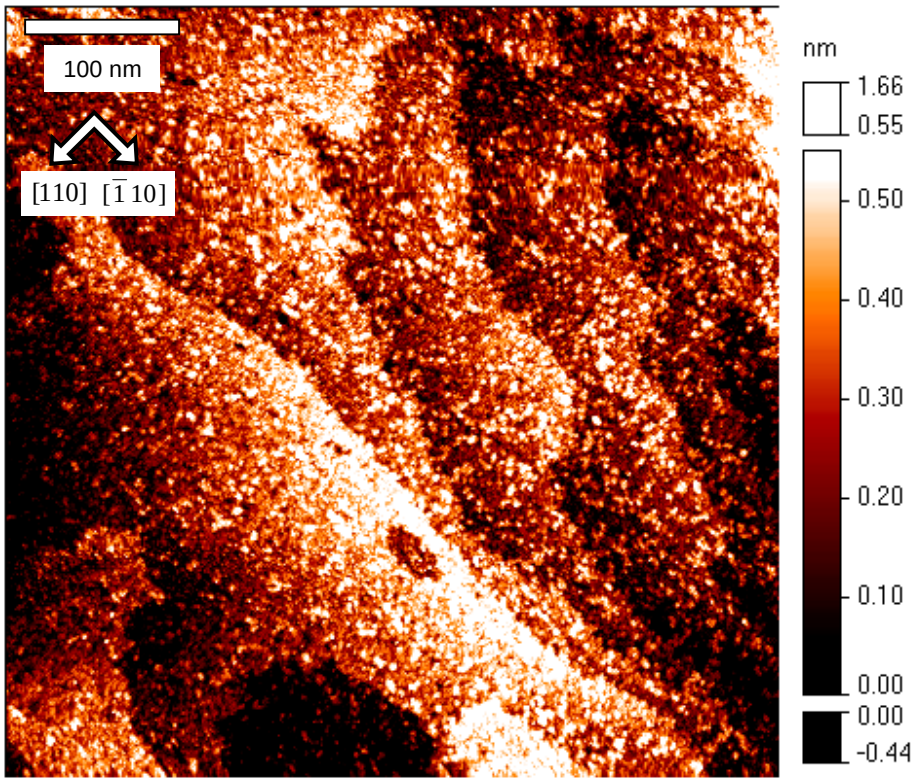

Figure 7.25: Image 28/46. Reconstruction evolution induced roughness. 0.5 - 1.5 ML islands from various reconstruction domains have roughened the surface.

After 1.0 ML, the surface quickly begins to roughen. It was initially assumed that these were 2D islands and that the surface was entering a pre-QD stage, where 1 or 2 ML high islands form in a transition stage close to critical thickness (Belk et al. 1997; Bell et al. 2000). Upon investigation the islands are not 1 or 2 ML in height, but mostly 0.5 or

1.5 ML. This means the roughening at ~1.1 ML is not due to islanding growth, which is discussed later. What is the nature of these 0.5 or 1.5 ML islands? Consider the surface reconstructions present. The initial (2 × 4) is mostly transformed to c(4 × 4) at the onset of growth. The transformation from (2 × 4) to c(4 × 4) produces 3 atomic layers of roughness where the phases co-exist. When the (2 × 4) / c(4 × 4) is replaced by (n × 3), i.e. at 1 ML InAs coverage, no (2 × 4) remains, however the 2 atomic steps of roughness remain in the form of 2D islands. The fact that c(4 × 4) evolves to (n × 3) whilst planarising the surface is acceptable, since these reconstructions co-exist on the same atomic layer. The theoretical prediction (Kratzer et al. 2003) and experimental observation (Kita et al. 2002) of $In_{2/3}G_{1/3}As$ (n × 3) transforming to InAs (2 × 4) would again introduce 3 atomic layers of roughness where the phases co-exist. The group III bonding sites of the accepted β2(2 × 4)-model could allow for low strain In incorporation resulting in $\beta2_{In}(2 \times 4)$ **(Figure 7.23e)**. $\beta2_{In}(2 \times 4)$ has the same As dimer structure as β2(2 × 4), but instead of 6 Ga atoms in the second atomic layer, the 4 outer atoms are replaced with In. The $\beta2_{In}(2 \times 4)$ shown maintains the same group III composition ($In_{2/3}Ga_{1/3}$) as the (n × 3) but the missing group III species every 4^{th} atom allows the In to laterally relax. **Figure 7.25** shows image #28, where the additional roughness produced is clearly visible. Any $\beta2_{In}(2 \times 4)$ where the In has laterally relaxed into the trench would be distinguishable from typical (2 × 4) by the narrowing of the trench width in STM images.

The InAs epilayer is now ~1.1 ML. The surface undergoes little change between images #28 and #34, where the 2D growth is becoming hindered by increasing strain and reconstruction change is dominant, a result expected from the WCNH mechanism (Walther et al. 2001; Cullis et al. 2002; Cullis et al. 2005). The WL is increasingly strained and In cannot find sufficient bonding sites to perpetuate coalescing epitaxial growth. However, In is being supplied at a constant rate, hence the In must be incorporated. The upper surface requires a critical In population under the WCNH mechanism to achieve 3D growth, however, In incorporation would lead to increased strain. It is therefore necessary for the In bonds to bend, effectively increasing the dimer bonding length, in order to partially relax this increasing strain. Now the surface begins to roughen stacking 2D islands of small areal coverage. This partial relaxation would

support In incorporation up to the 2D to 3D transition at 1.5 ML at 400 °C. No evidence of a floating In population is observed in the STM images during the final phase of the S-K transition. Whilst no direct evidence can be inferred from the images presented, excess In could be stored in the missing dimer trenches of the typical α2(2 × 4)-model reconstruction resulting in $\alpha2_{In}(2 \times 4)$ as shown in **Figure 7.23f**. $\alpha2_{In}(2 \times 4)$ has the same structure as α2(2 × 4) with a missing As dimer in the upper atomic layer, however the As dimers in the trench are now broken to accommodate the excess In. This structure disobeys the electron counting model, however stoichiometric variations, resulting in disordered rows and missing dimers could restore surface charge neutrality (Bone et al. 2006). The $\alpha2_{In}(2 \times 4)$ reconstruction displays a $In_{3/4}Ga_{1/4}As$ composition, approaching the 85 % In composition fraction suggested by WCNH to precede QD formation (Walther et al. 2001; Cullis et al. 2002; Cullis et al. 2005). It is clear that the As rich reconstructions no longer allow for additional In incorporation. In an extension of the established reconstruction progression, the small 2D islands may contain In rich domains of either (3 × 1) which exists in the same atomic plane as (2 × 4) or (4 × 2) which exists in the same atomic plane as (1 × 3) and c(4 × 4). Either domain would accommodate the excess In and their instability would inherently support large In adatom mobilities. This phenomenon requires further investigation.

7.6.2 S-K Transition

This section follows directly from **Section 7.6.1**, discussing the last images of the series. In images #35 to #46 a number of unstable 3D structures appear and vanish. These are typically 1.5 nm in height and 10 - 15 nm in diameter. Assuming they are hemi-spheroids in shape, the volume delineates 100 - 150 atoms, suggested to be the critical mass for 3D structures (Krzyzewski et al. 2002; Krzyzewski et al. 2003).

Figure 7.26 shows the upper-left area of images #35, #39, #40 and #46. Note that this is the area which receives the largest In and As dose and hence will exhibit the 2D to 3D transition before the lower section of the image.

In **Figure 7.26a** (upper left of Image #35) the arrow points to a white feature which marks the first observed 3D island, a notably small QD-like structure with base diameter 11 nm and height 1.5 nm. The tip slightly clipped the formation of the dot, and

gave it a flat upper edge. This is possibly due to the relatively large forces present and electrical bias of the apex. The area is not a tip drop, since there is no contrast change or distortion of the image. The cluster remains through one image and vanishes in the next. **Figure 7.26b** shows the same area of Image #39 where three 2D islands now occupy the precursor QD site, further evidence that this is not a tip drop. The ~100 atoms of the QD must now be present on the surface, and would cover a ~60 nm^2 area. Since there is little change in the island density between the two images, it is probable that the afore mentioned In rich reconstructions absorbed the adatom population.

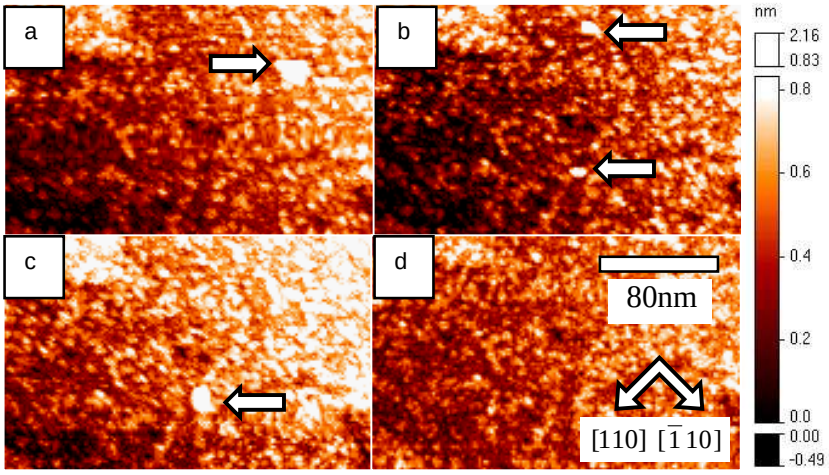

Figure 7.26: Unstable 3D islands: a) Image #35: arrow points to a dot, the upper side has been "clipped" by the tip, giving it a flat edge, b) Image #39: the dot from (a) has devolved into a cluster of 2D islands, two new dots have formed indicated by the arrows. The lower dot has been "clipped" by the tip, c) Image #40: the lower dot from (b) is still present (arrow) whereas the upper dot has devolved, d) Image #46: no dots are present on this area of the sample.

Two 3D structures are indicated by arrows in **Figure 7.26b**, note the lower structure has once again been clipped by the tip. Both structures are small, with 1.5 nm height and 10 nm diameter. In all cases the small 3D islands do not form on a noticeable 2D island footprint and no 2D island of equal base diameter is present after the 3D islands have dissolved. Very small islands, little more than dimer chains by their areal coverage, are however constantly appearing and disappearing amidst re-entrant single atomic layer "islands", indicative of isolated In-rich reconstruction domains. This highly mobile In

population is bound to lattice sites by unstable reconstruction stoichiometries and, by way of small In-rich nucleation centres, could provide the mechanism for QD formation (Migliorato et al. 2002).

The lower structure of **Figure 7.26b** is still present in image #40 (**Figure 7.26c**) and is now fully formed. This re-entrant behaviour has been independently observed for samples prepared *in vacuo* (Ramachandran et al. 1997a; Ramachandran et al. 1997b) though it was not clear whether it was merely a consequence of the quenching procedure. In this case the re-entrant behaviour is not a result of quenching. The small 3D islands are inherently quasi-stable, however after successfully imaging the 3D islands from image to image it seems the presence of the tip is not responsible for their re-entrant behaviour.

In image #46 (**Figure 7.26d**) the two islands have vanished from this area whilst other islands have formed elsewhere across the 500 x 500 nm^2 image (not shown). After image #46, the upper right of the image becomes heavy with 3D islands of 50 - 100 nm diameter and 10 - 15 nm height, as expected from low deposition rates at low temperatures (Joyce et al. 2000). The transition in the upper quadrant of the image is hence complete and mature QDs have formed.

7.7 Summary

The sample heating profile is somewhat higher in the STM stage when compared to the MBE chamber. Chiefly this is a result of the absence of cooling in the STM chamber and hence a high average ambient temperature. However once adjustments have been made to compensate for this fact, the temperatures achieved in the STM stage are repeatable and stable.

The STM head typically needs around 6 hours to reach equilibrium conditions in terms of drift after heating has been applied to the sample. Whilst imaging can be performed inside that 6 hour window, the Z-drift correction requires activation of the coarse piezo to manually correct drift which ultimately moves the tip to a new and random area of the sample. To this end the heating of a GaAs(001)-β2(2 × 4) surface can be performed up to ~ 450 °C without problem, however operating at higher temperatures would require an As over pressure in order to stabilise the surface.

The e-beam sources performed adequately for both group III and V deposition. In terms of group V, the As gave a constant flux from 200 nA to 1000 μA flux current, which proved suitable for reconstruction changes and MBE growth respectively. The main problem with the sources is their short charge lifespan, typically 8 - 12 hours depending on flux levels. This results in the requirement for a high frequency of replenishments and system bakes for III-V MBE growth where the group V element is typically over supplied 10:1.

The group III e-beam source was operated with In. The flux levels and hence growth rates were lower than for normal MBE, however the experiment successfully observed InAs/GaAs growth for these parameters. With the e-beam sources in operation, images became significantly effected. Scan lines are seldom avoided, however they tend to occupy a small fraction of the picture. Tip shadowing is apparent on the surface, especially in the case of MBE growth. Scanning toward the source has proven to reduce shadowing, however the actual degree of shadowing and possibilities to reduce the effect further require investigation.

Reconstruction resolution on GaAs(001) requires lateral resolution < 1.6 nm for (2 × 4) and < 0.8 nm for c(4 × 4). Reconstruction stability of the highly ordered As-rich β2(2 × 4) surface has been investigated. At temperatures < 300 °C, the initial surface is inherently stable. However as the temperature is increased the As atoms gain enough thermal energy to reorder into more thermally stable reconstructions. Between 300 °C and 350 °C, there is not enough thermal energy to instigate a surface-wide reconstruction transformation, however localised regions can reconstruct, especially at weakly bound step edge sites. The β2(2 × 4) surface was found to be stably thermal in the absence of an As flux between 350 °C and 410 °C, important for high temperature STM observations of the (2 × 4) surface. Upon exceeding this narrow temperature band the surface swiftly roughened as As-dimers were desorbed from the upper layer. The temporary storage of Ga in localised (1 × 3) was observed, and the parallels to InAs/GaAs whilst apparent require further investigation.

A sequence of images have been presented showing near-dynamic observation of the As-rich reconstruction evolution from β2(2 × 4) to c(4 × 4) under an As flux. The multi-layer c(4 × 4) formed both above the β2(2 × 4) dimer rows and beneath where the

original β2(2 × 4) desorbed. Evidence has been presented that supports highly ordered c(4 × 4) domain propagate via step-edge incorporation of islands. Small islands initially exhibit mixed reconstruction, indicating hetero-dimers transiently exist to incorporate the excess Ga on the surface. Whilst desorption of β2(2 × 4) occurs readily at step edges, the results prove that random domains desorb throughout the original ML creating a roughened 2 ML high c(4 × 4) surface.

InAs deposition up to ~1 ML has been shown to planarize the surface due to alloyed InGaAs(001)-(n × 3) wetting layer and GaAs(001)-c(4 × 4) occupying the same atomic plane. Alloyed growth appears to be supported by Ga desorption from type-A steps. After ~ 1.1 ML mixed reconstruction domains wrought roughness upon the surface, as layer-by-layer epitaxial growth is slowed. Before critical WL thickness, small re-entrant 3D islands of up to 150 atoms were then observed on the surface. These quasi-stable structures have been observed dynamically in the absence of quenching effects. The increasingly In-rich reconstruction domains have been proposed to occupy different atomic planes on the surface, resulting in sub-ML roughness. These domains could provide local storage for In adatoms when 2D layer-by-layer growth is hindered and whilst 3D islands exhibit re-entrant behaviour.

7.8 Reference

A.R. Avery, D.M. Homes, J. Sudijono, T.S. Jones and B.A. Joyce (1995) Surf. Sci. **323**(1-2): 91.

J.G. Belk, C.F. McConville, J.L. Sudijono, T.S. Jones and B.A. Joyce (1997) Surf. Sci. **387**(1-3): 213.

J.G. Belk, J.L. Sudijono, D.M. Holmes, C.F. McConville, T.S. Jones and B.A. Joyce (1996) Surf. Sci. **365**(3): 735.

G.R. Bell, J.G. Belk, C.F. McConville and T.S. Jones (1999) Phys. Rev. B. **59**(4): 2947.

G.R. Bell, T.J. Krzyzewski, P.B. Joyce and T.S. Jones (2000) Phys. Rev. B **61**(16): R10551.

P.A. Bone, J.M. Ripalda, G.R. Bell and T.S. Jones (2006) Surf. Sci. **600**(5): 973.

A.G. Cullis, D.J. Norris, M.A. Migliorato and M. Hopkinson (2005) Appl. Surf. Sci. **244**(1-4): 65.

A.G. Cullis, D.J. Norris, T. Walther, M.A. Migliorato and M. Hopkinson (2002) Phys. Rev. B **66**: 081305.

O. Dehaese, X. Wallart and F. Mollot (1995) Appl. Phys. Lett. **66**(1): 52.

Q. Gong, R. Nötzel, H.P. Schönherr and K.H. Ploog (2002) Physica E **13**(2-4): 1176.

C. Heyn (2001) Phys. Rev. B **64**(16): 165306.

M. Itoh, G.R. Bell, A.R. Avery, T.S. Jones, B.A. Joyce and D.D. Vvedensky (1998) Phys. Rev. Lett. **81**(3): 633.

P.B. Joyce, T.J. Krzyzewski, G.R. Bell, T.S. Jones, S. Malik, D. Childs and R. Murray (2000) Phys. Rev. B **62**(16): 10891.

K. Kanisawa and H. Yamaguchi (1997) Phys. Rev. B. **56**(19): 12080.

T. Kita, O. Wada, T. Nakayama and M. Murayama (2002) Phys. Rev. B **66**(19): 195312.

A. Kley, P. Ruggerone and M. Scheffler (1997) Phys. Rev. Lett. **79**(26): 5278.

P. Kratzer, E. Penev and M. Scheffler (2002) Appl. Phys. A **75**(1): 79.

P. Kratzer, E. Penev and M. Scheffler (2003) Appl. Surf. Sci. **216**(1-4): 436.

T.J. Krzyzewski, P.B. Joyce, G.R. Bell and T.S. Jones (2002) Phys. Rev. B. **66**(12): 121307.

T.J. Krzyzewski, P.B. Joyce, G.R. Bell and T.S. Jones (2003) Surf. Sci. **532**: 822.

V.P. LaBella, M.R. Krause, Z. Ding and P.M. Thibado (2005) Surf. Sci. Rep. **60**(1-4): 1.

J.G. LePage, M. Alouani, D.L. Dorsey, J.W. Wilkins and P.E. Blöchl (1998) Phys. Rev. B. **58**(3): 1499.

M.A. Migliorato, A.G. Cullis, M. Fearn and J.H. Jefferson (2002) Phys. Rev. B **65**(11): 115316.

A. Ohtake, J. Nakamura, S. Tsukamoto, N. Koguchi and A. Natori (2002) Phys. Rev. Lett. **89**(20): 206102.

B.G. Orr, C.W. Snyder and M. Johnson (1991) Rev. Sci. Inst. **62**(6): 1400.

A. Ouerghi, A. Cavanna, D. Martrou, Y. Garreau and B. Etienne (2008) Surf. Sci. **602**(9): 1631.

E. Penev, S. Stojković, P. Kratzer and M. Scheffler (2004) Phys. Rev. B **69**(11): 115335.

T.R. Ramachandran, R. Heitz, P. Chen and A. Madhukar (1997a) Appl. Phys. Lett. **70**(5): 640.

T.R. Ramachandran, R. Heitz, N.P. Kobayashi, A. Kalburge, W. Yu, P. Chen and A. Madhukar (1997b) J. Cryst. Grow. **175**: 216.

S. Tsukamoto, G.R. Bell and Y. Arakawa (2006) Micro-Elec. J. **37**(12): 1498.

S. Tsukamoto and N. Koguchi (1999) J. Cryst. Grow. **201-202**: 118.

S. Tsukamoto, M. Pristovsek, B.G. Orr, A. Ohtake, G.R. Bell and N. Koguchi (2002) arXiv:physics/0202013v1.

T. Walther, A.G. Cullis, D.J. Norris and M. Hopkinson (2001) Phys. Rev. Lett. **86**(11): 2381.

Z.M. Wang and G.J. Salamo (2003) Phys. Rev. B. **67**(12): 125324.

H. Yang, V.P. Labella, D.W. Bullock and P.M. Thibado (1999) J. Vac. Sci. & Tech. B **17**(4): 1778.

Chapter 8: Conclusions and Future Work

8.1 Summary and Conclusions

The first stage of this work involved developing a prototype apparatus into an operational MBSTM. Integrating MBE into a pre-existing STM system necessitated addressing the problems of sample heating and source operation. Sample heating concerns the ability to supply repeatable and accurate sample heating regimes with high stability in order to accommodate STM imaging. Source operation requires low-heat e-beam cells in order to further perpetuate a stable sample temperature.

In addition, the integration of MBE into an STM system requires the inclusion of an *in vacuo* MBE system to prepare high-quality substrates for subsequent STM analysis. The e-beam sources have a maximum 0.75 cc capacity and can, therefore, only accommodate short growth cycles and low deposition rates.

Chapter 4 explored the use of samples as resistors in a direct heating (DH) methodology to facilitate sample heating. However the temperature spikes and instabilities that are inherent to the method proved detrimental to the III-V group MBE operation. The rapid quenching potential of DH was not relevant to the current study intended to obtain stable temperatures in the STM chamber, hence an overview was carried out solely for the purpose of comparison to the preferred PBNRH method.

Chapter 5 concerned the fabrication of tunnelling tips for STM. The work focused on DC in-solution etching with the intention of optimising a two-step procedure from tip production. The initial etching step identified numerous parameters that had interrelated effects on the etching procedure. Extensive parameter variations were used to identify conclusively a parameter set that could routinely produce < 10 nm ROC tips with >90 % success. The later cleaning and oxide removal focused on *in vacuo* annealing. The operation of e-beam heaters below the electron-bombardment melting point of the tips allowed efficient oxide removal to be realised. The resulting tips were proven to yield atomic resolution.

Chapter 6 provided a progression from chapters 4 and 5, investigating the suitability of PBNRH and DH for GaAs sample preparation. The work focused on the production of a flat, low defect surface suitable for STM observations. Both “clean-up” and “quenching” techniques were investigated to explore their impact on the resultant growth surface. Classic oxide desorption at 580 °C was compared to the relatively undocumented Ga desorption technique from 450 to 520 °C. Results from STM pre- and post-buffer layer growth indicated that the Ga desorption technique largely eliminated the occurrence of micro-pits that represent damage to the cleaned surface. Ga desorption requires precise flux calibrations and adatom delivery in order to perfectly compensate the oxide layer. Performing oxide removal at 520 °C under a Ga flux allows the clean up point to be accurately determined by RHEED transitions.

After clean-up, buffer layer growth proceeded with an emphasis to produce low-defect upper surfaces with both β2(2 × 4) and c(4 × 4) reconstruction. Compensation cooling on the PBNRH sample plate proved adequate in both cases. Temperature-power characteristics for this methodology proved repeatable and reliable.

Chapter 7 consisted of a culmination of the previous chapters to realise the operation of MBE in the STM chamber. A step-wise, systematic approach to source operation and high-temperature STM identified a clear path for progression toward the ultimate aim of concurrent MBE-STM operation.

The final results came in three stages. Initially stable imaging conditions were ascertained in terms of both tunnelling and the sample reconstruction. Next the first major achievement of the work involved successful imaging of the As-rich temperature stable β2(2 × 4) reconstruction undergoing a transition under an As flux to become an As-rich temperature stable c(4 × 4) structure. The reconstruction formed both above and below the original (2 × 4) and as a result a degree of roughening occurred.

This proved that simultaneous MBE and STM can be performed within the STM chamber. The final step involved applying both group III and V sources during imaging. The resulting experiment followed the GaAs (2 × 4) / c(4 × 4) surface being overgrown with a (n × 3) InAs epilayer. The surface followed a number of transitions involving 2D island growth, reconstruction induced roughening, re-entrant 3D islands and finally QD

growth. A degree of tip shadowing retarded growth, though it was evident that the fundamental dynamics of MBE growth still hold.

The successful operation of this new merger of technologies has opened up an exciting avenue for future exploration of III-V semiconductor growth dynamics. Establishing the technology in this work has provided the first step towards achieving a much better understanding of III-V surface science.

8.2 Future Work

The apparatus is fully operational, however the small e-beam sources are only sufficient for short growth cycles between openings, especially with a need to have the As overpressure some ten times greater than the group III source. It would be desirable to provide a larger As source for operation in the STM. At the time of writing, however, no such sources were available on the market.

With regard to the group III e-beam source in the STM, there is clearly a need to operate with both Ga and In. However with only a single port available, only a single element can be deposited at any given time. To this end it may be useful to begin to utilise the triple source mentioned in **Chapter 3.** However with the small crucible charges of 0.2 cc this may be unfeasible for III-V growth operation.

Even without these additional features, the MBSTM is primed to perform a number of attractive experiments, which could be carried out for the first time in real time. In the first instance these would involve deposition of group III Ga, In and Al onto GaAs(001)-(2 × 4) and GaAs(001)-c(4 × 4) to better understand the effects of strain on reconstructions and incorporation. Of particular interest is the InGaAs ternary (n × 3) reconstruction which precedes QD growth, a better understanding of the reconstruction could lead to knew knowledge in QD nucleation mechanics. Additionally an atomic scale investigation into the storage sites for In immediately prior to the S-K transition could provide a definitive insight into the mechanics of the 2D to 3D transition. In a similar manner group V As, Sb and Bi can be deposited and compared to understand how strain affects group V incorporation.

Single elemental source deposition onto other surfaces III-V and IV surfaces would be the next logical extension. MBSTM examination of anti-phase domains (APDs) on polar/non-polar III-V/IV systems could be investigated, with an aim to observe and eliminate APD formation. The stability of Ge and Si at high temperatures lend them well to high temperature STM observation, especially concerning adsorption and desorption of III-V species.

Dual source MBSTM deposition with both group III and V can be used in both homo- and hetero-epitaxial systems. The growth of GaAs/GaAs(001) (2×4) and $c(4 \times 4)$, with particular attention to island formation and Ga incorporation in the two reconstructions would be fundamental in understanding epi-layer growth. With regard to homo-epitaxy, the InAs/GaAs(001) work performed in **Chapter 7** relates to small 3D island stability and WL formation at low resolution. Other InAs/GaAs(001) studies involving QD nucleation, accretion zones, ripening, capping and self-assembly are unexplored by MBSTM. Other systems, including GaSb/GaAs and GaBi/GaAs would also prove exciting material systems.

The MBSTM performed in **Chapter 7**, followed moderate temperature ranges from 300 - 410 °C, using samples heated without As flux before high temperature scanning proceeded. For more realistic growth observations, temperatures from 400 - 600 °C should be utilised, with As overpressure throughout the heating cycle and during scanning. However such studies would deplete the As source much more swiftly.

The e-beam sources can be used for all III-V deposition in the STM chamber, however the system would require a substantial upgrade to deposit those materials in the MBE chamber. Ge is particularly required when cleaning and preparing Ge substrates, due to the damage induced by oxide removal.

The Ga oxide desorption experiment of **Chapter 6** can be extended along two avenues. Fundamentally, the whole experiment can be performed in the STM chamber with a Ga e-beam source. This would enable real time STM observation of the oxide desorption process. Further the clean-up technique can be used to create planar surfaces after oxide removal allowing e-beam lithography patterned samples to be used for a number of select site QD experiments.

MBSTM is a powerful tool for observing semiconductor growth in real time. Additional cross section techniques, such as TEM and XSTM provide complimentary analysis, especially involving post-growth annealing effects. A broad, combined study incorporating multiple analysis techniques is necessary to increase understanding of growth processes and atomic resolution MBSTM is clearly a key element for fundamental surface science studies.